Università degli Studi di Padova

Sede Amministrativa: Università degli Studi di Padova

Dipartimento di Fisica e Astronomia "Galileo Galilei"

Corso di Dottorato di Ricerca in Astronomia

XXXI Ciclo

Dynamics of Single and Binary Black Holes in Galactic Nuclei

Tesi redatta con il contributo finanziario dell'Istituto Nazionale di Astrofisica

Coordinatore:	Ch.mo Prof.	Giampaolo	Piotto
Supervisore:	Ch.ma Prof.ssa	Michela	Mapelli
Co-Supervisore:	Ch.ma Dott.ssa	Alessia	Gualandris

Dottoranda: Elisa Bortolas

November 30, 2018

A mio papà

e tu lascia ch'io guardi questi occhi
che Dio ti ha dati,
così densi di cielo –
profondi come secoli di luce
inabissati al di là
delle vette

Bellezza, A. Pozzi

Abstract

Galactic nuclei are among the dynamically richest regions in the Universe. They are often found to host supermassive black holes (SMBHs) of millions to tens of billions solar masses; plus, they frequently harbour nuclear star clusters, stellar gatherings attaining densities up to $\sim 10^7 M_\odot$ pc^{-3}. These unique features make galactic nuclei ideal laboratories for the study of a broad range of N-body dynamical phenomena, including the genesis of both low and high frequency gravitational wave (GW) sources, the ignition of tidal disruption events, the formation of stellar cusps about SMBHs.

The Milky Way nucleus, the Galactic Centre (GC), is by far the best known galactic nucleus in the Universe: it accommodates the closest known SMBH, enshrouded in a gas rich and star forming nuclear stellar cluster, whose stellar orbits can be tracked with incomparable precision. In fact, the orbital monitoring of the young S-stars, separated by less than 0.04 pc from the SMBH, provides the most compelling indication for the existence of an SMBH. Still, numerous physical processes occurring in this unique environment remain enigmatic. Theoretical arguments predict that a steep density cusp should develop near the SMBH, but the observed density profile of giant stars appears shallower than expected; furthermore, a large population of neutron stars is predicted to closely orbit the SMBH, but only a single pulsar has been observed within the innermost parsec.

The significant number of young and massive stars inhabiting the GC implies that supernova (SN) explosions should occur frequently in this region. The associated SN kicks may have a relevant dynamical role at the GC, as they effectively reshuffle stellar orbits near the SMBH. Motivated by this, in Chapter 2 I address the role of SN kicks occurring in young binary systems located in the GC innermost parsec. I find that SN kicks typically either unbind neutron stars from the SMBH, or set them on very eccentric orbits; therefore, the apparent dearth of neutron stars in the GC might be a result of SN kicks. In contrast, stellar black holes do not change their orbits significantly in response to the kick. Thus, several star formation episodes in the GC may have built-up a concentration of stellar black holes within the SMBH sphere of influence; this hypothesis is supported by the recent detection of a cusp of quiescent accreting X-ray binaries in the GC innermost parsec.

SN kicks may play an additional crucial role, if they occur in the close vicinity to the SMBH: they may induce the generation of extreme mass ratio inspirals (EMRIs), i.e. GW driven decays of stellar mass compact objects onto SMBHs. In the standard picture, EMRIs are induced by repeated two-body scatterings between stars; in Chapter 3, I show that SN kicks may effectively funnel infant black holes and neutron stars on low angular momentum orbits, promoting their decay onto the SMBH via GW emission. By applying this argument to the S-stars in the GC, I predict one SN kick out of 10^4 to induce an EMRI event. My result implies a rate

of SN-driven EMRIs up to $\sim 10^{-8}$ per Milky Way per year: such rate is only one order of magnitude smaller than the standard estimate obtained assuming EMRIs to be promoted by repeated two body encounters between stars.

Investigations on EMRI events are crucial as these phenomena are predicted to be a promising GW source detectable by the forthcoming space-borne LISA observatory, the straw-man mission selected by ESA for L3. However, what is currently believed to be the loudest source target for LISA is the coalescence of SMBH binaries (BHBs); in fact, BHBs are suspected to form in large numbers along the cosmic epochs, being a natural outcome of repeated collisions between galaxies. The paramount importance of LISA detections stems from the fact that the signals released by EMRIs and BHB mergers will deliver unprecedented information on SMBH masses, spins and host environments; plus, they will provide an exquisite probe for general relativity and for the hierarchical clustering of galaxies and SMBHs.

The debate on whether a BHB could actually find its way to the final coalescence within the age of the Universe has been standing for a long time. Before reaching the GW emission stage, a BHB evolving in a gas-poor nucleus shrinks primarily by slingshot ejections of stars intersecting its orbit: at the beginning of this phase, the BHB promptly expels from the galaxy almost all stars able to reach its neighbourhood. After that, the BHB shrinking can persist only if any physical process can guarantee a steady repopulation of the binary loss cone, the region of phase-space containing stars that can interact with the BHB. In fact, initial studies of BHBs evolving in spherical systems suggested that the separation between the two SMBHs cannot drop below ~ 1 pc. However, there is circumstantial evidence that SMBH pairs are rare and BHBs are more likely to merge: this motivated a series of works aimed to solve the so-called *final parsec problem*.

In Chapter 4, I contribute to the forge of possible solutions by exploring the infall of a young massive stellar cluster onto a BHB. Young clusters are common in galactic nuclei, and may form in a burst of star formation following the galaxy merger. My results show that a cluster approaching the BHB along a non-zero angular momentum orbit fails to enhance the BHB shrinking; in contrast, the same cluster reaching the BHB on a radial orbit considerably contributes to the loss cone refilling, as the BHB semimajor axis shrinks by $10 - 15\%$. My results indicate that the angular momentum of the infalling cluster plays a crucial role in the BHB hardening.

While the infall of a star cluster represents a promising way to shorten the binary path to coalescence, a more general solution to the final parsec problem is currently believed to reside in the non-sphericity of the host galaxy. If the host galaxy is triaxial (e.g. as a result of a galaxy merger), large scale gravitational torques ensure the diffusion of stars in angular momentum space, guaranteeing a steady repopulation of the BHB loss cone. This conclusion initially came from direct summation N-body simulations, whose reliability was questioned due to the modest achievable number of particles ($\lesssim 10^6$). For instance, resolution limits enhance the amplitude of the BHB random walk, artificially boosting the loss cone refilling. In Chapter 5, I explore the significance of this spurious effect via a suite of galaxy merger simulations. I show that Brownian motion considerably enhances the binary shrinking rate in runs with less than 10^5 objects, while it does not significantly affect

the evolution of BHBs in simulations including more than a million objects. These findings provide more reliability to the conclusion that non-spherical gravitational torques ensure an efficient binary shrinking via three-body stellar scatterings.

While the influence of the galactic shape on the BHB shrinking rate has been largely explored, yet little is known about the opposite effect, i.e. the influence of a BHB on the morphology of its host stellar system. In Chapter 6, I show that BHBs have a strong impact on the geometry of merger remnants. In particular, a BHB is found to induce maximum triaxiality within its sphere of influence; plus, the presence of single or binary SMBHs makes the stellar system more axisymmetric (oblate) up to a radius enclosing 100 SMBH masses, compared to SMBH-free merger relics. My results confirm that BHBs are able to coalesce within a few Gyr, even if their host systems retain nearly axisymmetric mid- and large-scale geometries. In addition, my study suggests that no strong connection exists between the galaxy merger remnant morphology and the BHB shrinking rate, which seems to depend only on the inner density slope of the non-spherical galaxy. Such result may be particularly relevant for low-frequency GW science, as the timescale needed for a binary to reach the GW-emission stage could be assumed to scale only with the central density of the host galaxy.

In summary, this thesis is organized as follows: after a general introduction on galactic nuclei and SMBHs (Chapter 1), I address the role of SN kicks in the GC. Chapter 2 explores the dynamical role of such kicks occurring in young binary stellar systems within the central parsec of our Galaxy, while Chapter 3 investigates the possibility that SN kicks trigger EMRIs in the GC. The subsequent chapters are devoted to the study of BHBs: Chapter 4 explores the effect of a young stellar cluster infalling onto an SMBH binary; Chapter 5 rules out the possibility that the numerical wandering of the binary skews the results of simulations adopting the direct-summation technique; Chapter 6 investigates the influence of SMBHs and SMBH binaries on the shape of galaxy merger remnants, and the relation between the binary shrinking and the morphology of the host galaxy. Finally, the ending chapter presents the conclusions of this thesis, and expands on its future developments.

Contents

1

Supermassive black holes in galactic nuclei

As curious as it may seem, Einstein was wrong. And not just him: until a handful of decades ago, many bright scientists would firmly reject the possibility that black holes (BHs) – objects so compact that not even light can escape their surfaces – could exist, let alone the idea that they could weigh billions of solar masses.

Einstein in person committed himself to prove that Nature would never allow such outrageous objects to form: *"The essential result of this investigation is a clear understanding as to why the Schwarzschild singularities do not exist in physical reality"*, he asserted in his 1939 paper, ultimately refusing the possibility that the most extraordinary legacy of his theory could ever come into existence (Einstein, 1939).

However, as Werner Israel later commented, "*there might be more in heaven and earth than Western science was prepared to dream of"* (Thorne, 1994). And this was the case: in the following decades, not only circumstantial evidence was brought that BHs with near solar mass exist; the discovery of quasars gradually forced the astronomical community to accept that supermassive black holes (SMBHs), weighting up to tens of billions solar masses, are common inhabitants of galaxy nuclei.

1.1 Astrophysical black holes

In principle, any mass M can become a BH, as long as there is a process able to confine such mass inside the so-called Schwarzschild radius,

$$r_s = \frac{2GM}{c^2} \approx 10^{-5} \left(\frac{M}{10^8 M_\odot} \right) \text{ pc} \tag{1.1}$$

where G is the gravitational constant and c is the light speed. Nowadays we know that stellar evolution provides a valid mechanism for generating such exotic objects: stars with initial mass in excess of $\approx 8 M_\odot$ generally end their lives in a violent supernova (SN) explosion, leaving behind a compact remnant in the form of either a neutron star (NS) or, if the star initial mass exceeds $\approx 25 M_\odot$, a BH.

Hints for stellar mass BHs existence initially arose from the X-ray observations of accreting stellar binaries, the first being the pioneering study of Cyg X-1, whose BH nature was strongly suspected since 1972 (Webster and Murdin, 1972).

In the same years, evidence started building up that heavier BHs lurk in the nucleus of many galaxies: SMBHs. In 1963, the first of many distant quasars, named 3C 273, was discovered (Schmidt, 1963); after rejecting all other possible explanations for its nature, astronomers started accepting the idea that quasars energy was released by the accretion of matter onto an SMBH (Lynden-Bell, 1969; Rees, 1984).

In the 1980s, it became evident that quasars are rare in the local Universe compared to their occurrence at higher redshift (Schmidt and Green, 1983); hence, the idea emerged that dormant, non-accreting SMBHs lurk in galactic nuclei in the present day Universe. The existence of quiescent SMBHs in the local Universe was later unambiguously confirmed through the tracking of Keplerian stellar orbits in the Milky Way centre (Schödel et al., 2002; Ghez et al., 2003), and by VLBI observations of the maser-emitting circumnuclear disk in NGC 4258 (Miyoshi et al., 1995). Today, astronomers are reasonably sure that SMBHs inhabit almost all galaxies whose stellar mass $M_\star$ exceeds $\sim 10^{11} M_\odot$, while their occurrence in lighter stellar systems remains ambiguous (Ferrarese and Ford, 2005; Kormendy and Ho, 2013).

Although SMBHs relevance in astrophysics is nowadays unquestionable, their cosmological formation path is still largely unconstrained. Owing to this, SMBH low and high mass end remain widely debated, and our knowledge of SMBHs mass function largely comes from observations. This being said, it is customary to refer to SMBHs as objects with masses between $\sim 10^6 - 10^{10} M_\odot$.

A mass desert appears between the heaviest stellar mass BHs ($\sim 100 M_\odot$) and the lightest SMBHs ($\sim 10^6 M_\odot$). BHs inhabiting this loosely populated mass range have been named intermediate mass black holes (IMBHs). Only very recently, the first indirect IMBH observations started to come forward (Filippenko and Ho, 2003; Straub et al., 2014; Baldassare et al., 2015; Lin et al., 2018). However, it remains obscure whether IMBHs are in fact rare objects, or rather observation-related biases prevent astronomers to find IMBHs in large numbers.

1.2 Supermassive black holes and their host stellar systems

Although gas accretion first revealed SMBHs existence, SMBHs appear most often to be associated with stellar spheroids, being either elliptical galaxies or bulge components of disk galaxies(1) (Kormendy and Richstone, 1995; Magorrian et al., 1998). The surface brightness profile I of stellar spheroids is generally well fitted by the Sérsic model (Sersic, 1968)

$$\ln\left(I(R)\right) = \ln\left(I(R_e)\right) - b(n)\left[\left(R/R_e\right)^{1/n} - 1\right], \tag{1.2}$$

where R is the projected galaxy radius, while b is a constant chosen so that R_e contains half of the total spheroid's light; the Sérsic index n is a 'shape' parameter

(1) In the present thesis, both structures will be referred to as 'bulges' or 'stellar spheroids'. While SMBHs seem to be present in almost all galaxies with a classical bulge component, the inverse is not true, and stellar spheroids no longer seem to be necessary equipment for SMBH formation and growth (Kormendy and Ho, 2013).

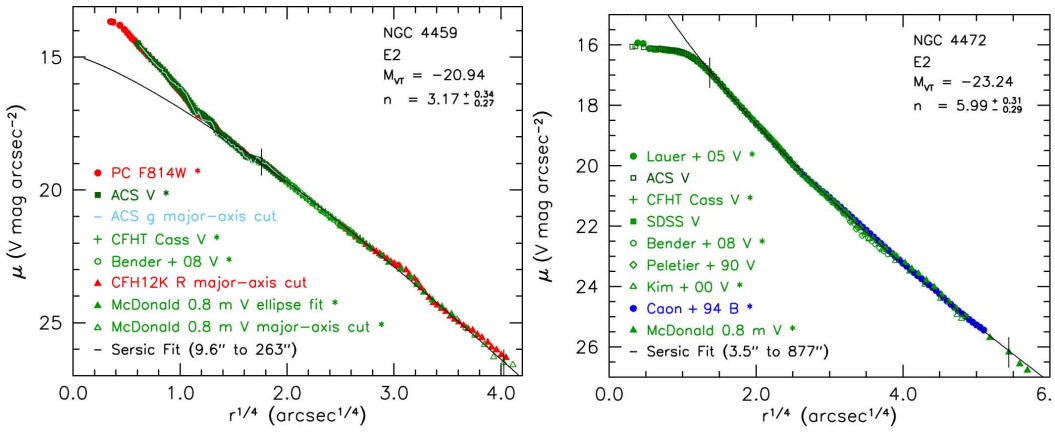

Fig. 1.1. $V-$band brightness profiles and associated Sérsic fits of (i) NGC 4459 (left-hand panel), a prototypical low-luminosity elliptical galaxy exhibiting a central brightness enhancement, associated with the presence of a NSC; (ii) NGC 4472 (right-hand panel), a typical giant elliptical galaxy, with clear signature of a density core within the innermost $2''$. Image credits: Kormendy and Ho (2013); photometry from Kormendy et al. (2009); references to data sources are in the legend.

that depends on galaxy morphology. The Sérsic profile has been known for long to well reproduce the brightness profile of many spheroids (Graham et al., 2003); however, deviations are often observed at the smallest radii (Fig. 1.1). Such variations are significant for the study of galactic nuclei, as they could be source of crucial insights on the physics and evolution of galaxies and SMBHs.

1.2.1 Nuclear Stellar Clusters

Hubble Space Telescope (HST) imaging surveys have revealed that bulges fainter than $\sim 10^{10.3} L_{\odot}$ almost universally exhibit central enhancements in the surface brightness profile (see the left-hand panel of Fig. 1.1), due to the presence of bright and compact nuclear star clusters (NSCs; Carollo et al. 1997; Böker et al. 2002; Côté et al. 2006; Carson et al. 2015). NSCs extend for $2-10$ pc in radius, and have masses of $\sim 10^5 - 10^8 M_{\odot}$: thus, their stellar density can attain $10^7 M_{\odot}$ pc^{-3}, making them the densest and perhaps dynamically richest stellar systems in the Universe (Phillips et al., 1996; Prodan et al., 2015).

Interestingly, NSCs are known to co-exist with SMBHs across a wide range of galaxy masses ($10^8 \lesssim M_{\star}/M_{\odot} \lesssim 10^{10}$, Seth et al. 2008). However, no NSC is detected in the central regions of galaxies with $M_{\star} \gtrsim 10^{10} M_{\odot}$, where only SMBHs seem to sit. On the contrary, NSCs dominate the nuclei of small galaxies ($M_{\star} \lesssim 10^8 M_{\odot}$), where SMBHs are either lacking or too light-weighted to be identified (Ferrarese et al., 2006; Graham and Spitler, 2009). These circumstantial facts would suggest that NSCs and SMBHs evolution is strictly connected, and the two objects could be a natural by-product of galaxy evolutionary processes (Ferrarese et al., 2006). However, a comprehensive theory on the genesis of the aforementioned aspects, as much as on the origin of NSCs, remains to be found.

At the moment, two leading scenarios have been proposed to explain NSCs formation. (i) According to the so-called *migration scenario*, NSCs grow their mass by progressively accreting stellar clusters that formed elsewhere in the galaxy and

gradually decayed in the central region via dynamical friction (cf. §1.6.1, Tremaine et al., 1975). (ii) The *in-situ scenario* proposes instead that NSCs build up through the collapse of gas that accumulates in the galaxy nucleus, then undergoing bursts of star formation (Milosavljević, 2004; Aharon and Perets, 2015).

Clues on the origin of NSCs may come from observational grounds: NSCs exhibit a complex star formation history, and contain a mixture of stellar populations whose ages range from a few Myr to ∼10 Gyr (Rossa et al., 2006; Kacharov et al., 2018). On the one hand, the presence of very young stars would imply that at least part of the NSC mass builds up in-situ; however, as Antonini et al. (2015b,a) suggest, both proposed formation scenarios probably play a relevant role in the genesis of the densest stellar clusters in the Universe.

1.2.2 Galaxy cores

Stellar spheroids brighter that $\sim 10^{10.3} L_{\odot}$ not only lack NSC, but often exhibit a central deficit in the surface brightness, compared with an inward extrapolation of their Sérsic profile (as in the right-hand panel of Fig 1.1; Kormendy, 1985). The central voids (historically referred to as *cores*) typically extend for $r_c \sim 10 - 10^3$ pc.

Aside from cores, the structural properties of the bright ellipticals are in continuity with the features of their fainter (and less extended) counterparts (Graham et al., 2003; Graham and Guzmán, 2003; Trujillo et al., 2004). One may thus infer that a mechanism has acted to devoid the brighter ellipticals of their central luminous mass.

Clues on the matter may come from an estimate of the 'missing' mass inside a core, m_{def}. This generally translates in computing the difference in integrated mass between the observed density profile, $\rho(r)$, and an inward extrapolation of the outer galaxy profile, $\hat{\rho}(r)$ (Milosavljević et al., 2002):

$$m_{def} = 4\pi \int_0^{r_c} (\hat{\rho}(r) - \rho(r))\, r^2 \, dr. \tag{1.3}$$

It turns out that the missing mass is often of the order of the inferred mass of the central SMBH (Graham, 2004; Ferrarese et al., 2006), implying again a connection between the most massive SMBHs and the core of their host stellar systems. In fact, the bulk of nuclear cores are now believed to be carved out via the injection of large energy amounts operated by binary SMBHs evolving in the galaxy centre (Begelman et al., 1980, cf. §1.6.1).

1.2.3 A matter of scales

If one wants to understand the dynamical effect of a SMBH on its environment, the typical radius of its host galaxy ($r_{gal} \sim 1 - 100$ kpc) has to be compared with the spatial extent (r_h) over which the SMBH gravitational force is non-negligible. This region is referred to as the SMBH sphere of influence, and its radius is usually defined as the length enclosing twice the SMBH mass ($M_\bullet$) in stars

$$M_\star(r < r_h) = 2M_\bullet. \tag{1.4}$$

Generally, observational astronomers adopt an alternative definition for the influence radius:

$$r'_h = \frac{2GM_\bullet}{\sigma^2}, \tag{1.5}$$

where σ is the uni-dimensional stellar velocity dispersion in the galaxy centre. This second quantity has the advantage to be easily estimated by observers. A useful scaling for r'_h can be obtained by exploiting the relations that will be presented in the next section(2),

$$r'_h \approx 35 \text{ pc } \times (M_\bullet/10^8 M_\odot)^{0.56}. \tag{1.6}$$

Although the gravitational pull of a SMBH is non-negligible at $r \approx r_h$, stellar trajectories can be safely described as Keplerian ellipses only at scales $\sim 0.1 r_h$, where the SMBH influence significantly exceeds that of the extended mass distribution. The Keplerian approximation breaks down again at the smallest scales: when an object approaches the SMBH at separations of a few to a few tens Schwarzschild radii (r_s, Eq. 1.1), orbital velocities reach significant fractions of the light speed, and General Relativity is required to give a proper description of the orbital motions near the SMBH (Merritt, 2013a).

From the characteristic length-scales described above, it is evident that the SMBH fingerprint can be detected only within a tiny fraction of the galaxy extent, being $r_h \sim 10^{-5} - 10^{-3}\ r_{gal}$. The best resolution achievable by modern electromagnetic telescopes, as the HST, only allows to resolve influence spheres within a few tens of Mpc in galaxies hosting the largest SMBHs. A corollary to these considerations is that the relativistic effects induced by the SMBH remain virtually undetectable, with the noticeable exception of the Milky Way nucleus (Gravity Collaboration et al., 2018). In spite of all the mentioned complications, a number of rather compelling SMBH detections have been reported so far.

1.3 Supermassive Black Holes Observability

The SMBHs detection techniques practically translate in the measurement of their mass $M_\bullet$, and several methods have been identified to serve this purpose (comprehensive reviews on the matter can be found in e.g. Kormendy and Ho 2013 and Peterson 2014). In general, $M_\bullet$ is obtained either by *test particle measurements*, based on the detection of spatially resolved Keplerian orbital motions of single stars or maser-emitting gas, or by revealing the *ensemble* line-of-sight velocity rise

$$v^2 \propto GM_\bullet/r \tag{1.7}$$

in the integrated light of unresolved stars or gas clouds. An alternative approach, named *reverberation mapping*, is used to measure the SMBH mass in Seyfert I active galaxies via an analogous equation: the delay in the variability of the broad nuclear emission lines with respect to the continuum emission constrains the extent of the emitting region (r), while the profile of the spectral features allows to estimate the velocity of the emitting gas (v).

(2) This scaling has been derived for cored elliptical galaxies, but it provides an order of magnitude estimate for r'_h that remains valid in many different systems (Merritt et al., 2009).

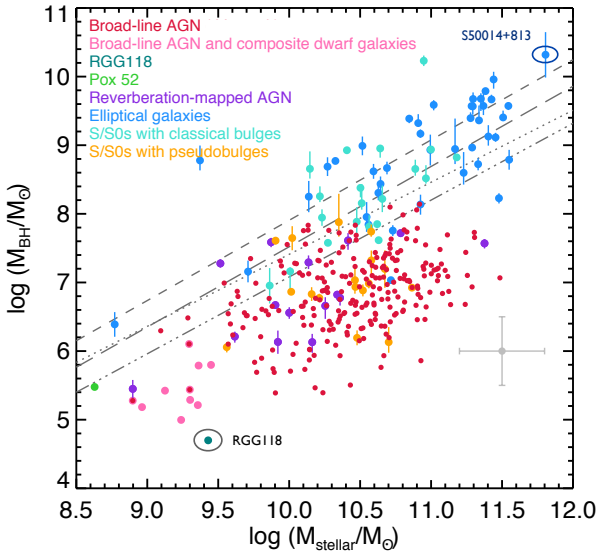

Fig. 1.2. SMBH masses against the total stellar mass of their host galaxies. The plot comprises a large set of galaxies with different morphologies and SMBH activity levels. The gray lines display the $M_\bullet - M_{\rm bulge}$ relation by several authors, including Kormendy and Ho (2013); elliptical galaxies and classical bulges appear to follow the aforementioned relation, contrarily to accreting active galactic nuclei (AGNi). The error bar indicates uncertainties on most of the displayed points. Reproduction of fig. 6 from Colpi and Sesana (2017); image credit and further details in Reines and Volonteri (2015).

1.3.1 Supermassive black hole – host relations

What matters most is that the aforementioned mass measurements allowed to pinpoint a number of relations connecting SMBH masses to several properties of their host stellar spheroids. Initially, the SMBH mass was found to correlate with the K-band luminosity of its bulge via a power-law relation (Marconi and Hunt, 2003; Kormendy and Richstone, 1995). Given that light is assumed to track luminous matter, one would also expect $M_\bullet$ to scale with the spheroid's stellar mass ($M_{\rm bulge}$, Fig. 1.2); in fact, it was found that $M_\bullet \approx 10^{-3} M_{\rm bulge}$ with a small scatter (Magorrian et al., 1998; Marconi and Hunt, 2003; Merritt and Ferrarese, 2001).

However, the correlation that most surprised astronomers at the time of its discovery connects SMBH masses to the stellar velocity dispersion σ of their host stellar systems, $M_\bullet \propto \sigma^{4.86}$ (Ferrarese and Ford, 2005; Gebhardt et al., 2000). The so-called $M_\bullet - \sigma$ relation was considered the most fundamental one, as its intrinsic scatter was found to be consistent with measurement errors (Ferrarese and Merritt, 2000; Gebhardt et al., 2000). For this, astronomers started adopting it for predicting SMBH masses via σ measurements. Today, the $M_\bullet - \sigma$ and $M_\bullet - M_{\rm bulge}$ relations are both considered good $M_\bullet$ proxies, the latter working well even in very massive core elliptical galaxies where the $M_\bullet - \sigma$ relation no longer holds (Kormendy and Ho, 2013).

It has been suggested that even NSC masses correlate with the mass and velocity dispersion of the surrounding spheroids; Ferrarese et al. (2006) even argue that, in

galaxies hosting both a NSC and a SMBH, the combined mass of the two components correlates better with $M_{\rm bulge}$ than either mass taken separately. However, the latter result has been questioned in recent years (Balcells et al., 2007; Scott et al., 2013; Scott and Graham, 2013).

1.3.2 Physics behind co-evolution

A recurrent idea emerges from the aforementioned relations: SMBHs and their stellar spheroids 'get to know about each other' at some point in their evolution; in particular, SMBHs affect the properties of their bulges well beyond the influence radius r_h. The reason for this is most probably manifold, but the commonly accepted explanation is that SMBHs and bulges co-evolve by regulating each other's growth: SMBH binding energy is extremely large compared to the bulge energy; if $\approx 1\%$ of the former couples with gas in the growing stellar system, all gas can easily get blown up from the galaxy (Haehnelt et al., 1998; Silk and Rees, 1998; King, 2003). In a nutshell, high redshift ($z \sim 2 - 2.5$) SMBHs would accrete gas until their mass sits on the previously mentioned relations, then quenching both their growth and star formation via intense accretion feedback on galactic scale (Kormendy and Ho 2013; see Fig. 1.2); this process is usually referred to as AGN feedback(3). In support to this argument, the mass density of SMBHs in nearby massive galaxies is compatible with the inferred gas accretion of quasars and active galaxies at high redshift (Soltan, 1982; Marconi et al., 2004); furthermore, the histories of SMBHs growth and star formation in the Universe look remarkably similar (Madau and Dickinson, 2014).

Although the AGN-feedback theory presented above has many advantages, it has to be regarded with caution. In fact, the era of feedback driven co-evolution seem to be over in the present-day Universe: Although some processes may help to maintain the observed correlations down to $z \sim 0$, other mechanisms may progressively wash them out (Kormendy and Ho 2013; see their sec. 8 for a discussion on the matter). Furthermore, AGN-feedback theory fails to predict the deviations to the Sérsic brightness profile observed at the smallest galactic scales.

Additional aspects must be considered to better constrain the physics behind the SMBH-host correlations. Even if most of the SMBHs growth seem to result from gas accretion, other events are known to participate in the process. Tidal disruption of stars on low angular momentum orbits, together with the gravitational wave (GW) induced decay of stellar mass compact objects onto SMBHs help increase SMBH masses. Most importantly, galaxies are observed to aggregate via repeated collisions of smaller galactic fragments, a fraction of which could host a SMBH from early times. Thus, galaxy mergers at all redshifts grow concurrently larger SMBHs in larger stellar hosts (Begelman et al., 1980), the former possibly coalescing via intense radiation of GWs (Thorne and Braginskii, 1976). The unavoidable averaging in SMBH and bulge masses that result from multiple galaxy merger events (in the assumption that SMBHs merge soon after their hosts, and keep sitting

(3) In fact, it can be shown that energy driven accretion feedback naturally produces a relation in the form $M_\bullet \propto \sigma^5$, while momentum driven feedback yelds $M_\bullet \propto \sigma^4$; reassuringly, the two dependencies bracket the actual, observed $M_\bullet - \sigma$ relation (Haehnelt et al., 1998; Silk and Rees, 1998).

in the galaxy centre afterwards) possibly produces, or at least helps maintaining, the scaling relations presented in the previous section (e.g. Peng, 2007). Defining themselves as 'heretic', Kormendy and Ho (2013) propose that *it is possible that merger averaging is at least as important as feedback-driven coevolution in creating the observed SMBH-host galaxy correlations.*

1.3.3 The gravitational wave revolution

The importance of SMBHs coalescence is not limited to the merger-averaging theory described above. SMBHs coalescence, as well as the inspiral of stellar mass compact objects onto SMBHs (the so-called *extreme mass ratio inspirals*, EMRIs), are driven by the emission of GWs, ripples in the fabric of spacetime radiated by accelerated gravitational masses. Albeit being a prediction of 1915 Einstein's theory of Relativity (Einstein and Lawson, 1961), GWs have not been directly detected until 2015, when the LIGO collaboration first revealed the signal from two merging stellar mass BHs (Abbott et al., 2016), marking the beginning of a new era for Astronomy.

Binary (stellar and/or supermassive) BHs are ideal sources for detectable GWs. First of all, binarity is needed as GWs are released by at least quadrupolar variations in the gravitational potential, thus sperically or axi-simmetric sources do not serve the purpose. The fact that BHs are the most compact objects in the Universe also matters. GW detectors measure the GW *strain* $h = \Delta L/L$, i.e. the relative variation in the spatial length L due to the wave passage. It can be shown that

$$h \propto \frac{G^2 m_1 m_2}{a c^4} \frac{1}{D} \approx 2 \times 10^{-20} \left(\frac{m_{12}}{10^6 M_\odot}\right)^2 \left(\frac{a}{10^{-3}\ \mathrm{pc}}\right)^{-1} \left(\frac{D}{100\ \mathrm{Mpc}}\right)^{-1}, \quad (1.8)$$

where m_1 and m_2 are the involved masses ($m_{12} = \sqrt{m_1 m_2}$), a is the binary semi-major axis and D is the distance from the emitting source (see e.g. Misner et al., 1973; Le Tiec and Novak, 2017). Eq. 1.8 implies that objects that can get extremely close to each other prior to their merger, as BHs and NSs, are optimal sources of GWs.

Before the GW-induced coalescence, the GW frequency roughly equals twice the orbital frequency of the emitting Keplerian binary, i.e. $\omega_{\mathrm{GW}} = 2\sqrt{G(m_1+m_2)/a^3}$. Knowing that two BHs roughly merge when their separation drops below $\sim r_{\mathrm{ISCO}} = 6G(m_1+m_2)/c^2$, one can obtain the highest GW frequency emitted just prior to coalescence as a function of the BH binary total mass (Misner et al., 1973; Le Tiec and Novak, 2017)

$$\omega_{\mathrm{GW,final}} = \frac{2c^3}{6^{3/2} G(m_1+m_2)} \approx 27.6\ \mathrm{mHz} \left(\frac{m_1+m_2}{10^6 M_\odot}\right)^{-1}. \quad (1.9)$$

Fig. 1.3 shows the characteristic strain against the GW frequency for a variety of GW sources and the associated detectors. The currently available ground-based detectors LIGO and VIRGO can only reveal GW mergers of *stellar mass* and *intermediate mass* BHs; phenomena involving SMBHs will be observed either by the already operational Pulsar Timing Array, which uses accurate timings of pulsating NSs to detect merging SMBHs with masses of $\sim 10^9 M_\odot$ (Hobbs and Dai, 2017), or by space-borne laser interferometers as the forthcoming LISA observatory, the

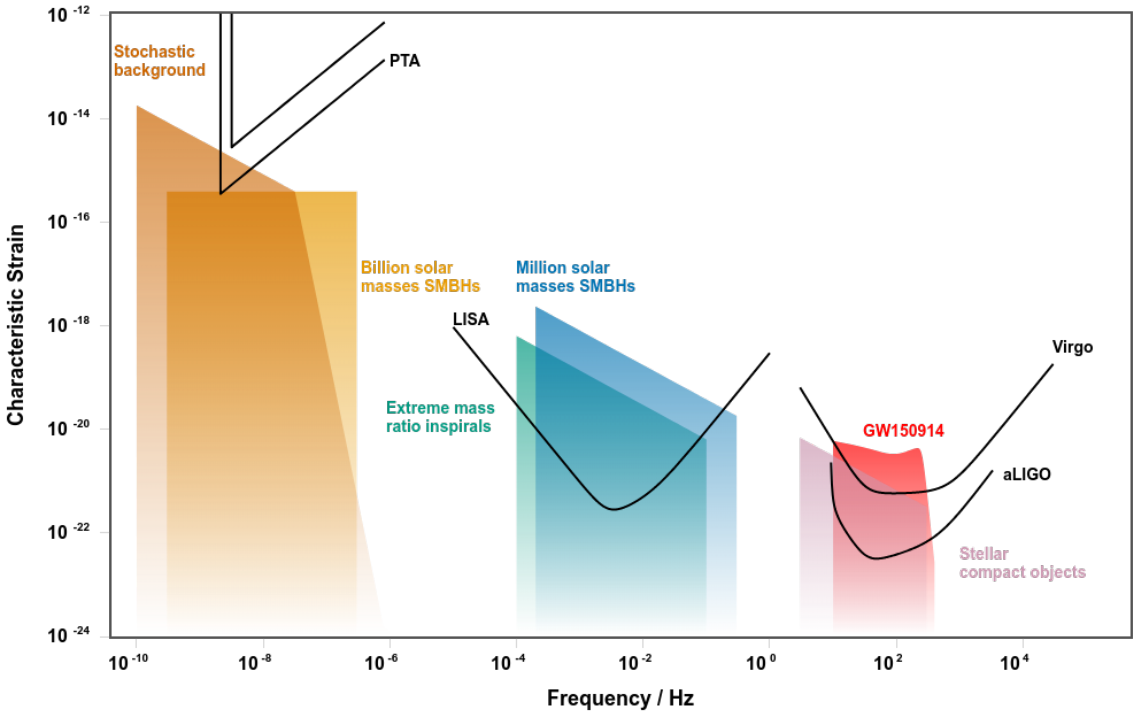

Fig. 1.3. Plot of the characteristic strain against the GW frequency for a variety of sources, combined with the limiting sensitivity of the associated detectors: (i) the Pulsar Timing Array, which is already operational and using the very accurate timings of pulsars to observe GWs from low frequency sources as $\gtrsim 10^9 M_\odot$ SMBH mergers; (ii) LISA, the space-borne interferometer that will observe, inter alia, mergers of $\sim 10^4 - 10^6$ SMBHs and EMRIs on SMBHs of the same size; (iii) the operational, high-frequency ground based interferometers LIGO and VIRGO. The latter instruments can observe GWs released in the coalescence phase of stellar mass compact objects (BHs, NSs, white dwarfs); they already revealed signals from 4-5 BH binaries and one NS binary. Image produced via `gwplotter.com`; see Moore et al. (2015) for further details.

ESA L3 mission whose launch is planned for the early 2030s (Amaro-Seoane et al., 2017). The variety of sources detectable by the low-frequency LISA mission include mergers between 10^4 to $10^6 M_\odot$ SMBHs, and EMRIs onto SMBHs of the same size.

The opening of a low-frequency GW window is crucial for a number of reasons. GW detections will provide exquisite measurements of SMBH masses, spins and distances, making it possible to trace the origin and history of the small-sized SMBHs via their mergers across all stages of galaxy evolution (up to $z \sim 20$). At $z \lesssim 1$, EMRI detections will provide a probe for testing general relativity, investigating the dynamics of dark relic stars in close vicinity to a SMBH and exploring the occupation fraction of small-sized galaxies by IMBHs (e.g. Colpi, 2014; Colpi and Sesana, 2017; Amaro-Seoane et al., 2017).

However, BHs and other compact objects have to find themselves at extremely small distances in order for their orbital energy to be effectively drained via GWs. The detailed study of the gravitational radiation generated by the motion of two point masses has been first performed by Peters (1964), who provided an approximated

estimate of the time required by a compact binary to reach the final coalescence

$$t_{gw} = \frac{5}{256}\frac{c^5}{G^3}\frac{1}{f(e)}\frac{a^4}{\mu(m_1+m_2)} \approx \\ \approx \frac{14\ \mathrm{Gyr}}{f(e)}\left(\frac{a}{0.7\ \mathrm{mpc}}\right)^4\left(\frac{\mu}{10^4\ M_\odot}\right)^{-1}\left(\frac{m_1+m_2}{10^6 M_\odot}\right)^{-2}; \tag{1.10}$$

here $\mu = m_1 m_2/(m_1+m_2)$ is the reduced mass of the binary. In order for two emitting objects to coalesce within a Hubble time, extraordinarily small separations (and, possibly, very high eccentricities) must be reached: the typical spatial scale is as small as ~ 1 mpc for two Milky-Way like SMBHs.

In the framework of stellar mass compact objects, stellar evolutionary processes occurring in binaries may significantly help shrinking the pair down to the scale at which GW emission becomes significant (e.g. Mapelli, 2018). However, in most astrophysical scenarios, violent stellar dynamical events are required in order for GWs to bring a compact stellar or supermassive binary to its ultimate coalescence (e.g. Celoria et al., 2018). For this, the next section briefly reviews several dynamical processes relevant in the study of galactic nuclei and GW sources.

1.4 Stellar dynamics near supermassive black holes

Stellar dynamics is crucial for the study of galactic nuclei harbouring SMBHs. Apart from GW-source generation, the study of stellar motions is relevant as galactic nuclei are often the densest regions in the Universe, thus they are natural places where to look for the most extreme dynamical events to occur (Phillips et al., 1996; Prodan et al., 2015), including the generation of stellar cusps and tidal disruption events. In what follows we touch upon the dynamical phenomena that can be ascribed to the accumulation of two-body close and distant encounters between stars or more massive objects.

1.4.1 Two-body relaxation

In the framework of stellar dynamics, a galactic nucleus is a self gravitating system, as its internal dynamics is determined by its mass distribution. If in an equilibrium state, it can be approximated as a steady-state system in which the gravitational potential is a smooth and continuous function of the position, and each star conserves its orbital energy over time. However, if one waits for long enough, gravitational two-body interactions between stars[(4)] cause them to significantly change their orbital energy, and the whole system loses memory of its initial properties. Such time period is called *relaxation time* (Spitzer, 1988; Binney and Tremaine, 1987)

$$t_r = \frac{0.34\sigma^3}{G^2 m_\star \rho \ln\Lambda} \approx 10^{10}\mathrm{yr}\left(\frac{\sigma}{200\mathrm{km\ s^{-1}}}\right)^3\left(\frac{\rho}{10^6\ M_\odot \mathrm{pc}^{-3}}\right)^{-1}\left(\frac{m_\star}{M_\odot}\right)^{-1}\left(\frac{\ln\Lambda}{15}\right)^{-1}. \tag{1.11}$$

(4) In this section, we will generally refer to the gravitational masses that constitute a self-gravitating system as 'stars' or 'particles'. In general, the phenomena discussed in this section are applicable to systems of different nature and constituents, including galaxies, dark matter halos and clusters of galaxies.

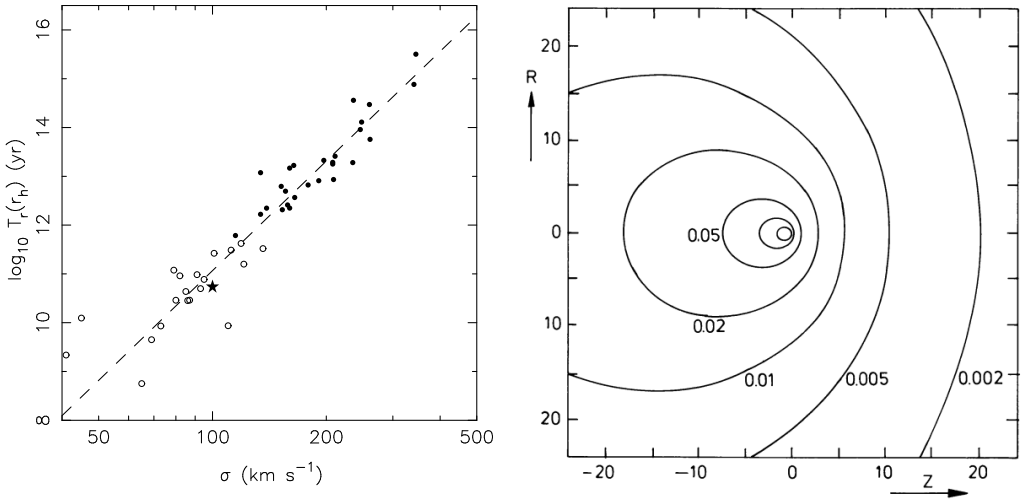

Fig. 1.4. Left-hand panel: relaxation time of several galactic nuclei, evaluated at radius r_h, as a function of the one-dimensional velocity dispersion of the system. Filled symbols represent galaxies in which the SMBH influence radius is resolved, while the star represents the Milky Way nucleus. A complete sample of early type galaxies in the Virgo cluster is displayed (Côté et al., 2004); image credit: Merritt et al. (2007b). Right-hand panel: the massive object in the origin travels from left to right. Dynamical friction acts to slow down the body, as gravitational focusing enhances the stellar density at its back. The lines show equal stellar density contours. Image credit and further details in Mulder (1983).

Here $m_\star$ is the mean stellar mass in the system, ρ is the stellar density, σ is the one-dimensional velocity dispersion and $\ln\Lambda \approx \ln(r_2/r_1)$ is the Coulombian Logarithm, r_1 and r_2 being respectively the minimum inter-particle distance and the system extent. $\ln\Lambda$ is best approximated by $\ln(M_\bullet/m_\star)$ within the SMBH sphere of influence (Merritt, 2013a). A manipulation of Eq. 1.11 yields

$$t_r \sim \frac{N}{\ln N} t_c \tag{1.12}$$

where $t_c = R/\sigma$ is the crossing time of the system and R is its typical radius; that is, t_r substantially depends on the number N of particles in the system.

The relaxation time is used to distinguish between *collisionless* and *collisional* systems, i.e. systems whose typical age is respectively shorter and longer than their t_r. Typical collisional systems include globular and galaxy clusters, while massive galaxies and dark matter haloes can be safely assumed to be collisionless.

Galactic nuclei lie on a middle ground, as their relaxation time is often close to the age of the Universe (Merritt, 2013a). The left-hand panel of Fig 1.4 shows relaxation times for galactic nuclei as a function of σ, which can be easily translated into the SMBH mass via the $M_\bullet - \sigma$ relation (Ferrarese et al., 2006). As a rule of thumb, SMBHs more massive than $\sim 10^7 M_\odot$ can generally be assumed to reside in collisionless nuclei, if one evaluates t_r at the edge of the SMBH influence sphere (Merritt, 2013a). A large fraction of galactic nuclei, including the Galactic Centre, are probably not fully collisionless, but not old enough for gravitational encounters to have completely 'washed out' their primitive properties – thus, to some degree, they should still reflect the details of their formation process.

1.4.2 The Bahcall-Wolf solution

An important prevision of the relaxation theory is that stars orbiting a SMBH over a timescale longer than $\sim t_r$ are expected to redistribute in a universal mass profile: they develop a *Bahcall-Wolf density cusp* $\rho(r) \propto r^{-\gamma}$ within the SMBH influence radius, with $\gamma = 7/4$ in the assumption of a single mass group (Bahcall and Wolf, 1976). Initial searches for SMBHs in galactic nuclei actually consisted in looking for central enhancements in the stellar density (Peebles, 1972a,b), but this strategy was found to be flawed for several reasons. Among them: (i) recent star formation (Aharon and Perets, 2015; Baumgardt et al., 2017) and galaxy mergers (especially those involving SMBH binaries, Milosavljević and Merritt 2003a) alter the nuclear stellar distribution and virtually turn back dynamical clock of the system; (ii) the presence of massive dark stellar remnants (BHs, NSs) in the nuclear region significantly alters the expected slope γ of the visible, lighter stars (e.g. Bahcall and Wolf, 1977; Preto and Amaro-Seoane, 2010).

1.4.3 Dynamical friction

Another important dynamical insight helps to understand why SMBHs usually reside at the very centre of their host stellar spheroids. When a heavy object of mass $M \gg m_\star$ and velocity v_M is travelling into a stellar aggregate, gravitational encounters with lighter stars slow down the subject body, which experiences the so-called *dynamical friction* (Chandrasekhar, 1942, 1943). Stars are deflected by the massive satellite in such a way that the density of background stars behind M is greater than in front of it. The trailing overdensity (Fig. 1.4, right-hand panel) exerts a drag force parallel and opposite to v_M, and the massive body gradually inspirals towards the centre of the system. Assuming that the host stellar system has a density profile which can be described via $\rho = \sigma^2/(2\pi G r^2)$ (a singular isothermal sphere), where σ is the position-independent one-dimensional velocity dispersion, the timescale needed by the subject mass to reach the nucleus is roughly

$$t_{df} = \frac{2.3 R_e \sigma^2}{\ln\Lambda G M} \approx 17\ \mathrm{Gyr} \frac{6.6}{\ln\Lambda} \left(\frac{R_e}{10\mathrm{kpc}}\right)^2 \left(\frac{\sigma}{300\mathrm{km\ s^{-1}}}\right) \left(\frac{M}{10^8 M_\odot}\right)^{-1}, \quad (1.13)$$

where R_e is the effective radius of the host system, at which the infalling mass is supposed to initiate its inspiral. The previous equation is derived in the assumption that only stars whose velocity is lower that the velocity of the infalling body (here assumed to equal σ) participate in the frictional force. Nevertheless, the aforementioned equation works remarkably well in a large number of astrophysical systems (e.g. Tremaine and Weinberg, 1984). It is worth mentioning that Eq. 1.13 can be manipulated to show that $t_{df} \sim t_r\,(m_\star/M)$; this scaling does not appear incidentally: in fact, both relaxation and dynamical friction share the same driver, i.e. stellar encounters.

The consequences of dynamical friction are manifold, and are particularly relevant in galactic nuclei. Dynamical friction is likely responsible for processes as galaxy mergers (e.g. Peirani et al., 2010), the orbital decay of massive stellar clusters and galaxy satellites (Gan et al., 2010; Arca-Sedda and Capuzzo-Dolcetta, 2014) – provided that they survive the galactic tidal shear (Merritt, 1984; Colpi et al., 1999) – and the early inspiral of SMBH pairs (Begelman et al., 1980; Dosopoulou and Antonini, 2017).

1.4.4 Mass segregation

A further consequence to dynamical friction and relaxation is *mass segregation* (Spitzer, 1988). Stellar systems are typically composed of a population of stellar objects ranging from light main sequence stars ($\sim 0.1 M_\odot$) to massive stellar BHs (a few $\times 10 M_\odot$). If the fraction of heavy stellar objects (with mass $m_{\rm heavy}$) is low, dynamical friction induces their gradual clustering near the centre of the system over $t \sim t_r(m_\star/m_{\rm heavy})$ (*strong mass segregation regime*; Alexander and Hopman, 2009; Preto and Amaro-Seoane, 2010); if the heavy stellar population is dominant instead, the same clustering is driven by self scatterings among the massive stellar population over $\sim t_r$ (Bahcall and Wolf, 1977).

In general, heavy stellar objects aggregate around a SMBH more strongly than the lighter stars, and this has important implications for the Bahcall-Wolf cusp development (Merritt 2013a; §1.4.2). If the dark stellar relics dominate the mass distribution, they roughly follow a Bahacall-Wolf profile ($\rho \propto r^{-\gamma}$, $\gamma \approx 7/4$) at the smallest radii, which turns steeper further out, where massive relics cease to dominate the density profile; the dark cusp gets even steeper if the dark and massive objects are sub-dominant (Alexander and Hopman, 2009; Vasiliev, 2017). As a result of mass segregation, the lighter stars in the system get scattered outwards and they distribute into a somewhat shallower cusp with typically $3/2 \lesssim \gamma \lesssim 7/4$.

All these facts tangle the observations of density cusps in galactic nuclei, as even dynamically relaxed systems should exhibit a density cusp whose slope significantly depends on the amount of the *dark* stellar relics.

1.5 The Galactic Centre

The main complication in exploring extreme dynamical processes occurring in galactic nuclei is their distance, which limits astronomers to the observation of stellar lights integrated over several (tens of) parsecs. This difficulty can be circumvented by studying what is by far the closest galactic nucleus to us, the Galactic Centre (GC, Fig. 1.5). Being only ≈ 8.3 kpc away (Gillessen et al., 2017), the GC is the sole nucleus where single stars can be tracked along their orbits on scales of the mpc, exploiting HST or adaptive optics infrared observations (e.g. Schödel et al., 2002; Ghez et al., 2003). For this, the GC is the best known galactic nucleus in the Universe.

1.5.1 The Galactic Centre environment and its nuclear star cluster

The GC is an extremely rich environment (Melia, 2003; Genzel et al., 2010; Mapelli and Gualandris, 2016): most remarkably, it hosts the radio source SgrA* (Balick and Brown, 1974; Brown, 1982), that has been identified as a $4.3 \times 10^6 M_\odot$ SMBH beyond any reasonable doubt (e.g. Schödel et al., 2002; Ghez et al., 2008). Despite the SMBH presence renders the innermost parsecs of our Galaxy a hostile region, prolonged observations of this area have revealed that the SMBH is in fact surrounded by a very lively environment.

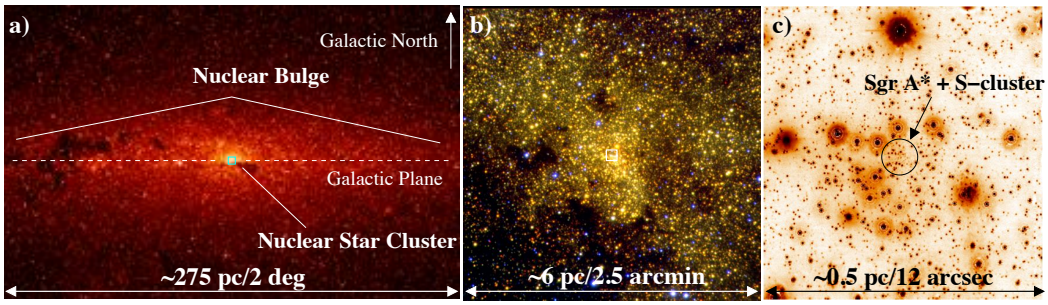

Fig. 1.5. View of the GC at different scales and centered on the radio source SgrA*. a) Extinction-corrected Spitzer/IRAC image of the Milky Way bulge; b) ISAAC zoom-in of the area marked by the cyan box in (a), i.e., the NSC; c) NACO/VLT holographic image of the innermost 0.5 pc, marked with a white square in (b); the innermost arcsecond (containing the S-star cluster) is surrounded by a black circle. Image credit and further details in Schödel et al. (2014b).

The nuclear star cluster

First of all, SgrA* is embedded in the closest known NSC (Gillessen et al., 2012). The NSC is observed to have a mass of $\sim 2 \times 10^7 M_\odot$ and half-light radius of ≈ 4 pc (Schödel et al., 2014a,b). Owing to its vicinity, to the SMBH presence and to its extreme density, this NSC possibly represents the best region in the Universe where to explore the occurrence of the previously described dynamical processes in the vicinity to an SMBH (§1.4). In addition, the Milky Way NSC looks like a prototypical NSC, thus it can serve as a benchmark for the more distant, unresolved galactic nuclei (Schödel et al., 2014a).

A gas-rich environment

The central 20 pc of the Milky Way are rich of gas, both in atomic, molecular and ionized form; such gas reservoirs are distributed in a series of structures near the dormant central engine (see e.g. the review by Mapelli and Gualandris 2016). The closest region to the SMBH is also populated by peculiar gaseous objects: two faint and dusty cloudlets, named G1 and G2, have been found to orbit the massive giant along highly eccentric trajectories (Clénet et al., 2004a,b; Ghez et al., 2005; Gillessen et al., 2012; Pfuhl et al., 2015); very recent observations revealed the existence of at least three further G-objects, whose inferred properties match those of G1 and G2 (Keck Observatory, 2018). G2 reached its periapsis in 2014, approaching the SMBH to ~ 200 AU. Surprisingly, it was not completely disrupted by the SMBH, as it would be expected for a low-density gas cloud (Witzel et al., 2014). G1 and G2 have been extensively studied since their first discovery: they have been proposed to be gas clouds (Schartmann et al., 2012), dust-enshrouded low-mass stars (Burkert et al., 2012; Ballone et al., 2013; Prodan et al., 2015) or planetary embryos (Mapelli et al., 2005), but the origin of the compact cloudlets remains debated.

The cusp of old stars

The GC stellar population is very heterogeneous. The bulk of stars ($\approx$ 80%) probably formed more than 5 Gyr ago, and they are possibly coeval to the Milky Way bulge (Pfuhl et al., 2011). Owing to its age, the stellar population at the GC would be expected to distribute in a relaxed cusp (Bahcall and Wolf, 1976), that should be detected via the observation of red clump stars: luminous red giants should be both sufficiently bright ($K_s \approx 15.5$) to be resolved in the crowded and extinction-affected GC environment, and old enough to be a proxy for the relaxed stellar population at the GC.

Albeit the red giants density profile looks consistent with the Bahcall-Wolf profile on scales $\gtrsim 1$ pc (Schödel et al., 2014a), the giants density cusp seems to break at the innermost ~ 0.5 pc, turning into a flat or even declining profile (Alexander, 1999; Buchholz et al., 2009; Do et al., 2013). Only very recently, the apparently missing inner cusp has been finally detected via the deep observations of resolved and unresolved fainter giants and sub-giants, down to magnitude $K_s \approx 18.5$ (Left-hand panel of Fig. 1.6; Schödel et al., 2017a; Gallego-Cano et al., 2017); the measured density profile of such dimmer population looks shallower ($\gamma \approx 1.2$) than the Bahcall and Wolf solution ($\gamma = 1.75$), but it is consistent with numerical models accounting for recent star formation episodes and for the presence of an undetectable cusp of dark remnants (Aharon and Perets, 2015; Baumgardt et al., 2017; Vasiliev, 2017).

The *missing cusp problem* turned into a *missing giants problem* in the innermost parsec: the apparent dearth of bright red clump stars within 0.5 pc has been proposed to be a result of giant envelopes being stripped either by collisions with other stars (Genzel et al., 1996; Bailey and Davies, 1999) or by the interaction with a gaseous thick disc that subsequently fragmented into stars, and possibly gave birth to the currently observed young population at the GC (Amaro-Seoane and Chen, 2014; Kieffer and Bogdanović, 2016).

The early-type stars

$\sim$ 200 young ($\sim 4 - 8$ Myr), massive stars, mostly of O and Wolf-Rayet type, are observed within the Milky Way central parsec (e.g. Paumard et al., 2006; Bartko et al., 2009). About $\sim 20 - 50$% among them have been found to lie in a disc-like structure extended between 0.04 and $\sim$ 0.13 pc, which is generally referred to as the clockwise (CW) disc, and whose total estimated mass is of a few $\times 10^4 M_\odot$ (Do et al., 2013; Lu et al., 2013; Yelda et al., 2014); the stars in the disc are observed to have a mild (≈ 0.3) but non-zero orbital eccentricity (Yelda et al., 2014). Although most of the stellar formation at the GC probably followed a Kroupa (2001) initial mass function (Pfuhl et al., 2011), the most recent episode associated to the CW disc formation seems compatible with a top-heavy initial mass function (Lu et al., 2013).

The CW disc of young stars is truncated at the innermost arcsecond. A cluster of ≈ 50 fainter and possibly lower mass ($8 - 14 M_\odot$) B-type stars, named S-stars, orbit the SMBH at distances smaller than $\sim$0.04 pc (Morris, 1993; Ghez et al., 2003; Gillessen et al., 2017). If one excludes the ≈ 8 S-stars that are compatible with being CW disc members, the cluster orbits are consistent with being spatially

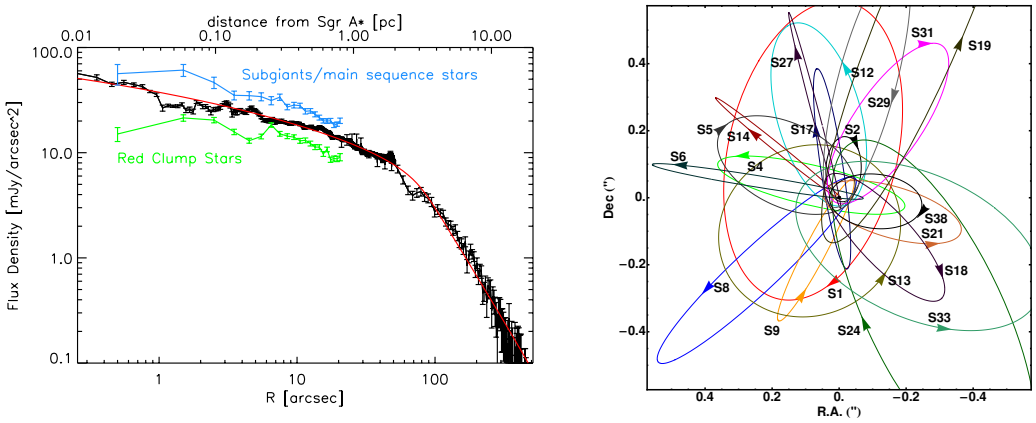

Fig. 1.6. Left-hand panel: projected stellar density versus the projected distance from the SMBH in the GC. Number densities of sub-giants and main sequence stars (blue) and red clump stars (green) are from Gallego-Cano et al. (2017); the surface light of unresolved stars (black) is from Schödel et al. (2017a). The red line is the best theoretical model fitting the data. Image credit and further details in Schödel et al. (2017b). Right-hand panel: inferred orbits of some among the S-stars, as obtained by Gillessen et al. (2009).

isotropic (right-hand panel of Fig. 1.6), while their eccentricity distribution well matches the thermal one, i.e., $n(e) \propto e$ (Gillessen et al., 2017).

Remarkably, the infrared monitoring of single S-cluster orbits provided the most compelling proof of the SMBH presence (e.g. Schödel et al., 2002; Ghez et al., 2003, 2005, 2008). In particular, the 14 $M_\odot$ S2 star (Habibi et al., 2017) has the best resolved close orbit, and its tracking produced the tightest constraints on the SMBH mass and distance (Ghez et al., 2008; Gillessen et al., 2017; Gravity Collaboration et al., 2018).

The missing pulsars

Based on the large number of massive stars, one would expect a large population of NSs in the Milky Way innermost region (up to few thousands within 0.01 pc, according to Pfahl and Loeb 2004), but only one was unambiguously observed so far: PSR J1745-2900, a magnetar orbiting SgrA* with 0.1 pc of projected separation (Kennea et al., 2013; Mori et al., 2013; Rea et al., 2013). A strong interstellar scattering screen toward the GC has been suggested to impede the observation of the bulk of pulsars (e.g. Macquart and Kanekar, 2015); however, the magnetar detection would rather suggest that the lack of NS observations implies an intrinsic dearth of this stellar species near the SMBH (Dexter and O'Leary, 2014).

1.5.2 Unexpected star formation in the inner parsec

The SMBH presence has long been thought to hinder star formation in its close vicinity, as molecular clouds should get disrupted by the strong SMBH gravitational potential prior to turning into stellar nurseries (Sanders, 1998). However, numerous young stars are observed in the GC innermost parsec: this is the famous *paradox of youth* (Ghez et al., 2003).

Different scenarios have been invoked to solve it: according to *migration* models,

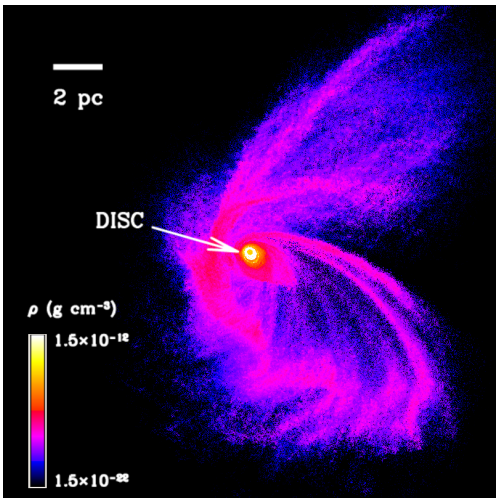

Fig. 1.7. A gaseous disc is produced via the disruption of a $\sim 10^5 M_\odot$ molecular cloud onto a Milky-Way like SMBH. The image shows the logarithmic gas density map projected in the plane where the disc is seen face-on. The image refers to a snapshot at $t = 0.48$ Myr in run E of Mapelli et al. (2012); image credits: Gualandris et al. (2012b).

stellar clusters could form at large distances, then gradually inspiralling via efficient dynamical mechanisms down to the SMBH influence area (Kim and Morris, 2003; Fujii et al., 2008; Perets et al., 2009; Perets and Gualandris, 2010). However, a cluster should be very dense and massive in order to get to the innermost pc within the lifetime of its massive stars (Kim et al., 2004): Petts and Gualandris (2017) showed that even in the most extreme assumptions for the cluster mass and density, the morphology of young stars at the GC is hardly reproduced via this scenario.

The alternative *in situ* scenarios assume instead that star formation could efficiently occur close to the SMBH under particular conditions. It has been proposed that the tidal disruption of a molecular cloud operated by the SMBH may result in extended star formation within the resulting circumnuclear gaseous disc (Fig. 1.7; Sanders 1998; Nayakshin and Sunyaev 2005; Nayakshin et al. 2007; Bonnell and Rice 2008; Mapelli et al. 2012; Alig et al. 2013). This model is supported by the fact that stars formed in situ would naturally exhibit a top-heavy mass function if the GC background temperature is $\gtrsim$100 K (Mapelli et al., 2012). However, the observed non-negligible stellar orbital eccentricities within the CW disc ($< e >= 0.3 \pm 0.1$, Yelda et al. 2014) require a fine tuned orbit for the cloud infall, that should occur nearly radially (Wardle and Yusef-Zadeh, 2008); such free-fall trajectory could possibly result from cloud-cloud collisions that seem to often occur at larger distances (Tsuboi et al., 2015, 2018). Alternatively, Naoz et al. (2018) suggested that the non-negligible orbital eccentricities observed in the disc could be an observational artefact, if most stars in the disc are members of stellar binaries; if it were the case, the actual disc membership of young stars would be much higher than the number inferred from observations ignoring the contribution of binaries. Alternative explanations for the fact that only a fraction of young GC stars belong to the CW disc have been put forward: e.g. the contribution of SN kicks and two-body encounters with single and binary stars (Perets and Alexander, 2008; Bortolas et al., 2017; Trani et al., 2018).

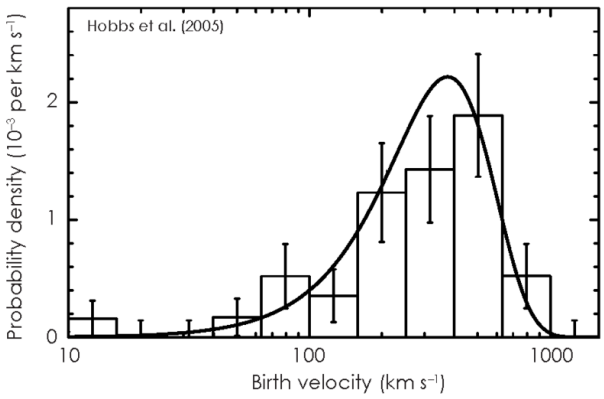

Fig. 1.8. Distribution of birth velocities of Galactic pulsars (bars), based on the observation of 233 pulsar proper motions. The distribution is well described by a Maxwellian, with a mean of $\approx$ 400 km s^{-1} and a velocity dispersion of 265 km s^{-1}. Image credit, data and further details in Hobbs et al. (2005).

If the origin of stars in the disc is enigmatic, the genesis of the S-star cluster is even more debated. The thermal eccentricity distribution of S-stars and their isotropic orbital orientation would suggest that their origin is not linked to the CW disk. An interesting possibility is that S-stars are deposited on their current orbits as a result of tidal breakup of field stellar binaries approaching the SMBH (the so-called *Hills mechanism*, Hills 1991). One of the two components in the broken pair would remain bound to the SMBH on a highly eccentric orbit ($e \gtrsim 0.97$), while the second would be ejected as a hyper-velocity star. This scenario has been regarded as promising as it can explain both the S-star orbits (provided that dynamical processes are successful in thermalizing orbital eccentricities, Hopman and Alexander 2006; Perets et al. 2009; Perets and Gualandris 2010; Antonini et al. 2010, 2011; Antonini and Merritt 2013) and the observation of several hyper-velocity stars in the Milky Way, a few of them being consistent with a GC origin (e.g. Brown et al., 2005, 2015, 2018).

Alternatively, it has been proposed that the S-stars could be rejuvenated old stars that underwent either a stellar merger or severe atmosphere alteration via envelope stripping (Lee, 1987; Davies and King, 2005).

The most recent estimate of stellar ages of eight among the S-stars (Habibi et al., 2017), though, indicates that they are genuinely coeval to the CW disc. S2 would be $\approx$ 7 Myr old, while the other stars in the sample appear to be $\lesssim$ 15 Myr old, and consistent with the age of S2 within the errors (Habibi et al., 2017). This finding would lead to believe that the S-stars were born in the recent star formation episode that generated the CW disc stars as well. In this picture, the thermal eccentricity and spatial isotropy of S-stars could have been generated via Kozai-Lidov-like processes (Kozai, 1962; Lidov, 1962), acting (i) on S-stars born in a previously more extended CW disc (Chen and Amaro-Seoane, 2014) or (ii) on binary stars initially in the CW disc, that later underwent the Hills mechanism (Šubr and Haas, 2016).

1.5.3 The supernova kicks at the Galactic Centre

The presence of young stars in the innermost GC parsec, combined with the fact that stars seem to form there in a top-heavy fashion (thus favouring the production of massive stars with respect to the field), suggests that a number of SN explosions have occurred in the GC, and many more will happen in the next few million years. This argument is supported by the fact that Sgr A East, a gaseous shell displaced 2.5 pc from SgrA*, is most probably a SN remnant aged $\sim 10^4$ yr (Novak et al., 2000; Maeda et al., 2002; Tsuboi et al., 2009). The dynamical consequences of multiple SN events occurring in the close vicinity to SgrA* can be manifold: for instance, Perets et al. (2008) propose that repeated SN kicks in stellar binaries within the CW-disc, combined with efficient two-body scatterings, could motivate the fact that only a fraction of young stars in the GC belong to the CW-disc; the effect of SN-kicks in triplets (the third body possibly being a SMBH) has recently been investigated from a in great theoretical details by Lu and Naoz (2018).

When a SN event occurs, the asymmetric expulsion of the stellar ejecta likely results in a net kick imparted to the newborn stellar relic. In fact, the analysis of 233 Galactic pulsar proper motions, operated by Hobbs et al. (2005), indicates a Maxwellian distribution for SN kicks[(5)] affecting NSs, with one-dimensional variance $\sigma_k = 265$ km s^{-1} (Fig 1.8).

The elusive nature of stellar BHs renders the inference of their natal kick distribution significantly more challenging. Repetto et al. (2012, 2017) analysed the allocation of X-ray binaries in the Milky Way halo, and deduced that the velocity distribution of BH kicks should be similar to the NSs one. On the other hand, theoretical arguments support the idea that BHs experience lower kicks, having the same momentum (rather than the same speed) as NS ones; in fact, a often adopted momentum based approach consists in either normalising the BH kick to the mass of the ejected material, or to the mass of the final remnant (Hurley et al., 2002; Spera et al., 2015). Furthermore, it is generally believed that the most massive stellar BHs cannot experience a SN kick, as they are expected to form via the direct collapse of their progenitor (Fryer et al., 2012; Mapelli et al., 2013b). In general, thus, the velocity distribution of SN kicks remains highly debated, especially if the newborn object is a stellar BHs.

1.5.4 Supernova kicks in binary stellar systems within the CW disk

The large number of SN kicks that most probably interested the history of the GC could have played a relevant dynamical role: owing to their inferred high velocities (Hobbs et al., 2005), SN kicks may strongly perturb the orbit of the newborn compact stellar remnants, possibly reshaping the density distribution of stars and dark relics in the vicinity to SgrA* (Bortolas et al., 2017; Lu and Naoz, 2018). Motivated by this, In Chapter 2 we run a large suite of three-body highly accurate (regularized, Mikkola and Tanikawa 1999a,b) simulations to investigate what is the role of SN kicks occurring in *massive stellar binaries* within a CW disc-like structure. Our choice to deal with binaries stems from the fact that massive stars,

(5) Possibly, a superposition of two Maxwellians, a second one with $\sigma_k' \approx 20 - 50$ km s^{-1}, would better match observations and account for different mechanisms of SN explosions and NS formation (Beniamini and Piran, 2016; Giacobbo and Mapelli, 2018, and references therein).

as the ones observed in large numbers within the central parsec, are often found to be born in pairs (Sana and Evans, 2011); plus, the binary fraction in the CW disc has been inferred to lie in the range $\approx 30-85\%$ (Pfuhl et al., 2014; Gautam et al., 2017).

Our investigation provides interesting clues on several GC long-standing puzzles. First of all, we find that SN kicks do not change significantly the orbits of newborn stellar mass BHs[(6)]. As a result, several CW-disc like star-forming episodes may have built-up a inner concentration of BHs (Bortolas et al., 2017). This effect may add to mass segregation, and increase the density of massive stellar relics in the innermost GC region. The inferred presence of a dark cusp is supported by several arguments:

(i) the mild slope of of the recently observed luminous stars profile at the GC (Schödel et al., 2017a; Gallego-Cano et al., 2017) could be justified assuming that a steeper, dark cusp of stellar relics lurks in the close vicinity to SgrA* (cf. §1.5.1; Vasiliev, 2017; Baumgardt et al., 2017);

(ii) a dark cusp of at least 500 $M_\odot$ within the innermost 0.4 pc would help to reproduce the isotropic orbits of S-star, in the hypothesis that the S-cluster is generated via a combination of the Hills (1991) and Kozai-Lidov mechanism (Kozai, 1962; Lidov, 1962) acting on binaries initially belonging to the CW disk (cf. §1.5.2; Šubr and Haas, 2016);

(iii) Hailey et al. (2018) recently reported the detection of a dozen quiescent accreting X-ray binaries, settled in a density cusp in the central Milky Way parsec, strongly supporting the existence of hundreds of compact binary systems in the GC, and probably many more isolated BHs.

Contrarily to stellar BHs, our investigation suggests that NS and low mass secondary binary member orbits get strongly affected by the SN kick. In general, these objects are scattered away from the SMBH, possibly becoming unbound hyper-velocity stars ($\approx 5\%$); otherwise, they end up swiping higher energy orbits, enhancing their orbital eccentricity and inclination (Bortolas et al., 2017). This aspect could be closely related to the *missing pulsars problem*: the effect of SN kicks acting on NSs in the innermost parsec may at least help to reduce the number of pulsars inhabiting the central region of the Milky Way.

Finally, the effect of SN kicks is relevant for secondary binary members: when the kick does not unbind the pair ($\approx 40\%$ of cases), the system might light-up as an X-ray binary through Roche lobe filling; when the pair gets broken, instead, the produced stellar trajectories of companion stars might explain the highly eccentric orbits of some among the S-stars and G-cloudlets (Bortolas et al., 2017).

1.5.5 Supernova kicks in the Galactic Centre as EMRI generators

There is a second important consequence to SN kicks in galactic nuclei that deserves investigation, i.e. whether they can possibly induce the generation of EMRIs. In the standard picture, an EMRI is triggered if a stellar mass compact object is

(6) In the assumption that BH velocity kicks get smaller if the BH mass increases, i.e., adopting a momentum-based approach for the SN kick.

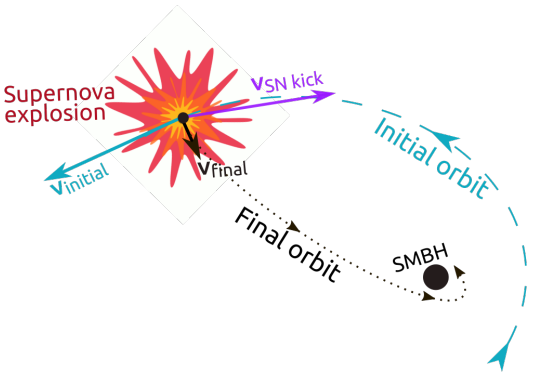

Fig. 1.9. The image qualitatively depicts the process inducing an EMRI via a SN kick. A massive star initially spans a high angular momentum orbit around the SMBH (blue dashed line); when it undergoes the SN, its orbital velocity gets instantaneously modified, thus the orbit of the generated dark stellar relic could be significantly different. If the SN kick velocity almost cancels out with the instantaneous orbital velocity of the star (as shown in the figure), the final remnant would settle onto a nearly radial orbit (black dotted line) and its GW inspiral timescale may become shorter than the timescale for other orbital perturbations to occur.

scattered in the vicinity to an SMBH by means of traditional relaxation processes (Amaro-Seoane et al., 2007). The alternative possibility that SN kicks may induce the generation of EMIRs has been investigated in Chapter 3 of the present thesis: the strongly perturbed orbit of a newborn BH or NS may attain a very eccentric orbit, and the timescale over which the compact object is expected to decay onto the SMBH via GW emission (Eq. 1.10) may drop below the timescale for other orbital perturbations, as two-body relaxation, to occur (see Fig 1.9).

In our study, we adopt a Monte-Carlo approach to mimic the effect of SN kicks in the GC star forming nucleus. Remarkably, we find that a fraction up to a few $\times 10^{-4}$ of compact objects born in the Milky Way central parsec may produce EMRIs as a result of their natal kicks, while the time spanning from the SN event to the final plunge is typically of the order of million years. If we combine this finding with the fact that SNe in a GC-like environment are expected to happen nearly every 10^4 yr (e.g. Rimoldi et al., 2015), this brings to the conclusion that SN-EMRIs occur at a rate up to 10^{-8} yr^{-1} per Milky Way, resulting in up to $\sim$10% of EMRIs being possibly triggered via this mechanism. Our study also shows that the clockwise disc and especially the S-cluster inhabit an optimal region of phase space for guaranteeing a substantial production of SN-EMRIs.

The importance of foreseeing EMRIs production mechanisms and the associated rates stems from the fact that these GW signals would be detected in the near future by LISA. However, EMRIs are not the principal target for the forthcoming space-based observatory. In fact, the possibly strongest GW signals detectable by the LISA mission are expected to be released in the coalescence of SMBH pairs.

Even if several arguments have been put forward to reject the possibility that the Milky Way centre hosts a binary SMBH (e.g. Gualandris and Merritt, 2009), many other galaxies are believed to harbour such massive pairs, and even the Milky Way nucleus most probably witnessed a galaxy major merger in its distant

past (Fakhouri et al., 2010; Iorio and Belokurov, 2018) possibly resulting in the coalescence between two SMBHs. A throughout understanding SMBH binaries dynamical evolution will be crucial to interpret the GW events that LISA will soon reveal; thus, in the next section we review the processes governing the binaries evolution down to their GW emission driven coalescence.

1.6 A story of supermassive black hole pairs

The idea that the formation SMBH binaries occurred in large numbers along the history of our Universe naturally arises from the currently accepted cosmological paradigm (White, 1978). In fact, galaxies are believed to efficiently aggregate through the agglomeration of small sub-galactic units, owing to the catalyst effect of their extended dark matter haloes. According to Fakhouri et al. (2010), the time intercurring between two subsequent major mergers (i.e. mergers between galaxies whose mass ratio is greater than $\sim 1/4$) would range from ~ 0.2 Gyr at redshift $z = 10$ to ~ 10 Gyr at $z = 1$. As a consequence, the majority of large galaxies conceivably experienced at least one major merger in their lifetime.

A further notable fact is that quasars are observed down to very high redshift, suggesting that at least part of the often colliding proto-galaxies harboured a SMBH from the dawn of galaxy formation (Haehnelt et al., 1998; Fan et al., 2003; Wu et al., 2015). During a galaxy collision, dark matter haloes drag along both their luminous component and the SMBHs that may dwell in their centres (Barnes, 2001). Consequently, two SMBHs would frequently find themselves in the same galaxy merger relic in the aftermath of a galaxy encounter.

1.6.1 Evolution of SMBH binaries

In order for the SMBH pair to merge in a burst of GWs, the two objects should shrink from the kpc scale of the galactic collision down to the ∼mpc separation at which GW emission dominates the binary energy loss. The dynamical mechanisms governing this long journey have been first pointed out by Begelman et al. (1980). The pair shrinking in gas poor galaxies(7) can be divided in the following major steps (Fig. 1.10):

(i) a dynamical-friction-induced sinking towards the centre of the galactic potential well, taking approximately a dynamical friction timescale (Eq. 1.13) and ending roughly when the mass enclosed in the binary orbit equals the mass of the smaller SMBH (a_f);

(ii) a phase in which dynamical friction and three-body stellar scatterings (slingshot ejections) concurrently reduce the binary semimajor axis a (until the binary is said to be *'hard'*);

(iii) the continued hardening (i.e. shrinking) of the binary, induced by continual stellar slingshot ejections; the efficiency of this phase has been found to crucially depend on the supply of novel stars to the SMBHs close vicinity;

(7) The present thesis solely explores the binary evolution in pure stellar systems devoid of gas, as massive elliptical galaxies.

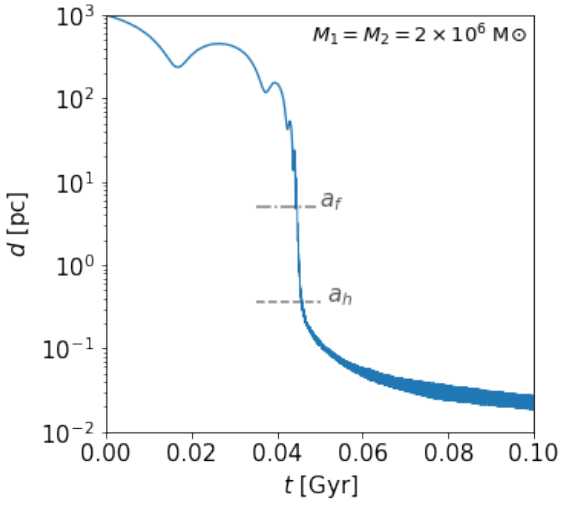

Fig. 1.10. The plot shows the typical evolution of the distance between two SMBHs as a function of time. An equal mass binary of $M_b = 4 \times 10^6 M_\odot$ is considered. The initial evolution is governed by the dynamical friction of the SMBHs and their stellar entourages against the galactic background; at the separation marked with a_f, the binary swiftly shrinks via the combined effect of dynamical friction and three-body stellar scatterings, and excavates a core in the galaxy centre. Once the binary has become hard (a_h), its evolution slows down considerably, and the shrinking rate crucially depends on the supply of novel stars in the loss cone region.

(iv) at roughly mpc scale, GWs dominate the ultimate binary inspiral and bring to the final coalescence.

An important landmark in the evolution of supermassive pairs is the moment at which the binary becomes *hard*. This happens when the binary Keplerian velocity roughly exceeds the velocity of stars in the stellar background (σ):

$$a_h = \frac{G\mu}{4\sigma^2} \approx 0.27 \text{ pc}(1+q)^{-1} \left(\frac{M_b}{10^7 M_\odot}\right) \left(\frac{\sigma}{200 \text{ km s}^{-1}}\right)^{-2}; \tag{1.14}$$

here we assume that the binary members have masses $M_1 \geq M_2$, their total mass is $M_1 + M_2 = M_b$, their mass ratio is $q = M_2/M_1 \leq 1$ and μ is the binary reduced mass $M_1 M_2 / M_b$ (Merritt, 2013a).

The *hard* binary is no longer affected by dynamical friction, and its energy loss is primarily induced by three-body scatterings of stars that closely approach it (on scales $\lesssim a$). If $m_\star$ is the typical stellar mass and $E = -G\mu M_b/(2a)$ is the binary energy, it can be shown that each stellar interaction, on average, results in a relative energy loss for the binary

$$\frac{\Delta E}{E} \approx -2C \frac{m_\star}{M_b}, \tag{1.15}$$

where C is the *dimensionless energy change*

$$C \equiv \frac{M_b}{2m_\star} \left|\frac{\Delta E}{E}\right|; \tag{1.16}$$

scattering experiments determined C to be typically of the order of unity (Hills, 1983; Quinlan, 1996).

The binary energy loss turns into an enhancement of the interacting star orbital energy: the star velocity after the interaction is $v_f \sim \sqrt{G\mu/a}$; if we set $a = a_h$, it follows that $v_f \sim 2\sigma$; that is, a hard binary tends to irreparably unbind interacting stars from the system.

Even if binaries with roughly equal mass swiftly become hard, their subsequent evolution in gas-poor environments has been put under scrutiny in the past years, and several authors have pointed out that the subsequent three-body scattering phase might not be efficient enough to ensure the binary coalescence (Begelman et al., 1980; Milosavljević and Merritt, 2003b; Makino and Funato, 2004). Here below we review in better detail the dynamics of SMBH binaries, the reasons behind their possible stalling and the dynamical mechanisms that have been put forward to ensure an effective binary hardening down to the smallest scales.

(i) Dynamical friction driven inspiral

Initially, the SMBH pair experiences a phase of rapid sinking under the effect of dynamical friction on the stellar and gaseous background. The typical associated timescale t_{df} can be approximated via Eq. 1.13 (Chandrasekhar, 1942, 1943), as long as the two SMBHs evolve independently. A more accurate computation of the sinking time should account for the fact that a SMBH retains part of the galaxy nucleus during the inspiral: the sinking mass increases to $M_s \sim 10^3 M_\bullet$ (assuming $M_\bullet - M_{\rm bulge}$ relation, Merritt 2001) and the decay timescale would shorten to $t'_{df} \sim 10^{-3}\ t_{df}$. However, the stripping operated by the galaxy tidal field would progressively shear the entourage of stars surrounding each SMBH; accounting for this, a simple estimate of the dynamical friction timescale yields

$$t''_{df} \approx \frac{R_e\sigma^2}{\ln\Lambda'\sigma_s^3} \approx 0.15\ {\rm Gyr}\frac{2}{\ln\Lambda}\left(\frac{R_e}{10{\rm kpc}}\right)\left(\frac{\sigma}{300{\rm km\ s^{-1}}}\right)^2\left(\frac{\sigma_s}{100{\rm km\ s^{-1}}}\right)^{-3}, \quad (1.17)$$

where R_e is the effective radius of the bigger system, $\Lambda' = 2^{3/2}\sigma/\sigma_s$, while σ and σ_s are respectively the one dimensional velocity dispersions of the bigger and sinking galaxy (Dosopoulou and Antonini, 2017).

Once the Keplerian binary forms, the following evolution significantly depends on the SMBHs mass ratio. If $q \gtrsim 0.1$, the standard dynamical friction equations properly describe the swift binary inspiral down to $\sim a_h$. If not, the time required to bridge the gap between the influence sphere of the bigger SMBH and a_h can protract for long, even exceeding a Hubble time for binaries with $q \lesssim 10^{-3}$, especially if they are found in shallow-density cores ($\gamma \lesssim 1$, Dosopoulou and Antonini 2017; Tamfal et al. 2018).

(ii) Core excavation

Once the stellar mass enclosed in the binary orbit drops below the mass of the smaller SMBH,

$$M_\star(a_f) = M_2, \quad (1.18)$$

dynamical friction gradually ceases its effectiveness, and three body stellar scatterings begin to dominate the binary shrinking. The transition between a_f and a_h is

very swift, and the energy given up in this phase is

$$\Delta E \approx -\frac{GM_1M_2}{2}\left(\frac{1}{a_f}-\frac{1}{a_h}\right) \approx -\frac{1}{2}M_2\sigma^2 + 2M_b\sigma^2 \sim 2M_b\sigma^2, \tag{1.19}$$

comparable to the total energy of stars orbiting the binary within its sphere of influence. The energy instilled by the binary is absorbed by the stellar background, which significantly reshuffles its phase-space distribution. As a result, a core gets excavated within the SMBHs influence sphere (Ebisuzaki et al., 1991; Volonteri et al., 2003; Sesana et al., 2007); this mechanism possibly justifies the almost ubiquitous presence of cores at the centre of the most luminous galaxies (i.e. the ones that likely experienced the largest number of mergers)[(8)].

(iii) Binary hardening

Once the binary has become hard, its shrinking results from repeated slingshot ejections of the nearby stars (Saslaw et al., 1974). Any star that undergoes a close encounter with the binary will have its trajectory deflected as a result of the strong binary potential, and its closest approach distance (p) would turn appreciably smaller than its impact parameter b (i.e., the minimum distance measured along the unperturbed trajectory). In the limit of close encounters ($GM/b \gg v^2$, with v velocity of the incoming star at infinity), the nearest approach occurs at

$$p \approx \frac{b^2v^2}{2GM_b} \tag{1.20}$$

(e.g. Hills, 1983; Quinlan, 1996). The binary cross section for close encounters can be expressed as $\Sigma_b = \pi b^2$; in the limit of close interactions for which $p \approx a$ (i.e. the sole ones that efficiently shrink the pair) Eq. 1.20 can be adopted to express the cross section as

$$\Sigma_b = \frac{2\pi GM_b a}{v^2} \tag{1.21}$$

(Sigurdsson and Phinney, 1993). The average interaction rate per unit time of the binary can be obtained via $dN/dt = \Sigma_b \sigma n$, where n is the number density of stars in the field and σ is their one-dimensional velocity dispersion. If we further assume that $v \approx \sigma$, we get that

$$\frac{dN}{dt} = \frac{2\pi GM_b a n}{\sigma}. \tag{1.22}$$

Finally, the rate of energy exchange suffered by the binary can be computed by combining Eq. 1.22 and Eq. 1.15,

$$\frac{dE}{dt} = \Delta E \frac{dN}{dt} = 4\pi GC\frac{\rho a}{\sigma}E; \tag{1.23}$$

(8) In fact, alternative scenarios have been proposed to explain galaxy cores: for instance, Perets and Alexander (2008) suggest that the core excavation may occur on scales larger than the SMBH influence sphere as a result of massive perturbers (as massive molecular clouds, IMBHs, stellar clusters) scattering stars close to the binary from relatively large separations. Alternatively, Gualandris and Merritt (2008) propose that anisotropic GW emission resulting from the coalescence between two SMBHs could eject the merger product from the galaxy nucleus, and the displaced SMBH could wander in the galaxy outskirts and excavate a large core.

it follows that the rate of change of the inverse binary semimajor axis as a function of time (the so-called *binary hardening rate*) is

$$s \equiv \frac{d}{dt}\frac{1}{a} = 4\pi C\left(\frac{G\rho}{\sigma}\right) \equiv H\left(\frac{G\rho}{\sigma}\right), \tag{1.24}$$

where H can be determined to be ≈ 18 (Quinlan, 1996; Sesana et al., 2006). Eq. 1.24 has a profound implication for the study of SMBH binaries: *hard binaries harden at a constant rate, if the stellar background remains fixed*[9] (Hills, 1983). If it were the case, the GW emission phase (entered at $a = a_{\rm GW}$) would be reached in a very short timescale

$$t_{h,\rm short} \sim \frac{\sigma}{HG\rho\, a_{\rm GW}} \approx 0.25\ {\rm Gyr}\left(\frac{18}{H}\right)\left(\frac{\rho}{10^4 M_\odot {\rm pc}^{-3}}\right)^{-1}\left(\frac{\sigma}{200\ {\rm km\ s}^{-1}}\right)\left(\frac{a_{\rm GW}}{1\ {\rm mpc}}\right)^{-1}; \tag{1.26}$$

(e.g. Colpi, 2014). Unfortunately, binaries cannot harden at a constant rate, as the stellar background gets modified via the energy injection operated by the binary itself (e.g. Merritt, 2013a). In fact, Eq. 1.26 typically underestimates the hardening timescale, and a loss-cone treatment is required to properly follow the binary evolution down to the GW emission stage.

1.6.2 Loss cone theory

In order for a star to efficiently interact with the binary, it has to reach a small periapsis, roughly equal to the binary semimajor axis a: it has to be *centrophilic*. This can be translated in the angular momentum space by saying that the magnitude of the star specific angular momentum has to drop below

$$L_{LC} = \sqrt{2GM_b a}. \tag{1.27}$$

The region of phase-space harbouring stars with specific angular momentum lower than L_{LC} (i.e., stars on centrophilic orbits) is named *loss cone* (Merritt, 2013b). Every time a slingshot interaction occurs, the ejected star abandons both the galaxy nucleus and the binary loss cone. It follows that (in spherical geometries) the loss cone is effectively evacuated via binary-induced three-body scatterings within a typical stellar orbital period, and only *centrophobic* orbits can survive in the galactic potential. After the initial depletion, the binary hardening rate crucially depends on the supply of novel stars in the loss cone (Begelman et al., 1980; Milosavljević and Merritt, 2003a). If the replenishment of this region is ineffective, the binary would never reach the GW emission stage and endlessly orbit in the galaxy core (Milosavljević and Merritt, 2001, 2003a), as too few stars can participate to its hardening.

(9) Eq. 1.24 can be rewritten in a more general form: since the binary hardening results from the interaction with stars with a given phase-space distribution, the isotropic assumption yields

$$s = \int_0^\infty 4\pi v_\star^2 dv f(\varepsilon)\frac{HG}{v_\star} = 4\pi GH\int_{\Phi_0}^0 f(\varepsilon)d\varepsilon, \tag{1.25}$$

where $\varepsilon = \frac{1}{2}v_\star^2 - \Phi$ is the specific energy of each star, $v_\star$ is its velocity and $\Phi(r)$ is the gravitational potential at its position r; $f(\varepsilon)$ is the energy distribution function of stars; finally Φ_0 is the depth of the galactic potential not accounting for the binary contribution (Vasiliev et al., 2015).

The most straightforward mechanism to repopulate the loss cone is collisional relaxation (Valtonen, 1996; Yu, 2002; Milosavljević and Merritt, 2003a); the timescale over which it occurs (t_r, Eq. 1.11), though, can be safely assumed to exceed the age of the Universe in many real galaxies. Thus, the binary loss cone should remain empty any time after its initial depletion. Accordingly, direct summation N-body simulations of SMBH binaries inspiralling in gas-free *spherical* models demonstrated both the N dependence of the hardening rate (as $t_r \propto N/\ln N$, Eq. 1.12) and the binary stalling at roughly a parsec separation (Makino and Funato, 2004; Berczik et al., 2006; Merritt et al., 2007b).

This is the infamous *final parsec problem* (Milosavljević and Merritt, 2003b). Even if several candidate SMBH pairs have been identified in the recent years (Rodriguez et al. 2006; Valtonen et al. 2008; Boroson and Lauer 2009; Severgnini et al. 2018; see Dotti et al. 2012 for a review), circumstantial evidence suggests that most SMBHs are in fact single objects, implying that massive binaries should effectively find their way to coalescence.

In the last decades, several solutions to the binary stalling have been proposed. They include the effect of gas drag (Escala et al., 2004; Goicovic et al., 2017, Bortolas et al., in prep), the influence of a massive perturber that may scatter new stars in the loss cone (Perets and Alexander, 2008; Matsui and Habe, 2009), the merger-induced formation of spiral arms that refill the binary loss cone (Hamers and Perets, 2017), and the infall of star clusters onto the evolving binary (Arca-Sedda et al., 2017; Bortolas et al., 2018b). In what follows, we describe this latter idea in better detail.

1.6.3 Star cluster infall onto the massive binary

Chapter 4 investigates the possibility that the infall of a young stellar cluster onto the shrinking binary would significantly affect the evolution of the latter, and shorten its journey to GWs (Bortolas et al., 2018b). In fact, (i) massive young clusters often inhabit galactic centres, a beautiful example being the Arches and the Quintuplet cluster, that lie near the centre of our relatively quiescent Galaxy (see e.g. the review by Portegies Zwart et al., 2010); (ii) galaxy mergers at the origin of binaries formation are known to possibly trigger bursts of star formation, that may bring to the production of young and massive stellar clusters (Sanders et al., 1988).

Motivated by this, we performed a suite of direct N-body runs simulating a $\sim 10^5 M_\odot$ stellar cluster infalling onto a $10^6 M_\odot$, pc-scale binary (i) along a radial orbit (Fig. 1.11 shows a few snapshots) and (ii) along a non-zero angular momentum orbit.

When the cluster infalls radially, a large fraction ($\approx 30\%$) of stars are found into the loss cone region since the beginning of the run: this fraction more than doubles at periapsis, as a consequence of the tidal torque induced by the presence of the SMBHs. The significant loss cone fuelling results in a binary shrinking of the $\approx 10\%$; this finding suggests that the interaction of the binary with a ~ 10 times more massive cluster (or equivalently, the consecutive infall of ~ 10 equally massive ones) might bring the pair close to the GW emission regime.

If some angular momentum is added to the infalling cluster though, the interaction

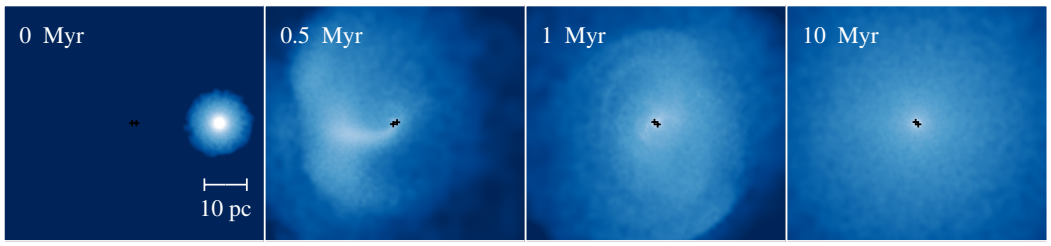

Fig. 1.11. Different snapshots of the evolution of a young stellar cluster stripped and then disrupted during its interaction with a SMBH binary (black central crosses). The cluster is initially on a radial orbit (run 2p in Bortolas et al. 2018b); the interaction is swift, and is concluded after rougly 10 Myr, with the complete disruption of the cluster. During the interaction, the binary shrinks its semimajor axis by $\approx 10\%$.

efficiency is significantly suppressed. In this case, a negligible amount ($< 1\%$) of stars is found to inhabit the loss cone at all times, as the binary-induced torques are not efficient in dragging a conspicuous amount of stars on centrophilic orbits. Accordingly, the resulting binary hardening is virtually nil.

The main conclusion to this investigation is that the cluster angular momentum constitutes a key parameter for the loss cone refilling, and only close-to-radial infalls bring to an efficient binary interaction. It is thus licit to wonder how often such radial interactions occur. Several recent studies (Tsuboi et al., 2015; Tanaka, 2018) show that at least part of the star formation observed in the centre of our Galaxy is consistent with being triggered by the collision between molecular clouds. A cluster formed as a result of such collision may attain a very low angular momentum (Mapelli et al., 2012), thus it is expected to freely infall towards the centre of its host system. This result is particularly relevant considering that one of the two observed GC young stellar clusters, the Quintuplet, probably attains a relatively radial orbit (Stolte et al., 2014).

1.6.4 Collisionless loss cone refilling in aspherical galaxies

Albeit being first proposed many years ago (e.g. Yu, 2002), what is now considered the ultimate solution to the final parsec problem has not been definitely accepted until very recently (Vasiliev et al., 2015; Gualandris et al., 2017). This long-standing problem is solved in a very general way by the deviations from spherical symmetry that naturally arise in realistic galactic potentials (Yu, 2002): collisionless diffusion of stars in angular momentum can be produced via gravitational torques arising in the non-symmetric potential, and acting over timescales much shorter than the relaxation time (Pontzen et al., 2015).

In spherical galaxies, the initial amount of stars on loss cone orbits is generally low; in addition, once the loss cone has been emptied for the first time, no straightforward dynamical mechanism can replenish it over a short time-period, as the total specific angular momentum L of each star has to be conserved along the orbit (Merritt, 2013a, cap. 4). In an axisymmetric (e.g. disc) galaxy, stars must solely conserve the component of angular momentum L_z parallel to the symmetry axis of the system. It follows that the angular momentum of each stellar orbit has a lower bound equal to L_z. Stars with $L_z < L_{LC}$ can thus wander outside the loss cone as their total angular momentum exceeds L_{LC}, until, at some point, they may attain

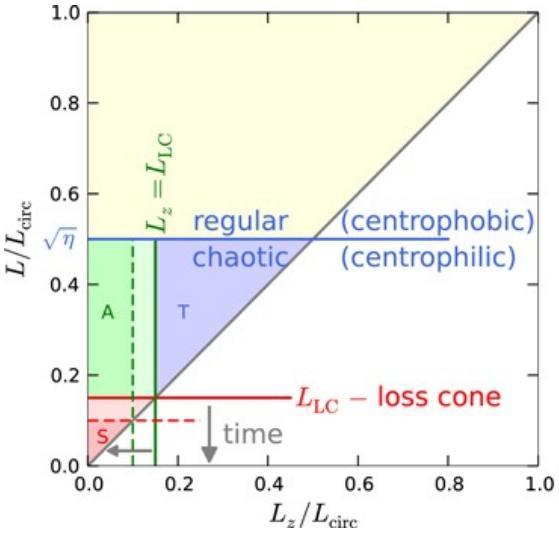

Fig. 1.12. The image displays a slice of the phase space ($L/L_{\rm circ}$,$L_z/L_{\rm circ}$) at fixed specific stellar energy; $L_{\rm circ}$ is the angular momentum of a circular orbit at that energy. In a triaxial potential (T), the extended basin (blue and green) where stars can be found prior to reaching the binary is depicted as the region satisfying $L < \sqrt{\eta} L_{circ}$. Many stars in triaxial geometries can wander anywhere in the blue and green areas as a result of gravitational torques, until finally they reach the red, proper loss cone region ($L < L_{LC}$) and undergo a binary interaction. In a spherical potential (S) instead, only the small amount of stars that inhabit the small red area can ever undergo a slingshot ejection. The axisymmetric (A) is an intermediate case: stars that may end up undergoing a binary encounter are bound to orbit in the green area where $L_z < L_{LC}$, prior to finally reaching the red region. Both the blue and green areas gradually shrink with L_{LC}, as the binary semimajor axis gets smaller and smaller; dashed lines in the image delimit the S and A regions at a later time. Image credit and a comprehensive discussion on the collisionless loss cone refilling in Vasiliev et al. (2015).

$L \sim L_z < L_{LC}$ and undergo an interaction with the binary. In triaxial systems, no component of the stellar angular momentum has to be conserved, thus stars with initially arbitrarily high L can suddenly (i.e., even after a large number of crossing times) enter the loss cone (Poon and Merritt, 2004; Merritt and Vasiliev, 2011). The described picture is beautifully illustrated in Fig. 1.12 (Vasiliev et al., 2015).

All these aspects suggest that the described *collisionless* loss cone repopulation may ensure an efficient binary hardening down to the GW emission stage (Norman and Silk, 1983; Poon and Merritt, 2004). In support to this argument, the first N-body simulations evolved *ab initio*, i.e. starting from the large-scale galaxy merger, displayed both an efficient binary hardening and a non-spherical galactic geometry induced by the merger itself (Khan et al., 2011; Preto et al., 2011; Gualandris and Merritt, 2012; Khan et al., 2012). In general, these numerical studies show that the binary finds its way to coalescence in 10 Myr to 10 Gyr (Khan et al., 2012, 2016). However, the complexity of galaxy merger simulations leaves open the possibility that processes other than the collisionless loss cone repopulation actually drive the loss cone refilling.

This mainly stems from the fact that the aforementioned studies adopted the direct summation technique to evolve the galaxy interaction (that is, particles accelerations are computed via the brute-force evaluation of the Newtonian equation). On

the one hand, the direct summation technique is the sole one ensuring an extremely detailed modelling of the binary dynamics; on the other hand, its N^2 computational complexity limits its applicability to numbers of particles that cannot currently exceed $N \sim 10^6$. In recent years, reliability of direct summation simulations has been questioned, as low-N effects may cause both an increased random walk of the binary (Merritt, 2001), and the spurious enhancement of two-body relaxation (Vasiliev et al., 2014); both artificial phenomena lead to an underestimation of the binary coalescence time.

1.6.5 Brownian motion of the massive binary

Whenever the massive binary ejects a star, the binary centre of mass experiences a recoil whose amplitude depends on the mass of the interacting body (Merritt, 2001). In low-N simulations, where stars are orders of magnitude more massive than in real galaxies (as $m_\star \propto N^{-1}$), the binary undergoes an exaggerated, unphysical Brownian motion. As a consequence, the wandering binary can intersect more stellar orbits than it would in real (high-N) systems, and its wide random walk artificially enhances the loss cone repopulation.

For this, Chapter 5 of the present thesis investigates the significance of this spurious effect in equal-mass galaxy merger simulations. We performed a suite of direct-summation N-body runs varying the number of stars in the system from 8k to 1M. This allowed us to obtain the scaling with N of both the typical Brownian motion amplitude r_b and the binary hardening rate. Our investigation clearly shows that $r_b \propto N^{-0.5}$ as expected from theoretical arguments (Merritt, 2001; Merritt et al., 2007a), while the binary hardening rate exhibits a weaker dependence on N, suggesting that the numerical wandering has a negligible effect on the binary evolution.

A more conclusive proof to this was obtained by performing additional runs in which the binary centre of mass was anchored at the centre of the galaxy potential. The comparison of the hardening rate for binaries (i) fixed and (ii) free to wander in the galaxy is shown in Fig: 1.13. First of all, the hardening rate (s) converges to similar values for $N \sim 1M$, strongly suggesting that Brownian motion plays a negligible role in shrinking the binary in most of real galaxies, as well as in numerical simulations with the best currently achievable resolution. Moreover, the hardening rate measured at low-N was found to be sensibly higher in systems where the massive binary was left free to wander. This could imply that the loss cone repopulation in systems with $10^4 \lesssim N \lesssim 10^6$ might be dominated by the roaming of the massive binary, rather than the effect of accumulated two body encounters between stars.

1.6.6 The final proof of the collisionless loss cone refilling

Once the spurious Brownian motion in numerical simulations had been discarded, the significance of artificial (low-N) collisional loss cone refilling caused by relaxation had to be addressed. This aspect was recently investigated adopting numerical techniques other than direct summation: Vasiliev et al. (2015) adopted a Monte Carlo code that allows to tweak the significance of two-body relaxation; in Gualandris et al. (2017), we made use of an accurate fast multipole method that

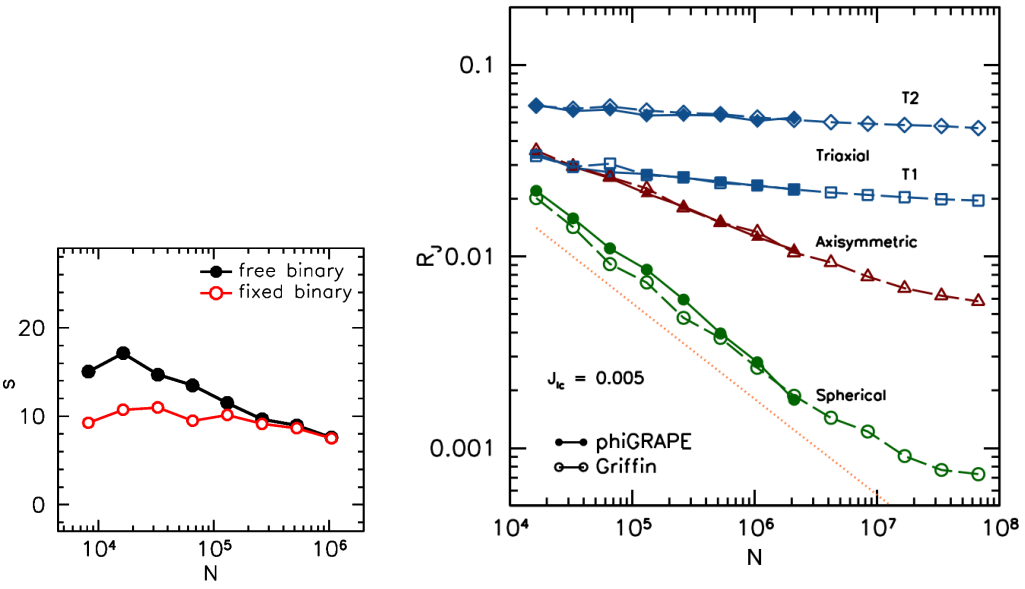

Fig. 1.13. Left-hand panel: Mean value of the binary hardening rate, s, as a function of the number of stars included in the simulation. The binary centre of mass is either free to wander as a result of slingshot interactions with stars (black) or kept fixed at the centre of the galaxy potential (red). The plot shows that the spurious hardening of the binary due to its Brownian motion is only important at low N, while its effect becomes negligible at $N \gtrsim 1$ M (Bortolas et al., 2016). Right-hand panel: the refilling parameter R_j, a proxy for the binary hardening rate, is plotted against the number of particles N in the simulation for systems of different shapes. Two different deegrees of triaxiality (T1, T2) are explored. The plot clearly shows that the hardening rate significantly depends on N ($\propto N^{-0.5}$, thin red dotted line) in spherical systems; the N-dependence is significantly reduced in axisymmetric models, and disappears in triaxial galaxies. The hardening rate of the binary can thus lead to the coalescence in galaxies with realistically high N only in the triaxial case. Empty and filled shapes show respectively results obtained via a fast multipole and a direct summation integrator. Image from Gualandris et al. (2017).

allowed to simulate the motion of $N \sim 10^8$ objects. Both studies investigated the binary hardening rate in purely spherical, axisymmetric and triaxial systems; they agreed that binaries should be able to efficiently merge in realistic triaxial galaxies owing to collisionless, torque-induced repopulation of the loss cone. Axisymmetric models were found to have hardening times that are often too long to guarantee the binary coalescence in a Hubble timescale, while the simplified assumption of spherical symmetry was proven to be the real cause to the final parsec problem (right-hand panel in Fig: 1.13).

1.6.7 The fingerprint of binaries on galaxy morphology

While the influence of the galactic shape on the binary shrinking rate has been largely explored, yet little is known about the opposite effect, i.e. the influence of the binary on the morphology of its host stellar system. In Chapter 6 we explore this effect by running a large suite of direct N-body simulations of equal-mass galaxy collisions, varying the initial orbits (from almost radial to more circular)

and density profiles ($\gamma = 0.5$, 1, 1.5) of the merging galaxies and evolving the same simulation both with and without central SMBHs. To our surprise, we find that when a binary (or even a single SMBH) is found in the centre of the merger relic, the galaxy becomes significantly oblate (i.e., disc like) up to a radius enclosing 100 times the binary mass. When the exactly same simulation is run without accounting for the central SMBHs instead, the galaxy often displays a prolate inner figure (i.e., it looks more like a bullet). This finding suggests that galaxies that harbour one or two SMBHs generally attain a more axisymmetric central geometry, a finding that is qualitatively supported by recent observations (Dullo and Graham, 2015; Foster et al., 2017). In spite of their inner axisymmetric shape, the simulated binaries are able to coalesce within a few Gyr at most.

Our study additionally shows that the degree of non-sphericity of the remnant galaxy depends not only on the SMBHs presence, but also on the parameters of the galaxy merger: radial encounters of shallower galaxies generally tend to produce more triaxial or prolate systems.

Finally, we analyse the binary hardening rate in merger remnants displaying different degrees of non-sphericity: no strong connection is found between the remnant morphology and the binary hardening rate, which seem to depend only on the inner density slope of the remnant galaxy. Such result may be particularly relevant for low-frequency GW science, as the timescale needed for a binary to reach the GW-emission stage could be assumed to scale only with the central density of the host galaxy.

2

Supernova kicks and dynamics of compact remnants in the GC

Based on:
Bortolas, E., Mapelli, M. and Spera, M.,
"Supernova Kicks and Dynamics of Compact Remnants in the Galactic Centre", 2017, MNRAS 469, 1510
–

In this Chapter we investigate the role of supernova (SN) explosions occurring in massive binary stellar systems lying in a disc-like structure within the innermost parsec of our Galaxy. In fact, SN events are expected to occur frequently in our star forming nucleus, and their associated fast kick may have an important impact on the dynamical evolution of stars near the central SMBH (Lu and Naoz, 2018).

We adopt three-body simulations to investigate the role of SNe in binaries within the clockwise (CW) disc: we explore the possibility that SN kicks contribute to the dearth of pulsars in the Galactic Centre (GC), and to the generation of a steep cusp of undetectable stellar remnants. Our investigation suggests that SN kicks are efficient at reshuffling stellar orbits and significantly contribute to sculpt the density profile at the GC. We suggest that these effects should be taken into account when performing a detailed modelling of the Milky Way innermost regions.

2.1 Methods

To study the evolution of GC binaries after SN explosions, we run 30,000 three-body encounters of systems composed of a SMBH and a stellar binary. The mass of the SMBH is fixed to $4.3 \times 10^6\, M_\odot$ (Gillessen et al., 2009).

The binary centre of mass is initially assumed to sweep a Keplerian orbit around the SMBH, with eccentricity and semi-major axis in agreement with recent observations of the CW disc: the eccentricity e is drawn from a Gaussian distribution centred in $\langle e \rangle = 0.3 \pm 0.1$ (Yelda et al., 2014), while the semi-major axes a follow the distribution $f(a) \propto a^{0.07}$ (Do et al., 2013), and we chose the mean anomaly of the orbit from a uniform distribution between 0 and 2π; this ensures that the

surface density profile of stars is $\Sigma(r) \propto r^{-0.93}$, consistent with the surface density distribution of the early type stars in the disc (Do et al., 2013); a can vary in the range $[0.04, 0.13]$ pc or $[0.001, 0.13]$ pc depending on the simulation set, as detailed below.

The eccentricity e_* of the stellar binary is randomly extracted from the thermal eccentricity distribution $f(e_*)\mathrm{d}e_* = 2e_*\mathrm{d}e_*$ (Jeans, 1919), while the semi-major axis a_* distribution takes the form $f(a_*)\mathrm{d}a_* \propto {a_*}^{-1}\mathrm{d}a_*$, i.e. follows the so-called *Öpik's law* (Öpik, 1924). The semi-major axis of the binary system spans from a minimum of 0.2 AU to a maximum distance equal to $0.4\,r_\mathrm{j}$, where $r_\mathrm{j} = a\,(1-e)\,(\frac{1}{3}M_{b,i}/M_\bullet)^{1/3}$ is the Jacobi radius (where $M_{b,i} = M_{1,i} + M_2$, $M_{1,i}$ is the mass of the primary before the SN explosion, M_2 is the mass of the secondary, and $M_\bullet$ is the mass of the SMBH)[(1)]. This ensures by construction that the binary star will not break by tidal forces at the closest passage with the SMBH, as shown in Trani et al. (2016). We also ran a sub-sample of 3000 three-body simulations without SN kicks, to check that the binary does not break if SN kicks are not included in the simulations. We found that a_* and e_* change by less than 10^{-5} in the test simulations without SN kicks, indicating that our initial conditions are stable against tidal forces.

Since a large fraction of stars (especially massive stars) form in binary systems (e.g. Sana et al. 2011), many CW disc members are expected to be binary stars. Gautam et al. (2017) found that the binary fraction of early-type main sequence stars within the CW disc is at least 32% (within the 90% confidence level). Stars with mass in excess of $\sim 9M_\odot$ are thought to undergo SN explosions after about $3-50$ Myr, depending on their initial masses. Given the young age of stars in the CW disc ($\sim 2.5-6$ Myr, Lu et al. 2013), most SN events will occur in the next Myrs. However, we use the orbital properties of the CW disc as initial conditions, because it is reasonable to expect that a series of CW-disc like star-forming events have occurred in the past and may occur in the future (it is unlikely that we live in a special time for the history of the GC, Loose et al. 1982).

The masses of the two stars are computed as follows: the zero age main sequence (ZAMS) mass of the more massive (primary) binary component ($M_{1,\mathrm{ZAMS}}$) is randomly distributed in the range $[9, 150]M_\odot$, sampling a top-heavy (TH) mass function ($\mathrm{d}N/\mathrm{d}m \propto m^\alpha$, with $\alpha = -1.7$), in agreement with the observations of the GC (Lu et al., 2013). The ZAMS mass of the less massive (secondary) binary component ($M_{2,\mathrm{ZAMS}}$) is either extracted from the TH mass function in the range $[0.1,\ 150]M_\odot$ (simulation sets A and C) or assumed to be equal to 0.9 times the ZAMS mass of the primary star (simulation set B), as detailed below. We then evolve each primary star from $M_{1,\mathrm{ZAMS}}$ to its pre-SN mass $M_{1,i}$, according to the PARSEC stellar evolutionary tracks (Bressan et al., 2012; Chen et al., 2015); the pre-SN mass of a star as a function of its ZAMS mass is shown in Figure 2.1. Similarly, we calculate the mass of the secondary star at the time of the SN explosion of the primary (M_2) using the PARSEC stellar evolutionary tracks for a star of ZAMS mass $M_{2,\mathrm{ZAMS}}$.

We start the simulations at the time of the SN explosion, by giving the binary a SN kick. The mass of the compact remnant is computed using the delayed SN model

(1) The resulting initial orbital period of the stellar binaries ranges from ~ 0.1 yr to $\sim 10^3$ yr, and about one fourth of them has a period < 1 yr.

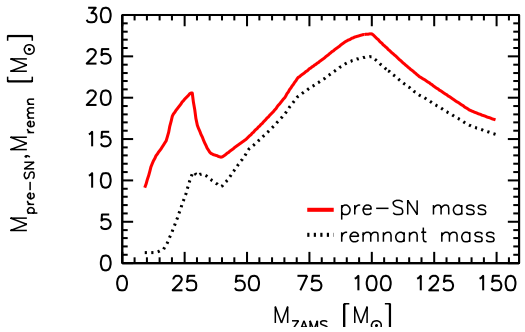

Fig. 2.1. Red solid line: pre-SN mass of a star as a function of its ZAMS mass according to the PARSEC stellar evolutionary tracks (Bressan et al., 2012; Chen et al., 2015). Black dotted line: mass of the SN compact remnant as a function of the the progenitor ZAMS mass according to Spera et al. (2015); we assume the delayed SN model.

Tab. 2.1. Initial conditions and differences between the three sets of simulations.

	set A	set B	set C
$M_{2,\mathrm{ZAMS}}$	TH, $0.1-150M_{\odot}$	$0.9\times M_{1,\mathrm{ZAMS}}$	TH, $0.1-150M_{\odot}$
CW disc	$0.04-0.13$ pc	$0.04-0.13$ pc	$0.001-0.13$ pc
N	10,000	10,000	10,000
Δt_{sim}	1 Myr	1 Myr	1 Myr

Each row indicates, for the three sets, (i) how the ZAMS mass of the secondary component ($M_{2,\mathrm{ZAMS}}$) is chosen, (ii) the extension of the CW disc, (iii) the number N of simulations in each set, (iv) the time Δt_{sim} over which each system was evolved.

(Fryer et al., 2012), according to Spera et al. (2015). We distinguish between NSs and stellar-size black holes (BHs) depending on whether their mass is respectively below or above $3M_{\odot}$. The mass of the SN relic as a function of the progenitor ZAMS mass is shown in Figure 2.1. The distribution of SN kicks is uncertain, especially for BHs (see e.g. Gualandris et al. 2005; Fragos et al. 2009; Repetto et al. 2012; Janka 2013; Beniamini and Piran 2016; Mandel 2016). For NSs, we adopt the kick distribution reported by Hobbs et al. (2005), i.e. a Maxwellian distribution with one-dimensional variance equal to $\sigma = 265$ kms^{-1}, derived on the basis of peculiar motions of 233 pulsars. If the remnant is a BH, the kick velocity is then normalized to the mass of the remnant, assuming linear momentum conservation. The natal kick is given to the binary members as detailed in Appendix A.

We performed three sets of three-body simulations composed of 10,000 runs each: (i) in set A, the ZAMS mass of the secondary star is extracted from the TH mass function between 0.1 and $150M_{\odot}$ and the disc inner and outer limits are 0.04 and 0.13 pc, respectively; (ii) set B differs from set A as the ZAMS mass of the secondary is set equal to 0.9 times the ZAMS mass of the primary; we explored this possibility due to the uncertainty in the mass correlation of binary stars (Kobulnicky and Fryer, 2007; Sana et al., 2011); (iii) in set C the ZAMS mass of the secondary is computed as in set A, but the disc is assumed to span from 0.001 to 0.13 pc, according to Chen and Amaro-Seoane (2014), who suggested that the CW disc inner edge was closer to SgrA* in the past. The differences among the three sets and the parameters of the simulations are summarized in Table 2.1. We chose to

perform 10^4 runs per each set of simulations because each set aims at reproducing the population of the CW disc, which has been estimated to be as massive as a few$\times 10^4 M_\odot$ (Lu et al., 2013). Moreover, we checked that 10^4 runs per each simulation set are sufficient to filter out statistical fluctuations.

Each three-body system is evolved from the moment of the SN explosion and for $\Delta t_{\rm sim}$=1 Myr; this timescale ensures that stars still bound to the SMBH generally complete $\sim 100 - 1,000$ orbits by the end of the simulation, thus they totally absorb the effect of the kick. On the other hand, our simulations cannot account for the two-body relaxation, which can affect stellar orbits of a CW disc structure within $10 - 100$ Myr (Šubr and Haas, 2014); thus a choice of $\Delta t_{\rm sim} > 1$ Myr would not be beneficial.

The simulations are evolved by means of a fully regularized N-body code that implements the Mikkola's algorithmic regularization (MAR, Mikkola and Tanikawa 1999a,b). This code is designed for studying the dynamical evolution of few-body systems in which strong gravitational encounters are frequent and the mass ratio between the interacting objects is large. The MAR scheme removes the singularity of the two-body gravitational potential for $r \to 0$, by means of a transformation of the time coordinate (see Mikkola and Tanikawa 1999b for details). Our implementation uses a leapfrog scheme in combination with the Bulirsh-Stoer extrapolation algorithm. The code integrates the equations of motion employing relative coordinates by means of the so called chain structure. This change of coordinates reduces round-off errors significantly (Aarseth, 2003): the relative error in the energy conservation of our simulations is always below 10^{-10}. The code can be used as a stand-alone regularized N-body code or as a module of the direct N-body code HiGPUs-R (Spera, in preparation; see Capuzzo-Dolcetta et al. (2013) for the current version of HiGPUs).

Figure 2.2 shows an example of the binary orbit before and after the SN kick in set C: two stars of 9 and 0.1 $M_\odot$ orbit the SMBH with semimajor axis $a \approx 45.0$ mpc and eccentricity $e \approx 0.34$. In this particular case the binary breaks, but both members remain bound to the SMBH. The secondary star settles on a different orbit with respect to the initial one (with semimajor axis ≈ 53.0 mpc, eccentricity ≈ 0.60 and change in the orbital inclination of ≈ 32 degrees) while the 1.3 $M_\odot$ NS produced by the SN only experiences a small ($\lesssim 10\%$) change in its orbital parameters.

2.2 Results

In this Section, we present the results of our three-body simulations. Figure 2.3 shows the density profile of the simulated binaries reconstructed from the individual three-body experiments, by considering the distance of each star from the SMBH at time $t = 1$ Myr (i.e. the end of the simulations). Figure 2.4 shows the orbital parameter distribution of objects that are still bound to the SMBH at the end of the simulation. The semi-major axes, eccentricities and pericentre radii are computed with respect to the SMBH, while the inclination is computed with respect to the CW disc. In the plots, we distinguish between BHs ($\sim 54\%$ of the remnants), NSs ($\sim 46\%$ of the remnants) and secondary stars. We stress that the large number of BHs is due to the assumed TH mass function. The distribution of BHs resembles

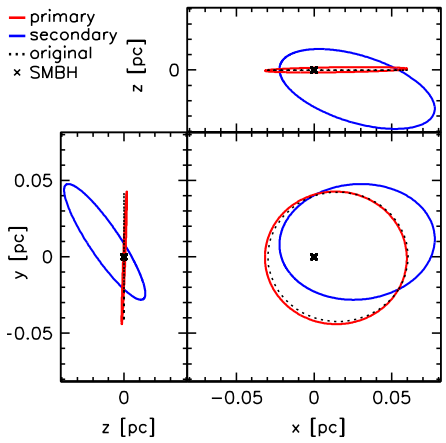

Fig. 2.2. Orbit of the binary components in a selected simulation of set C. Black dotted line: pre-SN orbit of the centre of mass of the binary around the SMBH; red solid line: orbit of the compact remnant (a NS with mass = 1.3 $M_\odot$) around the SMBH, after the SN explosion (which breaks the binary); blue solid line: orbit of the secondary star (mass = 0.1 $M_\odot$) around the SMBH, after the SN explosion; black cross: position of the SMBH. Initial orbital parameters of the binary centre of mass: semimajor axis $a \approx 45.0$ mpc, eccentricity $e \approx 0.34$; orbital parameters of the secondary binary member at the end of the integration: semimajor axis $a \approx 53.0$ mpc, eccentricity $e \approx 0.60$, difference in the orbital inclination ≈ 32 degrees; the NS changes its orbital parameters by $\lesssim 10\%$ by the end of the run, as its semimajor axis becomes $\approx$45.6 mpc, its eccentricity ≈ 0.38 and its inclination ≈ 2 degrees.

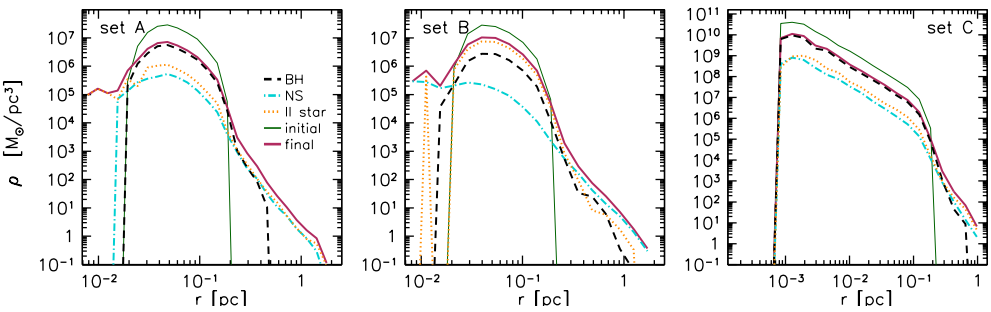

Fig. 2.3. Mass density profile of stars and compact remnants reconstructed from the individual three-body runs, for set A (left), B(centre), C(right). Dark green solid thin line: total initial distribution; dark red solid line: total final distribution; black dashed line: BHs at 1 Myr; light blue dash-dotted line: NS at 1 Myr; orange dotted line: secondary stars at 1 Myr. The density profiles are normalized assuming an initial total mass equal to $10^5 M_\odot$.

the pre-SN distribution, implying that most BHs are anchored to their initial orbit and SN kicks are not efficient in scattering them in different regions of the phase space. In contrast, NSs are more easily scattered by the SN explosion and spread in the innermost and outermost regions of the GC. This is valid for all the sets of simulations.

In both sets A and C, $75-80\%$ of the mass within $0.1-1$ pc is in the form of BHs. From Figure 2.3 it is also clear that in set A and C BHs dominate the final mass distribution for a large range of radii, i.e. within $\sim 0.02-0.2$ pc in set A and $\sim 5\times10^{-4}-0.2$ in set C. We stress that our simulations were run only for 1 Myr and that they only account for three bodies at a time: we cannot say anything about the effect of two-body relaxation on the BHs confined in the central pc. However, it is likely that the BHs will relax their distribution near the SMBH within ~ 100 Myr; the relaxation time within the disc is computed as described in Šubr and Haas (2014)[(2)].

The behaviour of the secondary stars strongly depends on their masses: in set A and C, the secondary binary member is a low-mass star in most cases ($\sim 90\%$ secondary stars have masses lower than $3M_{\odot}$) and is easily scattered on a completely new orbit after the SN kick, while in set B the secondary is a high-mass star ($\gtrsim 9M_{\odot}$) and keeps memory of its initial orbit. In set B, secondary stars are much more massive than the remnants of primary stars, thus they dominate the mass distribution within $\sim 0.02-0.5$ pc. This would be true only within a short timescale, as most of the companion stars in set B will undergo a SN explosion within a few Myr and they will turn into compact remnants.

Figure 2.4 shows that NSs notably change their orbit in set B, with respect to set A and C. We detail the case of eccentricity: in set A and C only $\sim 16\%$ of NSs have eccentricities $e > 0.5$, while in set B the fraction of NS with $e > 0.5$ is as high as $\sim 55\%$. On the other hand, $\sim 25\%$ of secondary stars have eccentricities $e > 0.5$ in set A and C, while their fraction drops to $\sim 5\%$ in set B. All the other orbital parameters show a similar behaviour, and show that SN kicks are distributed between the two binary components, with weights that anti-correlate with the mass of the bodies.

Figure 2.5 shows stellar pericentre distance versus eccentricity for the three sets of runs, distinguishing between compact remnants and secondary stars. This Figure highlights that heavy objects are spatially more confined. The bulk of stars and remnants still show orbital parameters that resemble the ones of the CW disc; however, several stars are scattered to highly eccentric orbits.

Most of stars and compact remnants continue orbiting the SMBH by the end of the simulation, and only $\sim 5\%$ objects become unbound from the SMBH. In set B, NSs absorb most of the SN kick and about one fourth of them escapes the SMBH potential, while secondary stars are strongly anchored to their initial orbit and all but five of them stay on a bound orbit by the end of the simulation. We find an

(2) As a matter of fact, the relaxation time-scale of the old and almost isotropic stellar component within the SMBH influence radius has been estimated to be ~ 10 Gyr or even longer (Merritt, 2010, fig. 3). However our investigation focuses on the young population of stars in the CW disc: due to their coherent motion, stars in a disc self-relax on a much shorter time-scale $T_{\langle e^2\rangle}$, that can be computed as the time over which the mean-square-eccentricities of stars grow from zero to a given $\langle e^2\rangle$ (Stewart and Ida, 2000). If we assume a CW-disc like structure and we use $\langle e^2\rangle^{1/2}\approx 0.3$, it follows that $T_{\langle e^2\rangle}\sim 100$ Myr (Šubr and Haas, 2014, equation 4).

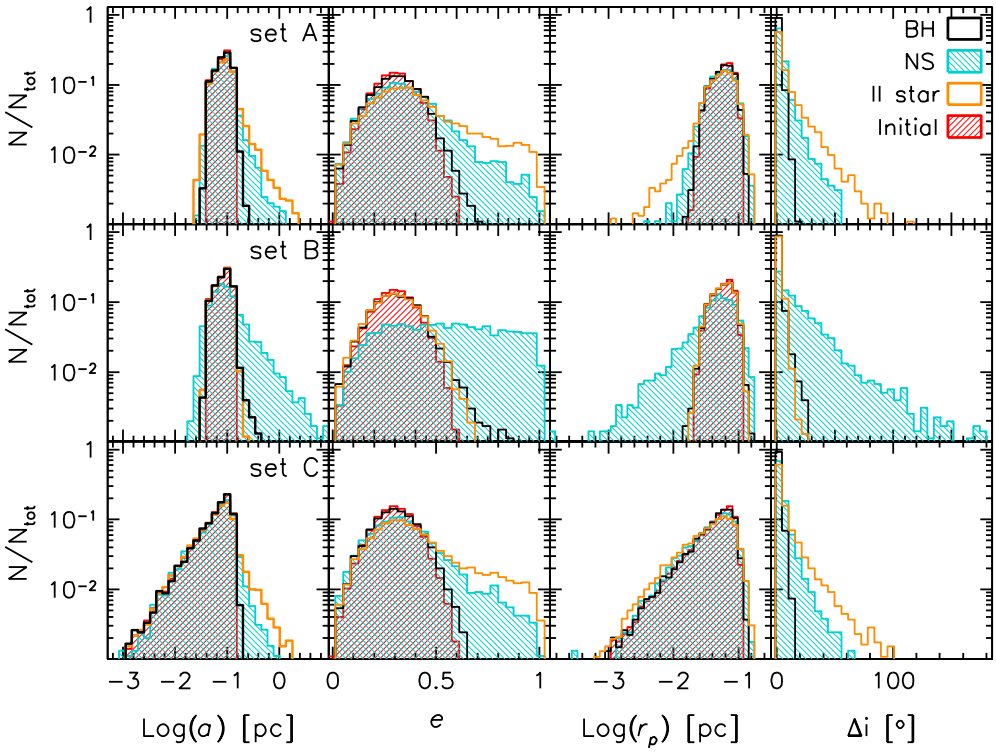

Fig. 2.4. From left to right: distribution of semi-major axes, eccentricities, pericentre radii, and inclinations for objects still bound to the SMBH. Inclinations are calculated with respect to the initial orbit of the binary (i.e. the CW disc plane). Top row: set A; central row: set B; bottom row: set C. Red shaded histograms: initial distribution; black histograms: BHs at 1 Myr; light blue dashed histograms: NSs at 1 Myr; orange histograms: secondary stars at 1 Myr. Each histogram is normalized to unity.

Tab. 2.2. Fraction of objects that become unbound from the SMBH.

Object type	set A	set B	set C
all	6%	6%	5%
BHs	0%	0.4%	0.04%
NSs	3%	24%	2%
II star	10%	0.05%	8%

Column 1: 'Object type' indicates if a given object is a BH, a NS, a secondary (II) star or all possible objects. Columns 2, 3, and 4: 'set A', 'set B', and 'set C' indicate the statistics for each set of runs. Per each set, we list the fraction of unbound bodies over their total number, the relative fraction of unbound BH, NSs and secondary stars.

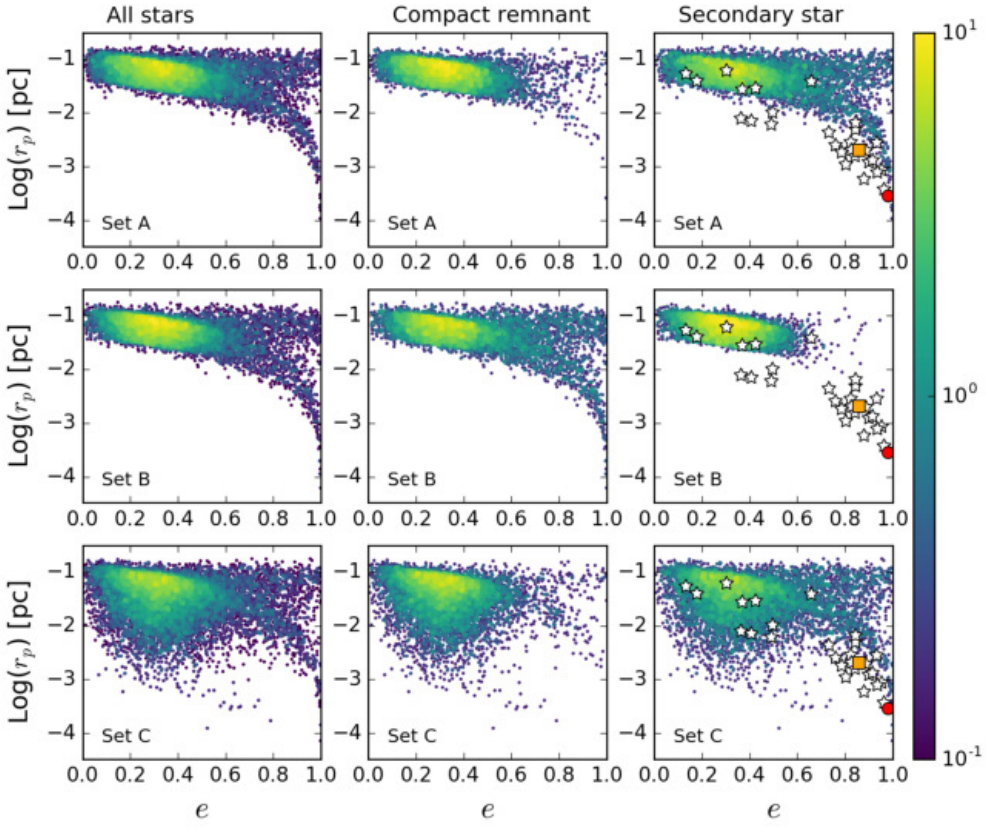

Fig. 2.5. Stellar pericentre distance (r_p) versus eccentricity (e) of stars and compact remnants in set A (top), B (centre) and C (bottom), at the end of the simulations. The left-hand column shows all stars in each simulation set, the central panel shows only compact remnants, and the right-hand panel shows the secondary stars. For comparison, we plot the values of e and r_p for G1 (orange square), G2 (red circle), and for the S-cluster members (white stars) over the scatter plot of secondary stars. The colour bar represents the density of points.

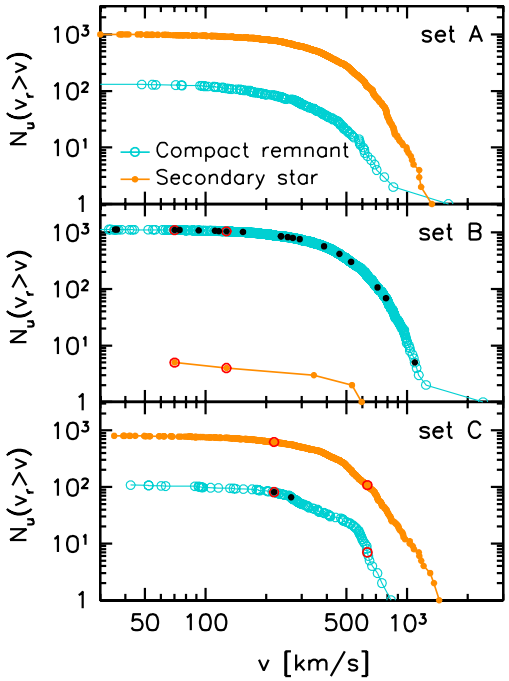

Fig. 2.6. Cumulative distribution of objects that escape (i.e. become unbound from) the SMBH, N_u, with radial velocity component v_r greater than a threshold velocity v, as a function of v, at the end of the simulations. Light blue open circles: SN compact remnants; orange filled circles: secondary binary members. Escaping BHs are marked with a black filled circle. Bound binary systems that escape the SMBH are marked with a red circle. From top to bottom: cumulative radial velocity distribution for sets A, B and C.

Tab. 2.3. Fraction of stellar binaries that do not break 1 Myr after the SN kick.

Object type	set A	set B	set C
all	38%	48%	39%
BHs	69%	80%	71%
NSs	2%	11%	2%

Column 1: 'Object type' indicates if we consider all the binaries in the simulation, the binaries with a BH or the ones with a NS. Columns 2, 3, and 4: 'set A', 'set B', and 'set C' indicate the statistics for each set of runs. Per each set, we list the fraction of objects that are still bound in a binary stellar system 1 Myr after the SN explosion; we list the fraction of survived binaries over the total initial number of binaries and the fraction of BHs or NSs in a bound binary normalized to the total of BHs or NSs in our simulations.

opposite trend in sets A and C, where secondary binary members are generally lighter than NSs: about 10% companion stars end up unbound, while only a few per cent of NSs escape. Only few BHs become unbound from the SMBH: 0%, 0.4%, and 0.04% in sets A, B and C, respectively. Table 2.2 is a summary of these possible outcomes.

Figure 2.6 shows the cumulative distribution of radial velocities of stars and compact remnants that escape the SMBH potential well. One to a few per cent of these objects attain escape velocities > 900 km s^{-1}, thus they may potentially be detected as hyper-velocity stars escaping the galactic potential (a more accurate investigation was already done by Zubovas et al. 2013). In set A and C, hyper-velocity stars are secondary binary members (except for one NS in set A). In set B only five secondary stars escape from the SMBH, while the NSs are the fastest escapers. In four cases, both binary members escape the SMBH potential and they stay bound in a binary system.

Stellar binaries break after the SN explosion in the $50-60\%$ of runs. Table 2.3 lists the fraction of binaries that survive the SN kick. A higher fraction of binaries do not break in set B, because secondary stars are more massive than compact remnants; however secondary stars will undergo SN explosion in a short timescale, thus even these binaries might be disrupted in few Myr.

2.3 Discussion

2.3.1 The population of dark remnants

Our results show that in all simulation sets SN explosions are not effective in scattering massive objects on new orbits. If we assume continuous star formation in the inner pc, our simulations predict that a dark cluster of BHs may have formed within the influence radius of the SMBH, because natal kicks do not modify the BH orbital properties significantly.

In set B, secondary stars (which are particularly massive) behave in a similar way as BHs, dominating the mass distribution within $\sim 0.02-0.5$ pc. However, almost all these high-mass stars will undergo a SN explosion within a few Myr and will get a further kick, changing their density distribution around the SMBH.

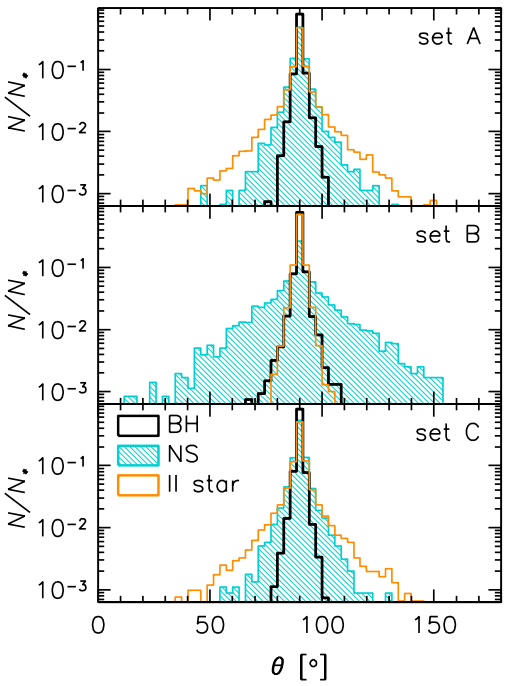

Fig. 2.7. Azimuthal angle (θ) distribution of secondary stars and compact remnants still bound to the SMBH at the end of the integration. The initial disc is located at $\theta = 90^{o}$. Top panel: set A; central panel: set B; bottom panel: set C. Black histograms: BHs at 1 Myr; light blue dashed histograms: NSs at 1 Myr; orange histograms: secondary stars at 1 Myr. Each histogram is normalized to unity.

Addressing their subsequent evolution is beyond the aim of this study; however we can speculate about their possible final distribution. It is reasonable to expect that a considerable fraction of the heavier BHs generated from secondary stars will keep moving in the same region, as SN kicks are expected to be weaker if the remnant is a BH. As a consequence, we expect the BH population of set B to acquire further members after the SN explosion of secondary stars. Thus, our simulations clearly show that an excess of dark remnants may hide inside the central parsecs of the Galaxy.

The angular distribution of objects resembles the initial one, i.e. all stars and remnants are preferentially found in the plane of the CW disc, even if light stars spread more their angular distribution, as shown in Figure 2.7 and in agreement with (Mikhaloff and Perets, 2017); the final distribution of stars and compact remnants is flattened in our simulations. However, several star formation episodes might have occurred in disc-like structures (such as the CW disc) around the SMBH, with possibly different orientations; this possibility is theoretically explored e.g. in Aharon and Perets (2015). This might have contributed to build a cluster of dark remnants along the history of the GC. Several episodes of star formation within randomly oriented discs would result in a relatively isotropic distribution of remnants; in addition, secular processes as Kozai-Lidov oscillations (Kozai, 1962; Lidov, 1962), resonant relaxation (Rauch and Tremaine, 1996) or efficient two-body relaxation (Perets et al., 2008; Mikhaloff and Perets, 2017) may have assisted the

isotropisation of stellar orbits[3].

The presence of a cusp within the inner parsec of our Galaxy can also give new hints on the origin of S-stars: Hills (1988) proposed that both the S-star cluster and hyper-velocity stars within the galactic bulge may have originated by the tidal breakup of binaries passing close to the SMBH; Šubr and Haas (2016) investigated this possibility via N-body simulations, and they reproduce fairly well the orbital parameters of S-stars when they take in account the presence of a possible stellar or dark cusp.

2.3.2 The NS distribution

In our simulations, NSs are easily scattered far away from the SMBH, especially when they are bound to a massive companion. SN kicks are believed to have isotropic orientations; our simulations show that NSs have a greater probability to end up further away from the SMBH rather than closer in, as expected from geometrical arguments[4]. NS natal kicks may attain high velocities according to Hobbs et al. (2005); in our simulations, we implicitly assumed that SN kicks have a constant distribution in momenta rather than in velocities, thus it is not surprising that NSs are heavily affected by their natal kick. We also expect that SN kicks will deeply affect NS orbits, even when they are not part of a binary system. Thus, we suggest that the dearth of NSs observed in the GC may be due to SN kicks.

Assuming a star formation rate in the GC of $\sim 10^{-3}$ stars yr^{-1} (Pfuhl et al., 2011) and introducing a correction factor to account for the fact that we did not simulate the low-mass end of the initial mass function (see Section 2.1), we can compute the number of NSs that may remain in the GC within 10 Myr or 1 Gyr, i.e. the typical lifespan of respectively a canonical pulsar (CP) and a millisecond pulsar (MSP). Considering only sets A and C, we find that ~ 500 (~ 800) NSs would be located within the innermost 0.1 pc (1 pc) after 10 Myr, and $\sim 5 \times 10^4$ ($\sim 8 \times 10^4$) would be found in the same region after 1 Gyr.[5]

Rajwade et al. (2016) recently estimated the observable fraction of NSs in the inner pc of the Galaxy, and found that only the ∼2% of CPs and 0.1% of MSPs are nowadays detectable, even neglecting free-free absorption and multi-path scattering. They conclude that the maximum number of pulsars pointing toward us compatible with the null result of present-day surveys is 50 CPs and 1430 MSPs, suggesting that we still do not have a definitive proof of missing pulsars. Following the calculations of Rajwade et al. (2016) and the results in the survey by Mac-

(3) Note that earlier CW-disc like structures are expected to maintain a relatively thin configuration even after 100 Myr, thus they could still be observed in the GC (Mikhaloff and Perets, 2017).

(4) If we take a sphere S of radius r, centered on the SMBH and passing through the position P of the exploding SN, and we consider the family of straight lines through P (i.e. all possible directions of the SN kick), half of them is found to avoid the sphere S; the other half will enter S, but it has to exit the sphere after covering a distance in the range $(0, 2r)$. This means that if we consider all the possible directions of the kick, in most cases the NS will end up farther away from the SMBH.

(5) Note that the estimates we present are to be considered upper bounds on the number of NS that would remain inside 0.1 or 1 pc; as a matter of fact, we neglected NSs without a companion by assuming the binary fraction to be 1, but isolated NSs cannot share their natal kick with a companion and we expect them to spread farther away from the SMBH even more than NSs in binaries.

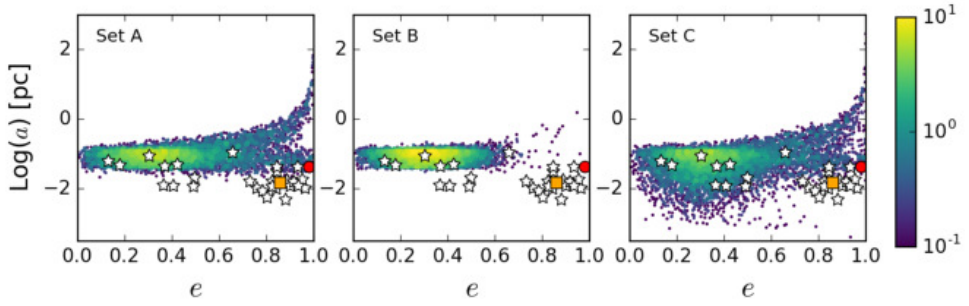

Fig. 2.8. Eccentricity (e) versus the semi-major axis (s) of secondary stars at the end of the simulations, in set A (left), B (centre) and C (right). For comparison, we plot the values of e and a for G1 (orange square), G2 (red circle), and for the S-cluster members (white stars).

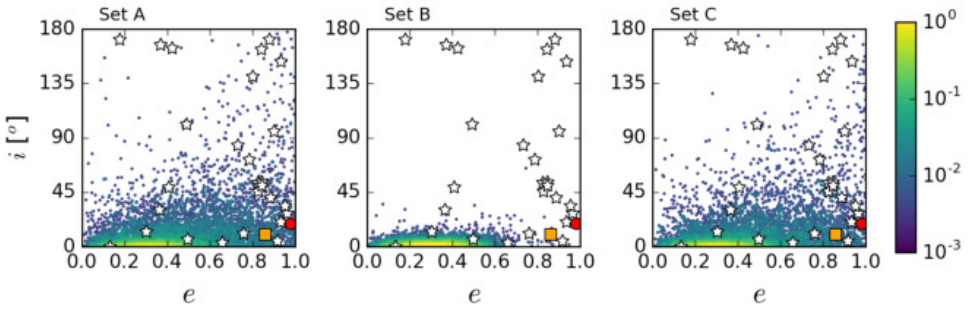

Fig. 2.9. Eccentricity (e) versus the orbital inclination (i) with respect of the CW disc of kicked secondary stars in set A (left), B (centre) and C (right), at the end of the simulations. For comparison, we plot the values of e and i for G1 (orange square), G2 (red circle), and for the S-cluster members (white stars).

quart and Kanekar (2015), if we assume that all our simulated NSs behave as CPs (MSPs), we would expect to observe $\sim$5 ($\sim$ 250) of them at most; in addition, NSs can behave as MSP only in case they stay bound to the companion star or they dynamically acquire a massive companion; only 2% of NSs in sets A and C do not break after the SN explosion, thus the number of candidate MSP in our sample could be reduced by a factor $\sim 10^2$. We will investigate these aspects in more detail in a forthcoming paper.

2.3.3 The S-cluster, G1 and G2

The third column of Figure 2.5 and the three panels in Figure 2.8 and 2.9 compare the orbital elements of secondary stars in our simulations with those of the S-stars, G1 and G2. The scatter plots show the pericentre radii ($r_{\rm p}$), semi-major axes (a) and orbital inclinations (i) versus the orbital eccentricity (e), respectively. From these Figures it is apparent that the orbits of the S-stars with $e \lesssim 0.5$ may originate from the SN kick of a massive companion, especially in Set C, where the inner edge of the disc is closer to the SMBH. However, most S-stars with eccentricities $\lesssim 0.5$ are compatible with a CW-disc origin even without invoking a SN event.

A second bunch of S-stars have eccentricity $e \gtrsim 0.7$; the orbits of these S-stars (as

well as those of G1 and G2) are marginally consistent with our distributions in sets A and C, but not in set B. In particular, the 2.5% (3%) of secondary stars have $r_{\rm p} < 10^{-2}$ pc and $e > 0.7$ in our simulation set A (set C).

The orbital properties of a small fraction of the simulated stars in set A and C match those of G1 and especially G2. The fraction of secondary stars with eccentricity and semi-major axis compatible with those of G2 is 0.8% and 1.0% in set A and C, respectively. The fraction of secondary stars with eccentricity and semi-major axis compatible with those of G1 is equal to 0.15% for set C, while no stars match G1's orbit in set A. Low-mass stars experience a long pre-main sequence phase, and by the time they exit this phase a massive star born in the same star formation episode may experience the SN explosion; we propose that G1 and G2 are pre-main sequence stars that were orbiting a massive star in the CW-disc, and they were kicked on a highly eccentric orbit by the SN kick of the companion.

2.3.4 X-ray binaries

Chandra X-ray observations of the GC and Galactic bulge show that X-ray emitters are highly concentrated in the GC, in excess with respect to the expectations from stellar distribution models (Muno et al., 2005; Hong et al., 2009). This excess is mainly attributed to magnetic cataclysmic variables and primarily intermediate polars (Hong et al., 2009). At least part of this X-ray excess might originate from an accreting BH or NS binary.

In our simulations, a significant fraction $(40-50\%)$ of stars is still part of a binary after the SN kick (Table 2.3). To provide an order-of-magnitude estimate of how many of these simulated binaries might become X-ray emitters, we consider the minimum ($\min(R_*)$) and maximum ($\max(R_*)$) radius of each secondary star during its life, as obtained from the PARSEC stellar evolutionary tracks (Bressan et al., 2012). We then compare the minimum and maximum radii with the Roche lobe limit, obtaining a lower and upper limit for the number of binaries that may undergo Roche lobe overflow in our simulations. Our calculations show that $0-30\%$ of surviving binaries may undergo a phase of Roche-lobe overflow in sets A and C. The fraction of estimated Roche-lobe overflow systems is $0-76\%$ in set B: if the secondary star is almost as massive as the primary, a non-negligible fraction of binaries in our simulation may become X-ray binaries (but we stress that our back-of-the-envelope calculation does not account for the lifetime of the companion star). Table 2.4 shows these results.

Hong et al. (2009) found that the density of X-ray sources within a region of 40×40 pc^2 surrounding SgrA* is $\sim 10^{-6} M_{\odot}^{-1}$, compatible with our generous upper limits. However, Hong et al. (2009) take into account all observed X-ray sources within an area much larger than the central pc, thus a direct comparison with our results cannot be done. Moreover, to compare our results with observations we would need to account for binary evolution processes (such as Roche lobe overflow and wind accretion), which are not included in our simulations. A more accurate study of this aspect will be the subject of a forthcoming paper.

Tab. 2.4. Fraction of stellar binaries that may turn on as X-ray emitters.

	set A	set B	set C
$\min(R_*)$	0	0.1%	0.01%
$\max(R_*)$	27%	76%	29%

Columns 1, 2, and 3: 'set A', 'set B', and 'set C' indicate the statistics for each set of runs. Per each set, we list the fraction of stellar binaries surviving the SN kick that may turn on as X-ray sources, normalized to the total number of surviving binaries; the first line indicates a lower limit, the second line an upper limit in the possible X-ray emitters; see text for details.

2.3.5 Caveats

In our simulations, we did not take in account any secular processes. Mass precession may occur due to the spherical distribution of late-type stars in the GC; however this process would only cause pericentre advance and would let our results unaffected (Šubr and Haas, 2012). Kozai-Lidov resonances (Kozai, 1962; Lidov, 1962) may have a role especially for stars with large semi-major axes; however Kozai cycles are expected to occur for stars misaligned to the CW disc; in addition, the spherical distribution of old stars would damp the cycles even for stars with inclined orbits. The net effect we may expect is a change in the longitude of the ascending node and argument of the pericentre, but again our results would probably be unchanged (Mapelli et al., 2013a; Trani et al., 2016). Moreover, two-body encounters can significantly affect the distribution of eccentricities and semi-major axes (e.g. Trani et al. 2016).

A second possible issue of our simulations is the dependence of our results on the adopted kick distribution. The SN kick distribution is still highly debated (e.g. Beniamini and Piran 2016, and references therein). We aim at investigating this issue in a future paper. However, we notice that our main result (i.e. the formation of a dark cusp) remains mostly unaffected by the prescription we adopt for the kick. In fact, recent studies (Fryer et al., 2012; Mapelli et al., 2013b) suggest that BH kicks might be close to zero for all direct-collapse BHs, while our model attributes quite large kicks to BHs, even if they come from direct collapse. In this respect, our results represent a lower-limit for the building-up of a dark cusp.

2.4 Summary

In this chapter, we investigated the possibility that SN kicks occurring in binary systems affect the orbits of stars and stellar remnants in the GC, by means of regularized three-body simulations. We performed three main sets of simulations, changing the mass distribution of the secondary component of the binary and the inner edge of the initial disc.

Our results show that BH remnants do not change their orbits significantly. Thus, several episodes of star formations in the GC may have built-up a cusp of BHs within the radius of influence of the SMBH. In contrast, NSs are generally scattered away from SgrA* and they may end up sweeping highly eccentric orbits; thus the *missing pulsars problem* may be a result of SN natal kicks, especially if a great

number of NS progenitors are initially bound to a companion with a similar mass. Finally, we propose that G1 and G2 might have been low-mass stellar companions to massive CW-disc stars. When their massive companions underwent a SN explosion, G1 and G2 attained their highly eccentric orbits around the SMBH.

3

Can Supernova Kicks trigger EMRIS in the Galactic Centre?

Based on:
Bortolas, E. and Mapelli, M.*,*
"Can Supernova kicks trigger EMRIs in the Galactic Centre?",
to be submitted

–

Extreme mass ratio inspirals (EMRIs) are gravitational-wave (GW) driven decays of stellar-mass compact objects (COs) onto supermassive black holes (SMBHs). In recent years, a growing body of literature has been devoted to the generation of EMRIs (e.g. Levin 2003; Miller et al. 2005; Hopman and Alexander 2005, 2006; Amaro-Seoane et al. 2007; Merritt et al. 2011; Amaro-Seoane et al. 2013; Brem et al. 2014; Aharon and Perets 2016; Bar-Or and Alexander 2016; Babak et al. 2017; Chen and Han 2018; see also the recent review by Amaro-Seoane 2018) as they could be detected in the near future by LISA, the space-borne GW interferometer selected by ESA for L3 (Amaro-Seoane et al., 2017). Tipically, EMRIs will shine in the milli-Hertz band of LISA completing up to $\sim 10^5$ cycles over the lifetime of the detector: such long-lived waveforms will exquisitely map the spacetime around SMBHs, and will provide unprecedented information on the SMBH masses, spins and host environments (Gair et al., 2013; Barausse et al., 2014).

In the standard picture, EMRIs are generated when a CO orbiting a SMBH is pushed on a sufficiently bound, low angular momentum orbit via two-body stellar scatterings (Hils and Bender, 1995; Sigurdsson and Rees, 1997). The efficiency of this process is expected to be rather low: the event rate of relaxation-driven EMRIs has been inferred to lie in the range $10^{-9} - 10^{-6}$ per galaxy per year. Yet, given that LISA will observe EMRIs up to $z \approx 1$, a few up to a few thousand EMRI signals are expected to enter the LISA band every year (Babak et al., 2017).

In this paper, we propose a novel, alternative mechanism for triggering EMRIs: through the supernova (SN) natal kick received by neutron stars (NSs) and stellar-mass black holes (BHs) at their birth. Circumstantial evidence suggests that NS kicks are very fast, and considerably exceed the typical orbital velocity of stars in

the field (Hobbs et al., 2005), even if a slow-kick NS population may also exist (Fryer et al., 1998; Pfahl et al., 2002; Arzoumanian et al., 2002; Beniamini and Piran, 2016; Verbunt et al., 2017; Mapelli and Giacobbo, 2018; Giacobbo and Mapelli, 2018). The kick distribution of BHs is much more debated, but theoretical and observational arguments suggest that, on average, BHs receive kicks that are either below or comparable to the fast NS kicks (Willems et al., 2005; Gualandris et al., 2005; Fragos et al., 2009; Repetto et al., 2012; Janka, 2013; Mandel, 2016; Repetto et al., 2017; Mirabel, 2017).

When a SN kick occurs near a SMBH, the infant CO is likely scattered on a completely different orbit (Bortolas et al., 2017), which might attain a very low angular momentum. Therefore, the newborn CO could gradually sink onto the SMBH via GW emission, reaching its ultimate coalescence before stellar orbital perturbations significantly deflect its trajectory. In what follows, we will refer to these events as SN-EMRIs.

SN-EMRIs can solely occur in galactic nuclei hosting young ($\lesssim 30$ Myr) and massive ($\gtrsim 9M_{\odot}$) stars whose life terminates in a SN explosion; furthermore, SN-EMIRs can be detected by LISA only if the inspiral occurs about a SMBH of $10^4 - 10^7 M_{\odot}$ at $z \lesssim 1$ (Amaro-Seoane et al., 2017). The closest nucleus to us, the Galactic Centre (GC), meets all the aforementioned requirements: it hosts a SMBH of $\approx 4.3 \times 10^6 M_{\odot}$ (Schödel et al., 2002; Ghez et al., 2003; Gillessen et al., 2017), and several hundreds of young massive (O, B and Wolf-Rayet) stars have been spotted within the innermost 0.5 pc (Paumard et al., 2006; Bartko et al., 2009; Do et al., 2013; Yelda et al., 2014). Furthermore, observations suggest that the recent ($\lesssim$ a few Myr, Lu et al. 2013; Habibi et al. 2017) star formation episode in the GC is associated to a top-heavy mass function (Lu et al., 2013), implying that massive stars formed more effectively near the SMBH compared to the field. Owing to its vicinity, the GC is by far the best known galactic nucleus (see e.g. the review by Mapelli and Gualandris 2016), thus we can model it with a great detail; in particular, the nuclear stellar cluster at its centre appears similar to other analogous regions observed in nearby galaxies (Schödel et al., 2014a), thus the GC can serve as a benchmark for the study of other nuclei.

Motivated by this, in the present paper we adopt a Monte-Carlo approach to investigate the genesis of EMRIs triggered by SN kicks at the GC. Sec. 3.1 lays out the theoretical framework for SN-EMRIs production (3.1.1), presents our modelling of the distribution functions adopted in the study (3.1.2) and describes our numerical Monte-Carlo approach (3.1.3). Sec. 3.2 details the results of our investigation, which are then discussed in Sec. 3.3.

3.1 Model and methods

3.1.1 Theoretical framework

Let us suppose that a SMBH of mass $M_\bullet$ sits at the origin of the coordinate system, and that a massive star (of mass $m_i \ll M_\bullet$) orbits in a Keplerian fashion within its sphere of influence, with initial semimajor axis a_i and eccentricity e_i. When the star undergoes an SN, its orbit gets significantly perturbed. For the sake of simplicity, the SN event is assumed to occur instantaneously: this allows to

keep fixed the position $\mathbf{r}$ (of modulus r) at which the SN takes place; the pre-SN Keplerian velocity at $\mathbf{r}$ is indicated with $\mathbf{v_i}$. The SN kick can be mimicked by adding a velocity vector $\mathbf{v_k}$, so that the newborn CO velocity is $\mathbf{v} \equiv \mathbf{v_i} + \mathbf{v_k}$, and lowering the pre-SN stellar mass m_i to the post-SN, CO mass ($m_{\rm CO}$).

After the kick, the CO is still bound to the SMBH if its energy per unit mass

$$E = \frac{1}{2}v^2 - G\frac{M}{r} \tag{3.1}$$

is negative; here $v^2 = \mathbf{v}\cdot\mathbf{v}$, G is the gravitational constant and $M = M_\bullet + m_{\rm CO} (\approx M_\bullet)$. If $E > 0$, the CO gets unbound from the SMBH and we assume it to be lost for the purpose of SN-EMRIs. If, instead, $E < 0$, the new semimajor axis a and eccentricity e of the CO can be computed via

$$a = -\frac{GM}{2E}; \tag{3.2a}$$

$$GMa(1-e^2) = |\mathbf{r}\times\mathbf{v}|^2. \tag{3.2b}$$

Given the new orbital parameters, the timescale required for the CO to inspiral onto the SMBH via the release of GWs is (Peters, 1964):

$$t_{\rm GW} \approx \frac{5}{64}\frac{c^5 a^4}{G^3 M^2 m_{\rm CO}} f(e); \tag{3.3a}$$

$$f(e) = (1-e^2)^{7/2}\left(1 + \frac{73}{24}e^2 + \frac{37}{96}e^4\right)^{-1}, \tag{3.3b}$$

where c is light speed. Notably, $t_{\rm GW}$ is a strong function of the eccentricity. The inspiral timescale can be re-written as

$$t_{\rm GW} \approx 14\ {\rm Gyr}\left(\frac{a}{3.3\times10^{-4}{\rm pc}}\right)^4\left(\frac{M}{4.3\times10^6 M_\odot}\right)^{-2}\left(\frac{m_{\rm CO}}{25 M_\odot}\right)^{-1}(1-e^2)^{7/2}; \tag{3.4}$$

in the assumption of $e \approx 1$. Even if $t_{\rm GW}$ has to be shorter than a Hubble timescale (here assumed of 14 Gyr) in order for the CO to be an EMRI candidate, this condition does not guarantee the inspiral to be successful, as repeated two-body encounters with background stars may irreparably perturb CO orbit and suppress the GW-induced decay.

Two-body relaxation (NRR)

The effect of two-body, non-resonant relaxation (NRR) is two-folded: on the one hand, it may push stars on low angular momentum orbits and trigger the generation of EMRIs (Hils and Bender, 1995; Sigurdsson and Rees, 1997; Amaro-Seoane et al., 2007). On the other hand, and crucially in the SN-EMRI framework, NRR gradually perturbs the orbit of COs, thus EMRI candidates are likely to fail their inspiral if the duration of their GW decay exceeds the typical timescale over which NRR significantly deflects their trajectory. The time for gravitational two-body

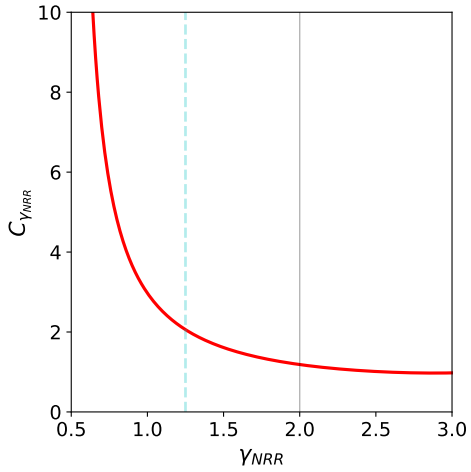

Fig. 3.1. Value of $C_{\gamma_{\rm NRR}}$ (adopted for the evaluation of the angular-momentum NRR timescale in Eq. 3.6) as a function of $\gamma_{\rm NRR}$ (i.e. the slope of the assumed power-law density profile, $n_{\rm NRR}(r) \propto r^{-\gamma_{\rm NRR}}$). The dashed cyan and solid grey lines mark the values of $\gamma_{\rm NRR}$ adopted in the present work for the background population (1.25 and 2); as a reference, $C_{\gamma_{\rm NRR}} = \{5.74, 2.97, 2.06, 1.61, 1.35, 1.19, 1.01, 0.98\}$ for $\gamma_{\rm NRR} = \{0.75, 1, 1.25, 1.5, 1.75, 2, 2.5, 3\}$.

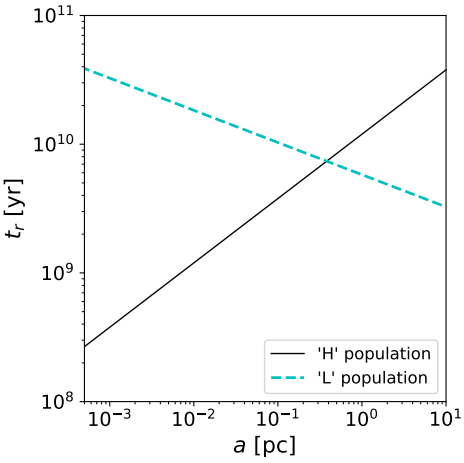

Fig. 3.2. NRR timescale (t_r, computed via Eq. 3.6), as a function of the semimajor axis a of stars orbiting the $4.3 \times 10^6 M_\odot$ SMBH at the GC. The NRR timescale is evaluated assuming that relaxation effects are induced either by a steep cusp of relatively heavy stellar BHs (H population, solid black line) or by a shallower cusp populated by $1 M_\odot$ stars (L population, dashed cyan line); the quantities adopted for the computation of t_r in the two cases are detailed in Tab 3.1.

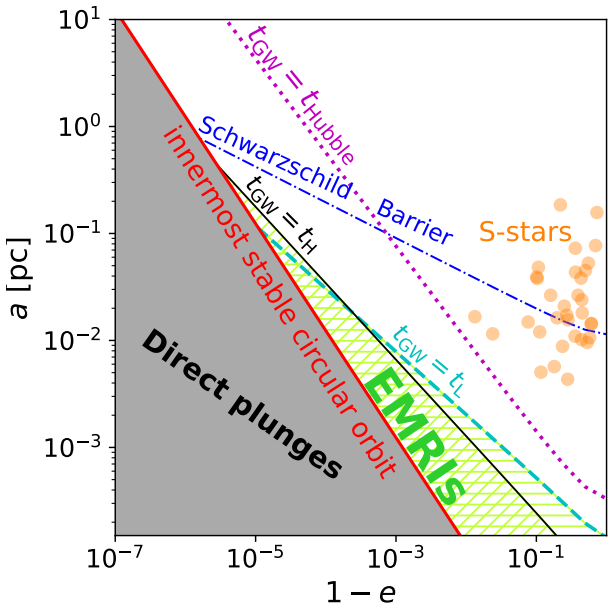

Fig. 3.3. $(1-e, a)$ phase space about the SMBH . COs scattered (either by NNR or via their natal kick) below the red solid line are classified as *direct plunges*, for which $r_p \equiv a(1-e) < 6r_g \equiv r_\bullet$. The black solid (cyan dashed) line represents the outermost border of the region were proper EMRIs may occur according to Eq. 3.7, assuming that the H (L) population dominates NRR at the GC. COs need to be scattered in the green hatched area to be classified as proper EMRIs. The plot further shows the phase space location of the S-stars (Gillessen et al. 2017, orange circles), excluding the eight S-stars classified as CW disc members; the violet dotted line delimits the region for which the GW inspiral timescale of a 10 $M_\odot$ CO equals the Hubble time. Finally, the blue dash-dotted line displays the Schwarzschild barrier (Eq. 3.8, Merritt et al., 2011) traced assuming $C_{\rm SB} = 0.7$ and the properties of the H background population; we stress that the Schwarzschild barrier does not affect the generation of SN-EMRIs.

Tab. 3.1. Properties of the two populations assumed to dominate NRR at the GC

Background pop.	$m_\star$	$\gamma_{\rm NRR}$	$N_{\rm NRR}(<1$ pc)	$t_r(0.1$ pc)
Light stars ('L')	1 $M_\odot$	1.25	10^6	1×10^{10} yr
Heavy stars ('H')	10 $M_\odot$	2	10^4	3.8×10^9 yr

We report the quantities adopted in the computation of the NRR time in Eq. 3.6, exploring two possible stellar populations that dominate the GC relaxation effects: a shallow cusp of standard, relatively light stars (L, first row), and a steeper cusp of heavier stellar BHs (H, second row). Each column indicates, for each population: the typical stellar mass $m_\star$; the slope of the density profile, assumed to take the form $n_{\rm NRR}(r) \propto r^{-\gamma_{\rm NRR}}$; the number of objects $N_{\rm NRR}$ with semimajor axis shorter than 1 pc relative to the central SMBH; the NRR timescale t_r evaluated at $a = 0.1$ pc.

encounters to change the angular momentum j of a body of the order of itself is (Hopman and Alexander, 2005; Merritt et al., 2011)

$$t_j = \left(\frac{j}{j_c}\right)^2 t_r = (1-e^2)t_r \xrightarrow[e\to 1]{} 2(1-e)t_r, \tag{3.5}$$

where j_c is the angular momentum of an object with the same semimajor axis on a circular orbit, and t_r indicates the NRR timescale (Spitzer, 1988). Such latter quantity is best obtained by accounting for the fact that NRR acts more efficiently on very eccentric COs (i.e. those expected to undergo an EMRI, Amaro-Seoane et al. 2007) as implied in Eq. 3.5: that is, low-angular-momentum bodies relax more efficiently(1). For this reason, we chose to compute the NRR time t_r associated with angular momentum changes rather than the typically adopted one, evaluating energy changes. Following Hopman and Alexander (2005), we derived the orbit-averaged, Fokker-Plank diffusion coefficient describing NRR scattering in angular momentum, and we define t_r as the inverse of such coefficient (see Appendix B in Merritt et al. 2011). The obtained timescale as a function of the semimajor axis a of a generic star within the SMBH influence sphere is

$$t_r = \frac{3\sqrt{2}\pi^2}{32 C_{\gamma_{\rm NRR}}} \left(\frac{GM_\bullet}{a}\right)^{3/2} \frac{a^{\gamma_{\rm NRR}}}{G^2 m_\star m' N_0 \ln\Lambda}; \tag{3.6}$$

here we assumed that stars distribute isotropically and homogeneously about the SMBH, and the number density $n_{\rm NRR}$ of stars about the SMBH scales as $n_{\rm NRR}(a) \propto a^{-\gamma_{\rm NRR}}$, $\gamma_{\rm NRR} > 0.5$; N_0 is the normalizing constant to the number $N_{\rm NRR}$ of stars within a given a, i.e. $N_{\rm NRR}(<a) = N_0 a^{3-\gamma_{\rm NRR}}$. $C_{\gamma_{\rm NRR}}$ is a constant that solely depends on $\gamma_{\rm NRR}$; $C_{\gamma_{\rm NRR}}$ as a function of $\gamma_{\rm NRR}$ is plotted in Fig. 3.1. In Eq. 3.6, $m_\star$ represents the typical mass of stars that dominate NRR, while m' is the mass of the star undergoing NRR. Finally, $\ln\Lambda$ is the Coulombian logarithm, which can be approximated as $\ln\Lambda = \ln\left[M_\bullet / (2m_\star)\right]$ within the SMBH sphere of influence (following Merritt et al. 2011). The relaxation time t_r as a function of a for two assumed populations at the GC is displayed in Fig. 3.2; we assumed a shallow cusp of relatively light stars (L population) and a steep cusp of heavier stellar BHs (H population); the properties of the two groups are summarized in Tab. 3.1 and justified in Sec. 3.1.2.

In order for a potential EMRI to complete its GW inspiral before NRR scatters it on a new trajectory, its GW decay timescale ($t_{\rm GW}$, Eq. 3.3) has to be shorter than $2(1-e)t_r$, with t_r computed via Eq. (3.6). Equating the two timescales, it is possible to compute the limiting semimajor axis below which NRR is no longer efficient at quashing GW inspirals:

$$a_{\rm NRR}^{-\gamma_{\rm NRR}+11/2} = \frac{6\sqrt{2}\pi^2}{5 C_{\gamma_{\rm NRR}}} \frac{1-e^2}{f(e)} \frac{(GM_\bullet)^{5/2}}{c^5} \frac{M_\bullet}{m_\star} \frac{1}{N_0 \ln\Lambda}. \tag{3.7}$$

(1) The diffusion in angular momentum resulting from NRR (addressed here) should not be confused with the so-called *resonant relaxation*: the former results from uncorrelated two-body encounters with stars; the latter occurs as stars orbiting the SMBH in a Keplerian fashion swipe roughly the same elliptical orbit over a long coherence period, maintaining a fixed relative orientation between each other; thus, in the latter case the gravitational interactions between stars are highly correlated, and produce an enhanced random walk of stars in angular momentum. An enlightening discussion on the mentioned mechanisms can be found in See sec. 2 of Bar-Or and Alexander (2016).

The separatrix between the two regimes (Eq. 3.7) is displayed in Fig. 3.3 with a solid black (cyan dashed) line assuming the H (L) population to dominate NRR at the innermost GC parsec. If a CO sits at the left-hand side of such line (i.e., $a < a_{\rm NRR}$), NRR does not have enough time to perturb the CO orbit prior to the final coalescence.

The 'Schwarzschild barrier'

It has been suggested that potential EMRIs induced by traditional NRR processes would hardly cross the so-called Schwarzschild barrier, a boundary in phase space resulting from the coupling between resonant relaxation and relativistic precession (Merritt et al., 2011). The the barrier can be parametrized via

$$(1-e^2)_{\rm SB} = 1.9\,(C_{\rm SB}/0.7)^2\,(r_g/a)^2\,(M_\bullet/m_\star)^2\,N_{\rm NRR}(a)^{-1}, \tag{3.8}$$

where $C_{\rm SB} \approx 0.1-1$ (Merritt et al., 2011; Brem et al., 2014) is an empirically determined constant and $N_{\rm NRR}(a)$ is the number of bodies inside a (Merritt et al., 2011). The Schwarzschild barrier is shown as a blue dash-dotted line in Fig. 3.3. The presence of the barrier was originally believe to significantly suppress the rate of EMRIs induced by NRR (Merritt et al., 2011), but more recent studies suggest that the effect of the barrier is not as severe (Amaro-Seoane et al. 2013; Brem et al. 2014; see Sec. 7.6 of Amaro-Seoane 2018); in any case, *SN-EMRIs ignore the presence of the barrier*, as they are generated via a process other than NRR.

Direct plunges

In order for an EMRI to be successfully detected, the CO needs to swipe its orbit multiple times while emitting detectable GWs. COs directly plunging into the SMBH innermost stable circular orbit (ISCO, $r_\bullet$), without undergoing a proper inspiral, are referred to as *direct plunges*, and they are expected to be swallowed by the SMBH without emitting significant GW radiation, thus being undetectable by LISA unless they they originate from the GC (Hopman and Alexander, 2005); in any case, the information contained in the signal would be very little. The gravitational radius of an SMBH is defined as

$$r_g = \frac{GM_\bullet}{c^2}; \tag{3.9}$$

if a SMBH is not rotating (Schwarzschild SMBH), then $r_\bullet = 6r_g$. If the CO periapsis $r_p = a(1-e)$ falls inside $r_\bullet$, the CO is assumed to directly enter the SMBH and avoid a proper EMRI, thus it is classified as a direct plunge. Traditionally, direct plunges have been distinguished from EMRIs by placing the direct-plunge line at $r_p = 8r_g$, as highly eccentric orbits with $6r_g < r_p < 8r_g$ emit significant GW only at periapsis, rather than emitting the continuously detectable, typical EMRI signal that best maps spacetime about the SMBH (e.g. Amaro-Seoane et al., 2017); such highly eccentric sources have been named 'extreme mass ratio bursts' (Rubbo et al., 2006). These events have been recently shown to be promising sources for LISA if they originate from the GC or from a very nearby nucleus (Berry and Gair, 2013a,b); for this, here we set the delimiting line between plunges and EMRIs at

$6r_g$. The line separating plunges from other outcomes is shown as a red line in Fig. 3.3.

For the sake of completeness, we mention that when a SMBH is significantly rotating, $r_\bullet$ assumes different values depending on the dimensionless SMBH spin parameter $\mathcal{S}$, and on the orientation of the CO orbital angular momentum with respect to the SMBH spin. Notably, EMRI rates (versus plunge rates) were found to be boosted up to a factor of ~ 30 if the SMBH is significantly rotating (Amaro-Seoane et al., 2013). Here we will assume a Schwarzschild, non-rotating SMBH ($\mathcal{S} = 0$, $r_\bullet = 6r_g$), consistently with the probably slowly spinning SMBH at the GC ($\mathcal{S} \approx 0.4$, Kato et al. 2010), as no substantial enhancement of the EMRI rates is induced by the SMBH spin if $\mathcal{S} \lesssim 0.7$ (Amaro-Seoane et al., 2013).

To sum up, a proper SN-EMRI can occur if the SN kick transfers the newborn CO on a orbit semimajor axis is smaller than the threshold value $a_{\rm NRR}$ (Eq. 3.7) at which NRR effects would deflect its orbit prior to coalescence, and whose pericentre is greater than $r_p = 6r_g$. We will refer to this as the 'EMRI' region of phase space.

Further rejection criteria

Depending on the progenitor star properties (i.e. its m_i, a_i, e_i) the SN-EMRI could be aborted prior to the SN event. Here we list the other cases in which we assume no EMRI can occur (even if the orbit is in the EMRI region of phase space).

1. If the progenitor star initially orbits very near the SMBH, its GW inspiral timescale (Eq. 3.3, using m_i instead of $m_{\rm CO}$) can be shorter than the time spanning from the star birth to its SN explosion. If this happens, the object is lost into the SMBH prior to experiencing the SN.

2. Analogously, if the progenitor star pericentre $r_{p,i} = a_i(1 - e_i)$ is smaller than its tidal disruption radius, i.e. $r_{p,i} < (2M_\bullet/m_i)^{1/3} R_{\rm strip}$, the star undergoes tidal disruption and is lost for the purpose of SN-EMRIs. In our model, we set $R_{\rm strip} = 2.4R\odot$.

Referring to point (ii) above, the progenitor star could survive tidal disruption, while being stripped solely of its outer envelope. Such naked stellar core can be identified by checking whether $r_{p,i} < (M_\bullet/m_i)^{1/3} R_{\rm max}$, where $R_{\rm max}$ represents the maximum radius attained by the star during its stellar evolutionary phases. We consider naked stellar cores to be valid SN-EMRI progenitors and we treat them as standard progenitor stars, although the missing envelope might affect their natal kick.

3.1.2 Model

In order to explore the generation of SN-EMRIs in the GC, one has to assume how stellar masses, orbits and SN velocity kicks of the young stellar population distribute around the SMBH. For this, in what follows we detail the distributions we adopted for our study.

Tab. 3.2. Initial conditions of the explored CO progenitor populations assumed at the GC

Population name	Label	$a_{i,\min}$ [pc]	$a_{i,\max}$ [pc]	γ_i	ecc. distr.	BH kicks
CW disc	CWD	0.040	0.13	1.93	GE	fast/slow
S-cluster	SCL	0.001	0.04	1.10	TE	fast/slow
concentr. profile, GE	CP-G	0.001	1.00	2.00	GE	fast/slow
concentr. profile, TE	CP-T	0.001	1.00	2.00	TE	fast/slow
shallow profile, GE	SP-G	0.001	1.00	1.25	GE	fast/slow
shallow profile, TE	SP-T	0.001	1.00	1.25	TE	fast/slow

Each row lists the parameters adopted for describing the different young populations at the GC that undergo SN kicks. We modelled the observed CW disc of stars and S-star cluster, and we further explored a generic cuspy distribution for young stars at the GC. The first column reports the name given to the population of progenitor stars; the second column shows the label we used to refer to each population throughout the paper; the third and fourth columns show the minimum and maximum value of the semimajor axis; the fifth column lists the slope of the density profile of the young stars, $n_i(a_i) \propto a_i^{-\gamma_i}$; the sixth column displays the eccentricity distribution adopted for each population, either a thermal one [TE, $n_e(e_i) \propto e_i$] or a Gaussian distribution (GE) centred at $< e_i >= 0.3$ and with dispersion of 0.1; finally, the last column indicated that the SN kicks imparted to stellar BHs have been both not normalized ('fast') or normalized ('slow') to the final CO mass (more details are in the text).

Stellar mass function and stellar evolution

The zero age main sequence (ZAMS) mass of the CO progenitor star is distributed between $9M_\odot$ and $100M_\odot$ according to a top-heavy mass function in the form $dN/dm \propto m^{-\alpha}$, with $\alpha = 1.7$, in agreement with the recent observations of young stars in the GC (Lu et al., 2013). We also verified that our results do not change significantly if we assume a Kroupa (2001) mass function instead.

For any given ZAMS mass, the PARSEC stellar evolutionary tracks at solar metallicity (Bressan et al., 2012; Chen et al., 2015) allowed us to obtain the progenitor mass m_i just prior to the SN; the final CO mass is then computed assuming a delayed SN explosion model (Fryer et al., 2012), following Spera et al. (2015)[(2)]. If $m_{\rm CO} < 3M_\odot$ ($\geq 3M_\odot$), the CO is classified as a NS (a BH). The PARSEC tracks are also used to compute the time intercurring from the ZAMS to the SN event for each star, and to estimate the maximum radius $R_{\rm max}$ attained by each star along its lifetime.

Initial orbit of the progenitor star

The distribution of the semimajor axes a_i and eccentricities e_i of stars undergoing SN are chosen assuming that young stars in the GC belong to one of the structures described below.

1. *The CW disc.* The clockwise (CW) disc is an eccentric discy structure of a few $\times 10^4 M_\odot$ populated by young and massive (B, Wolf-Rayet) stars occu-

(2) The zero-age main sequence mass versus m_i and $m_{\rm CO}$ is shown in fig. 1 of Bortolas et al. (2017).

pying the GC innermost fraction of parsec (Lu et al., 2013). According to recent observations, we modelled the CW disc as a region extended between 0.04 and 0.13 pc (Do et al., 2013); the eccentricity distribution in the CW disc was set as a Gaussian centred in $< e_i >= 0.3$ and with dispersion equal to 0.1 (Yelda et al. 2014; we will refer to the aforementioned Gaussian eccentricity distribution as GE throughout the paper), while the semimajor axis distribution was set as a power law in the form $f(a_i) \propto a_i^{0.07}$. This latter choice ensures that the surface density profile in the disc follows the observed $\Sigma(r) \propto r^{-0.93}$ (Do et al., 2013).

2. *The S-star cluster.* This is a cluster of at least $\sim$ 50 stars (mostly of B stellar type) isotropically distributed in the innermost arcsecond from the GC SMBH (Morris, 1993; Gillessen et al., 2013). We modelled the S-stars semimajor axes distribution so that their density profile follows the observed $n_i(a_i) \propto a_i^{-1.1}$ in the range [0.001, 0.04] pc (Gillessen et al., 2009, 2017). The eccentricity distribution of S-stars is observed to be thermal (Gillessen et al., 2017); accordingly, we represented S-star eccentricities as $n_e(e_i) \propto e_i$; in what follows, we will refer to the thermal eccentricity distribution as TE.

3. *A generic stellar profile.* Additionally, we also explored the possibility that progenitors to COs at the GC follow a density profile in the form $n_i(a_i) \propto a_i^{-\gamma_i}$ between $0.001 - 1$ pc. The smallest allowed a_i is comparable to the minimum observed semimajor axis among the S-stars (S55, with $a \approx 0.0043$ pc, Gillessen et al. 2017); the outer cluster limit is set to 1 pc, even if the influence sphere of the SMBH in the GC reaches ≈ 3 pc (Schödel et al., 2017a; Gallego-Cano et al., 2017): first of all, young stars at the GC are centrally concentrated, and 90% of them seem to be found in the innermost 0.5 pc (Feldmeier-Krause et al., 2015); secondly, stars orbiting the SMBH at larger distances are very likely to get unbound from the SMBH as a result of their natal kick, as shown in Fig 3.4. Two slopes for the density profile have been explored: $\gamma_i = 1.25$ and $\gamma_i = 2$, respectively referred to as the concentrated and shallow density profile. We explored two different eccentricity distributions for each: a TE and a GE distribution.

Tab. 3.2 summarizes the parameters of the studied progenitor populations and reports the associated labels we used throughout the paper. Given that the assumption of a Gaussian rather than a thermal distribution for the eccentricities in our initial conditions significantly affects our results, we will refer to the progenitor structures with an underlying TE distribution as the *TE cases*, while the progenitor structures assuming the GE distribution are referred to as the *GE cases*.

We also adopted a Dirac delta function for distributing a_i or e_i or both, in order to disentangle the effect of the progenitor orbital parameters on the obtained rates of SN-EMRIS. We further stress that the initial distribution of young stars undergoing SN is assumed to be unrelated to the the properties of the underlying, older stellar population assumed to induce NRR.

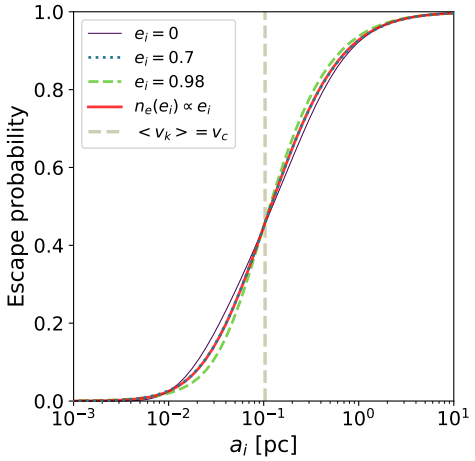

Fig. 3.4. The plot displays the probability of a CO to get unbound from the SMBH as a result of its natal kick, as a function of the semimajor axis of the progenitor star a_i. We modelled each a_i as a Dirac delta distribution; different lines show different assumptions for the initial eccentricity at each a_i; e_i is set equal to 0, 0.7, 0.98 (the violet solid, blue dotted and green dashed line respectively) or assumed to distribute with a TE (red solid line). We assumed the 'fast' prescription for SN kicks (Hobbs et al., 2005). The probability for each object to get unbound by the kick exceeds 50% at $a_i \approx 0.1034$ pc (vertical dashed grey line), at which the circular Keplerian velocity equals the mean value of the SN kick distribution (≈ 423 km s^{-1}).

Supernova kick

The SN velocity kick is assumed to distribute isotropically in space; the magnitude of the SN kick imparted to the progenitor star, v_k, is drawn from a Maxwellian distribution with one-dimensional velocity dispersion $\sigma = 265$ km s^{-1} in the case of NS COs, according to Hobbs et al. (2005). Owing to the large uncertainties on BH natal kick velocities, we adopted two different approaches: (i) the kick given to stellar BHs is drawn from the Hobbs distribution as that imparted to NSs ('fast' BH kicks); (ii) the BH kick is drawn from the same distribution and then normalized to the compact remnant final mass, assuming linear momentum conservation ('slow' BH kicks).

Stellar population dominating NRR effects

As anticipated above, we selected two different *old stellar populations* that may dominate the NRR effects (i.e., the computation of t_r) in our model of the Milky Way nucleus: (i) light-weighted normal stars with average mass $m_\star = 1 M_\odot$, slope of the density profile $\gamma_{\rm NRR} = 1.25$ and number within the inner parsec $N_{\rm NRR}(< 1\text{ pc}) = 10^6$ ('L' population, Schödel et al. 2017a; Gallego-Cano et al. 2017; Baumgardt et al. 2017); (ii) heavier stellar-mass BHs with average mass $m_\star = 10 M_\odot$, with a steeper density profile ($\gamma_{\rm NRR} = 2$) and for which $N_{\rm NRR}(< 1\text{ pc}) = 10^4$ ('H' population, Baumgardt et al. 2017; Hailey et al. 2018).

Our choice to explore two different populations is motivated by the fact that the density distribution within the inner parsec of the GC is hardly inferred via infrared observations and probably strongly affected by the presence of a massive, in-

visible cusp of dark remnants (see e.g. the recent observational results by Hailey et al. 2018, and the theoretical work by Baumgardt et al. 2017); such dark cusp is expected to result from of mass segregation (Baumgardt et al., 2017) possibly complemented by the fact that BHs might receive slow kicks at their birth (e.g. Bortolas et al., 2017). For this, we adopt the 'H' case as our fiducial one.

3.1.3 Methodology

Here we sum-up the steps we followed in our Monte Carlo approach to study SN-EMRIs.

1. We placed the CO progenitor star, whose mass m_i is distributed as described in Sec. 3.1.2, in a Keplerian bound orbit about a $M_\bullet = 4.3 \times 10^6 M_\odot$ SMBH. The star initial orbital parameters a_i, e_i are chosen according to the distributions presented in Sec. 3.1.2 and in Tab. 3.2. We rejected stars whose orbital properties lead to a disruption event by the SMBH (as described in Sec. 3.1.1). The exact point along the orbit at which the SN explosion occurs is obtained by drawing an orbital mean anomaly (which is uniformly distributed in time) from a uniform distribution in $[0, 2\pi]$.

2. We added the SN velocity kick to the Keplerian velocity vector of the star, following the distribution described in Sec. 3.1.2; we also turned the progenitor mass into the final CO mass according to the prescriptions in Sec. 3.1.2.

3. We computed the new energy of the CO, and we checked if it is still bound to the SMBH[(3)]. If so, we computed its new orbital parameters (a, e) via Eq. 3.2, and we checked whether the CO can be classified as an EMRI [if $6r_g/(1-e) < a < a_{\rm NRR}$] or a direct plunge [if $a(1-e) < 6r_g$].

For each of the explored initial conditions (Tab. 3.2) we performed a large number of Monte Carlo iterations to filter out statistical fluctuations.

3.1.4 Model limitations

Our investigation suffers from a number of limitations. First of all we neglect the possibility that stars exploding as SNe may be members of a binary system; this aspect is important, especially considering that the binary fraction in the CW disc most probably lies in the range $30 - 85\%$ (Pfuhl et al., 2014; Gautam et al., 2017). As a matter of fact, Lu and Naoz (2018) explore the dynamics of SN kicks in triple systems, the third body possibly being a SMBH; they touch upon the possibility of producing LISA sources via SN explosions occurring in stellar binaries, but a more focussed study would be needed to address this aspect in detail.

A second source of uncertainty is the fact that the SN kick velocity distribution remains largely debated, especially for BHs (e.g. Beniamini and Piran 2016 and

(3) It is worth stressing that objects that get unbound from the SMBH may remain bound to the galactic potential and get back to the SMBH at later times, even if we did not account for this possibility in the present study. However, we expect these objects will no longer be able to undergo an EMRI; rather, they might experience a direct plunge.

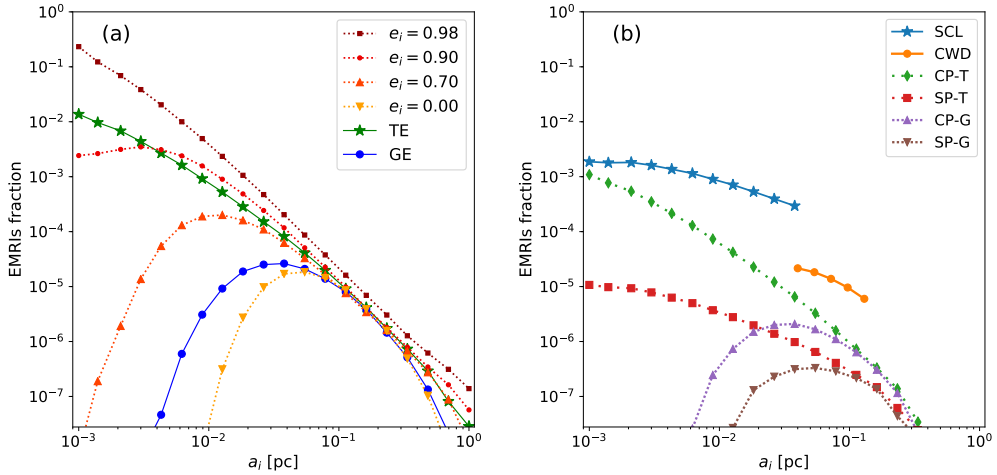

Fig. 3.5. Fraction of stars undergoing SN that lead to the generation of EMRIs, as a function of the initial semimajor axis of the progenitor star, a_i. In (a), each point assumes a Dirac delta distribution with the same height for each a_i (i.e., no physically motivated density distribution for the progenitor stars is considered); different curves in (a) show different values for the initial eccentricity: e_i is either fixed at $0, 0.7, 0.9, 0.98$ (dotted lines), or a TE (green stars) and a GE distribution (blue circles) is considered. Panel (b) shows the probability for a SN occurring within $a_i, a_i + \mathrm{d}a_i$ to result in a SN-EMRI, assuming the semimajor axes and eccentricity distributions in Tab. 3.2. We stress that the curves for the S-stars and CW disc assume larger values as these structures are far less extended than the other structures investigated, thus a larger fraction of progenitor stars is allowed within each $\mathrm{d}a_i$. Here we assumed the fast kick prescriptions and the H background population; if the slow kick prescription and/or the L background population is considered, the displayed curves behave similarly.

references therein). Reassuringly, we found that the two different BH kick prescriptions explored in this study typically lead to the same order of magnitude of SN-EMRIs.

Finally, our model cannot account for secular processes; among them, Kozai-Lidov resonances (Kozai, 1962; Lidov, 1962) induced by the CW disc may produce oscillations in the eccentricity and inclination of a candidate SN-EMRI, and potentially affect its inspiral. However, the Kozai-Lidov timescale (see e.g. fig. 23 in Mapelli and Gualandris 2016) becomes shorter than the typical time over which a SN-EMRI is expected to complete its inspiral (1 Myr) only at $a \approx 1$ pc, where only direct plunges can occur, as shown in Fig. 3.3. Resonant relaxation, in principle, could also affect the inspiral of a CO, but this effect is expected to be more relevant than the addressed NRR only above the Schwarzschild barrier (Alexander, 2017); thus we do not expect our results to be significantly influenced by resonant relaxation.

3.2 Results

3.2.1 EMRI rates as a function of the initial conditions

The fraction of SN explosions resulting in SN-EMRIs as a function of the progenitor star semimajor axis is shown in Fig. 3.5a. Each point in the plot assumes a Dirac

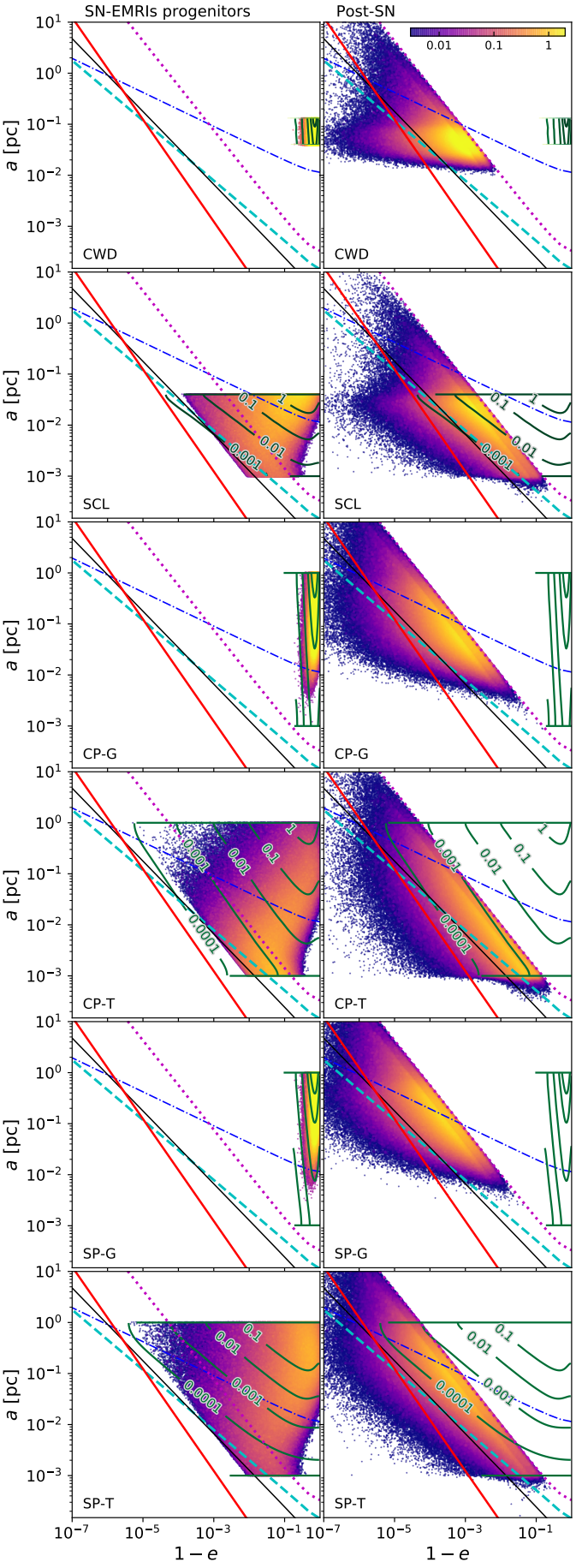

Fig. 3.6. (Caption on the following page.)

Fig. 3.6. The plots show how stars and COs dispose in the $(1-e, a)$ plane, for each of the initial young stellar structures considered, assuming fast BH kicks. The displayed lines are the same as presented in Fig. 3.3. The dark-green isocontours indicate how the population of progenitor stars was distributed initially, while the dark-green horizontal lines indicate their minimum and maximum allowed semimajor axes. The left-hand scatter plots shows the initial position of those progenitor stars which end up as SN-EMRI (assuming the H population to dominate NRR); the right-hand scatter plots display the position of the post-kick population, only displaying COs for which $t_{\rm GW} < 14$ Gy.

delta distribution for a_i, and e_i; we further explored the TE and GE distributions for each of the fixed a_i values. By looking at the plot, we can distinguish three important regimes.

1. At the smallest considered scales ($a_i \sim 10^{-3}$ pc), only parent stars with high initial eccentricity ($e_i \gtrsim 0.9$) induce a substantial fraction of SN-EMRIs (~ 0.001 to ~ 0.1); progenitor stars with lower orbital eccentricities ($e_i \lesssim 0.7$), instead, trigger a negligible amount of GW events. In fact, the typical stellar orbital velocities about the SMBH at these small separations are extremely high ($\gtrsim 1500$ km s^{-1}) compared to the average kick velocity ($v_k \approx 400$ km s^{-1} in the 'fast' BH kick scenario assumed in Fig. 3.5a). As a result, SN-EMRIs can be induced at such short separations from the SMBH only if a very small perturbation to the progenitor orbit suffices to funnel the CO in the 'EMRI' area of phase space: progenitors inducing SN-EMRIs at $a_i \sim 10^{-3}$ pc are thus either already inhabiting, or very close to the 'EMRI' area; lower eccentricity parent stars, instead, would require much larger kicks to induce the GW events.

2. At intermediate scales ($10^{-2} \lesssim a_i/\text{pc} \lesssim 10^{-1}$), SN kicks occurring in the GC have about the same speed of stars orbiting the SMBH. It follows that SN kicks in this region have the best chance to significantly perturb primitive stellar orbits without unbinding a large fraction of COs. The plot shows that a non-negligible amount of SN-EMRIs can be produced regardless of the assumed initial eccentricity, even in the $e_i = 0$ case.

3. At the largest investigated scales ($a_i \gtrsim 0.1$ pc) the average velocity kick imparted to a CO exceeds the typical velocity required to unbind it from the SMBH (Fig. 3.4). For this reason, most COs at $a_i > 0.1$ pc get unbound from the SMBH and cannot undergo EMRIs, while the relative fraction of SN-EMRIs starts steadily decreasing with increasing distance from the SMBH, regardless of the assumed initial eccentricity.

Owing to the fact that the GE distribution peaks at $e_i = 0.3$ and has a negligible amount of stars with $e_i > 0.9$, the behaviour of the curve assuming a GE function in Fig. 3.5a is similar to those referring to the low, fixed eccentricity cases bracketing it.

The behaviour of the curve assuming TE is less obvious: although the mean value of the TE distribution is ≈ 0.7, the associated curve shows a significantly larger fraction of SN-EMRIs at $a_i < 10^{-2}$ pc, compared to the curve assuming $e_i = 0.7$. In fact, in the TE case, 19% (2%) of objects attain $e_i > 0.9$ (0.99). If $a_i \sim 10^{-3}$ pc,

such stars are already very close or inside the 'EMRI' region of phase space prior to the SN explosion, thus they have better chances of triggering EMRIs.

Fig. 3.5a does not give a realistic physical estimate of the fraction of SNe resulting in EMRIs at different radii, as no physically motivated distribution is assumed for the semimajor axes of the progenitor stars. Fig. 3.5b, instead, shows the probability for a star whose initial semimajor axis lies in the range $(a_i, a_i + \mathrm{d}a_i)$ to become a SN-EMRI, assuming the progenitor stars semimajor axis and eccentricity distributions presented in Tab. 3.2. In general, more concentrated stellar distributions favour the generation of EMRIs close to the SMBH, as more objects are available at the smallest scales explored, where SNe hardly unbind newborn COs from the SMBH and progenitors are generally already close to the 'EMRI' phase space area, thus they only need a small orbital perturbation to enter it. Fig. 3.5b further shows that, assuming the same a_i distribution, TE cases induce the genesis of a significantly larger amount of EMRIs following a SN, compared to GE cases. The reason for this has to be sought in the low fraction of progenitor stars that are initially placed near the low-angular momentum, EMRI region of phase space in the GE assumption (as shown by the isocontours in Fig. 3.6).

3.2.2 EMRI and plunge statistics

The panels in Fig. 3.6 show how COs distribute in the phase space prior and after the SN-kick, while the total fractions of SN kicks resulting in the generation of EMRIs for each of the assumed populations are listed in Tab. 3.3. In general, the fraction of SN explosions that produce EMRIs lies in the range $10^{-7} - 4 \times 10^{-4}$. The S-cluster represents by far the most efficient structure for the production of SN-EMRIs among the investigated ones ($\sim 4 \times 10^{-4}$), owing to its small separation from the SMBH ($a_i < 0.04$) and to its TE distribution. In the CW disc, roughly one order of magnitude less SNe trigger EMRIs; this is mostly due to its larger separation from the SMBH and to the low orbital eccentricities of progenitor stars in the disc. However, the CW disc most probably hosts many more stars compared to the S-cluster, thus SN-EMRIs could still be more frequently triggered in the CW disc.

As expected, the concentrated profile (CP) is much more efficient in generating SN-EMRIs compared to the shallow one (SP), as many more objects are available at $a_i < 0.1$ pc; finally, the TE cases result in at least an order of magnitude greater fraction of SN-EMRIs compared to the TE cases.

A larger amount of SN-EMRIs are induced in the fast BH kick assumption compared to the fast kick case. Such larger kicks obviously have a more significant impact on the initial orbit: even if they unbind roughly two times more COs, they still manage to trigger more SN-EMRIs, as the GW events are mainly generated at small scales, where COs hardly get unbound. In any case, both the fast and slow kick assumptions lead to the same order of magnitude for the relative fraction of SN-EMRIs.

Different assumed background populations producing NRR also influence (even if only marginally) the relative fraction of SNe triggering EMRIs: a larger fraction of SN-EMRIs are generated in the GE cases if the H population is assumed; conversely, the L background population warrants a larger production of SN-EMRIs in the TE

Tab. 3.3. Statistics of SN-EMRIs, direct plunges, unbound objects, tidal disruption events and premature GW-inspirals for each of the different young stellar populations assumed to inhabit the GC

Population	EMRIs, H	EMRIs, L	direct plunges	unbound	TDE	pre-GW
CWD	1.4×10^{-5} (6.8×10^{-6})	8.1×10^{-6} (4.1×10^{-6})	9.9×10^{-6} (4.9×10^{-6})	0.396 (0.199)	$<10^{-10}$	$<10^{-10}$
SCL	3.2×10^{-4} (2.7×10^{-4})	4.2×10^{-4} (3.7×10^{-4})	9.8×10^{-5} (9.0×10^{-5})	0.118 (0.059)	4.6×10^{-4}	2.8×10^{-4}
CP-G	2.4×10^{-6} (1.2×10^{-6})	1.5×10^{-6} (7.3×10^{-7})	2.2×10^{-6} (1.2×10^{-6})	0.750 (0.408)	$<10^{-10}$	$<10^{-10}$
CP-T	3.7×10^{-5} (2.9×10^{-5})	6.4×10^{-5} (5.6×10^{-5})	1.0×10^{-5} (1.0×10^{-5})	0.760 (0.411)	6.2×10^{-5}	3.2×10^{-5}
SP-G	6.6×10^{-7} (3.4×10^{-7})	2.8×10^{-7} (1.4×10^{-7})	1.0×10^{-6} (6.4×10^{-7})	0.836 (0.462)	$<10^{-10}$	$<10^{-10}$
SP-T	2.2×10^{-6} (2.1×10^{-6})	2.2×10^{-6} (1.9×10^{-6})	1.6×10^{-6} (3.2×10^{-6})	0.847 (0.464)	2.1×10^{-5}	3.2×10^{-6}

First column: different young stellar populations assumed to inhabit the GC (Tab. 3.2); second (third) column: fraction of SN kicks resulting in the generation of EMRIs, assuming the H (L) population to dominate NRR effects; fourth column: fraction of SN events resulting in a direct plunge; fifth column: fraction of SN explosions unbinding the newborn CO from the SMBH; sixth column: fraction of stars undergoing a tidal disruption event prior to the SN explosion; last column: fraction of objects (excluding those reported in the previous column) for which the progenitor stars $t_{\rm GW}$ is shorter than the time they need to undergo SN: most probably, these objects will undergo a tidal disruption resulting from their GW-induced decay prior to the SN explosion. Non-bracketed numbers refer to the statistics obtained assuming 'fast' BH kicks, while numbers in parenthesis assume the 'slow' BH kicks; the statistics in the last two columns is not affected by the magnitude of the kick.

Tab. 3.4. Fraction of objects in the EMRI region prior to the SN

Structure	Already in 'EMRI' region of ph. space		SN-EMRIs from 'EMRI'		COs staying in 'EMRI'	
	H	L	H	L	H	L
SCL	1×10^{-5} (1×10^{-5})	1×10^{-4} (1×10^{-4})	1% (1%)	8% (15%)	24% (28%)	29% (47%)
CP-T	4×10^{-6} (4×10^{-6})	3×10^{-5} (3×10^{-5})	3% (4%)	20% (35%)	29% (31%)	37% (55%)
SP-T	6×10^{-8} (6×10^{-8})	6×10^{-7} (6×10^{-7})	1% (1%)	8% (14%)	24% (30%)	31% (48%)

First column: young stellar populations assumed to inhabit the GC; second and third column: fraction of the total SN progenitors already inhabiting the 'EMRI' region of phase space prior to the SN explosion; fourth and fifth column: fraction of SN-EMRIs from stars already in the 'EMRI' phase space region prior to the SN, relative to the total amount of objects undergoing SN-EMRIs; second-to-last and last column: fraction of objects among those inhabiting the 'EMRI' region prior to the SN that keep sitting in the same region after the kick, thus undergo a SN-EMRI. The 'H' and 'L' indicate that we assumed respectively the H or L background population to dominate NRR effects. Non-bracketed numbers refer to the statistics obtained assuming 'fast' BH kicks, while numbers in parenthesis assume the 'slow' BH kicks. The statistics is obtained by performing 10^9 Monte-Carlo experiments for each population; we do not show the GE cases as their fraction of stars in the EMRI region prior to the SN is $<10^{-10}$ of the total.

assumption. This fact can be explained as follows: the EMRI area in the $(1-e, a)$ plane is more extended to the right if $a < 10^{-2}$ ($> 10^{-2}$) pc and the L (H) background population is assumed; Fig. 3.6 (right) shows that the bulk of COs ending up in the EMRI area have their final semimajor axes larger than 10^{-2} pc in the GE cases, while the bulk of SN-EMRIs are produced at scales smaller than 10^{-2} pc in the TE assumption.

Tab. 3.3 further illustrates that some SN kicks induce direct plunges. The reported fraction of direct plunges with respect to the total number of SNe range from $\sim 10^{-6}$ to $\sim 10^{-4}$. This fraction is typically of the order of the fraction of SN-induced EMRIs for each of the investigated populations.

3.2.3 Lost progenitor stars

Finally, Tab. 3.3 reports the statistics of progenitor stars that are 'lost' prior to undergo a SN because they get disrupted by the SMBH tidal field. In particular, we distinguish between progenitors undergoing a 'standard' tidal disruption event solely due to the fact that their initial pericentre is too close to the SMBH, and those that decay onto the SMBH via GW emission (thus being again tidally disrupted) prior to experience a SN. No progenitor is lost in the GE cases, as the parent stars attain quite large pericentre distances prior to the SN; in the TE cases, instead, the fraction of objects experiencing a standard tidal disruption is $1-10$ times the listed fraction of SN-EMRIs. Progenitors inspiralling onto the SMBH via GW radiation prior to the SN are typically half to one tenth of those undergoing the standard tidal disruption.

3.2.4 Progenitors in the 'EMRI' region

The left-hand panels in Fig. 3.6 witnesses that a small amount of SN-EMRIs have been generated by progenitors already inhabiting the 'EMRI' region prior to the SN event. In fact, only the TE cases allow a fraction of SNe to occur in the 'EMRI' area of the phase space. Tab. 3.4 shows that $\sim 10^{-7}-10^{-5}$ ($\sim 10^{-6}-10^{-4}$) of the progenitors are initially in the EMRI region if the H (L) background population is assumed. The SN-EMRIs resulting from this sub-sample of progenitors are $\sim 10-30\%$ if we assume the L background population, while their amount is only a few per cent in the H case.

Furthermore, $\approx 25\%$ to 60% of progenitors initially in the EMRI area keep staying there after the SN explosion. This means that stars that form on an EMRI trajectory have a significant probability of undergoing an EMRI even if they experience a SN kick, and this is true even with the fast BH kick prescriptions.

3.2.5 SN-EMRI mass function

The assumed top-heavy mass function produces a roughly even amount of NSs and BHs (0.497 and 0.503, respectively), while the fraction of COs exceeding 10 $M_\odot$ is 0.29; here we compare this underlying CO mass function to the SN-EMRI one. If the fast BH kick prescriptions are adopted, the mass function of SN-EMRIs is largely consistent with the primitive one, as shown in Fig. 3.7 for the CW disc and S-cluster case; this remains valid for all the assumed populations of progenitor

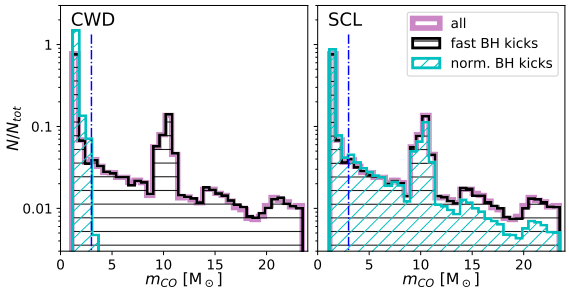

Fig. 3.7. Distribution of the CO masses. The thick violet line shows the underlying distribution obtained from the initial top-heavy mass function; the black and cyan histograms respectively show the mass distribution of SN-EMRIs undergoing a fast or slow BH kick. We show the CW-disc case (left) and the S-stars case (right). All the shown distributions are normalized to unity; the vertical dash-dotted line delimits what we define to be NSs ($< 3M_\odot$) and BHs ($\geq 3M_\odot$).

stars, and results from the fact that the $a_{\rm NRR}$ separatrix (Eq. 3.7) does not depend on the CO mass.

In contrast, if the slow BH kick prescriptions are assumed, SN-kicks are far less efficient in scattering the heaviest COs in phase space. As a consequence, the relative fraction of BHs (especially the most massive ones) undergoing SN-EMRIs decreases, but the drop is very large only in the GE cases. In the TE assumption, the fraction of NSs undergoing SN-EMRIs is ≈ 0.6 of the total population of SN-EMRIs, while the BH fraction is the remaining ≈ 0.4; the fraction of SN-EMRIs whose mass is in excess of $10M_\odot$ in the TE cases is ≈ 0.2. In GE cases, only the ~ 0.001 to ~ 0.01 of SN-EMRIs are BHs, and less than 10^{-4} of them has a mass in excess of $10M_\odot$. This aspect can be appreciated by comparing the SN-EMRI mass function in Fig. 3.7.

3.2.6 Inspiralling timescales

Figure 3.8 shows the distribution of timescales spanning from the SN explosion to the final merger into the SMBH, accounting solely for the COs undergoing a SN-EMRI. This figure suggests that most objects complete their inspiral in 10^{5-7} yr; the inspiralling timescale distributions exhibit a different shape depending on the choice of initial conditions.

In the TE cases, the histograms show a similar trend regardless of the BH kick prescriptions, and the distribution varies mainly depending on the population inducing NRR. If the H population is assumed, the distribution is narrower and peaks at $10^5 - 10^6$ yr; if the L population is assumed, instead, the distribution is much broader, and typically extends up to larger values (even touching 10^9 yr).

In the GE assumption, the histograms are rather narrow, peak at $10^5 - 10^6$ yr in all explored scenarios and may extend down to $\sim 10^4$ yr. The fast BH prescriptions induce a slightly shorter infall timescale ($\sim 10^5$ yr), while there is no clear dependence on the chosen background stellar population.

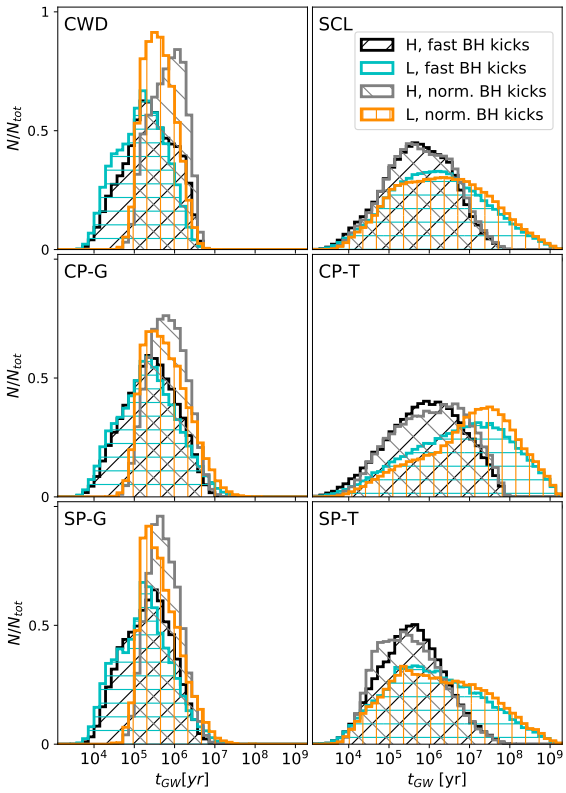

Fig. 3.8. Distribution of the time periods intercurring from the SN explosion to the final CO coalescence (computed via Eq. 3.3), for the COs undergoing a SN-EMRI. Each panel assumes a different young population of progenitor stars; within each panel, the black and grey (cyan and orange) histograms assume the H (L) background population and, respectively, the fast and slow BH kick prescriptions.

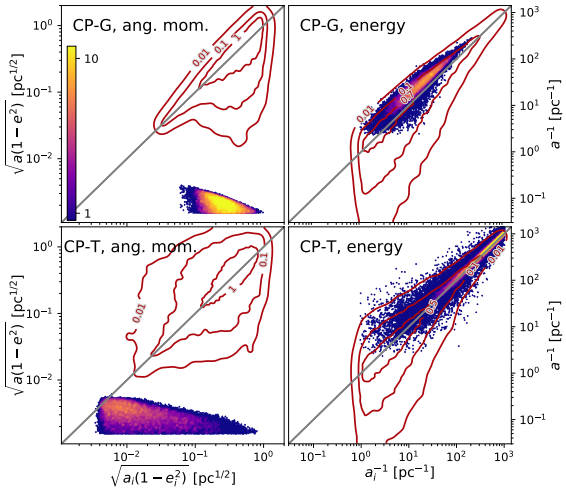

Fig. 3.9. The plots show the initial versus the final energy and angular momentum magnitude of the objects considered in our study. Scatter plots refer to the sole objects undergoing SN-EMRI (in the fast BH kick and H background assumption), while the contours show the distribution of all objects that remain bound after the kick. The left-hand plots display the initial versus the final angular momentum magnitude divided by $\sqrt{GM}$ for the CP-G (top) and CP-T (bottom) case. The right hand plots show the initial versus the final inverse semimajor axis, which is a proxy for the binding orbital energy, again for the CP-G (top) and CP-T (bottom) case.

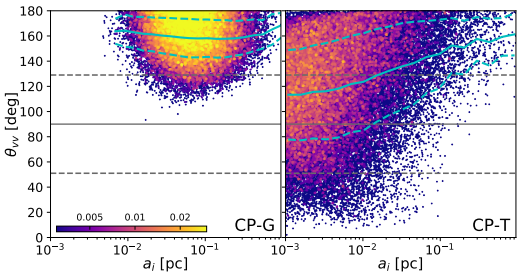

Fig. 3.10. Angle between the initial velocity at the SN and the SN velocity kick ($\theta_{\rm vv}$), as a function of the initial semimajor axis, for the objects undergoing a SN-EMRI. We show the compact profile with the GE (TE) distribution in the left-hand (right-hand) plot, assuming the fast BH kicks and the H background. In both panels, the cyan solid line shows the mean value of $\theta_{\rm vv}$ as a function of a_i, while the cyan dashed lines show the mean $\pm$ one standard deviation. The horizontal black solid line at 90°. shows the mean $\theta_{\rm vv}$ we would expect if it were isotropically distributed, while the dashed lines show the mean value $\pm$ one standard deviation.

3.2.7 Energy and angular momentum conservation

The panels in Fig. 3.9 show the initial versus the final specific binding energy and specfic angular momentum magnitude for the COs undergoing a SN-EMRI and the global population of COs that remain bound to the SMBH. We only display the CP-G and CP-T profiles; we verified that the former is representative of all explored GE cases, and the latter of all TE ones.

On average, the whole collection of COs that keep orbiting the SMBH tend to maintain the same specific binding energy after the kick. The specific binding energy of COs undergoing SN-EMRIs is roughly conserved after the kick in the TE cases, while it is slightly enhanced in the GE cases (i.e., in the latter, objects typically need to get more bound to the SMBH to achieve a SN-EMRI).

The overall distribution in angular momentum magnitude of all objects bound to the SMBH remains the same, on average, after the kick. On the other hand, the plot indicates that SN-kicks triggering successful SN-EMRIs are typically those that manage to significantly reduce the angular momentum magnitude of the newborn stellar remnant, as EMRIs require very low eccentricities to be produced at the scales investigated.

Figure 3.10 shows the angle between the original Keplerian velocity of the progenitor and the SN velocity kick distribution, as a function of the initial semimajor axis of the progenitor. We only show COs that undergo a SN-EMRI. The plots testify that SN explosions efficiently trigger EMRIs if the angle between the kick and the initial velocity almost cancel out, so that the final object finds itself onto a very low angular momentum orbit.

3.3 Summary and discussion

We used a Monte-Carlo method to address the possibility that BH and NS natal kicks could trigger EMRI signals in the GC. We showed that 10^{-7} to 10^{-4} of SN events occurring in a GC-like environment are expected to induce the production of EMRIs. Below we summarize and discuss our key results.

- EMRIs are produced much more efficiently if the stellar orbits have large eccentricity values, e.g. if their eccentricities distribute thermally. However, even assuming initial orbital eccentricities $\lesssim 0.4$ results in the generation of $10^{-7} - 10^{-5}$ EMRIs per SN. The majority of EMRIs are induced by SNe occurring at original semimajor axes shorter than 0.1 pc, and typically of the order of $10^{-2} - 10^{-3}$ pc.

- Our investigation shows that S-stars are located in an optimal region of phase space for triggering SN-EMRIs, as $3 - 4 \times 10^{-4}$ of SNe occurring in this region lead to their production. SN kicks occurring in the CW disc have lower, but still significant, chances of generating SN-EMRIs, as one in roughly 10^5 SNe is expected to induce these events; since many more stars are present in the CW disc, this region could anyway produce a higher rate of SN-EMRIs.

- SN kicks induce roughly the same order of magnitude of EMRIs and direct plunges. If the central SMBH has a large spin parameter, though, a fraction

of events classified as direct plunges in this study could be real EMRIs in disguise, as the SMBH ISCO moves closer to a rapidly spinning SMBH if the CO inspirals on a prograde orbit (Amaro-Seoane et al., 2013).

- Even if the bulk of SN-EMRIs is scattered in the EMRI area of phase space from the outside, a few progenitors inhabit that region from the beginning ($10^{-4} - 10^{-7}$ depending on the initial distribution of a_i and e_i). This population of progenitors has a consistent chance of remaining in the EMRI region of phase space even after the kick ($30 - 50\%$). This fact is relevant as non-traditional EMRI production mechanisms include (i) the in-situ formation of COs within the SMBH accretion disk (Levin, 2003), and (ii) the capture by the disc of massive stars (later turning into COs) on orbits that cross it (e.g. Syer et al., 1991; Rauch, 1995; Panamarev et al., 2018). Our study suggests that such objects have a significant chance to remain on a EMRI orbit even after receiving a quite large natal kick.

- In general, the derived distributions of $t_{\rm GW}$ (the timescale spanning from the SN kick to the final plunge onto the SMBH ISCO) clearly suggests that most SN-EMRIs complete their inspiral in 10^{5-6} yr. This aspect is remarkable as the aforementioned timescales roughly correspond to the age of the observed young population at the GC (Lu et al., 2013; Habibi et al., 2017) and are also of the same order of magnitude as the time intercurring from the birth of a massive star and its SN explosion. It follows that the most massive progenitors born in the most recent star formation episode at the GC may have undergone their SN a few Myr ago, and they might be on their route to undergo a SN-EMRI.

- The distribution of $t_{\rm GW}$ further suggests that, in galactic nuclei similar to the Milky Way, SN-EMRIs could be detected in coincidence with a still undergoing star formation episode close to the SMBH. On the other hand, SN remnants hardly survive over timescales longer than 10^4 yr in Milky Way like nuclei (e.g Rimoldi et al., 2015). Given that very few SN-EMRIs are expected to complete their inspiral within such time period (see Fig. 3.8) we suggest that it would be very unlikely to detect a SN-EMRI and to also identify the remnant of the SN that induced it.

- The mass distribution of COs is almost indistinguishable from the underlying CO mass function in the hypothesis that BHs and NSs receive the same kick velocity at their birth. If, instead, we assume BH kicks to be normalized to BH masses, the SN-EMRI mass function would privilege NSs and low-mass BHs. In particular, in the assumption of normalized kicks and a TE distribution, objects undergoing SN-EMRIs would be NSs in the $\gtrsim 99\%$ of cases, and BHs only in the $\lesssim 1\%$ of cases (while the underlying CO mass functions counts roughly the same number of NSs and BHs). If we assume a TE distribution and the normalized kicks, instead, SN-EMRIs would be NSs in the 60% of cases and BHs in the remaining 40%. The aforementioned results are interesting as multiple detections of SN-EMRIs could help to pinpoint the initial eccentricity distribution of progenitor stars and/or the BH kick velocity distribution.

So far, we solely presented the fraction of SNe that will result in a SN-EMRI. This number could be translated in a rate of SN-EMRIs per Milky Way galaxy per year. The easiest approach is to directly use the rate at which SNe occur in the GC. Such rate has been suggested to be of the order of 10^{-4} yr^{-1} both from theoretical arguments (Zubovas et al., 2013; Rimoldi et al., 2015) and from the observation of a $\sim 10^4$ yr old SN remnant spotted within the SMBH sphere of influence (Maeda et al., 2002).

A similar rate can also be derived in a more pedagogic manner, exploiting the star formation rate in the GC. Since the CW-disc seem to hosts a few$\times 10^4 M_\odot$ and it is $\sim 4-8$ Myr old (Lu et al., 2013), the associated star formation rate is $10^{-3}-10^{-2} M_\odot$ yr^{-1}; in fact, the accurate investigation by Pfuhl et al. (2011) suggests a comparable rate of stellar formation in the innermost parsec. Let us now assume that stars form with a top-heavy mass function with slope $\alpha = 1.7$ (Lu et al., 2013) between 0.1 and $100 M_\odot$, and that the rate of SN explosions coincides with the rate of formation of stars with mass in excess of $9 M_\odot$; under these assumptions, the SN explosion rate could be obtained by multiplying the star formation rate above by 0.02. That is, SN explosions would occur at a rate of 10^{-4} to a few $\times 10^{-5}$ yr^{-1}, consistent with the estimate presented in the previous paragraph.

Consequently, the rates of SN-EMRIs per GC can be obtained by multiplying the EMRI fractions in Tab. 3.3 to $\sim 10^{-4}$ yr^{-1}, yielding values up to a few $\times 10^{-8}$ yr^{-1} per Milky Way. The rate of EMRIs per Milky Way induced by standard NRR processes is still not well constrained, but a typically adopted value is a few$\times 10^{-7}$ yr^{-1} (assuming a non-spinning SMBH and strong mass segregation, Amaro-Seoane and Preto, 2011). Thus SN-EMRIs would constitute up to 10% of traditional NRR induced EMRIs.

We are currently working at generalizing our findings to a broader set of SMBH masses and host environments adopting an analytical approach, and this will be the subject of a forthcoming paper. In addition, it would be worth addressing the cosmological rate at which SN-EMRIs enter the LISA band every year, and to explore whether SN-EMRI signals detected by LISA can be disentangled from the EMRIs induced by other mechanisms, as NRR.

4

Star cluster disruption by a supermassive black hole binary

Based on:
Bortolas, E., Mapelli, M. and Spera, M.,
"Star cluster disruption by a massive black hole binary",
2018, MNRAS 474, 1054

–

SMBH binaries (BHBs) are expected to form in large numbers as a result of repeated galaxy mergers across the cosmic epochs (White, 1978). While BHBs early, dynamical-friction induced inspiral generally occurs in a short timescale (cf. Eq. 1.13), the subsequent shrinking due to three-body stellar scatterings has been recently put under scrutiny by both theoretical and numerical arguments (Begelman et al., 1980; Milosavljević and Merritt, 2001, 2003a). In fact, it has been argued that BHBs may stall at a parsec scale and never enter the GW emission stage if stars are not continually supplied to the BHB loss cone, i.e. the low-angular momentum region of phase space harbouring stars that can reach the binary. This is the well-known *final parsec problem* (Milosavljević and Merritt, 2003b).

In the present chapter, we adopt direct summation N-body simulations to test whether the infall of a stellar cluster (SC) onto the BHB may significantly replenish its loss cone, and shorten the journey to its GW-emission driven coalescence. Such investigation is motivated by the following arguments: SCs that form in proximity of a galactic nucleus are expected to rapidly sink to the central parsec by dynamical friction (Gerhard, 2001; McMillan and Portegies Zwart, 2003; Portegies Zwart et al., 2003; Kim and Morris, 2003; Kim et al., 2004; Gürkan and Rasio, 2005; Fujii et al., 2008). In fact, SC disruption has been proposed as one of the most promising mechanisms to form nuclear SCs (Capuzzo-Dolcetta, 1993; Capuzzo-Dolcetta and Miocchi, 2008; Arca-Sedda et al., 2015, 2016), including that of the Milky Way (Antonini et al., 2012). Plus, several young massive SCs (such as the Arches and the Quintuplet) lie in the nucleus of the Milky Way, which is a relatively quiescent galaxy (see Portegies Zwart et al. 2010 for a recent review). Young massive SCs are even more common at the centre of galaxy mergers, which are known to trigger

Tab. 4.1. Main features of the runs.

Run	Galactic Potential	Ang. Mom.	Orbit
run 1	No	No	Perpendicular
run 2	No	No	Coplanar
run 3	No	Yes	Coplanar
run 1p	Yes	No	Perpendicular
run 2p	Yes	No	Coplanar
run 3p	Yes	Yes	Coplanar

For each run (Column 1) we report whether an underlying galactic potential is included (Column 2), if the initial orbit has some angular momentum (Column 3) and whether the orbit is coplanar or perpendicular with respect to the BHB orbital plane (Column 3).

bursts of star formation (see e.g. Sanders et al. 1988). Since galaxy mergers are suspected to lead to the formation of both BHBs and young SCs, the dynamical-friction induced infall of a young SC onto a parsec-scale BHB should be a rather likely event.

4.1 Methods

In this chapter we performed direct N-body simulations of the infall of a SC onto a parsec-scale BHB. To run the simulations we use the direct summation N-body code HiGPUs (Capuzzo-Dolcetta et al., 2013). HiGPUs implements a Hermite sixth order integration algorithm (Nitadori and Makino, 2008) with block time steps (Aarseth, 2003) and has been designed to run natively on Graphics Processing Units.

To model the SC, we adopt a spherical King model (King, 1966), with central dimensionless potential $W_0 = 5$ and King's core radius $r_k = 0.4$ pc. The SC is composed of $N = 131070$ stars with masses distributed according to a Kroupa (2001) initial mass function, with mass range between $0.1 M_\odot$ and $100 M_\odot$. The initial total mass of the SC is $M_{\rm SC} \approx 8 \times 10^4 M_\odot$. Stellar evolution is not included in the simulations.

Two SMBHs are placed in circular orbit in the $x - z$ plane with their centre of mass at the origin of the reference frame and with angular momentum in the positive y direction. The initial distance between the SMBHs is 1 pc and each SMBH has mass 10^6 $M_\odot$. The softening parameter of the simulation is set to $\varepsilon = 10^{-4}$ pc, which is several orders of magnitude smaller than the minimum distance reached by the SMBHs.

In this work we explored three different orbits for the cluster infall. For each of them we perform two runs: with and without including the underlying galactic potential. Namely, the potential of the host galaxy is included in runs 1p, 2p and 3p, while it is absent in runs 1, 2 and 3. When present, the galactic potential is described as a rigid potential, represented by a Dehnen's density profile (Dehnen, 1993):

$$\rho(r) = \frac{(3-\gamma)\, M_{\rm g}}{4\pi} \frac{r_0}{r^\gamma (r + r_0)^{4-\gamma}}, \tag{4.1}$$

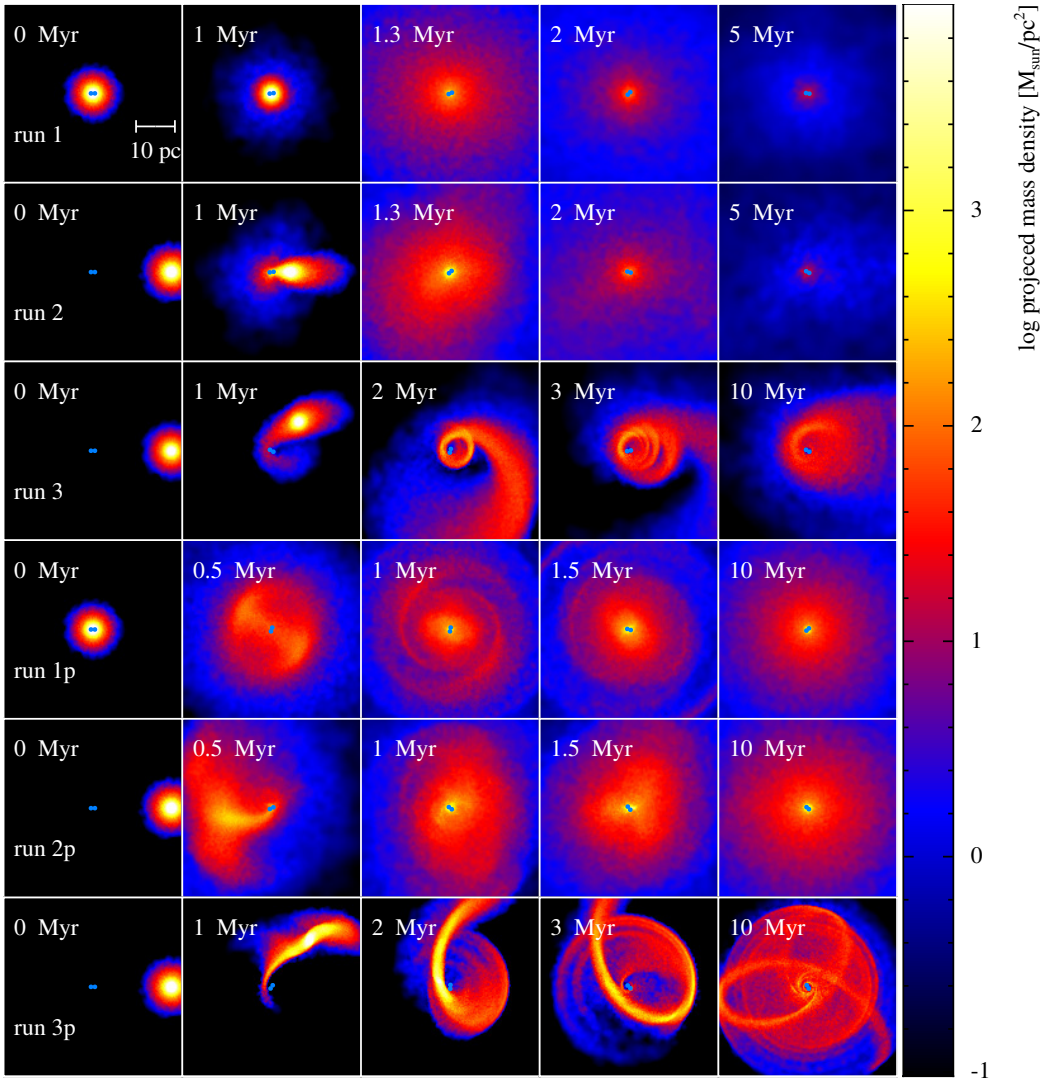

Fig. 4.1. Time evolution of the stellar surface density projected on the $x - z$ plane – i.e. the BHB orbital plane – for runs 1, 2, 3 (top three rows), and runs 1p, 2p, 3p (bottom three rows). The blue central dots mark the position of the two SMBHs. The colour code refers to the smoothed projected mass density of stars, and the colour scaling is the same for all panels.

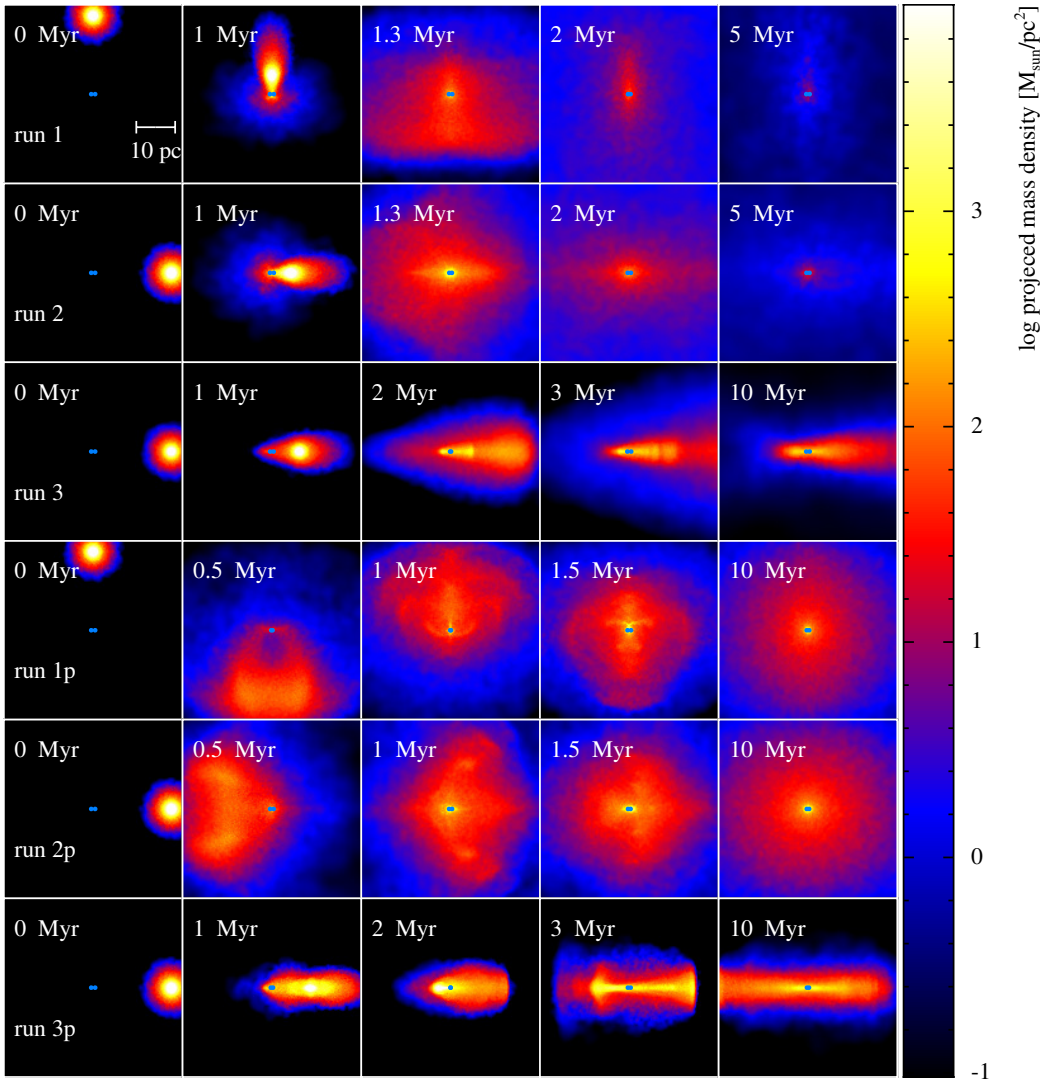

Fig. 4.2. Same as Fig. 4.1, but the stellar surface density is projected on the $x-y$ plane.

with total mass $M_{\rm g} = 5 \times 10^{10} M_{\odot}$, scale radius $r_0 = 250$ pc and inner density slope $\gamma = 0.5$.

In runs 1, 1p, 2, and 2p the SC is initially in free fall, i.e. on a radial orbit. In runs 1 and 1p (runs 2 and 2p), the orbital plane of the SC is perpendicular (coplanar) with respect to the BHB orbital plane. Finally, in runs 3 and 3p, the SC is placed at the apoapsis of an eccentric orbit ($e = 0.75$, defined through the periapsis and apoapsis distance in run 3p) with angular momentum along the y axis, but with opposite sign with respect to the BHB angular momentum; this maximises the relative velocity between the SC and the BHB. The centre of mass of the SC is initially located in $y = 20$ pc (runs 1 and 1p) and $x = 20$ pc (runs 2, 2p, 3 and 3p). Runs 1 and 2 (runs 1p and 2p) are evolved for 5 Myr (10 Myr), while runs with angular momentum (3, 3p) are evolved for 20 Myr. Table 4.1 is a summary of the initial conditions of the six runs.

During the simulation, the centre of mass of the BHB is anchored to its initial position. To ensure this, we modified HiGPUs so that, after each time step, the binary centre of mass is re-centered at the origin of the reference frame and its velocity is set to zero. The BHB recentering minimizes the binary wandering, which otherwise would be too high in runs without the underlying galactic potential (see Bortolas et al., 2016). For consistency, we anchored the BHB centre of mass even in the runs including the galactic potential. We checked that this choice does not affect the results of our simulations by re-running run 2p without the BHB anchorage. We find no appreciable differences in the evolution of the BHB and of the disrupted SC.

4.2 Results

Figures 4.1 and 4.2 show the time evolution of the simulations in the $x - z$ plane (i.e. the BHB orbital plane) and in the $x - y$ plane, respectively. From these Figures, it is apparent that the evolution of the system strongly depends on the initial angular momentum of the SC and on the presence of the Dehnen potential.

4.2.1 The evolution of the BHB without Dehnen potential

In this section, we discuss the evolution of the BHB in runs 1, 2 and 3, in which we do not include a rigid Dehnen potential.

In both run 1 and 2, the SC starts interacting with the BHB at time $t \sim 1$ Myr. During the interaction, stars belonging to the SC undergo three-body interactions with the BHB. Figure 4.3 shows the evolution of the BHB orbital separation as a function of time. The orbital separation changes very fast during the first interaction with the SC, at $t \sim 1 - 1.1$ Myr. Afterwards, the BHB keeps shrinking with a much shallower asymptotic trend, and the change in the semi-major axis a between 3.5 and 5 Myr is only $\mathrm{d}a/\mathrm{d}t \sim -0.0025$ pc Myr^{-1} in both runs. We also note that the BHB keeps orbiting in the initial orbital plane.

When the interaction is almost over (in less than 5 Myr), the BHB separation shrinks by ~ 10 and by ~ 12 per cent in run 1 and run 2, respectively. This implies that the SC infall effectively replenished the loss cone of the BHB. As expected, the shrinking effect is more important in run 2, where the orbit of the SC and

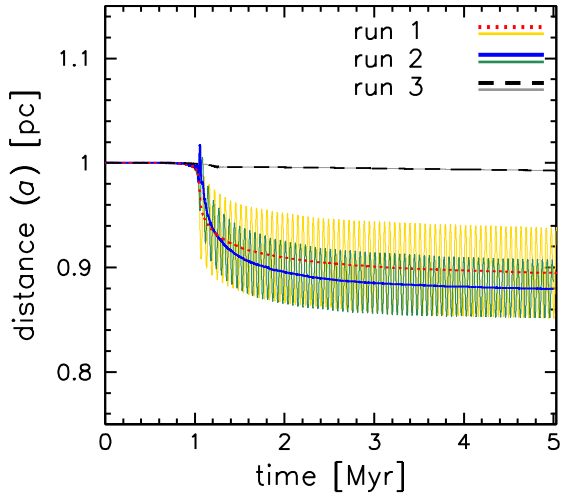

Fig. 4.3. Evolution of BHB separation and semi-major axis as a function of time for the runs without Dehnen potential. Red dotted thick line (orange solid thin line): semi-major axis (separation) in run 1. Dark blue solid thick line (sea-green solid thin line): semi-major axis (separation) in run 2. Black dashed thick line (grey solid thin line): semi-major axis (separation) in run 3.

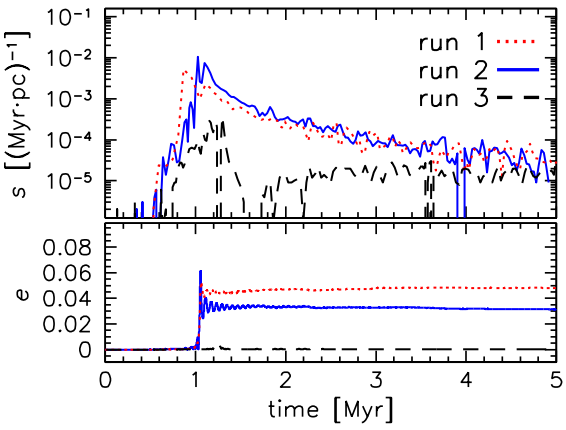

Fig. 4.4. Evolution of the hardening rate (s, top panel) and of the eccentricity (e, bottom panel) of the BHB as a function of time for the runs without Dehnen potential. In all panels, red dotted line: run 1, blue solid line: run 2; black dashed line: run 3.

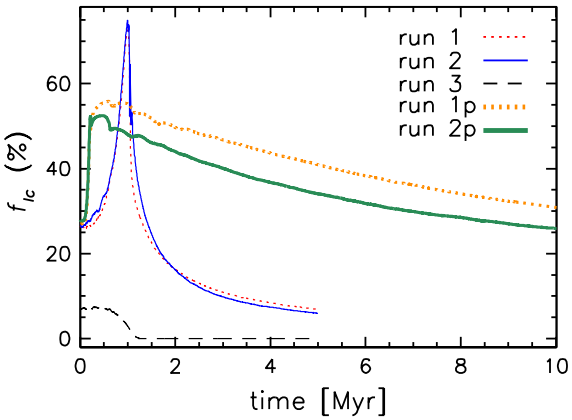

Fig. 4.5. Fraction of stars inside the loss cone (i.e. obeying to the condition in Eq. (4.3)) as a function of time. The plot shows the loss cone population in run 1 (thin red dotted line), run 2 (blue thin solid line), run 3 (black thin dashed line), run 1p (orange thick dotted line) and run 2p (sea-green thick solid line). Run 3p is not shown because the fraction of loss cone stars in run 3p is always below 0.3 per cent.

that of the BHB are coplanar. The reason is that the average relative velocity between the SMBHs and the stars is lower in run 2 than in run 1, maximizing the energetic exchange during the interaction. However, the difference of the final BHB semi-major axis between run 1 and 2 is only ~ 20 per cent.

Similarly, Figure 4.4 shows the behaviour of the hardening rate s, defined as

$$s(t) = \frac{\mathrm{d}}{\mathrm{d}t}\frac{1}{a}, \tag{4.2}$$

where a is the semi-major axis of the binary. The hardening rate $s(t)$ quantifies the time variation of the BHB binding energy (the SMBH masses do not change with time). $s(t)$ is maximum ($\sim 10^{-2}$ Myr^{-1} pc^{-1}) during the first encounter between the SC and the BHB, and then it rapidly drops to few$\times \sim 10^{-5}$ Myr^{-1} pc^{-1}. The SC infall also produces a small but sudden jump in the BHB eccentricity: e rises from 0 to ~ 0.05 and to ~ 0.03 after the first encounter with the SC in run 1 and run 2, respectively.

Figures 4.3 and 4.4 also show the time evolution of the BHB in run 3 (with non-zero orbital angular momentum). The SC starts interacting with the BHB at $t \sim 1.2 - 1.3$ Myr, but the interaction is noticeably weaker with respect to runs 1 and 2. The BHB immediately shrinks of about the 0.4 per cent, while after 5 Myr its semi-major axis is only 0.8 per cent smaller than its initial value; even after 20 Myr the BHB has shrunk by less than 1.5 per cent. In this run, the change in the BHB eccentricity is also negligible.

The difference between runs 1, 2 and 3 is related to the number of SC stars that are in the loss cone, defined as the region of the phase space harbouring stars with angular momentum per unit mass L lower than the angular momentum per unit mass of a circular binary with the same semimajor axis, i.e.

$$L < L_{\mathrm{LC}} = \sqrt{2GM_b a}, \tag{4.3}$$

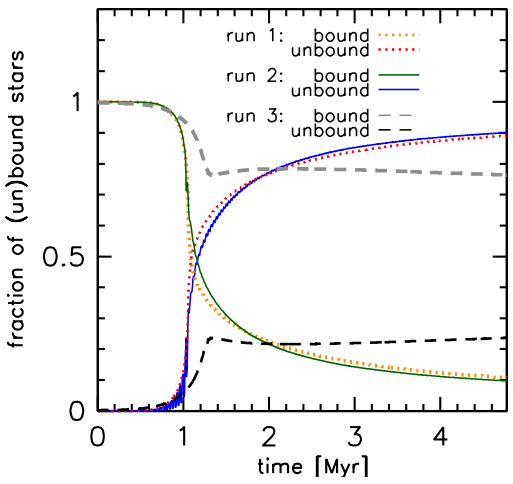

Fig. 4.6. Fraction of stars bound or unbound to the BHB as a function of time for runs without Dehnen potential. At the beginning of the simulation all stars are bound to the BHB in run 1 (orange dotted line), run 2 (sea-green solid line) and run 3 (grey dashed line). When the BHB-SC interaction takes place ($t \sim 1$ Myr), the fraction of unbound stars (red dotted line for run 1, blue solid line for run 2, black dashed line for run 3) rapidly increases, because a lot of stars are ejected due to the slingshot mechanism.

where M_b is the total mass of the BHB. The number of stars inside the loss cone[(1)] is shown in Figure 4.5.

In runs 1 and 2, about 27 per cent of the stars populate the loss cone at the beginning of the simulation. During the first approach, the SC is progressively stripped by the tidal forces of the BHB (see Figures 4.1 and 4.2). The tidal stripping forces many other stars to move on more radial orbits (Hills, 1991; Perets et al., 2009) and funnels them inside the loss cone: at the maximum approach between the SC and the BHB, $\sim$ 75 per cent of the stars lie in the loss cone. The BHB expels stars very efficiently, and the loss cone population gets gradually depleted as the stars are scattered on highly energetic orbits: after 5 Myr, only $\approx$ 6 per cent of the stars still inhabit the loss cone and they will likely become unbound in the next few Myr.

The evolution of the loss cone population is totally different in run 3. The SC orbit in run 3 has non-zero angular momentum, thus stars satisfying the condition given in (4.3) are initially only $\approx$ 7 per cent; in fact, the average angular momentum per unit mass of stars at the beginning of the simulation in run 3 is about twice the same quantity in runs 1 and 2. In run 3, the fraction of stars in the loss cone is almost constant for the first Myr, because the non-zero angular momentum protects the cluster against the BHB-induced tidal stripping. When the SC reaches the maximum approach with respect to the BHB, the slingshot interactions between stars and BHB expel nearly all stars from the loss cone, which is almost completely depleted.

Figure 4.6 shows the fraction of stars bound and unbound to the BHB as a function

(1) Stars with positive energy (escapers) are not part of the loss cone population even if their angular momentum is generally very low, as they will never interact again with the BHB.

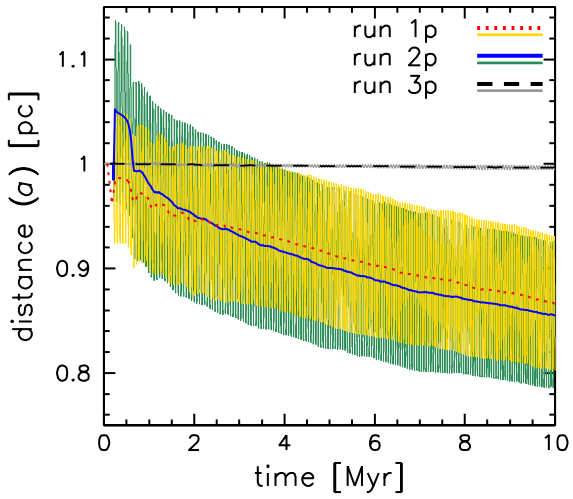

Fig. 4.7. Evolution of BHB separation and semi-major axis as a function of time for runs with the Dehnen potential. Red dotted thick line (orange solid thin line): semi-major axis (separation) in run 1p. Dark blue solid thick line (sea-green solid thin line): semi-major axis (separation) in run 2p. Black dashed thick line (grey solid thin line): semi-major axis (separation) in run 3p.

of time for runs without the Dehnen potential. In runs 1 and 2, the fraction of bound stars drops after the first interaction with the BHB. Only 10 per cent of stars are bound to the BHB at the end of the simulation, regardless of the initial inclination between the SC and the orbital plane of the BHB. This implies that most stars in runs 1 and 2 receive a slingshot kick after the interaction with the BHB, sufficiently strong to unbind them from the BHB.

In contrast, only ~ 23 per cent of stars escape the BHB potential in run 3. Given that the loss cone is almost empty after 5 Myr, stars still orbiting the BHB will probably not undergo slingshot ejections, unless stellar torques generated by other perturbers funnel such stars in the loss cone region.

We further stress that the large fraction of unbound stars in runs 1 and 2 is a consequence of the absence of an underlying galactic potential in these runs.

4.2.2 The evolution of the BHB with a Dehnen potential

In this section, we discuss the evolution of the BHB in runs 1p, 2p and 3p, which include a rigid Dehnen potential.

In runs 1p and 2p the first encounter between the SC and the BHB happens at ~ 0.2 Myr (Figs. 4.1 and 4.2) and the velocity of the SC at maximum approach is about twice that in runs 1 and 2, because of the Dehnen potential. Given the higher orbital speed, the SC in runs 1p and 2p is not entirely captured by the BHB during the first periapsis passage: the partially stripped remnant of the SC reaches the apoapsis and then falls back again onto the BHB (while the SC is entirely stripped and captured by the BHB at the first periapsis passage in runs 1 and 2). The Dehnen potential keeps most stars bound to the system, so that they fall back to the centre and interact with the BHB several times. In contrast, most stars interact with the BHB only once and then are ejected from the system in the runs without Dehnen potential.

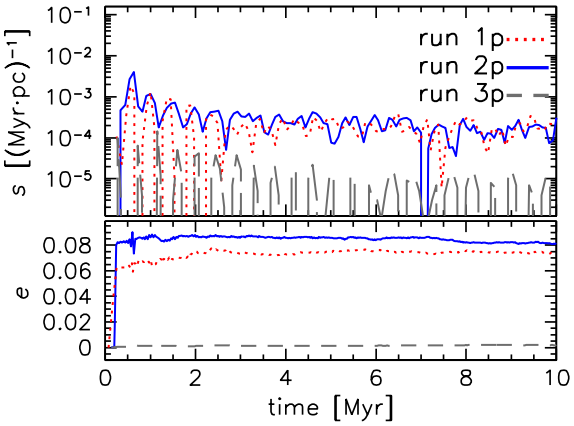

Fig. 4.8. Evolution of the hardening rate (s, top panel) and of the eccentricity (e, bottom panel) of the BHB as a function of time for runs with the Dehnen potential. In all panels, red dotted line: run 1p, blue solid line: run 2p; grey dashed line: run 3p.

Figure 4.7 shows the evolution of the BHB semi-major axis as a function of time for runs including the Dehnen potential. The final semi-major axis of the BHB in runs 1p and 2p is similar to what we found for runs 1 and 2: after 10 Myr, the BHB has shrunk by $\approx$ 13 per cent in run 1p and by $\approx$ 15 per cent in run 2p. As we already discussed for runs 1 and 2, the BHB shrinking is slightly more efficient when the SC orbit is coplanar, because the relative velocity between the SC members and the BHB is lower.

However, there are several significant differences with respect to runs 1 and 2. In the first $\sim$ 2 Myr, the semi-major axis of the BHB does not shrink monotonically: it seems to undergo damped oscillations between smaller and larger values in both runs 1p and 2p (Figure 4.7). In run 2p the BHB semi-major axis even jumps to a value of $\sim$ 1.05 pc after the first interaction[(2)].

This happens because, if the Dehnen potential is included, the BHB is a marginally soft binary (i.e. its binding energy is comparable to the average kinetic energy of an intruder, according to Heggie 1975) with respect to the SC as a single bullet. In fact, the binding energy of the BHB ($E_b = G\,M_1\,M_2/2\,a \simeq 4.3 \times 10^{52}$ erg, where M_1 and M_1 are the masses of the two SMBHs) is of the same order of magnitude as the total kinetic energy of the SC ($E_{\rm K,SC} \simeq 3.6 \times 10^{52}$) erg at the first periapsis passage ($E_{\rm K,SC} \approx 0.8 E_b$ for runs 1p and 2p). While a hard binary (i.e. with binding energy much larger than the average kinetic energy of an intruder) tends to shrink after a gravitational encounter, a marginally soft binary might either increase or decrease its semi-major axis (Heggie, 1975).

At the first periapsis passage the SC is still sufficiently compact to interact with the BHB as a single intruder, rather than a tidally disrupted system. Thus, initially the BHB is rather soft with respect to the intruder and its semi-major axis tends to oscillate between larger and smaller values. At later times ($>$ 2 Myr), when the SC is disrupted, the BHB interacts with single stars (rather than with the SC as a

(2) As a matter of fact, a small jump in the binary semi-major axis also appears at the beginning of the SC-BHB interaction in run 2 (Fig. 4.3); however, the immediate disruption of the SC by the binary hinders any further semi-major axis oscillation.

whole). In this late stage, the BHB starts shrinking monotonically, because it is a hard binary with respect to each single star it interacts with.

The second important difference with respect to runs 1 and 2 is the derivative of the semi-major axis with time ($\mathrm{d}a/\mathrm{d}t$). While in runs 1 and 2 the semi-major axis stalls after the first encounter (because the loss cone gets depleted), in runs 1p and 2p the semi-major axis keeps shrinking during the entire simulation. This is due to the fact that all stars in runs 1p and 2p remain bound to the system under the effect of the global potential. Thus, they can interact with the BHB more than once, when reaching the periapsis of their orbit.

This effect is also apparent from the hardening rate (Figure 4.8). The BHB hardening rate oscillates as a consequence of the oscillations in the BHB semi-major axis. The hardening rate between 3.5 and 5 Myr is $s \approx 0.019$ ($s \approx 0.014$) pc^{-1} Myr^{-1} in run 1p (run 2p), and even at later times (between 8.5 and 10 Myr) its value is of the order of 10^{-2} pc^{-1} Myr^{-1}. Thus the BHB hardening efficiency in runs 1p and 2p is higher than in runs 1 and 2 at late times.

From Figure 4.8 it is also apparent that the eccentricity of the BHB increases almost instantaneously to $0.06 - 0.08$ during the first interaction, while it does not change significantly afterwards. This result is similar to what we find for runs 1 and 2.

The fraction of stars inside the BHB loss cone f_{lc} for runs 1p and 2p is shown in Figure 4.5: at the beginning of the simulation, f_{lc} is the same as in runs 1 and 2 ($\approx$ 27 per cent). The BHB-induced tidal stripping funnels about half of the SC members into the loss cone during the first ≈ 0.2 Myr. The faster BHB-SC interaction in runs 1p and 2p results in a smaller number of stars initially funnelled in the loss cone; however, the depletion of the BHB loss cone is slower when the Dehnen potential is included. This results from the fact that stars may undergo repeated slingshot interactions before being definitely expelled from the loss cone.

Figures 4.7 and 4.8 also show the time evolution of the BHB in run 3p. Due to the initial orbital angular momentum of the SC, the fraction of stars in the loss cone is extremely low, and the binary shrinking is not effective. In particular, the BHB semi-major axis has shrunk by $\approx 0.4\%$ after 10 Myr, when its hardening rate is only $s \approx 2.5 \times 10^{-4}$ pc^{-1} Myr^{-1}, and even after 20 Myr it has shrunk only by $\approx 0.6\%$. Initially no stars inhabit the loss cone in run 3p; after 10 Myr (20 Myr) only ≈ 0.16 (0.27) per cent of stars are found in the loss cone. Also, the BHB eccentricity does not change significantly in run 3p (Figure 4.8). Thus, we can conclude that the properties of the BHB in runs 3 (without Dehnen potential) and 3p (with Dehnen potential) are very similar.

4.2.3 Structure of the SC remnant

The interaction with the BHB leads to the complete disruption of the SC. What is the final spatial distribution of stars around the BHB? Figures 4.1 and 4.2 show the projected stellar surface density in the $x - z$ and $x - y$ plane, while Figure 4.9 shows the final radial density distribution of stars.

In runs 1 and 2, the disruptive interaction lowers the central density of the SC by $2 - 3$ orders of magnitude. Most of the SC mass is scattered out of the initial tidal radius ($r_{\mathrm{t}} = 10$ pc) and the final density of the SC behaves as $\rho(r) \propto r^{-2}$. The

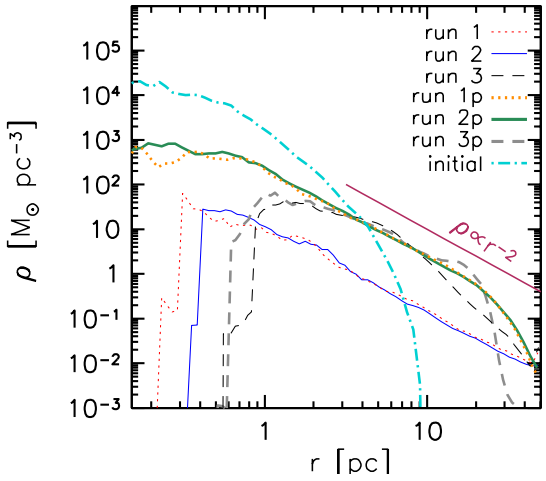

Fig. 4.9. Radial density distribution of stars after 5 Myr (10 Myr) in runs 1, 2, 3 (1p, 2p, 3p). The final density profile is compared with the initial density distribution (light-blue dash-dotted line). Thin dotted red line: run 1; thin solid blue line: run 2; thin dashed black line: run 3; thick dotted orange line: run 1p; thick solid sea-green line: run 2p; thick dashed grey line: run 3p. The initial density profile is computed with respect to the cluster center of mass, while the other density profiles are computed with respect to the BHB center of mass.

stars keep memory of their initial orbit, because stars still bound to the BHB after 5 Myr distribute on a prolate (triaxial) morphology in run 1 (run 2), whose longest axis lies along the cluster infall direction.

In runs 1p and 2p the stellar distribution after 10 Myr is almost isotropic and less influenced by the initial conditions. The density distribution is cored within the BHB orbit, and decreases as $\rho \propto r^{-2}$ between 1 and 20 pc, while it rapidly vanishes at larger distances. In fact, the density profile $\rho \propto r^{-2}$ resulting from the four radial runs is approximately what we expect for a relaxed stellar system around a point mass; Antonini et al. (2012) simulated the infall of several globular clusters on a SMBH and obtained a similar trend for the density at large radii.

If the SC is initially on a non-zero angular momentum orbit, stars settle on a disc-like structure (aligned with the initial SC orbit), whose external radius is $R \lesssim 20$ pc and whose thickness is $\lesssim 0.1\,R$. If the Dehnen potential is not included, the SC remnant is strongly asymmetric, as the BHB potential is almost Keplerian and most stars keep orbiting along the initial SC orbit. If the Dehnen cusp is present, the additional potential induces a precession on the stellar orbits, which results in a three-lobed overdensity within the disc (bottom-right panel of Figure 4.1). The density profile of stars in runs 3 and 3p is also shown in Figure 4.9, but one should keep in mind that the final stellar distribution in these two runs is far from being spatially isotropic.

4.2.4 Distribution of the stellar orbital elements

We now focus on the orbital parameters of stars that remain bound to the BHB and to the Dehnen potential (if present) by the end of the simulation. We stress

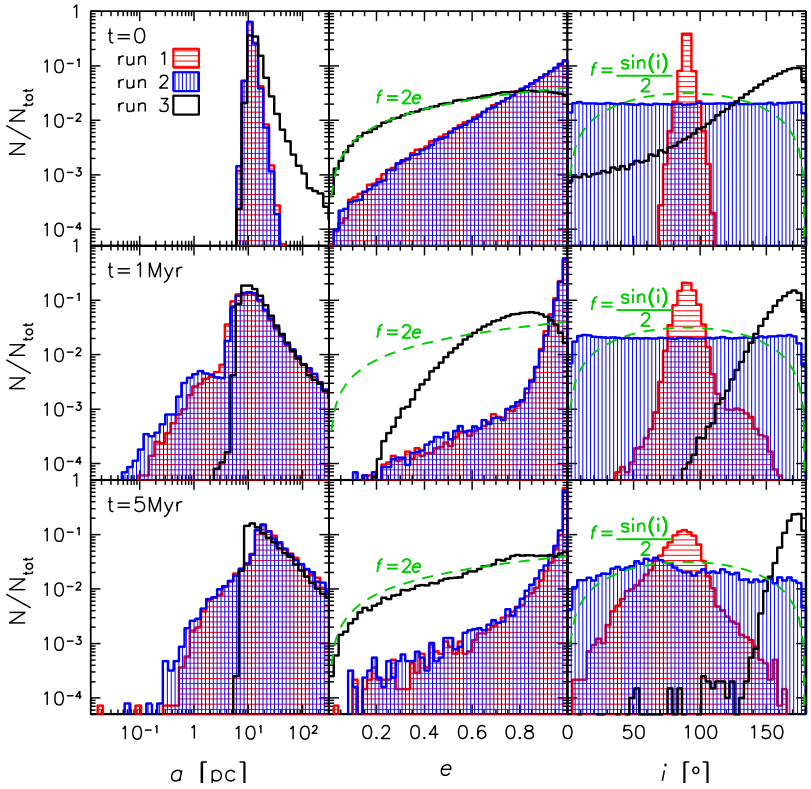

Fig. 4.10. Distribution of semi-major axis a (left-hand panels), eccentricity e (central panels) and inclination i (right-hand panels) of the stellar orbits (i is measured with respect to the plane of the BHB) in run 1 (red, horizontally shaded histograms), run 2 (blue, vertically shaded histograms) and run 3 (black empty histograms) at different simulation times: the top row shows the initial distribution ($t = 0$), the central row shows the distribution at $t = 1$ Myr and the bottom row shows the distribution at $t = 5$Myr. Green dashed line in the central panels: thermal eccentricity distribution $f(e)\ \mathrm{d}e = 2e\ \mathrm{d}e$ (Jeans, 1919); green dashed line in the right-hand panels: isotropic distribution of inclinations $f(i)\ \mathrm{d}i = \sin(i)/2\ \mathrm{d}i$.

that this study is limited by the fact that we cannot take in account any possible dynamical interaction between SC stars and the pristine nuclear stellar population.

Figure 4.10 shows the orbital properties of stars bound to the BHB in runs 1, 2, and 3 (without Dehnen potential), while Figure 4.11 shows the properties of stars bound to the BHB and the Dehnen potential for runs 1p, 2p, and 3p. The stellar orbital properties are shown at different times: (i) at the beginning of the integration, (ii) when the interaction between the SC and the BHB just started, and (iii) after 5 Myr (10 Myr) in runs without (with) the Dehnen rigid potential.

In all runs, the distribution of star semi-major axis initially peaks around ~ 10 pc, which is the initial average semi-major axis of stars in the SC. After the interaction, the distribution of semi-major axes becomes noticeably broader, especially in runs 1 and 2. Table 4.2 lists the fraction of non-escaping stars whose semi-major axis is smaller than a given threshold value; if the initial orbit is radial, $\lesssim 0.5$ per cent of stars have semi-major axis smaller than 1 pc: their final orbits are inside the semi-major axis of the BHB and they may further interact with it. While this percentage

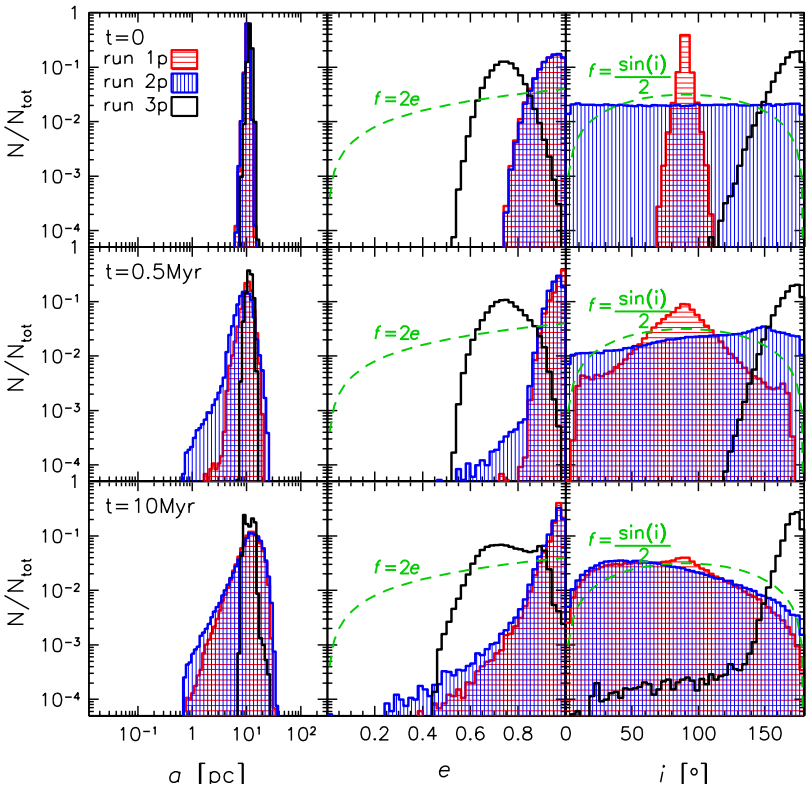

Fig. 4.11. Distribution of semi-major axis a (left-hand panels), eccentricity e (central panels) and inclination i (right-hand panels) of the stellar orbits (i is measured with respect to the plane of the BHB) in run 1p (red, horizontally shaded histograms), run 2p (blue, vertically shaded histograms) and run 3p (black empty histograms) at different simulation times: the top row shows the initial distribution ($t = 0$), the central row shows the distribution at $t = 0.5$ Myr and the bottom row shows the distribution at $t = 10$Myr. Green dashed line in the central panels: thermal eccentricity distribution $f(e)\,\mathrm{d}e = 2e\,\mathrm{d}e$ (Jeans, 1919); green dashed line in the right-hand panels: isotropic distribution of inclinations $f(i)\,\mathrm{d}i = \sin(i)/2\,\mathrm{d}i$.

Tab. 4.2. Fraction of bound stars with semi-major axis a smaller than 1, 5, 10 and 20 pc.

	a<1 pc	a<5 pc	a<10 pc	a<20 pc
run 1	0.25%	5.2%	12%	42%
run 2	0.64%	6.0%	13%	43%
run 3	0	0	8.2%	53%
run 1p	0.03%	4.5%	32%	92%
run 2p	0.14%	6.4%	31%	90%
run 3p	0	0	36%	99.9%

Column 1: run name; Columns $2-5$: fraction of bound stars whose semi-major axis is <1 pc (Column 2); <5 pc (Column 3); <10 pc (Column 4); <20 pc (Column 5). The listed fractions are computed after 5 Myr from the beginning of the simulation in runs 1, 2, and 3 and after 10 Myr in runs 1p, 2p, and 3p.

is small, these stars can have a further effect on the binary orbital shrinking. The fraction of stars with semi-major axis smaller than 5 pc is higher when the radial infall is coplanar (runs 2 and 2p), as the coupling between the SC and the BHB is stronger and more stars settle on low-energy orbits tightly bound to the BHB.

The distribution of inclinations i of the stellar orbit with respect to the BHB orbital plane strongly depends on the initial orbital plane of the SC in runs 1, 2 and 3: while bound stars in run 1 preserve a nearly perpendicular orbital inclination with respect to the orbital plane of the BHB, the distribution of bound stars in run 2 is more isotropic. In run 3, the SC-BHB interaction initially drives all stars with $i < 90$ degrees on orbits with $i \gtrsim 90$ degrees; by the end of the run almost all stars in run 3 rotate in the opposite direction to the BHB, except for a few stars that probably experienced a strong interaction with the BHB. The counter rotation of most stars results from the choice of giving to the SC an orbital angular momentum opposite to that of the BHB.

The final distribution of stellar inclinations in runs with the Dehnen potential is similar for runs 1p and 2p, suggesting that stellar inclinations may reach the same equilibrium configuration if one waits long enough; however, after 10 Myr a small fraction of stars in these runs still keep memory of the initial conditions of the simulation (e.g. there is a small peak in the distribution of inclinations at ~ 90 degrees in run 1p). In addition, ≈ 70 per cent of bound stars in runs 1p and 2p settle on orbits whose inclination is smaller than 90 degrees; this indicates that stars preferentially align their orbital angular momentum with the BHB one. Such result is not surprising as gravitational torques induced by the binary can drag a number of stars into corotating orbits (e.g. Mapelli et al., 2005). Despite the fact that in run 3p most stars keep memory of their initial inclination (~ 180 degrees), even in this run some stars are dragged onto corotating orbits by the gravitational torques of the binary, as 0.3 per cent of them have an inclination smaller than 90 degrees after 10 Myr.

In all radial runs the eccentricities of bound stars are much higher than a thermal distribution, as stars keep memory of the initial radial orbit of the SC; the eccentricity distributions look similar for such radial runs even if perpendicular runs 1, 1p always have a slight overabundance of highly eccentric stars compared to the coplanar runs 2, 2p. The large fraction of very eccentric objects also indicates that most bound stars are only marginally bound to the system.

The distribution of eccentricities in run 3 is initially very similar to the thermal distribution (Jeans, 1919), but this is probably because the initial orbital eccentricity of the SC is $e = 0.75$, i.e. it is really close to the mean-square value of the thermal eccentricity distribution. At later times, such distribution is still close to the thermal one, but more power is found at high eccentricities, indicating that the BHB funnels stars on more radial orbits.

The initial eccentricity distribution of stars in run 3p still peaks at $e = 0.75$, but the higher initial velocity of the SC in this run makes the distribution narrower compared to the one of run 3. At late times, the eccentricity distribution of run 3p slightly broadens and a small peak is found at $e \approx 0.9$, as a probable signature of weak slingshot interactions.

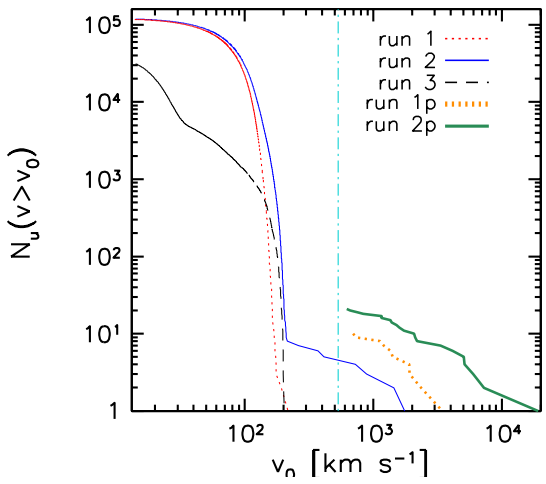

Fig. 4.12. Cumulative distribution of unbound stars $N_{\rm u}$ whose radial velocity is greater than a threshold velocity v_0 as a function of v_0 after 5 Myr in runs 1, 2 ,3 and after 10 Myr in runs 1p, 2p. Red dotted thin line: run 1; blue solid thin line: run 2; black dashed thin line: run 3; orange dotted thick line: run 1p; sea-green solid thick line: run 2p; no stars escape from the system in run 3p. The dash-dotted vertical line at $v_0 = 533$ km s^{-1} shows the escape velocity from the Milky Way at three virial radii (Smith et al., 2007; Piffl et al., 2014).

4.2.5 Hyper-velocity stars

Figure 4.12 shows the cumulative distribution of the radial velocity v_r of stellar escapers, i.e. stars that become unbound during the simulation; here v_r represents the component of the stellar velocity vector projected along the radial direction. From Figure 4.12, it is apparent that a large number of stars become unbound in runs 1, 2 and 3 (without Dehnen potential), but their velocity is > 100 km s^{-1} only in few cases.

The fastest escapers in runs 1 and 3 attain a velocity $v_r \sim 200$ km s^{-1} at most. Run 2 produces a marginally larger number of fast escapers: four objects attain an escape speed greater than the estimated escape speed from the Milky Way at three virial radii: ≈ 533 km s^{-1} according to Piffl et al. (2014).

In contrast, Figure 4.12 shows that only few tens of stars become unbound in runs 1p and 2p (with Dehnen potential), but their velocity is always > 600 km s^{-1}. In particular, only 10 and 21 stars out of 10^5 get unbound in run 1p and 2p, respectively, while no star leaves the potential well in run 3p.

The velocity attained by the escapers in runs 1p and 2p can reach values as high as 5,000 km s^{-1} and 20,000 km s^{-1}, respectively(3). Again, coplanar orbits (run 2p) are more efficient in producing high velocity stars than perpendicular SC orbits (run 1p). We stress that all the escapers in runs 1p and 2p can be classified as genuine hyper-velocity stars (Hills, 1988; Brown et al., 2005, 2006), produced by the interaction with the BHB.

(3) If we do not anchor the BHB centre of mass to the origin of our reference frame, the number of produced hyper velocity stars is similar to what we show in Fig. 4.12; however, the maximum velocity attained by such hyper velocity stars drops to about 6,000 km s^{-1}.

4.3 Discussion and conclusions

In this investigation, we simulated the disruption of a SC by a BHB. We explored several different configurations for the SC-BHB interaction: with and without a rigid Dehnen potential, considering a SC orbital eccentricity $e = 1$ and $e = 0.75$, and assuming 0 or 90 DEG inclination between the orbital plane of the SC and that of the BHB.

Runs without Dehnen potential are quite unrealistic, because the BHB is expected to lie in the centre of the galactic potential well. However, we ran them, because they represent a very simple test case, and because we can infer the role of the galactic potential from the comparison between runs with and runs without a galactic potential.

When the initial SC orbit has non-zero angular momentum ($e = 0.75$), only few stars enter the BHB loss cone. As a consequence, the hardening rate of the BHB is almost negligible. This result is nearly unaffected by the presence of a Dehnen potential.

In contrast, if the initial orbit of the SC is radial ($e = 1$), the infall of the SC effectively refills the loss cone of the BHB: the semi-major axis of the BHB changes by $\gtrsim$10 per cent within $5 - 10$ Myr. Even if nearly radial orbits are not expected to be common, they can be produced by collisions between molecular clouds. In particular, the collision of two molecular clouds close to the central parsec of a galaxy might trigger the formation of a SC with very low orbital angular momentum (e.g. Hobbs and Nayakshin 2009; Mapelli et al. 2012). For instance, Tsuboi et al. (2015) recently showed that at least part of the star formation observed within the Galactic Centre may be triggered by collisions between molecular clouds.

In our simulations, if the Dehnen potential is not included and the SC infalls radially, the semi-major axis of the BHB shrinks very fast during the first encounter with the SC, but then it stalls. In contrast, if the Dehnen potential is included, the hardening of the BHB is initially less efficient, but then the BHB keeps shrinking at a significant rate for the entire simulation (10 Myr). The reason of this difference is that most stars that interact with the BHB acquire a kick velocity of several ten to several hundred km s^{-1}. If only the SC and the BHB contribute to the potential well, these stars end up unbound and completely ejected from the system. Thus, they cannot undergo more than one interaction with the BHB.

In contrast, if the rigid Dehnen potential is included, these kick velocities are too low to unbind a star: most stars remain bound to the potential well. After reaching their new apoapsis, these stars fall back toward the centre of the potential well and might interact with the BHB several times. Thus, the BHB keeps shrinking for a longer time, because each star can undergo multiple interactions with the BHB.

We stress that the simulations presented here neglect the effects of dynamical friction induced by the pristine stellar population on the infalling SC (because the Dehnen potential is modelled as a rigid potential). Gravitational drag can bring the SC remnant on orbits closer to the BHB and further assist the BHB shrinking. However, Petts and Gualandris (2017) recently showed that dynamical friction is inefficient in bringing SC stars on orbits closer than ~ 2 pc from the central massive object(s), even if one assumes a very dense SC infalling from $5 - 15$ pc distance.

Another effect we neglected is the loss cone refilling induced by a massive perturber (the SC, in our case) on the pristine stellar population, as this mechanism was already explored in a series of previous studies (Perets and Alexander, 2008; Matsui and Habe, 2009): they demonstrated that a massive object is able to deflect the orbits of many stars belonging to the pristine galaxy core and funnel them onto the loss cone, enhancing the binary shrinking. In particular, Matsui and Habe (2009) analysed how the BHB shrinking rate can be boosted by the infall of a compact dwarf galaxy merging with the BHB host galaxy. They consider the infall of an object whose mass is ~ 10 times the BHB mass (while in our runs $M_{\rm SC} \approx 0.04 M_{\rm BHB}$) and they do not study the phase-space redistribution of stars belonging to the infalling stellar system, focusing on the effects of the dwarf-induced loss cone repopulation instead.

Finally, we stress that in our simulations the change in the BHB semi-major axis was explored only for a limited number of cases, and in a forthcoming study we will investigate what happens for different orbital properties and masses of the SC and different BHB separations. However, we can already make some guess on the effect of a different choice of initial conditions, by means of some analytic consideration. The change of the semi-major axis likely depends on (i) the initial semi-major axis of the BHB, (ii) the initial relative velocity between SC and BHB, (iii) the total mass of the SC, and (iv) the mass of the BHB.

The geometric cross section of the BHB scales as the square of the semi-major axis. Thus, the effect of SC infall would have been stronger for a wider BHB, because all SC members would have passed inside the separation between the two SMBHs. However, this effect is mitigated by gravitational focusing: the trajectory of a SC star is deflected by the gravitational pull of the BHB. Accounting for gravitational focusing, the effective periapsis distance between the centre-of-mass of the SC and that of the BHB is $p \approx b^2\, v_{\rm i}^2 / [2\, G\, (M_b + M_{\rm SC})]$, where b is the impact parameter, $v_{\rm i}$ is the initial relative velocity between the BHB and the SC, G is the gravitational constant, M_b is the BHB mass, and $M_{\rm SC}$ is the SC mass (Sigurdsson and Phinney, 1993). In our runs 1, 2, 1p, and 2p, we chose $v_{\rm i} = 0$, which implies $p \sim 0$. Thus, the result of these runs can be considered as an upper limit to the effect of three-body encounters on the BHB shrinking. For a small impact parameter (of the same order of magnitude as the BHB semi-major axis), the shrinking of the binary is completely determined by the ratio between the SC mass and the BHB mass, because the average relative change of the BHB binding energy $\Delta E_{\rm b} / E_{\rm b}$ per encounter scales as (Hills, 1983; Quinlan, 1996; Colpi et al., 2003; Mapelli et al., 2005)

$$\frac{\Delta E_{\rm b}}{E_{\rm b}} = \xi\, \frac{m_\star}{M_b}, \tag{4.4}$$

(cf. Eq.1.15) where $m_\star$ is the average mass of a single star, and ξ is a dimensionless factor ($\xi \sim 1 - 10$ for small impact parameters, Hills 1983). Equation 4.4 implies that the expected variation of the BHB semi-major axis due to SC infall is

$$1 - \frac{a_{\rm f}}{a_{\rm i}} \sim 0.1 \left(\frac{\xi}{1}\right) \left(\frac{N_\star}{10^5}\right) \left(\frac{m_\star / M_b}{10^{-6}}\right), \tag{4.5}$$

where $a_{\rm f}$ and $a_{\rm i}$ are the final and initial BHB semi-major axis, respectively, while $N_\star$ is the number of stars in the SC.

The change of semi-major axis derived from this back-of-the-envelope calculation is remarkably similar to the value we obtained from our runs 1, 2, 1p, and 2p (i.e. the simulations where the SC is on a radial orbit). Thus, we might expect that a SC with $N_* \gtrsim 10^6$ on a nearly radial orbit would have lead a $\sim 10^6 M_\odot$ BHB close to the regime where the orbital decay by GW emission is efficient. However, it must be kept in mind that only a small fraction of SC members can efficiently interact with the BHB once the semi-major axis has dropped to $\ll 1$ pc. Dedicated simulations are needed to probe this extreme situation. Moreover, to derive equation 4.5, we implicitly assumed that each star scatters with the BHB only once (as in the runs without Dehnen potential). As we have discussed in Section 4.2, this assumption gives us a lower limit to the efficiency of BHB hardening.

In this study, we also investigated the fate of the SC. In all runs, the SC is almost completely disrupted by the interaction with the BHB. SCs infalling with non-zero orbital angular momentum settle on a disc-like structure, whose morphology strongly depends on the initial SC eccentricity and on the presence of a Dehnen potential. No hyper-velocity stars are produced if the SC orbit has non-zero angular momentum.

If the SC is on a radial orbit and the Dehnen potential is not included, ~ 95 per cent of stars are kicked onto unbound orbits and only a small fraction of the initial SC keeps orbiting the BHB. These bound stars settle into a small subsystem whose shape is strongly influenced by the initial SC orbit; the final distribution of stars follows a trend $\rho(r) \propto r^{-2}$.

If the SC infall is radial and the Dehnen potential is included, most stars remain bound to the global potential and are generally confined within ~ 50 pc from the BHB. Only few tens of stars become unbound in this case, but their velocities are of the order of several thousand km s^{-1}. Thus, these are genuine hyper-velocity stars. These features represent the main observational imprints of a SC that was recently disrupted by a BHB.

5

Brownian motion of massive black hole binaries and the final parsec problem

Based on:
Bortolas, E., Gualandris, A., Dotti, M., Spera, M. and Mapelli, M., *"Brownian motion of massive black hole binaries and the final parsec problem",* 2016, MNRAS 461, 1023

–

The ultimate coalescence of a SMBH binary (BHB) is expected to occur in a burst of low-frequency GWs, which will be revealed by the forthcoming LISA mission (Thorne, 1994; Amaro-Seoane et al., 2017). This fact has led to a renewed interest in the study of BHBs dynamical evolution.

Even if the late BHB pairing, induced via stellar slingshot ejections, has been questioned for more than a decade (leading to the formulation of the so-called *final parsec problem* Milosavljević and Merritt 2003b), recent investigations strongly suggest that BHBs can efficiently merge within a Hubble time in most galaxies, provided that the host galaxy exhibits a significant degree of non-sphericity (Vasiliev et al., 2015; Gualandris et al., 2017). However, this conclusion initially came from simulations adopting the direct summation N-body method. This highly accurate numerical approach is required when one wishes to model the detailed evolution of the binary and of the orbits of stars interacting with it; however, its N^2 computational complexity limits applicability to a few million particles at most.

Simulations with low resolution (i.e., low N) might be plagued by both spurious two-body relaxation effects and, most importantly for the present Chapter, by an increased Brownian motion of the binary centre of mass (CoM). Whenever a slingshot interaction occurs, the binary CoM experiences a recoil whose amplitude depends on the mass of the ejected star. In low-N models, where stars are orders of magnitude more massive than in real galaxies, the binary experiences an enhanced Brownian motion. As it wanders within its typical Brownian radius, the binary can intersect more stars than it would were it confined to a smaller region. Therefore, the binary loss cone[(1)] is artificially enlarged, and the binary may harden more

(1) The loss cone is the region of phase-space harbouring stars with angular momentum low enough to undergo an encounter with the binary.

efficiently than it would in a real physical system.

What is the importance of Brownian motion and whether it depends on the resolution has been debated for a long time. It has been argued that *"a substantial fraction of all massive binaries in galaxies can coalesce within a Hubble time"* due to the effects of Brownian motion (Chatterjee et al., 2003). In contrast, other theoretical studies suggest that Brownian motion is modest for BHBs in real galactic nuclei (Merritt, 2001; Milosavljević and Merritt, 2003a), but it remains to be established whether it is responsible for the sustained hardening of BHBs observed in direct-summation merger simulations. In the present Chapter we study the Brownian motion of BHBs in galaxy merger simulations and its connection with loss cone repopulation and the final parsec problem.

5.1 Methods

We performed a suite of direct-summation N-body simulations of equal mass galaxy mergers, varying the resolution (i.e. particle number N) and the density distribution of the progenitor galaxies. Each galaxy follows a Dehnen's density profile (Dehnen, 1993):

$$\rho(r) = \frac{(3-\gamma)\,M_{\rm g}}{4\pi}\frac{r_0}{r^{\gamma}(r+r_0)^{4-\gamma}}, \tag{5.1}$$

with total mass $M_{\rm g}$, scale radius r_0 and inner slope γ. Two different realisations of the same model were placed on a bound elliptical orbit in the $x-y$ plane, with initial orbital eccentricity $e=0.5$, separation $\Delta r = 20r_0$ and semimajor axis $a = 15r_0$. The units were chosen in such a way that $G = r_0 = M_{\rm tot} = 1$, where $M_{\rm tot}$ represents the total stellar mass involved in each merger simulation. A point mass representing the MBH was placed at the centre of each spherical system, with a mass $M_\bullet = 0.005 M_{\rm g}$.

We performed three main groups of simulations, each characterised by a different inner slope for the colliding galaxies: $\gamma = 0.5$ for set A, $\gamma = 1$ for set B, and $\gamma = 1.5$ for set C. For each set, we considered different values for N from 8k to 1M. For set C the N=1M case was avoided due to the prohibitively long integration time required. The list of performed simulations is given in Table 5.1. Each model was evolved for $t \approx 500$ time units; this choice ensures that the binary is followed for $\Delta t \gtrsim 100$ after the MBHs form a bound Keplerian pair. The parameters of the performed N-body experiments are summarised in Table 5.2.

The initial conditions were evolved adopting the integrator `HiGPUs`, a direct-summation N-body code based on the sixth order Hermite scheme with block timesteps, designed to run on GPUs (Capuzzo-Dolcetta et al., 2013). The integrator adopts a Plummer softening kernel (Plummer, 1911); we chose a softening parameter $\varepsilon = 10^{-4}$; this length scale is smaller than the minimum separation reached by the binary during its evolution. In `HiGPUs`, the individual particle timesteps are computed via a combination of the sixth and fourth order Aarseth criterion (Aarseth, 2003; Nitadori and Makino, 2008), and the two accuracy parameters were set equal to $\eta_{\rm sixth} = 0.45$, $\eta_{\rm fourth} = 0.01$ (for details, see Capuzzo-Dolcetta et al., 2013). The minimum and maximum possible values in the hierarchy of timesteps were chosen as $\Delta t_{\rm min} = 2^{-29} \approx 1.863 \cdot 10^{-9}$ and $\Delta t_{\rm max} = 2^{-6} = 0.015625$.

All simulations of set A, B, and C were run allowing the BHB to wander (hereafter,

Tab. 5.1. List of simulations. Column 1: simulation set (A, B, C); column 2: run name; column 3: total number of particles N; column 4: slope γ of the inner profile in each galaxy model. All mergers are equal mass.

Set	Run	N	γ
A	1	8k	0.5
	2	16k	0.5
	3	32k	0.5
	4	64k	0.5
	5	128k	0.5
	6	256k	0.5
	7	512k	0.5
	8	1M	0.5
B	1	8k	1.0
	2	16k	1.0
	3	32k	1.0
	4	64k	1.0
	5	128k	1.0
	6	256k	1.0
	7	512k	1.0
	8	1M	1.0
C	1	8k	1.5
	2	16k	1.5
	3	32k	1.5
	4	64k	1.5
	5	128k	1.5
	6	256k	1.5
	7	512k	1.5

Tab. 5.2. Parameters of the simulations. From left to right: initial semi-major axis, initial eccentricity, initial separation of the two original galaxies, scale radius of each galaxy, total stellar mass in each simulation, mass ratio between the two merging galaxies, mass ratio between the BHB and the stellar mass in the simulation, softening parameter.

a_i	e_i	Δr	r_0	M_tot	q	$M_\mathrm{b}/M_\mathrm{tot}$	ε
15	0.5	20	1	1	1	0.005	10^{-4}

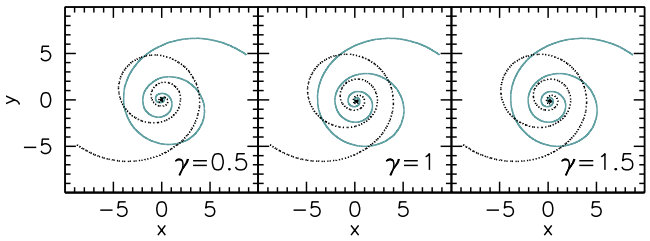

Fig. 5.1. Trajectories of the two MBHs in the $x-y$ plane for the three sets of simulations, corresponding to $\gamma = 0.5, 1.0, 1.5$, from left to right, and $N = 512$k. In this Figure and in the following, distances are in scalable $N-$body units.

free-binary simulations). Simulations of set B were then re-run while periodically re-centering the BHB at the centre of the merger remnant to quench the binary's wandering (hereafter, *fixed-binary simulations*).

5.2 Simulations and binary evolution

The trajectories of the MBHs in the $x-y$ plane are shown in Figure 5.1 for the three simulation sets. The initial evolution of the MBH pair reflects the orbit of the progenitor galaxies, which is the same for all three sets, and the trajectories are therefore quite similar.

The time evolution of the binary separation is shown in Figure 5.2, for the three different sets (free-binary simulations), and for $N = 512$k. This represents the maximum resolution available for all three γ values, and is therefore our fiducial resolution.

Here we recall the three central phases of BHB evolution. We consider an equal mass binary with total mass M_b. The first phase of evolution is driven by dynamical friction, which brings the MBH pair to a separation a_f, defined as the separation at which the stellar mass $M_\star$ enclosed in the binary orbit is twice the mass of the secondary MBH. In our case:

$$M_\star(a_f) = M_\mathrm{b}. \tag{5.2}$$

The time $t(a_f)$ at which this separation is reached approximately corresponds to the time of formation of a bound Keplerian binary in our equal mass simulations. Around this time, stellar encounters with stars on intersecting orbits start becoming important, and mark the beginning of the *strong three-body scattering regime* (Sesana, 2010). In this phase, which sees a rapid shrinking of the binary separation, slingshot ejections first combine with dynamical friction and then become the main driver of binary hardening. This phase is rather short, and ends when the loss cone consisting of stars initially on intersecting orbits has been emptied. At this point,

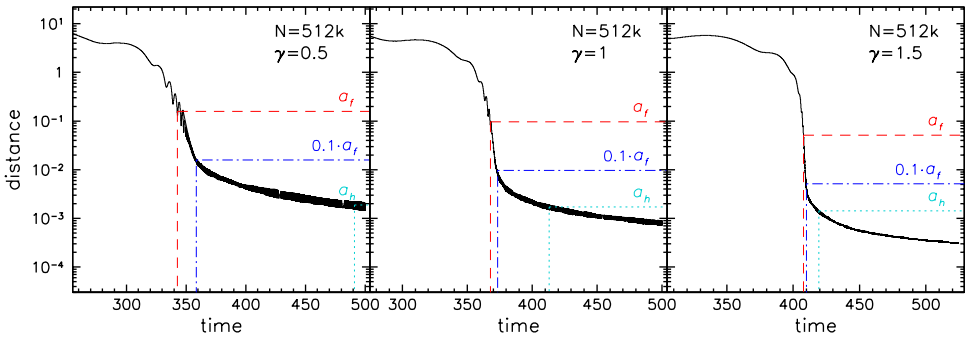

Fig. 5.2. Evolution of the binary separation as a function of time for the runs with resolution N =512k. From left to right, panels show the evolution for models with initial central density slope $\gamma = 0.5$, $\gamma = 1$ and $\gamma = 1.5$. The significant separations $a_{\rm f}$ (roughly at which the Keplerian binary forms, equation (5.2)), $a_{\rm f}/10$ and $a_{\rm h}$ (from which slingshot interactions expel unbound stars, equation (5.3)) and their corresponding times are marked in the panels. In this Figure and in the following, times and distances are in scalable $N-$body units.

the inner cusp of the remnant is destroyed and a core has been carved in the stellar distribution.

We define the binary to be hard when its binding energy per unit mass exceeds the kinetic energy per unit mass of the field stars, i.e. when it reaches a separation

$$a_{\rm h} = \frac{G\,M_{\rm b}}{8\sigma_*^2}. \tag{5.3}$$

Here σ_* represents the velocity dispersion of the field stars (Milosavljević and Merritt, 2001). From this moment, stars ejected from the nucleus via the slingshot mechanism attain a velocity greater than the escape velocity. The quantities a_f and a_h and their corresponding times are marked in Figure 5.2. The remnant mass distribution keeps memory of the initial slope γ, especially before the mass-carving has taken place; as a consequence, both $a_{\rm f}$ and $a_{\rm h}$ show a clear dependence on the initial value of γ (see Figure 5.2): the radius containing the mass of the binary is smaller for merger products generated by steeper initial models, inducing a smaller $a_{\rm f}$, while the velocity dispersion σ_*^2 of cuspier models is expected to be higher and produces a smaller $a_{\rm h}$.

We also recall the definition for the hardening rate

$$s(t) = \frac{\rm d}{{\rm d}t}\frac{1}{a}, \tag{5.4}$$

where a represents the semi-major axis of the binary. We compute s in all simulations by performing a linear fit to $a^{-1}(t)$ in small time intervals, and plot its time evolution in the middle panels of Figure 5.3. The hardening rate is approximately constant with time. This behaviour is expected for binaries hardening in constant density backgrounds (Hills, 1983), i.e. when the stellar field is unaffected by the binary evolution. Since this is not the case in a merger, the roughly constant nature of s implies that the loss cone is efficiently replenished, in agreement with previous studies that found the BHB to merge within a Hubble time (Preto et al., 2011; Khan et al., 2011; Gualandris and Merritt, 2012).

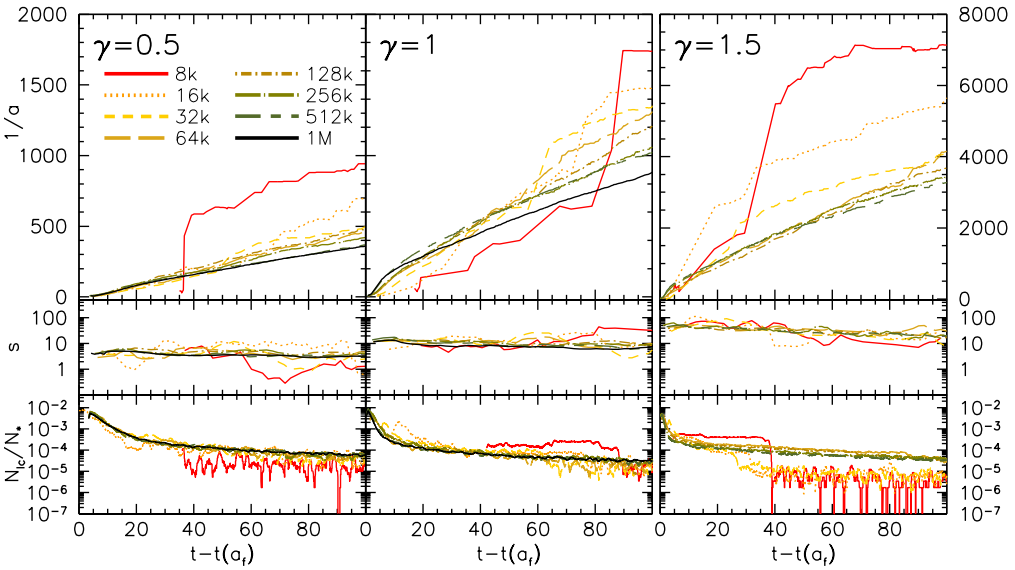

Fig. 5.3. Time evolution of the inverse semimajor axis $1/a$ (top panels), hardening rate (middle panels) and fraction of loss cone stars (bottom panels) for all the available resolutions from $N = 8$k to $N =$1M. We averaged the hardening rate over several time intervals, to smooth fluctuations. The left-hand panels refer to the set with initial density slope $\gamma = 0.5$, the central panels refer to the set with $\gamma = 1$ and the right-hand panels refer to the last set with $\gamma = 1.5$. Notice the different scale of the vertical axis in the top right panel. Time on the horizontal axis is given from the time corresponding to $a = a_{\rm f}$;

The Figure also shows the evolution of the inverse semi-major axis $1/a$ (top panels) and the number of stars inside the loss cone $N_{\rm lc}$, normalised to the total number of stars. Since hardening is assumed to be due to stars in the loss cone interacting with the binary, it is useful to monitor how many stars can be found in the loss cone at any given time. A star is considered to belong to the loss cone if its angular momentum per unit mass (L) is smaller than the angular momentum per unit mass of a circular binary with the same energy, i.e. $L \leq L_{\rm LC} = \sqrt{2G\,M_{\rm b}\,a}$. We find that after the binary has become hard, the fraction of stars in the loss cone is approximately constant, or only slightly decreasing, on the time scale considered in the simulations. The decrease is due to the fact that the loss cone shrinks with time as the binary separation shrinks (Vasiliev et al., 2015).

5.3 Brownian motion

5.3.1 Theoretical expectations

The Brownian motion of a single MBH in a nucleus is well described by a random walk due to encounters with field stars (Chandrasekhar, 1942, 1943). If a massive object with mass M is surrounded by an isothermal distribution of stars, its velocity dispersion σ is expected to obey energy equipartition with the background stars:

$$\sigma^2 = \frac{m}{M}\sigma_*^2, \tag{5.5}$$

where σ_* is the stellar velocity dispersion and m is the typical stellar mass. This result has been shown to remain valid for a wide range of stellar backgrounds (Dorband et al., 2003; Merritt, 2005; Merritt et al., 2007a). A similar behaviour is expected for the CoM of a BHB in a galactic nucleus. *Superelastic scattering* and the fact that stars are ejected in random directions slightly enhance the Brownian motion amplitude in the binary case; however, Merritt (2001) showed that the binary's random motion in phase space is dominated by distant encounters and therefore the wandering essentially obeys equation (5.5). Merritt (2001) derived an expression for the characteristic amplitude of the motion r_b, under the assumptions that (i) the binary is placed in a constant density core, (ii) the stellar potential is harmonic and (iii) the Brownian motion has no influence on the stellar velocity field and mass distribution:

$$\begin{aligned} r_\mathrm{b} =& \left(\frac{R_2}{R_1}\right)^{1/2} \left(\frac{m}{M_\mathrm{b}}\right)^{1/2} r_\mathrm{c} \\ =& 0.01\,\mathrm{pc} \left(\frac{R_2}{R_1}\right)^{1/2} \left(\frac{m}{M_\odot}\right)^{1/2} \left(\frac{10^8 M_\odot}{M_\mathrm{b}}\right)^{1/2} \left(\frac{r_\mathrm{c}}{100\,\mathrm{pc}}\right), \end{aligned} \tag{5.6}$$

where $(R_2/R_1)^{1/2}$ is a factor of order unity related to Chandrasekhar's coefficients, r_c represents the King core radius (King, 1966) and M_b is the total mass of the binary.

5.3.2 Free-binary simulations

In order to characterise the Brownian motion of the BHB, it is necessary to define a meaningful reference position to be compared with the binary CoM over time. In principle, one could think of using the centre of mass of the whole stellar system, but this is dominated by the outermost stars which have a negligible influence on the BHB evolution. A better option is the centre of mass of the 50% innermost stars in the system, which allows one to discard the outermost stars and consider only stars belonging to the density cusp to define the reference centre. Since at early times two stellar cusps are present, we started the Brownian motion characterisation from the moment when the binary separation reaches $a_\mathrm{f}/10$: at this stage, the Keplerian binary has formed and the two original systems have already merged into a single cusp[(2)].

We evaluated the typical wandering radius of the binary in the following way: (i) first we computed the CoM (C0) from 50% of the particles closest to the binary's CoM; (ii) then we reiterated the procedure by evaluating a more accurate CoM (C1) over the 50% stars closer to C0, once this quantity is known. The displacement of C1 from the BHB CoM constitutes our best estimate of the binary wandering amplitude r_b over time. It is worth stressing that our recursive approach avoids biases induced by the selection of stars with respect to the position of the BHB.

The proportionality relation $\sigma^2 \propto m$ from equation (5.5) can be verified by computing the BHB CoM velocity dispersion σ^2 with respect to the CoM velocity of

(2) This particular moment has been chosen since it corresponds approximately to the point when the binary decay slows down considerably in all the three sets of simulations performed. We avoided other approaches due to the noisy trend of the binary separation in the lower-N cases.

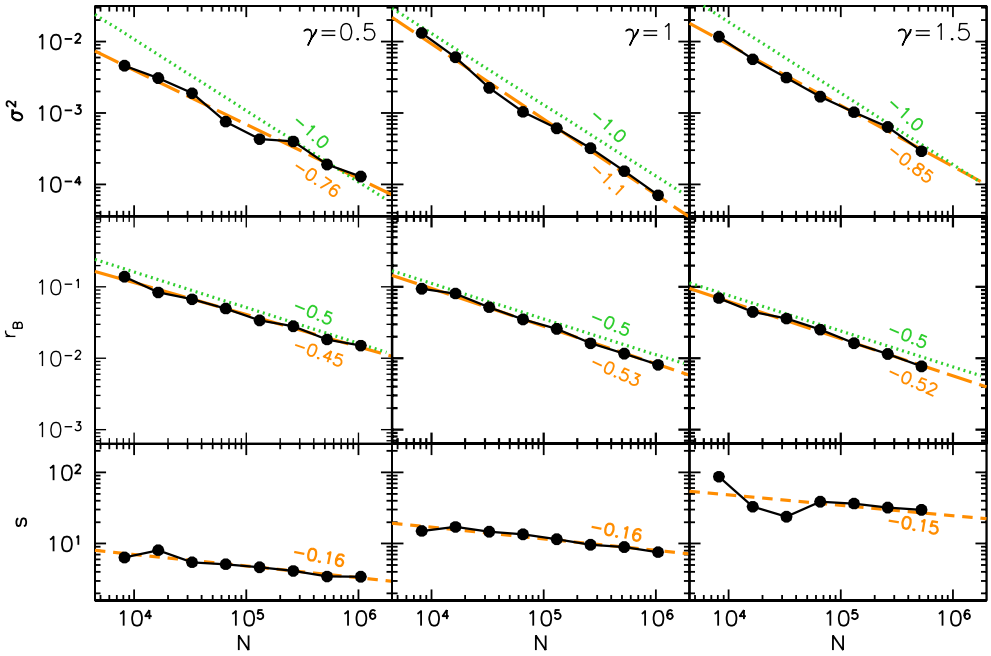

Fig. 5.4. Analysis of the BHB Browninan motion. Top: Time-averaged binary velocity dispersion as a function of the number of particles N in each simulation. Centre: Time-averaged wandering radius of the BHB as a function of particle number. Bottom: Time-averaged hardening rate versus particle number. In all cases, the average is computed from the time when a separation $a_{\rm f}/10$ is reached and over 100 time units thereafter. The orange dashed lines represent power-law fits to the data and the obtained best-fit slopes are given by the orange labels below the lines. The green dotted lines indicate the expected dependencies based on theoretical models, with slopes given by the green labels above the lines. In all cases, the left-hand panels refer to simulations with $\gamma = 0.5$, central panels refer to simulations with $\gamma = 1$, and right-hand panels to the set with $\gamma = 1.5$.

the stellar background σ_*. This velocity CoM has been computed over the same stars used for the calculation of C1.

In order to test the binary Brownian motion dependence on the number of particles in each simulation, we averaged the hardening rate s, binary wandering radius $r_{\rm b}$ and CoM velocity dispersion σ^2 over time from the moment at which the binary separation reaches $a_{\rm f}/10$ and for Δt=100 time units. From equation (5.5), we expect a theoretical dependence of $r_{\rm b} \propto N^{-0.5}$ and $\sigma^2 \propto N^{-1}$, given that $m = 1/N$ in the simulations. The averaged σ^2, $r_{\rm b}$ and s are shown in Figure 5.4 as a function of N. We performed a power-law fit of the obtained data points for each of these quantities as a linear least-square fit in logarithmic scale. We thus obtained a dependence of the form $r_{\rm b} \propto N^{p_r}$, $\sigma^2 \propto N^{p_{\sigma^2}}$ and $s \propto N^{p_s}$. The computed power-law indexes are listed in Table 5.3 and show a good agreement with the expected values $p_{\sigma^2} = -1$ and $p_r = -0.5$. Therefore the observed amplitude of the binary's Brownian motion follows the expected theoretical dependence on particle number.

If the loss cone refilling were driven by Brownian motion, a similar dependence on N would be expected for the hardening rate. However, this is not observed, and the hardening rate of the binary shows a much weaker dependence on N than the amplitude of the wandering. We argue that such dependence is due to

Tab. 5.3. List of best-fit power-law indexes of the BHB CoM velocity dispersion (σ^2), wandering amplitude (r_b) and hardening rate (s). Column 1: index name; column 2: expected values based on theoretical arguments; columns 3–5: results for simulations whose initial galaxies had inner slope $\gamma = 0.5, 1.0, 1.5$, respectively.

Index	exp.	$\gamma = 0.5$	$\gamma = 1$	$\gamma = 1.5$
p_{σ^2}	-1	-0.76	-1.1	-0.86
p_{r_b}	-0.5	-0.45	-0.53	-0.52
p_s	0	-0.16	-0.16	-0.15

a combination of collisional repopulation of the loss cone and Brownian motion at these moderate values of N, but should become negligible at more realistic particle numbers (Gualandris et al., in preparation).

5.3.3 Fixed-binary simulations

In order to draw a more robust conclusion about the role of Brownian motion in loss cone refilling, we re-ran the set of simulations with $\gamma = 1.0$ while periodically re-centering the binary at the centre of the merger remnant to quench the binary's wandering. To this purpose, we introduced the following modifications in the N-body integrator: (i) at each integration step, both MBHs were forced to advance with the smallest populated timestep in the hierarchy; (ii) the BHB was pinned down at the centre of the density cusp by shifting the binary CoM position during each corrector step and setting its velocity to zero. These new runs were started at the time when the binary separation in the original simulations drops below $a_\mathrm{f}/10$. The centre of the stellar density cusp was evaluated by computing the CoM of particles inside a sphere with radius l_0 (≈ 5), i.e. the sphere containing 50% of stars at the beginning of these new runs. During each corrector step the predicted positions of the stars were used to (i) estimate the CoM (S0) of particles within a distance l_0 from the binary CoM and (ii) reiterate the procedure by computing a more precise CoM (S1) using the just estimated CoM (S0) as new centre of the sphere. We refer to this new set of integrations as *fixed-binary* simulations, to distinguish them from the previous *free-binary* ones.

From Figure 5.5 it is apparent that the hardening rate is lower for the fixed-binary runs in the low-N limit. As the resolution is increased, though, the free-binary evolution resembles more and more the fixed-binary evolution. This aspect can be better appreciated from Figure 5.6: the time-averaged hardening rate in the free-binary runs approaches the hardening rate of the runs with anchored BHB as N increases, and the binary behaviour converges in the higher resolution simulations. Accordingly, the power-law dependence of the averaged hardening rate on N in the fixed-binary simulations is shallower ($p_s = -0.052$) compared to the one obtained from the free-binary runs ($p_s = -0.16$).

In addition, we note that the hardening rate measured in the low-N runs with fixed binary is only slightly larger than the same rate measured at the highest particle number. This implies that Brownian motion has a non negligible role in loss cone refilling for particle numbers in the range $10^4 \leq N \leq 10^6$, while it does not appreciably influence the BHB evolution if $N \gtrsim 10^6$.

Chatterjee et al. (2003) and Quinlan and Hernquist (1997) used a similar strategy

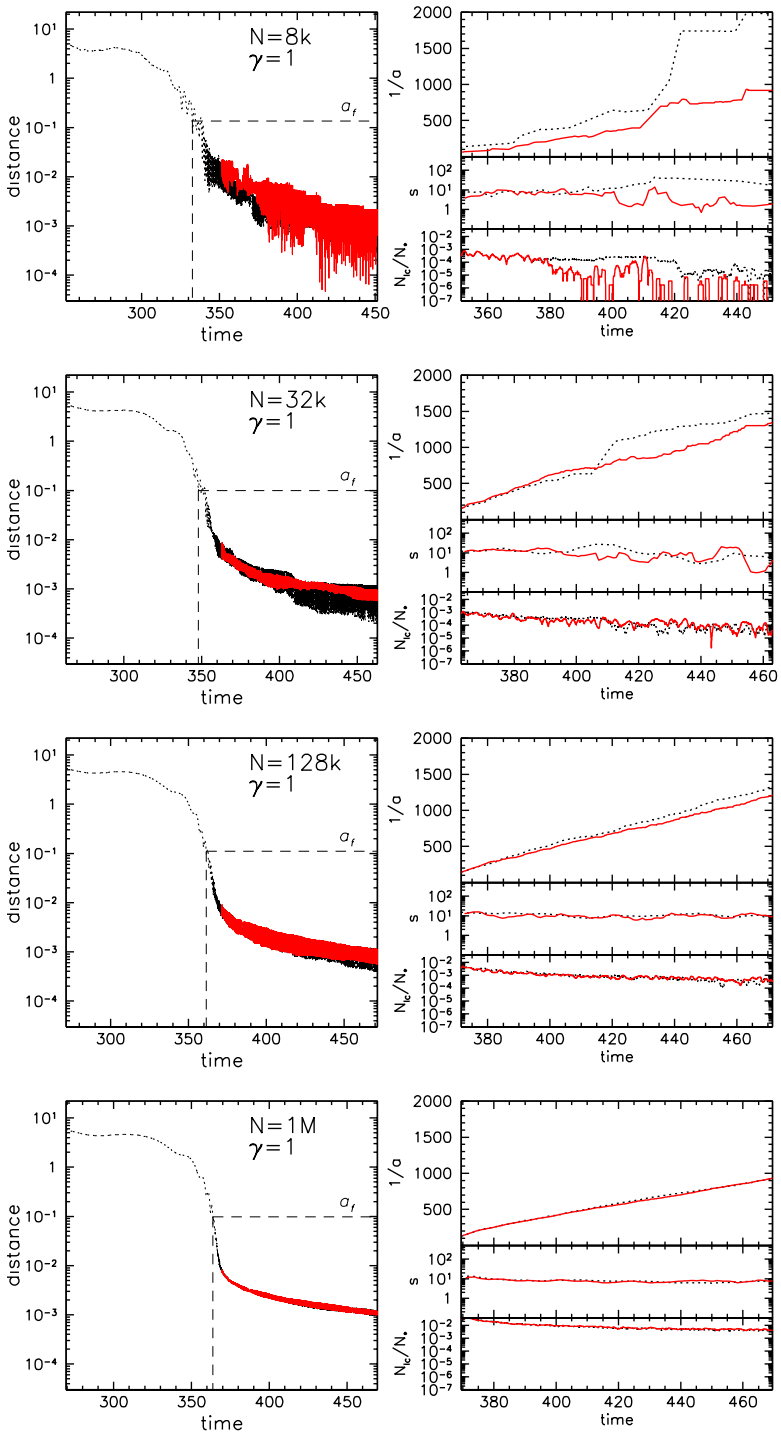

Fig. 5.5. Evolution of the binary separation (left-hand panels) and of the inverse semimajor axis $1/a$, hardening rate s and fraction of loss cone stars $N_{\rm lc}/N$ (from top to bottom, right-hand panels). The free-binary evolution is shown with a black dotted line, while the fixed-binary evolution is overplotted with a red solid line. We present the evolution for some of the available resolutions: from top to bottom, $N = 8$k, 32k, 128k, 1M. All panels refer to the set of simulations with $\gamma = 1$.

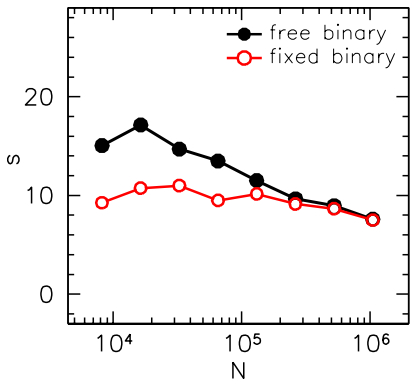

Fig. 5.6. Time-averaged binary hardening rate as a function of the number of simulated particles for the $\gamma = 1$ set in the case of free-binary evolution (black filled circles) and fixed-binary evolution (red empty circles). The two sets converge at the largest N values.

and compared simulations in which the binary is free to wander with simulations in which the BHB CoM is pinned down at the origin; however they both find that hardening quickly stops after the first loss cone depletion if the binary is not allowed to random walk. This discrepancy comes from the fact that (i) Chatterjee et al. (2003) and Quinlan and Hernquist (1997) used a different integration technique with respect to our paper, and (ii) they simulated the BHB evolution in spherical systems, where triaxial loss cone refilling is inhibited; this mechanism is indeed expected to be the main driver of the BHB hardening in high-resolution runs.

We conclude that Brownian motion has an appreciable influence on the BHB evolution only at small particle numbers, and it can be safely neglected in free-binary simulations for $N \gtrsim 1$M.

5.4 Summary

Massive BHBs are believed to form in the final stages of galaxy mergers. The formation of MBH pairs in gas-poor environments is driven by a combination of dynamical friction and close encounters with stars on low angular momentum orbits. However, both theoretical models and simulations show that evolution via the slingshot mechanism may be ineffective in bringing the binaries to coalescence if the loss cone region is not efficiently replenished. Recent simulations suggest that a departure from spherical symmetry in the merger remnant may lead to a change in the main mechanism driving loss cone refilling, from collisional two-body scatterings to collisionless torques in non-spherical systems. The reliability of these results may be questioned given the modest particle number achievable in current state-of-the-art direct-summation N-body simulations. In such cases, the inevitable wandering of the binary due to Brownian motion results in a larger population of stars on loss cone orbits.

In this work, we investigated the significance of Brownian motion of BHBs in merger simulations in the context of the final parsec problem. We performed three sets of direct-summation simulations corresponding to three different choices of the inner slope of the density profile ($\gamma = 0.5, 1.0$, and 1.5), and varying the particle number (from 8k to 1M particles).

We found that the effect of Brownian motion on the binary evolution is rather weak, and the Brownian motion amplitude $r_{\rm b}$ is in good agreement with the expected $r_{\rm b} \propto N^{-0.5}$ relation, while the binary hardening rate only exhibits a weaker dependence on N.

We also performed additional simulations in which the binary centre of mass was fixed at the centre of the density cusp (fixed-binary runs), and we found that the hardening rate of the BHB measured in the free-binary and fixed-binary case converge to similar values for $N \sim$1M. Moreover, the hardening rate measured in low-N models with a fixed-binary evolution is only slightly larger than the one measured in high-N free-binary runs. This suggests that the role of Brownian motion in merger simulations is comparable to the effect collisional loss cone repopulation for $10^4 \lesssim N \lesssim 10^6$. However, Brownian motion is not important for $N \gtrsim 1$ M even in free-binary simulations.

Our findings support the general belief that non-sphericity of merger remnants leads to efficient collisionless loss cone refilling (Preto et al., 2011; Khan et al., 2011; Gualandris and Merritt, 2012) and the final parsec problem disappears whenever this dominates over collisional effects.

6

The influence of SMBH binaries on galactic morphology

Based on:
Bortolas, E., Gualandris, A., Dotti, M., and Read, J.I.,
"The influence of Massive Black Hole Binaries on the Morphology of Merger Remnants", 2018, MNRAS 477, 2310

–

Several works have highlighted the key role of galaxy morphology in ensuring that SMBH binaries (BHBs) evolving in galactic nuclei efficiently coalesce via the emission of gravitational waves (GWs) on timescales shorter than the age of the Universe (Yu, 2002; Berczik et al., 2006; Khan et al., 2013; Vasiliev et al., 2014). In particular, recent studies claim that BHBs can efficiently harden via three-body stellar scatterings only if the host galaxy is triaxial, even if only modestly, as diffusion in angular momentum allows for efficient loss cone refilling even when two-body relaxation is negligible (Yu, 2002; Vasiliev et al., 2015; Gualandris et al., 2017). Departures from spherical symmetry are expected and are in fact observed in all merger remnants, and strongly suggest that BHBs are able to reach final coalescence within the age of the Universe in the vast majority of cases (e.g. Khan et al., 2011; Preto et al., 2011; Gualandris and Merritt, 2012; Khan et al., 2016). Purely axisymmetric remnants, however, seem unable to drive BHBs to coalescence (Vasiliev et al., 2015; Gualandris et al., 2017).

Even if all merger remnants show some degree of asphericity (e.g. de Zeeuw and Franx, 1991), the actual shape of the relic is known to depend on several factors, primarily the initial orbit and the properties of the progenitors. Linking the morphology and kinematics of present-day galaxies to their formation and merger histories is a long standing challenge, dating back to the very first astrophysical simulations (e.g. Holmberg, 1941; Toomre and Toomre, 1972; White, 1978, 1979). Galaxy mergers seem to play a major role in shaping present day ellipticals and in determining their size evolution (e.g. Cox et al., 2006; Naab et al., 2009; Oser et al., 2012; Hilz et al., 2012; Frigo and Balcells, 2016); a plethora of studies focus on the formation of ellipticals via mergers of spiral galaxies (Naab, 2013; Naab and

Ostriker, 2016, and references therein), but the possibility of producing ellipticals via collisions of pressure-supported systems has also been explored[1] (White, 1978, 1979; González-García and van Albada, 2005; Di Matteo et al., 2009; Hilz et al., 2012). An interesting result in such scenario is that the merging nuclei often experience a nearly head-on collision producing maximally triaxial or nearly prolate (bullet-like) remnants (González-García and van Albada, 2005; Di Matteo et al., 2009).

However, these findings may not apply if the colliding systems host an SMBH. Early studies on the stability of triaxial systems including a single central SMBH have shown that the massive body acts as a scattering centre, driving the system toward an oblate (disc-like) configuration (Gerhard and Binney, 1985; Merritt and Quinlan, 1998). More recently, Poon and Merritt (2001, 2002, 2004) demonstrated the existence of equilibrium configurations for maximally triaxial and nearly oblate systems hosting an SMBH, even when a large fraction of chaotic orbits are included; however nearly prolate shapes seem not to be sustainable in the presence of a central SMBH (Poon and Merritt, 2004).

The above work suggests that the morphology and kinematics of dry-merger remnants will be altered if at least one SMBH takes part in the galactic collision. This is important because the shape of the remnant has a strong influence on the hardening efficiency of any post-merger BHB (e.g. Gualandris et al., 2017).

In this Chapter, we explore the consequences of the presence of BHBs on the geometry of their host galaxies for the first time. We start our simulations from the merger of two spherical stellar systems, and we study the evolution of the remnant geometry when the BHB is not present and when it is included. We find that the central massive bodies strongly change the morphology of their hosts well beyond their sphere of influence, leading the system towards oblate (disky) shapes. The study of the effect of the environment on the BHB hardening is of utmost importance, since it has implications for the BHB coalescence rates expected for forthcoming GW observatories.

6.1 Methods

6.1.1 Initial Conditions

We consider the merger of two equal-mass galaxies, both set up with an isotropic, spherically symmetric, Dehnen density profile (Dehnen, 1993):

$$\rho(r) = \frac{(3-\gamma)\,M_{\rm g}}{4\pi}\frac{r_0}{r^{\gamma}(r+r_0)^{4-\gamma}}, \tag{6.1}$$

where $M_{\rm g}$ is the total mass of the galaxy, r_0 is the scale radius of the model and γ is its inner density slope. Each galaxy was sampled with $N = 512k$ equal mass

(1) It has long been known that present-day ellipticals cannot be formed from the mergers of present-day spirals (e.g. Ostriker, 1980; Cox et al., 2006). Indeed, many ellipticals require dissipational mergers (i.e. mergers that bring in fresh gas and promote star formation) to produce their observed kinematics (e.g Dubinski, 1998; Hilz et al., 2013). The most massive ellipticals, however, appear to only grow through dissipationless mergers (e.g Dubinski, 1998; Hilz et al., 2013) and so our focus in this Chapter is on gas-free 'dry' mergers.

Tab. 6.1. Identifiers of the runs. Columns refer to the initial concentration of the merging galaxies ($\gamma = 0.5, 1, 1.5$, respectively Low, Medium and High Concentration); rows refer to the initial orbital eccentricity ($e = 0.5, 0.7, 0.9$; labels 5, 7, 9 respectively) and to whether the merger remnant hosts no SMBHs (no additional label), only one SMBH (run labelled with 'o') or a BHB (runs labelled with 'b').

	$\gamma = 0.5$ (LC)	$\gamma = 1$ (MC)	$\gamma = 1.5$ (HC)
$e = 0.5$, no SMBHs	LC5	MC5	HC5
$e = 0.7$, no SMBHs	LC7	MC7	HC7
$e = 0.9$, no SMBHs	LC9	MC9	HC9
$e = 0.5$, BHB	LC5b	MC5b	HC5b
$e = 0.7$, BHB	LC7b	MC7b	HC7b
$e = 0.9$, BHB	LC9b	MC9b	HC9b
$e = 0.7$, one SMBH	-	MC7o	-

Tab. 6.2. Scaling of the models depending on the inner density slope of the primordial galaxies (γ). $M_\bullet$ is the SMBH mass at the centre of the Dehnen model, [M] is the unit mass, [L] is the length unit, [T] is the time unit and [V] is the velocity unit.

	$M_\bullet$, [M] ($M_\odot$)	[L] (pc)	[T] (Myr)	[V] (km/s)
$\gamma = 0.5$	4×10^6, 8×10^8	30	8.67×10^{-2}	339
$\gamma = 1$	4×10^6, 8×10^8	50	1.86×10^{-1}	262
$\gamma = 1.5$	4×10^6, 8×10^8	120	6.93×10^{-1}	169
$\gamma = 0.5$	10^8, 2×10^{10}	190	2.76×10^{-1}	673
$\gamma = 1$	10^8, 2×10^{10}	320	6.04×10^{-1}	518
$\gamma = 1.5$	10^8, 2×10^{10}	720	2.03	346

particles (we discuss our choice of force softening in section 6.1.3). The merging galaxies were initially on a bound Keplerian orbit with semimajor axis $a_i = 15r_0$ and separated by $\Delta r = 20r_0$.

We ran different simulations changing the density slope of the merging galaxies and their initial orbital eccentricity. Specifically, we varied the density profile by setting $\gamma = 0.5$ (low concentration systems, LC), $\gamma = 1$ (medium concentration systems, MC) and $\gamma = 1.5$ (high concentration systems, HC); we set the orbital eccentricity as $e = 0.5$ (runs labelled wit '5'), $e = 0.7$ (runs labelled wit '7') and $e = 0.9$ (runs labelled with '9') for a total of nine different configurations. We ran all the simulations both omitting and including (runs labelled with 'b') a SMBH in the centre of each colliding system; this last case leads to the formation of a BHB in the centre of the remnant. When present, the mass of the SMBH is $M_\bullet = 0.005 M_{\rm g}$. Table 6.1 lists the identifiers of each run in the suite of simulations.

We add a further run (MC7o) including a SMBH in only one of the two colliding systems; the properties of the merging galaxies in this last simulation are the same as in MC7, MC7b, while the SMBH mass is $M_\bullet = 0.01 M_{\rm g}$.

6.1.2 N-body Units

Non-dimensional units are used throughout the Chapter: the Newtonian gravitational constant G is set equal to 1, and we further set $r_0 = M_{\rm tot} = 1$, where $M_{\rm tot}$ is the total stellar mass in each simulation (i.e. since we have equal mass mergers,

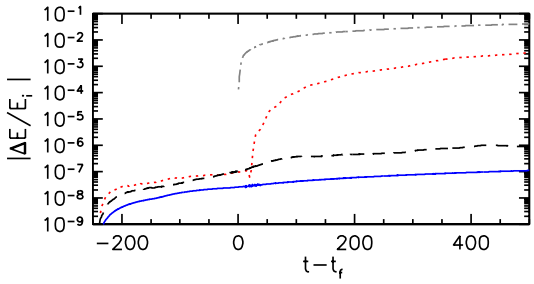

Fig. 6.1. The plot shows the time evolution of the relative energy error $|\Delta E/E|$ as defined in equation (6.2) for the runs with $\gamma = 1$ and $e = 0.7$. In particular, we show the energy error for runs with no SMBHs (solid blue line, run MC7), with only one SMBH (dashed black line, run MC7o), and with a BHB (dotted red line, run MC7b). For comparison, we also show the BHB binding energy in run MC7b with a grey dash-dotted line; such quantity is always at least one order of magnitude larger than the relative global energy error in run MC7b.

$M_{\rm tot} = 2M_{\rm g}$). It is possible to rescale the systems to real galaxies when the SMBHs are present by using the relation between the SMBH influence radius ($r_{\rm infl}$, i.e. the radius including $2M_\bullet$ in stars) and the SMBH mass ($M_\bullet$) using the relation presented in Merritt et al. (2009): $r_{\rm infl} = 30\,{\rm pc} \times (M_\bullet/10^8 M_\odot)^{0.56}$. Table 6.2 lists the scaling units; $r_{\rm infl}$ is computed analytically as the radius enclosing a stellar mass equal to $2M_\bullet$ in the Dehnen profile considered. The same scaling is assumed for equivalent runs without SMBHs.

6.1.3 Simulations

The simulations are performed adopting the direct summation N-body code `HiGPUs` (Capuzzo-Dolcetta et al., 2013), designed to run on GPU accelerators. `HiGPUs` integrates the evolution of the system via the sixth-order Hermite scheme and implements a hierarchy of block timesteps: in particular, the individual timesteps are computed via a combination of the sixth and fourth order Aarseth criterion (Aarseth, 2003; Nitadori and Makino, 2008); we set the respective accuracy parameters to $\eta_{\rm sixth} = 0.45$, $\eta_{\rm fourth} = 0.01$ (for details, see Capuzzo-Dolcetta et al., 2013). The minimum and maximum possible values in the hierarchy are chosen as $\Delta t_{\rm min} = 2^{-29} \approx 1.86 \times 10^{-9}$ and $\Delta t_{\rm max} = 2^{-6} = 0.015625$. We set the softening parameter to $\varepsilon = 10^{-4}$; such small softening avoids the formation of stellar binaries; at the same time it allows to follow the evolution of the BHB (when present) limiting errors in the energy conservation. Note that such a small softening is required to correctly model the interaction between the BHB and its surrounding stars. It will also slightly reduce the relaxation time of the surrounding stellar distribution, which is a numerical error. However, this error will be small since the relaxation time (see section 6.2.1) depends linearly on the particle number, N, and only logarithmically on the force softening, ε (Dehnen and Read, 2011).

The evolution of the relative energy error of the whole system, i.e.

$$\left|\frac{\Delta E}{E_{\rm i}}\right| = \left|\frac{E - E_{\rm i}}{E_{\rm i}}\right| \tag{6.2}$$

for runs with $\gamma = 1$ and $e = 0.7$ is displayed in Figure 6.1; here $E_{\rm i}$ is the initial

Tab. 6.3. Relaxation timescales in N-body units at different radii. The first column shows the name of the run, while the next columns list the relaxation timescales at the radius enclosing a different fraction $m_{\rm encl}$ of the total stellar mass, i.e. (from left to right) the 0.5%, 10%, 25%, 50%, 75%; the relaxation timescales are computed at $t \approx t_h$ for runs including the BHB and at the corresponding time for runs without SMBHs.

Run	$m_{\rm encl} = 0.5\%$	$m_{\rm encl} = 10\%$	$m_{\rm encl} = 25\%$	$m_{\rm encl} = 50\%$	$m_{\rm encl} = 75\%$
LC7	600	6,900	28,500	260,000	2.5M
LC7b	1,900	7,500	29,000	280,000	2.3M
MC7	160	4,300	19,000	220,000	2.0M
MC7b	850	4,500	20,500	191,000	2.0M
HC7	50	2,000	11,000	143,000	2.3M
HC7b	370	2,200	13,000	142,000	2.1M

energy of the whole system, while E is the same quantity evaluated at a given time t. The figure shows that energy is well conserved for the entire duration of the simulation when the BHB is not included, as the relative energy error is always below 10^{-6}; this is true for all simulations without a BHB. When a BHB is present, however, the energy error suffers a sudden increase around the time of binary formation ($t \approx t_f$). This is most likely due to the large number of encounters experienced by the binary at this time. Similar energy errors are obtained in the other simulations, and the energy error reaches values of a few $\times 10^{-3}$ at most.

Such energy errors do not invalidate our results regarding the morphology of the remnant since they can be attributed to energetic slingshot ejections of stars which then leave the system. However, they may affect the evolution of the binary parameters. Fig. 6.1 also shows the BHB binding energy in run MC7b; here the binary binding energy is at least an order of magnitude larger than the global energy error at any given time, and this holds for all simulations with a BHB.

6.2 Theory

6.2.1 Two-body relaxation

Two-body relaxation operates on a timescale t_r (Eq. 1.11) that strongly correlates with the number of particles in the system (Eq. 1.12), and it is known to exceed the Hubble time in almost all sufficiently luminous galaxies. However the limited number of particles ($N = 512k$) in our simulations results in a significantly smaller relaxation time. In table 6.3 we list the relaxation timescale of systems with $e = 0.7$, both with and without the BHB, at different shells of enclosed mass when $a_{\rm b} \approx a_h$; the relaxation time is computed from simulation snapshots via Eq. 1.11, estimating the Coulombian logarithm as $\ln \Lambda = \ln(M_{\rm b}/m_*)$ within the BHB influence radius (if the BHB is present) and as $\ln \Lambda = \ln(r_{80}/\varepsilon)$ otherwise; r_{80} is the radius enclosing 80% of the stellar mass.

In our runs, the relaxation time is significantly longer than the simulation time at radii containing a fraction of the total stellar mass of the order of 50% or above, but this no longer holds at smaller radii, in particular when the BHB is not present and

the progenitor galaxies are more concentrated[(2)]. The computation of t_r will enable us to disentangle the effects of spurious two-body relaxation from the consequences of the merger and BHB evolution.

6.2.2 Computation of triaxiality

The shape of the galactic merger remnant can be determined by computing the ellipsoid that best approximates the stellar distribution at a given distance. If $a > b > c$ are the axes of this ellipsoid, a deviation from perfect sphericity can be evaluated quantitatively as the departure of b/a, c/a from unity. When a single SMBH or a BHB is present, we evaluated the axes of the ellipsoid using all the stars enclosed within a sphere of radius r centered on the SMBH or on the BHB centre of mass; if the BHB is not present, the centre of the system is instead assumed to be the centre of mass of the 75% innermost particles; we verified that the different evaluations of the spheroid's centre do not affect the computation of the axis ratios. The procedure we adopt for the evaluation of the remnant shape is the same as in Katz (1991) and Antonini et al. (2009).

The first order axis ratios are determined from the eigenvalues (ξ, η, θ) of the inertia tensor I: $\xi = \sqrt{I_{11}/I_{\max}}$, $\eta = \sqrt{I_{22}/I_{\max}}$, $\theta = \sqrt{I_{33}/I_{\max}}$, where $I_{\max} = \max(I_{11}, I_{22}, I_{33})$. In order to get a better accuracy, we iterate the procedure and we computed new axis ratios by considering only particles enclosed in an ellipsoidal volume with the previously computed (ξ, η, θ), i.e. all particles i located in $(x_{\rm i}, y_{\rm i}, z_{\rm i},)$ satisfying

$$q_{\rm i}^2 = \left(\frac{x_{\rm i}}{\xi}\right)^2 + \left(\frac{y_{\rm i}}{\eta}\right)^2 + \left(\frac{z_{\rm i}}{\theta}\right)^2 < r^2. \tag{6.3}$$

The procedure is iterated until an accuracy of 10^{-5} is achieved in the computation of the axis ratios; the ellipsoid is free to rotate about its centre at each iteration. Finally, we define the ellipsoidal axes $a > b > c$ such that $(1, b/a, c/a)$ are equal to (ξ, η, θ) in the right order. It is then possible to compute the triaxiality parameter T of the system within r as:

$$T = \frac{a^2 - b^2}{a^2 - c^2}; \tag{6.4}$$

T is a quantity used to describe the deviation of a system from perfect sphericity and it can vary in the range $[0, 1]$:

1. if $0 \leq T < 0.5$ the spheroid is oblate;
2. if $T = 0.5$ the system is said to have maximum triaxiality;
3. if $0.5 < T \leq 1$ the spheroid is prolate.

(2) The relaxation time depends primarily on the density and the velocity dispersion of the system. Within the half mass radius, the density at a given fraction of enclosed mass significantly increases with γ, while σ^3 exhibits a weaker growth; as a result, at small scales, the relaxation time becomes shorter if the galaxy concentration is enhanced. However, at radii enclosing more than half of the total mass, the density increase with γ becomes milder, and can be hindered by the comparable growth of σ^3. For this, at large scales, the relaxation time may be found to grow with increasing γ (Table 6.3).

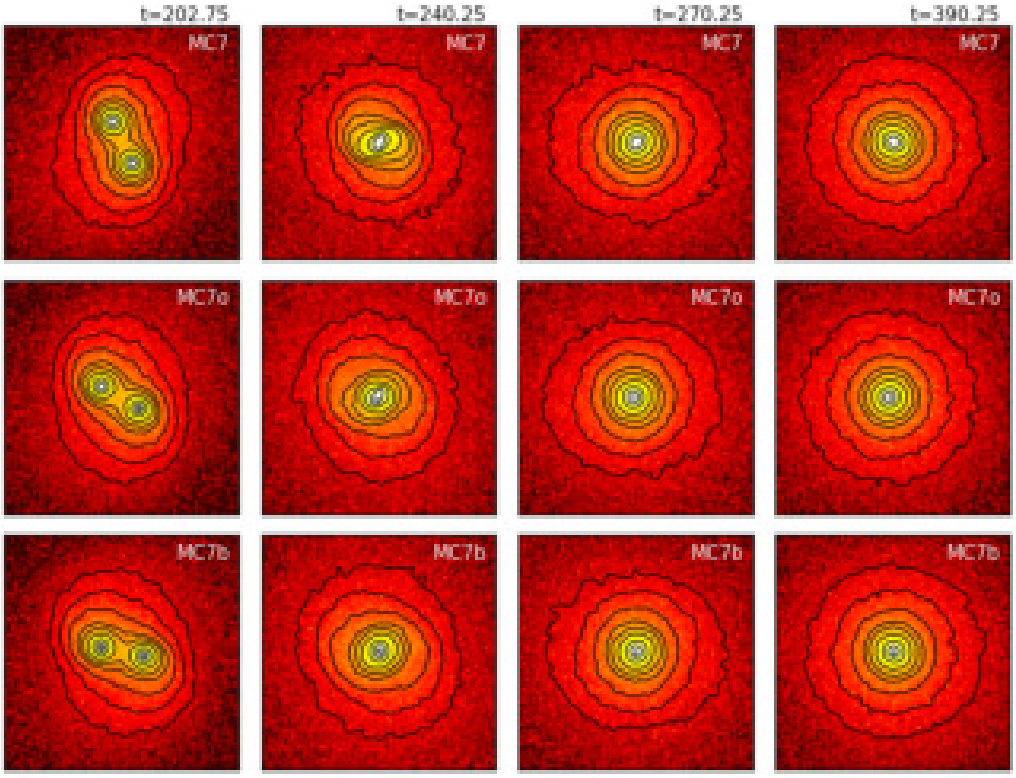

Fig. 6.2. The snapshots show the galaxy merger evolution in three different runs: MC7 (no SMBHs), MC7o (one SMBH) and MC7b (two SMBHs); small black crosses mark the position of the SMBHs and the colour code refers to the projected mass density, ranging from ≈ 500 to $\approx 2.5 \times 10^5$ particles per squared N-body unit. The $N-$body time associated with each snapshot is shown at the top of the image; each box is 13 N-body units wide.

In the description of the results, we will make use of both the axis ratios (b/a, c/a) and the triaxiality parameter T to characterize the shape of the remnant. We stress that the shortest axis of the spheroid typically lies perpendicularly with respect to the merger plane (when a BHB is present, the merger plane is always parallel to the BHB orbital plane).

6.3 Results

6.3.1 BHB evolution

Figure 6.2 shows the evolution of the galactic collision in the merger plane for runs MC7, MC7o and MC7b, i.e. three simulations with the same merger orbit and galaxy density profile, but including respectively zero, one and two SMBHs.

The trajectories of the two SMBHs in the plane of the merger for different values of the merger eccentricity are instead shown in Figure 6.3; we stress that when the SMBHs are not included, the orbital evolution of the centres of density are not significantly different to the analogous SMBH paths in Figure 6.3. The significant scales (a_f, a_h) in the BHB evolution and their associated times are listed in table 6.4: the merger is faster if the orbital eccentricity is higher, as galaxies experience

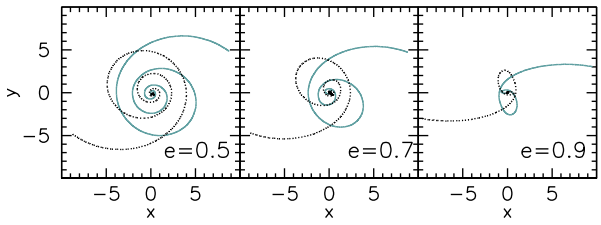

Fig. 6.3. Trajectories of the two SMBHs in the merger plane for runs MC5b, MC7b, MC9b, i.e. with $e = 0.5, 0.7, 0.9$, from left to right. We only show the orbits for simulations with $\gamma = 1$, as the large-scale SMBH paths only weakly depend on the density of the progenitor galaxies. In this Figure and in the following, distances are in scalable $N-$body units.

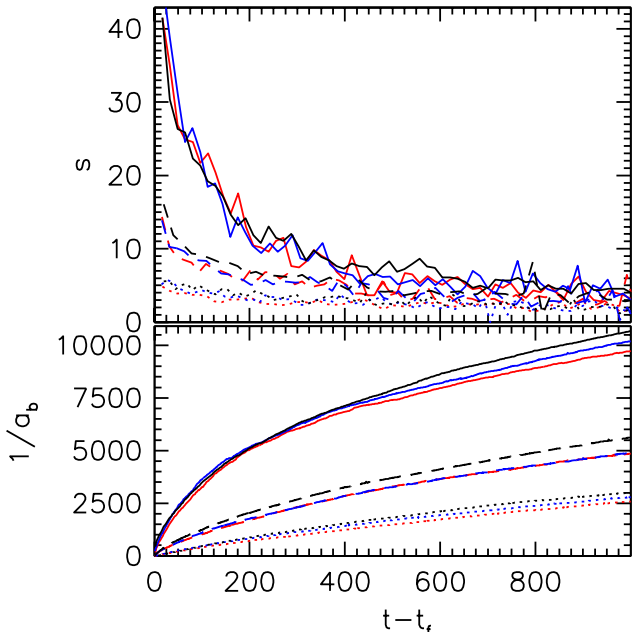

Fig. 6.4. Time evolution of the BHB hardening rate (s, top panel) and the inverse semi-major axis of the binary ($a_{\rm b}^{-1}$, bottom panel). Dotted lines: $\gamma = 0.5$; dashed lines: $\gamma = 1$; solid lines: $\gamma = 1.5$. Red lines: $e = 0.5$; blue lines: $e = 0.7$; black lines: $e = 0.9$. Time on the horizontal axis is given starting from t_f.

Tab. 6.4. Characteristic scales of the binary evolution in the simulations. First column: run identifier; second column: value of a_f; third column: time at which the BHB reaches a_f; fourth column: value of a_h; fifth column: time at which the BHB reaches a_h. See the text for further details.

Run	a_f	t_f	a_h	t_h
LC5b	0.165	342	0.0100	365
LC7b	0.152	238	0.0101	259
LC9b	0.137	127	0.00841	156
MC5b	0.097	368	0.00709	375
MC7b	0.096	240	0.00730	246
MC9b	0.083	124	0.00673	131
HC5b	0.051	408	0.00429	410
HC7b	0.045	254	0.00436	256
HC9b	0.038	118	0.00419	119

a closer pericentre passage. Note that we defined $t_f \equiv t(a_f)$ and $t_h \equiv t(a-h)$.

Figure 6.4 displays the temporal evolution of the BHB hardening rate and the inverse of the semimajor axis. The BHB hardening rate does not show any clear relation with the initial orbital eccentricity (Figure 6.4, top panel) but the binary appears to shrink slightly faster when the merger eccentricity is higher (Figure 6.4, bottom panel).

The hardening rate strongly depends on the density slope γ of the progenitors: if the system is more compact, more stars are initially available for three-body interactions with the BHB in the inner region of the remnant and the BHB hardening is more efficient, as already discussed in Sesana and Khan (2015) and Vasiliev et al. (2015). In addition, we note that the BHB hardening rate decreases in time, especially when γ is high; in particular, s in all our simulations tends to the same value ($s \approx 3-4$) towards the end of the runs. The decline in the BHB hardening rate has also been observed in a series of recent papers (e.g. Vasiliev et al. 2015; Sesana and Khan 2015; Gualandris et al. 2017); according to Vasiliev et al. (2015) it is due to the fact that low-energy orbits are more populated in steeper models, thus more stars are initially found in the BHB loss cone; once most of the low-energy orbits have been depleted, less stars on higher energy orbits are available to interact with the BHB. We mention that a slowing down of the hardening rate might also be caused by a loss of triaxiality in the system, as suggested in Vasiliev et al. (2015).

Finally, we note that the trend in the BHB hardening rate we find here is comparable to what found in previous similar studies that refute the final parsec problem (e.g. Khan et al., 2011; Preto et al., 2011; Gualandris and Merritt, 2012), thus our results confirm that BHBs should be able to coalesce in less than a Hubble time in most galaxies.

6.3.2 Triaxiality of the system

In this section we describe the morphology of the merger relic and its dependence on (i) the presence of the BHB and (ii) the initial conditions of the merger. Figure 6.5 shows the temporal evolution of the axis ratios and triaxiality parameter T, while Figure 6.6 shows how the same quantities vary as a function of the enclosed stellar

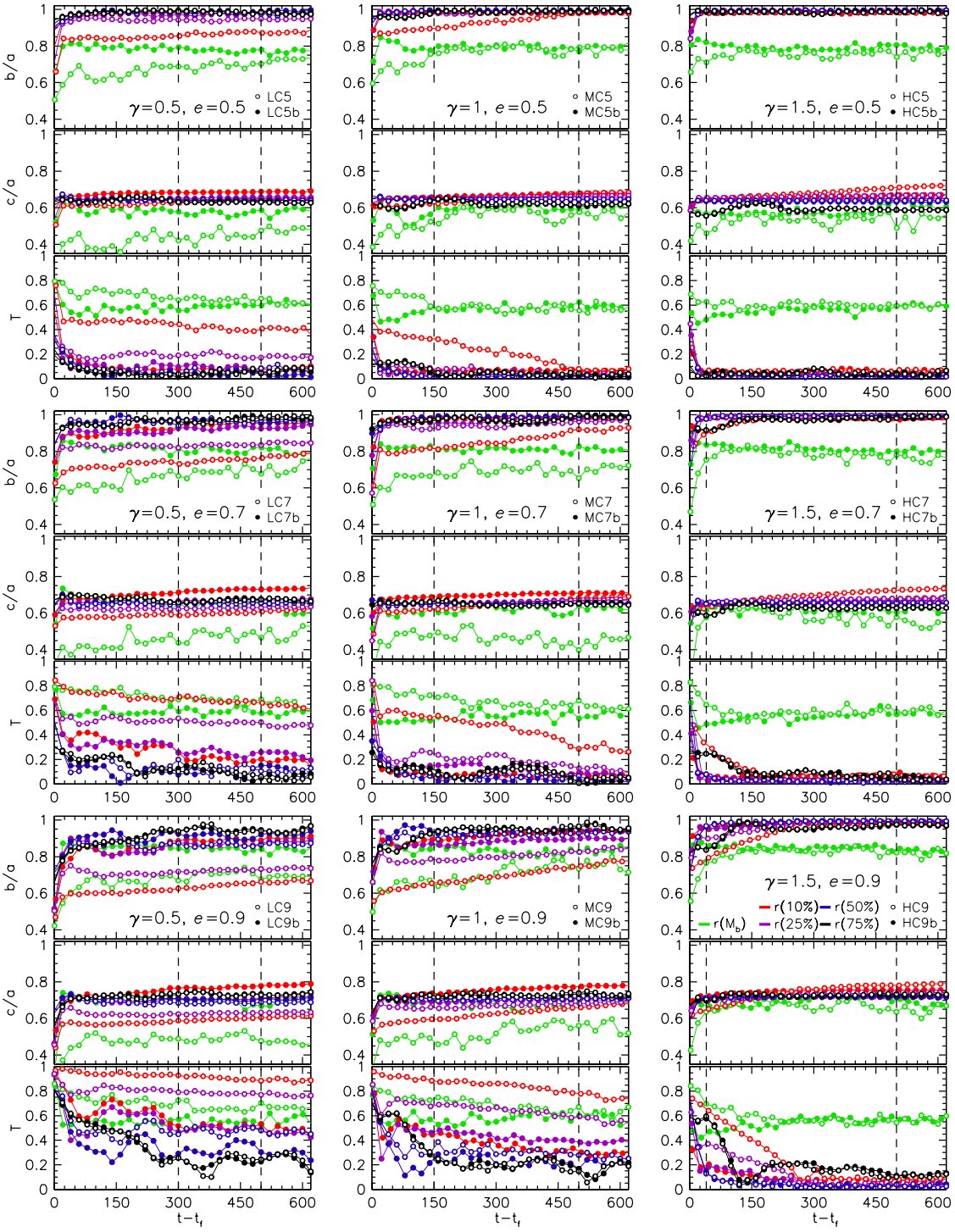

Fig. 6.5. (Caption on the following page.)

Fig. 6.5. Triaxiality parameter T and axis ratios as a function of time for models with $e = 0.5$ (top row), $e = 0.7$ (central row) and $e = 0.9$ (bottom row); simulations with initial galaxies having $\gamma = 0.5, 1, 1.5$ are shown respectively on the left, central and right-hand column. Each plot consists of three panels showing the temporal evolution of (from top to bottom) b/a, c/a and T; these quantities have been averaged over small time intervals to reduce noise; the time evolution is shown starting from t_f, i.e. when the galaxy merger is completed. Different lines indicate the parameters computed using particles within a sphere enclosing a fraction equal to the 0.5% (green), 10% (red), 25% (violet), 50% (blue) and 75% (black) of the total stellar mass; simulations including the BHB are shown with filled points, while simulations without SMBHs are shown in empty points. In all plots, the vertical dashed line on the left marks the reference time at which the axis ratios and triaxiality of the structure enclosing the 25% of the stellar mass is evaluated; the line on the right shows the reference time for evaluating the morphology of the system at larger scales. Note that the triaxiality increases for increasing orbital eccentricity (top to bottom) and for decreasing concentration (right to left).

mass; the system properties are shown for remnants both with and without a BHB.

Runs with the BHB: time evolution

In all simulations with the BHB, the merger remnant stays nearly maximally triaxial at the binary influence radius. At larger scales, the system turns into an oblate spheroid ($0.9 \lesssim b/a \lesssim 1$) immediately after the merger is complete in most of the realizations. The evolution towards oblateness generally occurs in less than ~ 20 time units (i.e. on a timescale of the order of the dynamical time), and cannot be a product of two-body relaxation. All the remnants in this suite of simulations are flattened, with the shorter axis ratio c/a in the range $0.6 - 0.7$.

The shortest axis c/a is typically aligned with the spin direction of the merger remnant, which always coincides with the spin direction of the initial galaxy merger, i.e. the positive z axis. The BHB co-rotates with the galaxy (i.e. its spin is also aligned with the positive z axis) in all but two runs: in run LC9b the BHB is counter-rotating, as its spin points towards the negative z axis; the same happens at $t \approx t_f$ in run MC9b. However, in the latter run the angle between the positive z axis and the BHB spin progressively changes from 180 degrees to about 100 degrees at $t = t_f + 1,500$. These results are not surprising: simulations by Wang et al. (2014) already found that a BHB may form with angular momentum misaligned to the spin of the host system; in addition, Gualandris et al. (2012a) showed that BHBs whose angular momentum is initially misaligned to that of the stellar environment generally tend to realign, and this is probably what is happening in run MC9b.

The very large-scale structure of the system, i.e. the region including 75% of the total mass, exhibits some oscillations over time, except for run HC5b. In this peripheral region the dynamical time over which the system finds a stable configuration is generally long due to the low stellar density, that results in a longer dynamical time: in particular, b/a increases from about $0.8 - 0.9$ to unity in almost all runs, and by the end of the simulation the large scale system tends to be an oblate spheroid. Again, this evolution cannot be attributed to two-body relaxation

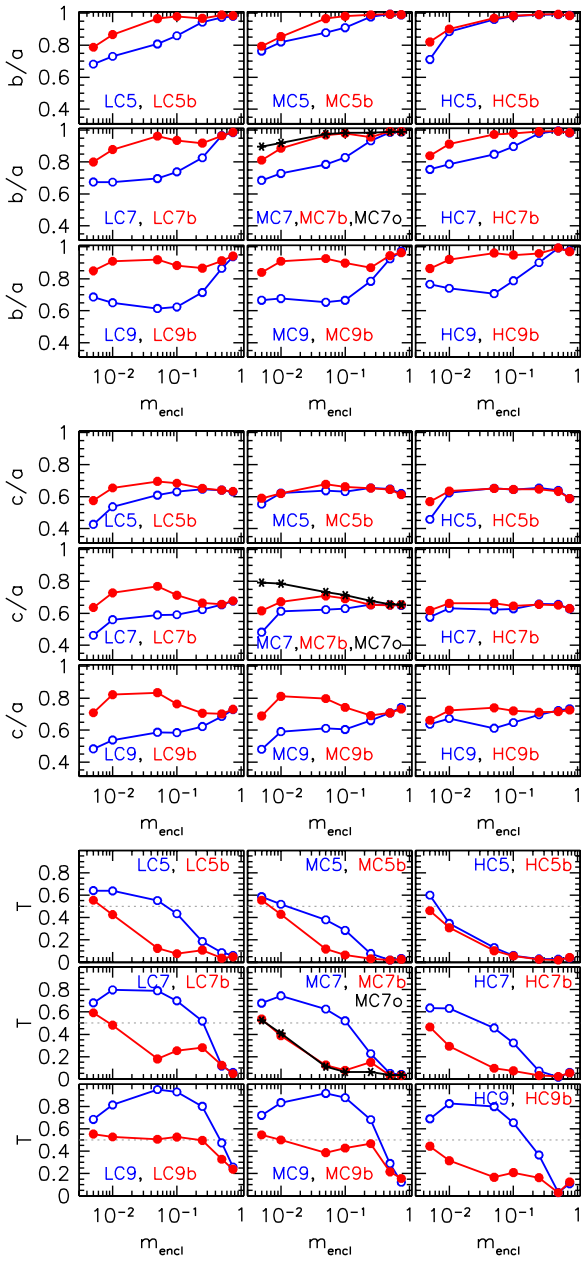

Fig. 6.6. Triaxiality parameter and axis ratios as a function of the enclosed mass $m_{\rm encl}$; from top to bottom, the plots show b/a, c/a and T for runs including the BHB (filled red points), omitting it (blank blue points) and for the run with only one SMBH (run MC7o, black asterisks in the central panels). Each panel is labelled with the name of the runs shown: from left to right, panels show runs with increasing concentration ($\gamma = 0.5, 1$ and 1.5), while from top to bottom, panels show runs with increasing eccentricity ($e = 0.5, 0, 7$ and 0.9) as in Fig. 6.5.

but rather to the merger itself, as the relaxation timescale in the peripheral regions of the remnant is $\sim 2 \times 10^6$ time units (see Table 6.3), much longer than the simulated time.

The eccentricity seems to play a major role in determining the temporal evolution of the system right after the merger: on the one hand, if the initial eccentricity is small ($e \approx 0.5$) the system does not show any appreciable oscillations in the axis ratios and it reaches its equilibrium state very quickly. On the other hand, if the eccentricity is high ($e = 0.9$) the axis ratios oscillate in time, and this is particularly true if one looks at the mid- or large-scale structure in systems with initial $\gamma = 0.5, 1$; the oscillations are related to the fact that the galactic collision occurs nearly head-on. Since the process is particularly violent, the whole system takes some time to settle down to a stable configuration; in runs LC7b, LC9b and MC9b the large-scale oscillations are still present more than 1,000 time units after the merger, even if they manifest some damping over time. The large-scale oscillations are more prominent if the system is shallower.

The persistence of the system shape also depends on the steepness of the progenitor galaxies. If $\gamma = 1.5$, the remnant is really compact and its initial shape is hardly modified, even by very eccentric mergers. As a consequence, highly concentrated models reach their final equilibrium in a short time and immediately turn into oblate spheroids, with $b/a \approx 1$. When the progenitors have shallower profiles, they are more affected by the merger and, if $e > 0.5$, the remnant displays some degree of triaxiality within 25% of the enclosed stellar mass.

In summary, highly concentrated ($\gamma = 1.5$) galaxies hosting SMBHs and colliding on mildly eccentric orbits ($e = 0.5$) lead to stable values for the remnant axis ratios and the resulting system is oblate, with $b/a \approx 1$; shallow models ($\gamma = 0.5$) on very eccentric orbits ($e = 0.9$) generate mildly oblate or triaxial remnants, and exhibit strong oscillations in the axis ratios over a long timescale. Simulations with $e = 0.7$ and $\gamma = 1$ show a transition behaviour between the two extremes discussed above. We stress that none of the remnants hosting a BHB shows any degree of prolateness outside the BHB sphere of influence after the merger process is completed.

Runs without the BHB: time evolution

At very large scales (i.e. beyond the half-mass radius) the models are unaffected by the SMBHs presence, and the behaviour of the axis ratios and triaxiality parameter T in the peripheral regions is almost the same for runs with and without SMBHs; in particular, the mid- and large-scale oscillations in the shape of the system when $e \sim 0.9$ and $\gamma \lesssim 1$ are a common feature of both configurations.

At smaller scales (enclosing 1% to 25% of the total stellar mass) the differences between runs with and without a BHB start to be evident: if the SMBHs are not included, the systems are initially nearly prolate or maximally triaxial, at least within the $\sim 10\%$ of the enclosed stellar mass if the merger eccentricity is higher than 0.5. The shortest axis of the system is generally aligned with the normal to the merger plane even in these runs without a BHB.

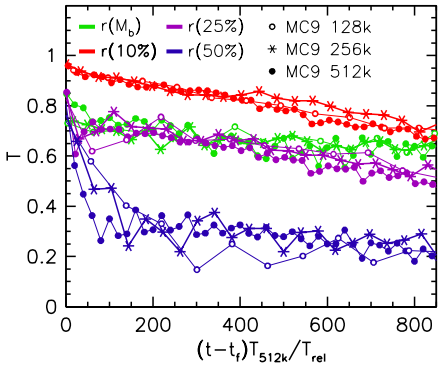

Fig. 6.7. Temporal evolution of the triaxiality parameter T in the run MC9. Different lines refer to different values of the enclosed mass (the colour code is the same as in Figure 6.5) using a different number of particles N for the simulation: $N = 128k$ (empty circles), $N = 256k$ (asterisks) and $N = 512k$ (filled circles). The triaxiality parameter is plotted against $(t - t_f) \cdot T_{512k}/t_r$, where t_r is the local relaxation timescale for each different model computed at $t \approx t_f$; T_{512k} is the local relaxation time for the run with $N = 512k$ particles. The factor T_{512k}/t_r ensures that the shape evolution of different merger remnants is evaluated along the same fraction of t_r. Lines with the same colour (i.e. evaluating T on the same spatial scale) well overlap regardless of N; this clearly suggests that relaxation is the main driver beyond shape evolution in runs without BHB.

Spurious relaxation effects

All the runs without BHB exhibit a slow but steady growth of the axis ratios (especially b/a) towards unity: within the $\sim 25\%$ of the enclosed mass, all the remnants generally evolve towards a more oblate shape, perhaps even towards sphericity. This is due to spurious relaxation rather than to the merger process, as the shape evolution is faster for more concentrated models, i.e. when the relaxation time is shorter (Table 6.3). To verify this, we re-ran simulation MC9 including a smaller number of particles, i.e. $N = 128k$ and $256k$, and we compared the results with the reference simulation with $N = 512k$. In this comparison, we find that models with lower N systematically evolve faster towards oblateness (i.e. lower T) at *all scales*, indicating that relaxation is the driver behind shape evolution. In order to confirm this, in Figure 6.7 we plot the evolution of the triaxiality parameter T for different N, as a function of the time-related quantity

$$\tau = (t - t_f)\frac{T_{512k}}{t_r}; \tag{6.5}$$

here t_r is the local relaxation timescale of each model (eq. 1.11) evaluated at $t \approx t_f$, while T_{512k} is the local relaxation time for the run with $N = 512k$ particles. The quantity τ coincides with $t - t_f$ in the model with $512k$ particles, while it represents $t - t_f$ extended by a factor proportional to t_r^{-1} in the other runs. In this way, Figure 6.7 shows the shape evolution, for each given spatial scale, across a fixed interval of the relaxation time. In the plot, lines describing the behaviour of T for a given fraction of enclosed mass (i.e., lines with the same colour) well overlap irrespective of N; this is strong evidence that two-body relaxation is the main driver of the shape evolution of models without BHB.

Obviously, relaxation effects are at play even in runs with the BHB. We checked

this aspect by re-running simulation MC9b with lower N values. The impact of relaxation is comparable to what we find in the run without any SMBH (i.e., the system evolves faster towards unitary axis ratios if N is lower) at scales enclosing more than $\approx 5\%$ of the total stellar mass. However, BHB hosts with high N tend to have axis ratios closer to unity within $\sim 2\%$ of enclosed stellar mass, compared to remnants with lower N; i.e., the trend with N is inverted at small scales, compared to what is found at larger separations. This might mean that real BHB hosts – typically with $N \gg 512k$ – display slightly larger axis ratios and lower T in their inner regions, compared to what we find in our reference runs with $N = 512k$. Thus the value of T within a few per cent of the total stellar mass in our runs including the BHB might be slightly overestimated, compared to real galaxies(3).

Given all these facts, and since real galaxies are generally unaffected by two-body relaxation, the actual shape of the merger remnants in our simulations has to be evaluated after the merger is completed, but before two-body relaxation has played a significant role in remodelling the systems. Isolating the action of two-body relaxation from the effects of the merger is not a trivial task; in fact, on the one hand one needs to evaluate the shape of the remnants early enough to avoid spurious relaxation effects; on the other hand, the system settles on a stable configuration after the merger over a timescale of the order of the dynamical time. Such time interval in the outer regions of the remnants can be very long, even larger than the nuclear relaxation timescale in the same system. For this, by considering the relaxation time as a function of radius and from Figure 6.5, we find it best to evaluate the shape of the model within 25% of enclosed mass at a time equal to: (i) $t_f + 300$ if $\gamma = 0.5$, (ii) $t_f + 150$ if $\gamma = 1$, (iii) $t_f + 40$ if $\gamma = 1.5$. The shape of the system at the half-mass radius and beyond is always evaluated at time $t_f + 500$. Such times are used for estimating both the remnant geometry and the kinematical properties of the merger remnants, i.e. the quantities shown in Figures 6.6, 6.8-6.11. The reference times are marked with vertical dashed lines in Figure 6.5.

Effect of the BHB

The most striking result of our simulation is particularly evident from Figure 6.6: remnants hosting SMBHs always keep a lower value of T at all scales compared to remnants resulting from equivalent runs without the BHB. When the massive bodies are present, the system geometry is more oblate at all scales and possibly closer to spherical. In particular b/a can be as low as 0.6 in runs without SMBHs, while it is always higher than 0.8 (and even 0.9 outside 1% of the enclosed mass) if the BHB is present. In addition, when the SMBHs are included, the system is generally less flattened (i.e. c/a is higher). The differences between remnants with and without SMBHs are extremely evident when the initial galaxies are less concentrated and the merger is more radial, while dense models colliding on more circular orbits (as HC5 and HC5b) do not show any clear difference in shape. A

(3) The described effect is likely rather small: the run with $N = 512k$ has axis ratios larger by $\lesssim 0.075$ compared to the axis ratios computed with $N = 256k$ even at the smallest scale we consider (enclosing 0.5% of the stellar mass), where the low-N effects are most extreme; this translates in a triaxiality parameter that is smaller in our reference run by 0.05 at most, compared to the run using $N = 256k$.

qualitative inspection of the remnants shape in time suggests that all our systems rotate; in particular, if one excludes run HC5, runs without a BHB host a rotating bar-like structure aligned to the merger plane, that may extend as far as the half-mass radius; the structure has an increasing extent and prolateness in remnants resulting from low-angular-momentum collisions of shallow systems. Outside the limiting radius, the bar-like structure loses coherence and the remnant rotates with a non-uniform angular speed. A maximally triaxial or slightly oblate figure is also present within the half mass radius in the most eccentric runs including the BHB. In all the other remnants hosting the SMBHs triaxiality is mostly limited to the binary's influence radius. In addition, Figure 6.6 shows very clearly that T never attains values higher than 0.5 outside the binary influence radius when the BHB is present.

Only one SMBH

At this stage it is worth investigating whether a BHB is necessary for producing the aforementioned differences, or even the presence of a single SMBH drives the remnant towards oblateness. For this purpose, we analize simulation MC7o: such simulation has the same initial orbit and density profile as in runs MC7, MC7b but it hosts a SMBH in only one of the two colliding galaxies. The results of this comparison are shown in the central panels of Fig. 6.6. Clearly, even a single SMBH erases all the triaxiality outside the SMBH's sphere of influence, meaning that the differences in the shape of the remnant are not driven by slingshot ejections but probably by the steep central potential induced by the SMBH(s) presence.

Interestingly, T has almost the same dependence on the enclosed stellar mass when only one or two SMBHs are present; however, the axis ratios b/a and especially c/a in runs MC7b and MC7o attain a different value within the SMBH(s) sphere of influence: the system gets closer to spherical ($b/a \approx 0.9$, $c/a \approx 0.8$) immediately after the merger when only one SMBH is present, while it is more flattened ($b/a \approx 0.85$, $c/a \approx 0.6$) when the remnant hosts a BHB.

In order to understand whether the triaxiality within the BHB influence radius survives after the BHB coalescence, we manually merged the two SMBHs into one in simulation MC7b at $t = t_f + 400$, and we studied the further evolution of the remnant morphology within the single SMBH sphere of influence. When two SMBHs are replaced with one, the inner regions of the remnant slowly migrate towards a more isotropic configuration and the axis ratios reach the same values as in run MC7o. This change of the system geometry takes roughly 500 time units to be completed, a timescale close to the relaxation time of the system at such scale, suggesting that two-body relaxation is the main driver behind the shape evolution. We thus expect the very central region of a galaxy to 'remember' the presence of a BHB for a timescale of the order of its relaxation time.

Dependence on the initial conditions

In this section we address how the initial conditions of the merger influence the morphology of the remnant. Figures 6.8 and 6.9 show the axis ratios and T dependence respectively on the merger eccentricity and on the density slope of the merging systems, for runs with and without BHB.

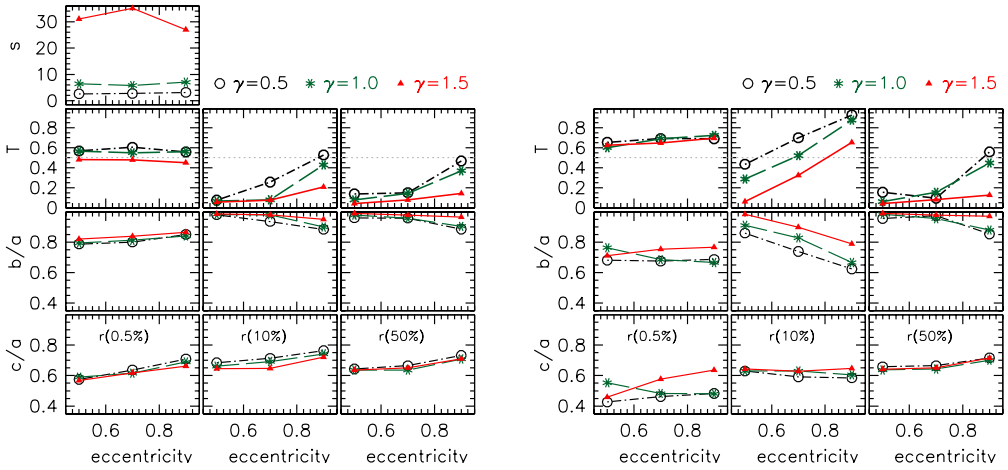

Fig. 6.8. Triaxiality parameter T and axis ratios as a function of the initial orbital eccentricity for runs with BHB (left) and without BHB (right). The panels show T, b/a and c/a as a function of e. The upper left plot also shows the hardening rate s for runs with the BHB; s is computed over the same interval of time used for computing the triaxiality and axis ratios. The columns refer to different fractions of enclosed mass: 0.5% (first column), 10% (second column) and 50% (third column). Different symbols show simulations with inner density slope of the progenitors, γ, equal to 0.5 (black circles), 1 (green asterisks) and 1.5 (red triangles).

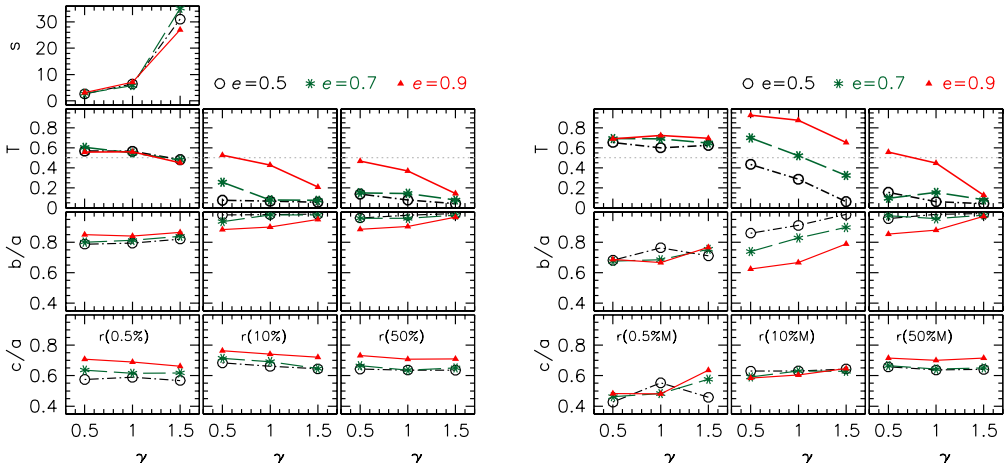

Fig. 6.9. Triaxiality parameter T and axis ratios as a function of the inner density slope of the progenitor galaxies, γ, for runs with BHB (left) and without BHB (right). The panels show T, b/a and c/a as a function of γ. The upper left plot also shows the hardening rate s for runs with the BHB; s is computed over the same interval of time used for computing the triaxiality and axis ratios. The columns refer to different fractions of enclosed mass: 0.5% (first column), 10% (second column) and 50% (third column). Different symbols show simulations with orbital eccentricity of the merger, e, equal to 0.5 (black circles), 0.7 (green asterisks) and 0.9 (red triangles).

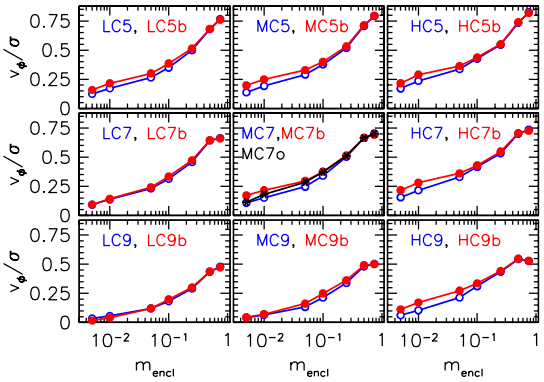

Fig. 6.10. Fraction of residual rotational velocity v_ϕ to velocity dispersion σ of the remnant as a function of the enclosed mass $m_{\rm encl}$. Each panel is labelled with the name of the runs shown. Filled red points: runs with the BHB; empty blue points: runs without the BHB; black asterisks: run MC7o with a single SMBH.

The axis ratio b/a outside the $\sim$ 1% of enclosed mass tends to decrease with increasing e, especially within the $10-25\%$ of enclosed stellar mass; this results in a higher value of T when the merger is more radial, and is true regardless of the presence of the BHB. The trend in b/a and T is more prominent when the BHB is omitted, as the system can attain a value of T that is greater than 0.6. When the BHB is included, an increasing eccentricity also determines the increase of c/a, i.e. the model is more flattened if the initial galaxies are on a higher angular momentum orbit. When the BHB is not included, this trend is clear only at large radii, while the mid- and small-scale structure exhibit a more stochastic trend in e. At very small scales (i.e. enclosing $\sim 0.5\%$ of the stellar mass) T seems not to depend on e, or the dependency is too weak to be distinguished from statistical noise.

The shape of the remnant also depends on the density profile of the merging galaxies: b/a increases with γ at any scale and independently of the presence of the two SMBHs, and this results in a declining value of the triaxiality parameter T. Such trend is more evident at radii enclosing 10% of the stellar mass when the BHB is omitted. The dependence of c/a on the concentration of the progenitors is less obvious: c/a seems to decline if γ is increased in runs with the BHB, especially in the central regions of the model; the trend seems to be opposite when the remnant does not host any SMBH; however such dependencies of c/a are very weak and might be a result of statistical noise.

Figures 6.8 and 6.9 also show the dependence of the hardening rate on e and γ. As already mentioned, s does not show any obvious relation with e while it strongly increases with increasing γ; moreover, *there is no clear correlation between s and the morphology of the system at any scale.*

6.3.3 Kinematics of the remnants

Rotational support

Even if the progenitor galaxies are pressure supported systems, the merger induces a certain degree of net rotation in the remnant, whose velocity vector always lies along the merger plane. To quantify this, we evaluated the magnitude of the velocity component aligned to the merger plane[4] (v_ϕ) and the local velocity dispersion of the remnant (σ, computed for different enclosed masses). In Figure 6.10 we show the ratio between such velocities, v_ϕ/σ, as a function of the enclosed mass: more radial mergers result in less rotationally supported remnants, as expected by the laws of conservation of angular momentum; this is true at all radii. The system exhibits a higher rotational support at large distances from the centre, as most of the orbital angular momentum is absorbed by the peripheral regions in the initial phases of the merger. Our simulations also show that the merger relic is only partially rotationally supported: v_ϕ/σ can be as high as 0.8 beyond the radius enclosing 25% of the mass; the rotational support gradually drops moving inwards, reaching $v_\phi/\sigma = 0 - 0.3$ within the 1% of enclosed stellar mass.

Figure 6.10 shows that the rotational support within 1% of enclosed mass in most runs with the BHB is slightly higher compared to runs without SMBHs and even to the run with only one SMBH. To explain this, we have to keep in mind that when a BHB is present, it expels stars on radial orbits, thus only stars on almost circular orbits can remain in the innermost regions. As a consequence, BHB-hosts attain a higher value of v_ϕ/σ in the centre of the remnant, while the same does not apply when only one or no SMBHs are present. This effect is enhanced in highly concentrated models, as more stars can interact with the BHB.

At larger scales, including up to 10% of the total mass, v_ϕ/σ is still higher in runs with the BHB compared to runs with no SMBHs; however the run with a single SMBH behaves as the case with the BHB, suggesting that a process different than slingshot ejection is at play. We propose such additional process to be the deposition of angular momentum due to the infall of the SMBH(s), when they are present. In order to test this possibility, we adiabatically grow a SMBH of mass $0.005M_{\rm tot}$ in the remnant of the originally SMBH-free run MC7, starting at $t = t_f + 10$, i.e. after the completion of the merger process; the SMBH is bound to grow linearly with time, reaching its final mass in 50 time units. In this test case, v_ϕ/σ behaves exactly as in run MC7 with no SMBHs. This confirms that if one or two SMBHs participate the merger process, their angular momentum loss due to dynamical friction increases the rotational support in the host galaxy; such effect is very small, and it is maximum at radii enclosing $5 - 10\%$ of the total stellar mass.

Velocity anisotropy

A stellar system can also be characterized by the *anisotropy parameter*

$$\beta = 1 - \frac{\sigma_T^2}{2\sigma_R^2}, \tag{6.6}$$

(4) In the computation of v_ϕ we averaged the tangential components of the velocities, and not their magnitudes. Stars with positive and negative tangential velocities cancel each other out. Therefore v_ϕ describes the degree of rotation of the system.

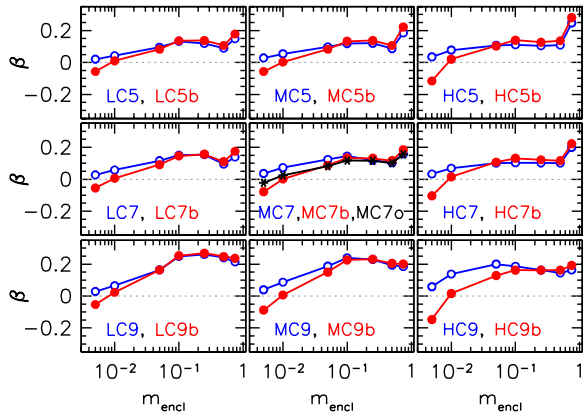

Fig. 6.11. Anisotropy parameter β as a function of the enclosed mass $m_{\rm encl}$. Each panel is labelled with the name of the runs shown. Filled red points: runs with the BHB; empty blue points: runs without the BHB; black asterisks: run MC7o with a single SMBH.

where $\sigma_T = (\sigma_\theta^2 + \sigma_\phi^2)^{1/2}$ is the tangential velocity dispersion, and σ_R represents the radial velocity dispersion. The anisotropy parameter measures whether a system is dominated by stars on radial orbits ($0 < \beta < 1$), tangential orbits ($-1 < \beta < 0$) or the two are perfectly balanced and the system is isotropic ($\beta = 0$, as in the progenitor galaxies).

The anisotropy parameter as a function of the enclosed stellar mass is shown in Fig. 6.11: in all runs, stars are mainly found on radial orbits beyond 1% of the enclosed mass, as β mostly lies in the range $0.1 - 0.3$; generally β attains higher values if the galactic merger is more radial, at least within the half-mass radius. Runs including the BHB exhibit a lower value of the anisotropy parameter at small scales; in particular, within a sphere including 0.5% of the mass β stays between 0 and 0.05 if the BHB is absent, while it lies in the range $[-0.15, -0.05]$ if the BHB is included. Such behaviour is again easily explained in terms of BHB slingshot ejections: at small scales, the BHB ejects stars on radial orbits, allowing only stars on tangential orbits to survive in the inner regions of the system. Such BHB-induced small scale effect is enhanced in runs with a high central concentration.

The anisotropy parameter for run MC7o with a single SMBH is also shown in Fig. 6.11: at small scales, the system is less tangentially biased compared to the run with a BHB, as slingshot interactions are not at play; however angular momentum deposition due to the infalling SMBH enhances the tangential anisotropy in this run compared to the run with no SMBHs, as already mentioned in the previous section.

Finally, in the peripheral region of the remnants, runs with the BHB are more radially biased compared to runs with one or no SMBHs: this is the large scale effect of slingshot interactions that scatter stars on very radial orbits.

6.3.4 Fraction of escapers

The fraction of stellar escapers as a function of time is shown in Figure 6.12. During the merger, escapers are mainly produced after each pericentre passage: in

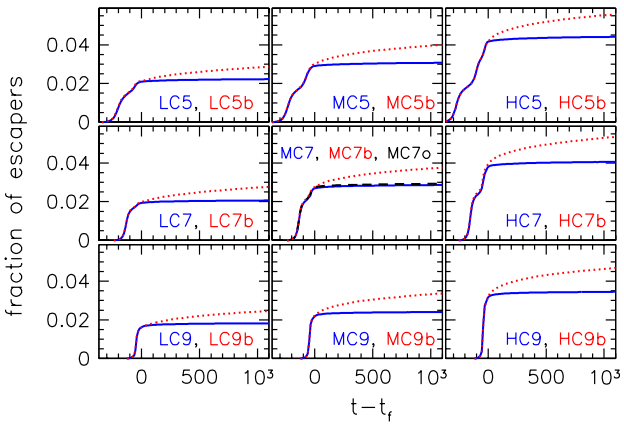

Fig. 6.12. The different panels show the fraction of stellar escapers as a function of time in runs with the BHB (red dotted lines), with only one SMBH (run MC7o, black dashed line in the central panel) and without SMBHs (blue solid lines). Each panel is labelled with the name of the runs shown.

this stage bound stars get destabilized due to the strong perturbation in the global potential, and may leave the system. As a consequence, more escapers are produced within t_f when the orbit is less eccentric: the merger is slower and the two galaxies undergo multiple pericentre passages before reaching coalescence. In addition, stars in more concentrated systems are more efficient at producing escapers: runs with $\gamma = 1.5$ generally have a fraction of escapers at t_f that is about two times the fraction of escapers in runs with $\gamma = 0.5$. Such effect is predicted by the theory of violent relaxation (Lynden-Bell, 1967): if the progenitor systems are cuspier, stars within each galaxy feel a stronger variation in the total gravitational potential during the merger, thus the average change in the energy per unit mass of each star is expected to be more substantial, and the fraction of stars gaining sufficient energy to escape the system is greater.

If the system does not host a BHB, escapers are no longer produced after the merger process is completed. In contrast, when a BHB is present a number of stars undergo slingshot interactions and get ejected from the remnant after the BHB semimajor axis has dropped below a_h. The effect of the BHB is clearly visible in Figure 6.12: the fraction of escapers steadily increases after t_f in remnants harbouring a BHB. More escapers are produced by the slingshot interactions if the initial system is more compact, as more stars are initially available on low energy orbits: the BHB generally unbinds two times more stars if $\gamma = 1.5$ compared to runs with $\gamma = 0.5$. When only one SMBH is included in the simulation, the number of escapers grows almost as it does in the analogous run without SMBHs (Figure 6.12, central panel), confirming that BHB slingshot ejections determine the continuous production of escapers after t_f.

6.4 Summary and discussion

In this study we carried out a suite of equal mass galaxy merger N-body simulations, varying the initial orbit and inner density slope of the merging galaxies and including or not a SMBH in the centre of the colliding systems; when a SMBH is

included in each merging galaxy, a BHB forms in the centre of the remnant. Using convergence tests and analytic estimates for the two-body relaxation time, we minimised the effect of spurious two-body relaxation by analysing our simulations at a time and on a spatial scale at which two-body relaxation time is always longer than the simulation time.

Our main aim was to analyze the link between the morphology and kinematics of the newly formed stellar system and: (i) the initial orbit and density profile of the two progenitor galaxies and (ii) the presence or absence of a BHB (or even a single SMBH) in the centre of the merger relic; finally, we studied how the shape of the remnant influences the BHB hardening efficiency. In what follows we summarize and discuss our main findings.

6.4.1 Morphology of the remnant and merger initial conditions

As expected, the mid- and large-scale geometry of the system strongly depends on the merger orbit: high angular momentum collisions generally lead to the formation of an oblate spheroid, while radial (or equivalently, lower impact parameter) mergers can produce maximally triaxial or (if no SMBHs are present) prolate systems, in agreement with the findings in González-García and van Albada (2005). This might be linked to the fact that the initial conditions for more radial galaxy collisions are more 'anisotropic' (i.e. the orbit of the galaxies is elongated in the merger plane, instead of being close to circular), thus the projection of the final remnant in the merger plane is more stretched. Alternatively, this effect may be a result of radial orbital instability, that drives a break in the symmetry of the system (Antonov, 1987; Saha, 1991; MacMillan et al., 2006; Barnes et al., 2009). Higher angular momentum mergers were also found to produce more flattened remnants (especially beyond the half-mass radius): as expected, a higher degree of net rotation is induced in the outskirts of the system for more circular collisions, and in turn the remnant shape appears to be more flattened.

The shape of the merger relic is also connected to the galaxy progenitors' density profile: while collisions between more concentrated galaxies generally produce oblate spheroids with b/a closer to unity, low concentration systems are found to be often maximally triaxial and possibly prolate. This may be connected to the fact that stars in systems with a shallower density profile are more sensitive to tidal torques, thus their orbit is more easily modified during the merger: it follows that the collision between less concentrated galaxies can affect the remnant shape more, and the resulting system will better remember the imprint of the merger orbit.

We further stress that the shortest axes (c/a) of the oblate systems produced in our simulations are always almost perpendicular to the merger orbital plane. In systems with the BHB, the orientation of the merger plane almost always coincides with the orientation of the BHB orbital plane, thus one may think that the BHB causes the system to be flattened in the direction of its angular momentum vector. However, even in runs with only one or no SMBHs the system is flattened in the direction of the merger plane, suggesting instead that the galaxy collision (and perhaps the resulting rotation) influences the orientation of the principal axes of the ellipsoid.

6.4.2 The role of the central SMBHs

Perhaps the most striking result in our simulations is the fact that if at least one SMBH is involved in the merger, the system shape is noticeably influenced by the SMBH well beyond its sphere of influence, and this is true from the very moment the remnant forms. Starting from the same initial orbit and density profile of the merging galaxies, we found that the central regions of merger relics hosting SMBHs are always closer to spherical, and the triaxiality parameter T is noticeably smaller compared to the same runs without SMBHs: a merger product hosting one or two SMBHs is generally found to be oblate, aligned with the galaxy merger plane, and never attains $T > 0.6$, while when no SMBHs are present the remnant is typically prolate (sometimes reaching $T \approx 1$) or maximally triaxial. The aforementioned differences are particularly evident within a radius including approximately $2 - 50$ times the mass of the central SMBH(s), while the remnant shape is generally the same beyond ≈ 100 SMBH(s) masses.

The fact that a central massive body may render the system rounder or closer to oblate was already evident from a number of studies (e.g. Lake and Norman, 1983; Gerhard and Binney, 1985; Merritt and Quinlan, 1998; Holley-Bockelmann et al., 2002), which addressed the evolution of equilibrium mass models (rather than merger relics) where a SMBH was adiabatically grown. In these studies, the evolution of the galaxy shape is attributed to the fact that the SMBH acts as a scattering centre, rendering centrophilic orbits stochastic: the volume filled by the scattered orbits is rounder and does not support the original galaxy shape, thus the global morphology of the system changes[(5)].

Similar studies found that a central strong cusp may have an analogous effect: it may act as an orbit scatterer evolving the system towards a more spherical shape (Merritt and Fridman, 1996; Merritt and Valluri, 1996). This could be the reason why, among our models without SMBHs, the ones with the highest initial concentration were those that either became immediately oblate, or retained a shape with $T > 0$ for a very short timescale.

Even if a SMBH (or possibly even a strong cusp) seems to drive the system towards oblateness or sphericity, a series of more recent studies were able to demonstrate that steady triaxial ($T \leq 0.5$) models involving a high fraction of chaotic orbits and hosting a SMBH can be constructed, and they were found to retain their shape over many dynamical times (Poon and Merritt, 2002, 2004). This means that triaxiality can be achieved in systems hosting a central SMBH. To our knowledge though, a stable steady state solution for a prolate system hosting a SMBH has never been found: according to Poon and Merritt (2004), mildly prolate models harbouring a central massive body always evolve towards an oblate axisymmetric configuration, in agreement with the fact that our SMBHs-hosting remnant never reach $T > 0.5$ outside the BHB sphere of influence. To our knowledge, the fact that T seems to have an upper limit if the system hosts a central massive body has no thorough explanation, and we reserve to better analyse this aspect in a forthcoming paper.

Recently, Vasiliev et al. (2015) studied the evolution of BHBs embedded in stable triaxial mass models via a Monte-Carlo method that allows them to switch off two-body relaxation effects: when they analyse the shape of a system hosting a

(5) The final axis ratios of the system in these studies were generally closer to unity compared to what we find here.

BHB, they also find an evolution towards axisymmetry, while when only a single SMBH is present the morphology of the system does not change significantly over a long timescale (Vasiliev, 2015). For this reason, they suggest that the shape evolution observed in studies involving a single SMBH (e.g. Merritt and Quinlan, 1998; Holley-Bockelmann et al., 2002) may be greatly affected by spurious two-body relaxation effects (Kandrup et al., 2000); when a BHB is included though, they speculate that resonant perturbations of chaotic stellar orbits resulting from the BHB time-dependent potential (Kandrup et al., 2003) may cause the observed shape evolution even if relaxation is not at play.

The results by Vasiliev et al. (2015) cannot be easily compared to ours, as we form our merger remnants self-consistently from galaxy collisions, inducing some rotation in the systems. But we can state with confidence that our results, on the scale and at the times we analyse the simulations, are not affected by spurious numerical two-body relaxation. Thus we propose that galactic collisions may have an important role in determining the differences in the shape of remnants with and without SMBHs. Given that evolution towards oblateness is believed to result from the scattering of stars into chaotic orbits due to the SMBH(s) presence, we propose that the merger itself may facilitate such scattering process (e.g. though violent relaxation) even if two-body relaxation is not at play, and regardless of whether one or two SMBHs are present.

6.4.3 One or two SMBHs

Even if the mid- and large-scale geometry of a remnant hosting only one or two SMBHs is very similar, some differences arise within the SMBH(s) sphere of influence. Small-scale differences in the geometry of galaxy centres are of great importance, as they might give interesting observational constraints for distinguishing systems that host (or hosted) a BHB from systems with a single SMBH. In our remnants, when only one SMBH is included, the geometry of the small-scale system is visibly rounder and less flattened compared to remnants hosting a BHB[(6)]. We also found that the system keeps the more flattened shape typical of a BHB-hosting remnant for about a relaxation timescale after the BHB coalescence.

The small-scale shape differences between systems with one or two SMBHs could be related to the fact that when only a single SMBH is present, the galaxies' inner cusps are not destroyed during the merger process and it is difficult to perturb their spherical shape due to their compactness. When two SMBHs are present instead, the central cusp within each merging galaxy is destroyed by BHB-induced stellar scatterings and the concentration of the merger relic is noticeably lowered in the centre, thus stars are more affected by global torques and the shape of the system is more easily modified. We further note that the BHB potential is as not spherically symmetric as the single SMBH potential is; the elongated and time dependent BHB potential may also affect the stellar orbits within its influence radius and render

(6) In the interpretation of such result, one should keep in mind that the described simulations started from simplistic initial conditions, i.e. from perfectly spherical, isotropic and non-rotating systems. In reality, progenitor galaxies undergoing a merger are likely to have suffered a number of mergers in their history, thus they possibly already exhibit some degree of non-spericity and some net rotation prior to the merger. For this, in principle a galaxy may appear rounder in its inner parts just because it underwent a number of repeated mergers, irrespective of the presence of a BHB. Such aspect deserves a further investigation in a forthcoming paper.

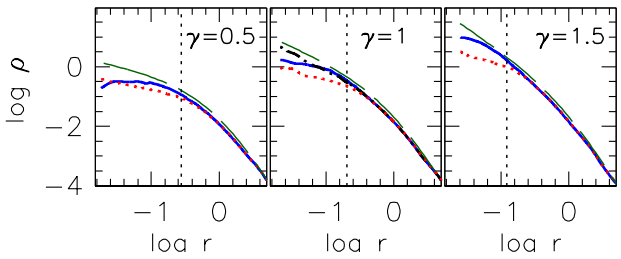

Fig. 6.13. Stellar mass density ρ as function of the radius r for merger remnants produced by a galactic collision with eccentricity $e = 0.7$; the curves refer to time $t_f + 250$. The progenitor galaxies' density profile is a Dehnen model with (from left to right) $\gamma = 0.5, 1, 1.5$. We show the density profile of remnants hosting a BHB (red dotted lines) and no SMBHs (blue solid lines); the black dash-dotted line in the central panel shows the density profile of run MC7o with a single SMBH. For comparison, the dark-green long-dashed line shows the density profile of the progenitor galaxies; the vertical dotted line marks the radius including two times the mass of binary in runs including it.

the small-scale structure of the system more triaxial.

There is a second effect that may be observationally helpful in distinguishing between systems with only one or two SMBHs: the so-called core scouring. If the system hosts a BHB, the binary-induced slingshot ejection of stars produces a lack of stellar mass in the central parts of the remnant. As a consequence, the inner density profile of a systems hosting (or that hosted) a BHB is expected to be less cuspy. We verified the occurrence of core-scouring in our simulations, and the results are shown in Figure 6.13: we compare the density profile of the progenitor galaxies with the density profile of remnants hosting zero, one and two SMBHs. When the merger relic hosts a BHB, the density profile is noticeably carved out beyond the radius including two times the BHB mass; this is a well established result (e.g. Milosavljević and Merritt, 2001; Gualandris and Merritt, 2012) and is supported by observations (Ferrarese et al., 1994; Lauer et al., 1995; Bonfini et al., 2018). As a matter of fact, even the infall of a single SMBH can produce a core in the system (Gualandris and Merritt, 2008; Goerdt et al., 2010); however our simulations suggest that in the single SMBH scenario the effect of core scouring is significantly smaller compared to the BHB case (Figure 6.13, central panel). In addition, we note that the small-scale density profile of remnants not hosting any SMBH is shallower compared to the one of the progenitor systems. This seems at odds with the results of Dehnen (2005), who asserts that the steeper cusp should always survive in a merger; however, the flattening of the inner density profile we observe in our simulations without SMBHs is most probably an effect of numerical relaxation. We suggest the density profiles in Figure 6.13 are more reliable outside the radius where the remnants without SMBHs and their progenitors start having a comparable density profile.

6.4.4 Rotation and velocity anisotropy

In our simulations, we find that the merger induces some rotation in the final remnant, even if the bulk of angular momentum is absorbed by the outer regions

of the relic, in agreement with previous findings (Di Matteo et al., 2009; González-García and van Albada, 2005). As expected, our simulations show that rotational support is enhanced if the merger eccentricity is lower.

When one or two SMBHs are present in the simulation, they considerably influence the kinematics of the final remnant: when a BHB is present, it ejects stars from the core of the system, which is found to be more rotationally supported. In addition, SMBHs lose their angular momentum when sinking towards the centre of the remnant, thus they both enhance the rotational support and lower the radial anisotropy parameter.

Angular momentum injection, together with high central concentrations, was previously found to irremediably change the shape of dark matter haloes (Debattista et al., 2008), thus it might connect with the morphology evolution we see in our runs, but we reserve to better investigate this aspect in a future paper.

Concerning the enhanced tangential anisotropy in the centre of systems hosting a BHB, our findings are at least in qualitative agreement with the observational results of by Thomas et al. (2014): they find hints of kinematical tangential anisotropy in the centres of elliptical galaxies hosting a depleted core, and such depleted core may well be the fingerprint of an evolving BHB. The measurements by Thomas et al. (2014) indicate that the inner regions of elliptical cored galaxies may be even more tangentially biased compared to what we find in our runs: however, one should consider that real galaxies (especially large ellipticals) have likely been through a number of mergers, each of which may have contributed to boost the tangential anisotropy in the inner regions.

6.4.5 BHB evolution

We find that the evolution of the BHB is not clearly connected with the shape of the host system, even if a clear correlation is present between the hardening rate and the concentration of the BHB host. In principle, such lack of connection might be due to the fact that the system looks always maximally triaxial within the BHB influence radius, and such triaxiality might ensure a similar hardening rate in simulations with the same γ. However, Vasiliev et al. (2015) point out that stars participating in the binary shrinking come from large distances from the centre, and this would mean instead that the maximum triaxiality within the BHB influence sphere does not influence the binary shrinking rate.

Alternatively, the lack of connection between the system shape and the BHB hardening could be related to the fact that all our remnants have a similar (nearly oblate) geometry at the largest scales considered in this study. In principle, one could also consider the possibility that spurious numerical relaxation plays the major role in determining the BHB hardening; however Vasiliev et al. (2015) recently showed that relaxation has a long-term effect on the BHB shrinking efficiency only when the host system is perfectly spherical or axisymmetric, that is never our case. Thus we suggest that a BHB could harden at the same rate for a given concentration of its host system, and the value of such fixed hardening rate might represent a critical value that would allow to simplify the forthcoming studies about BHBs evolution towards GW emission. Even if we do not have a throughout explanation for the aforementioned findings, we plan to perform an orbital analysis of our

merger remnants in order to get a better understanding of the BHB hardening connection with the geometry of their hosts.

A further interesting result is that the BHB hardening rate tends to the same value towards the end of all our runs (see e.g. Fig. 6.4); this perhaps reflects the fact that the BHB separation almost reaches the softening length by the end of the simulation, and possibly slows down the BHB hardening in more concentrated models. On the other hand, the decline of s in our runs is consistent or even less conspicuous compared to what found by Vasiliev et al. (2015) using a (totally different) Monte Carlo integration method; we suspect that the slowing down of s we see here is thus a real effect, possibly linked with the idea that the loss cone is replenished at approximately the same rate in all models, once the initial loss cone population has been entirely scattered and the system geometry has found its equilibrium state.

6.4.6 Conclusions

This study shows that BHBs formed from the dry merger of elliptical galaxies have a strong impact on the geometry of their host systems. In particular, binary (or even single) SMBHs render the host system more oblate, aligned with the orbital planes of both the BHB and the galaxy merger, up to a radius enclosing ~ 100 SMBH masses, compared to remnants produced by the merger of the same galaxies not hosting any massive body. In addition, the results of this investigation show that remnants hosting a single or binary SMBH never attain a triaxiality parameter $T > 0.6$, despite merger relics not hosting any SMBH generally exhibit a prolate inner figure. Furthermore, we find that stars within the influence radius of a single SMBH are distributed in a more compact and nearly spherical geometry, while the same region appears to be cored and triaxial if the system hosts a BHB.

Our study points towards a possible connection between the geometry of a galactic nucleus and the presence of zero, one or two massive central bodies. Our findings so far qualitatively support recent observations reported in e.g. Dullo and Graham (2015) and Foster et al. (2017), but we will perform a more quantitative analysis of this, properly projecting the simulations into observables in a forthcoming paper.

Another major finding was that the BHB shrinking rate seems to vary only with the central density of the host, while it appears to be less related to the geometry of the merger remnant. Such result might be particularly relevant for low-frequency GW science, as the timescale needed for a BHB to reach the GW-emission stage could be assumed to scale only with the core density of the merger remnant; however further studies must be carried out to pinpoint the physical reasons behind this finding.

Finally, our work confirms the idea that BHBs are able to reach their coalescence phase within a Hubble time in most galaxies, even if the BHB host systems are generally found to be nearly axisymmetric outside the binary influence radius.

Conclusions and outlook

In this thesis, I have adopted advanced numerical techniques to address the dynamical interplay between supermassive black holes (SMBHs) and their host stellar systems. Specifically, I explored the effect of supernova kicks occurring in the close vicinity to an SMBH, and the formation and evolution of low-frequency gravitational wave (GW) sources at the centre of galaxies, as extreme mass ratio inspirals (EMRIs) and SMBH binaries (BHBs).

First of all, my investigation suggests that supernova kicks may play a relevant role in regulating the dynamical evolution of star forming nuclei as my Galactic Centre: on the one hand, I propose supernova kicks to be at least partially responsible for the suspected dearth of neutron stars in the innermost parsec of our Galaxy; on the other hand, I predict that all black holes that form *in situ* in the Galactic Centre remain there in spite of their natal kick[(7)] (Bortolas et al., 2017); this, combined with mass segregation, would suggest a cusp of stellar relics to be present in the close vicinity to the SMBH at the centre of the Milky Way (a prevision supported by recent X-ray observations of the Galactic Centre, Hailey et al. 2018).

Secondly, I identified supernova kicks to be a relevant mechanism for funnelling newborn compact stellar remnants on EMRI orbits within the Galactic Centre. Specifically, I found that $\sim 10^{-5} - 10^{-4}$ supernova events occurring within the young stellar aggregates observed in the Milky Way nucleus would end up as EMRIs (Bortolas & Mapelli, in prep.). Remarkably, the EMRI rate induced via this novel process may constitute up to $\sim 10\%$ of the rate produced via two-body relaxation, which is traditionally assumed to trigger the bulk of EMRIs (e.g. Amaro-Seoane et al., 2007; Amaro-Seoane, 2018). Thus, I predict that supernova-driven EMRIs are an important source of GWs in the frequency range of LISA, the space-borne GW observatory whose launch is expected in the early 2030s (Amaro-Seoane et al., 2017).

In more general terms, my results strongly support the idea that supernova kicks play a relevant role in modelling the dynamics of the Milky Way centre, and they should be accounted for when exploring the complex physics of galactic nuclei.

Although my investigation has been tailored to the Galactic Centre, my results might be extended to other nuclei, if we educatedly guess that a number of galaxies in the Local Universe share similar properties to those of the Milky Way (e.g. an analogous SMBH mass, the presence of young stars and structures similar to the S-cluster and the clockwise disc). This possibility is currently difficult to probe, as the Milky Way centre is currently the sole nucleus where single stellar orbits can be individually tracked (Böker et al., 2002; Gillessen et al., 2017); however, the forthcoming class of 30-meter telescopes will be able to resolve the sphere of

(7) In the assumption that black hole natal kicks attain velocities proportional, on average, to the inverse of their mass.

influence of a number of SMBHs in the Local Universe, thus possibly constraining the occurrence of Milky-Way like nuclei (e.g. Gullieuszik et al., 2014; Davies et al., 2016).

While waiting for the forthcoming 30-m telescope observations, it would be worth exploring how much my results would change if we discard some of the assumptions adopted in the Milky Way case. In fact, most probably, even a mere variation in the SMBH mass would sensibly affect the dynamics of supernova kicks (e.g. Lu and Naoz, 2018). The presence of a conspicuous amount of gas, as an accretion disc about the SMBH, could also significantly alter the dynamical outcome of supernova kicks. In particular, it would be worth exploring (i) the effect of gas drag induced by the disc on the perturbed orbits of newborn stellar relics; and (ii) whether one can hope to detect a cusp of dark stellar relics via the interaction of such objects with the gaseous disc.

Unfortunately, the nature and the distribution of supernova kicks are still highly uncertain (e.g. Fryer et al., 1998; Janka, 2013; Giacobbo and Mapelli, 2018). In general, the prescriptions for supernova kicks are poorly constrained owing to the intrinsic difficulty of observing dark stellar relics, especially stellar black holes; (e.g. Gualandris et al., 2005; Repetto et al., 2012; Mirabel, 2017); hopefully, the high-frequency GW detections by LIGO and VIRGO (Wysocki et al., 2018; O'Shaughnessy et al., 2017), coupled with accurate observations of radio pulsars (e.g. via the *MeerKAT* telescope and the forthcoming *Square Kilometer Array*) and accreting X-ray binaries (Repetto et al., 2012, 2017; Hailey et al., 2018) would enable to tighten the constraints on the distribution of supernova kicks, potentially providing more reliability to my results and to forthcoming investigations on the role of such energetic events in galactic nuclei.

A second theme I largely addressed is the evolution of BHBs: these objects, likewise EMRIs, will constitute a relevant source of GWs accessible to the forthcoming LISA observatory (Amaro-Seoane et al., 2017); here the need to better constraining their dynamical evolution, in order to anticipate what LISA will observe in the near future.

Although BHBs have been suspected for a long time not to be able to merge within a Hubble time (e.g. Begelman et al., 1980; Milosavljević and Merritt, 2003a), all my results conclusively support the idea that the vast majority of these objects promptly reach their final coalescence: stars appear to be continually supplied near the BHB, thus promoting its shrinking down to the GW emission phase (Bortolas et al., 2016; Gualandris et al., 2017; Bortolas et al., 2018a). Accordingly, a growing body of literature claims the *final parsec problem* (i.e. the fact that BHBs were suspected not to shrink below a separation of $\sim$ 1 pc Milosavljević and Merritt 2003b) to be finally solved (e.g. Vasiliev et al., 2015; Khan et al., 2016; Gualandris et al., 2017).

First of all, my findings indicated that the shrinking of a BHB can be boosted by its encounter with a massive stellar cluster reaching the binary along a radial orbit (Bortolas et al., 2018b); such result provides a new effective way to bring the BHB closer to the GW emission stage. Secondly, I showed that the numerically induced Brownian motion of the BHB, that was suspected to artificially enhance the binary shrinking rate in direct summation N-body experiments (Chatterjee et al., 2003;

Milosavljević and Merritt, 2003a), can be safely assumed to be negligible in state-of-the-art simulations involving $\gtrsim 10^6$ particles (Bortolas et al., 2016).

Finally, my most recent investigation on BHBs explores the interdependence between the BHB hardening rate and the morphology of a galaxy merger remnant (Bortolas et al., 2018a). Although deviations from spherical and axial symmetry in the host system are now accepted to be the catalyst of the BHB hardening (Vasiliev et al., 2015; Gualandris et al., 2017), my investigation suggests its shrinking in non-spherical merger remnants to solely depend on the inner density slope of the host system. This finding has been recently confirmed by other authors (Khan et al., 2018; Tamfal et al., 2018). Such result could largely simplify predictions of LISA rates, as the theoretical modelling of the slingshot-driven BHB shrinking could ignore the information on the galaxy shape. As a second remarkable point, I found merger relics hosting SMBHs or BHBs to attain more oblate (disky) morphologies on scales enclosing up to 100 times the mass of the central object, compared to merger relics produced by the same initial conditions, but lacking the central SMBH(s) (Bortolas et al., 2018a): thus, my study points towards the existence of morphological features that may help discriminating which systems host SMBHs. It would be worth following up on such result and performing mock observations of my models, in order to properly compare them with observational data. This sort of investigation would be particularly relevant and timely in the present moment, in view of the spectacularly well resolved observations that will be allowed by the forthcoming 30-m telescopes.

However, what is possibly the most crucial step to take in the study of BHBs, is to explore their formation and evolution in a cosmologically motivated context. This means adopting cosmologically motivated initial conditions for the galaxy merger, and accounting for the presence of dark matter haloes. While Khan et al. (2016) demonstrated the feasibility of such investigations, a systematic study of this aspect would help to constrain the most probable orbital parameters inherited by the binary at the moment of its formation; this kind of investigation will be of utmost importance, given that the time needed by the BHB to reach its final coalescence significantly depends on its orbital parameters at the moment of formation (Sesana, 2010).

Being limited to gas-free galaxies and equal mass BHBs, my studies only apply to a limited range of scenarios. A further interesting possibility for future investigations, thus, is to couple the BHB evolution driven by slingshot ejections with that induced by the presence of a large amount of gas, typically in a disc. In fact, on the one hand the drag of gas is known to circularize the BHB orbit, on the other hand slingshot ejections typically enhance the BHB eccentricity (Sesana, 2010; Vasiliev et al., 2015); thus, it is non-trivial to anticipate which effect among the two will prevail, but this information would be central considering that the BHB eccentricity significantly affects the timescale a BHB needs to reach its final coalescence (Peters, 1964).

In summary, the present thesis added several pieces of information to the dynamical modelling of galactic nuclei and GW sources, and provided important information that will allow to anticipate forthcoming electromagnetic and GW observations. I highlighted the critical role supernova kicks assume in regulating the dynamical

evolution of star forming galactic nuclei as our Galactic Centre. Furthermore, I have suggested a novel formation mechanism for EMRIs; my work also strongly supports the idea that SMBH binaries find their way to coalescence within the age of the Universe, enhancing the landscape of GW sources in the LISA band. In general terms, the present work is one of the countless demonstrations that the study of galactic nuclei cannot, and must not, disregard the central role of stellar dynamics in defining the evolution of such spectacular environments.

A

Prescriptions for the natal kick on the binary members

Here we describe the procedure we adopted in Chapter 2 to distribute the SN kick to the two members of the stellar binary system, according to the prescriptions detailed in appendix A1 by Hurley et al. (2002).

If we consider a binary stellar system composed of two stars with initial masses $M_{1,i} > M_2$ and relative velocity vector $\mathbf{r}$, we can express their relative velocity as

$$\mathbf{v} = -v_0(\hat{\mathbf{i}}\sin\beta + \hat{\mathbf{j}}\cos\beta), \tag{A.1}$$

where β is the angle between the position and velocity vectors; we use the notation $\hat{\mathbf{i}}, \hat{\mathbf{j}}, \hat{\mathbf{k}}$ to denote the unit vectors relative to a reference frame X, Y, Z where the mass M_2 is in the origin and the specific angular momentum $\mathbf{h}$ of the binary lies along the positive Z axis. The system geometry is shown in Figure A1 of Hurley et al. (2002). The angle β can be expressed in terms of the orbital elements of the binary, i.e. the semimajor axis a, eccentricity e, eccentric anomaly E and the distance r between the stars:

$$\sin\beta = \left[\frac{a^2\,(1-e^2)}{r\,(2a-r)}\right]^{1/2} \tag{A.2}$$

$$\cos\beta = -\frac{e\sin\mathrm{E}}{(1-e^2\cos^2\mathrm{E})^{1/2}}. \tag{A.3}$$

We chose the distance at which the SN explosion occurs by drawing a mean anomaly $\mathcal{M}$ (that is uniformly distributed in time) from a uniform distribution between 0 and 2π. For a given $\mathcal{M}$, we compute the associated eccentric anomaly by recursively solving

$$\mathrm{E}_{i+1} = \mathcal{M} + e\sin\mathrm{E}_i, \tag{A.4}$$

where E_i denotes the i-th iteration for the computation of E; the tolerance for the convergence of E was set to 10^{-9}. Then the distance r between the stars can be computed as:

$$r = a(1 - e\cos\mathrm{E}). \tag{A.5}$$

The orbital speed v_0 can as well be expressed as a function of the orbital elements:

$$v_0^2 = GM_{b,i}\left(\frac{2}{r} - \frac{1}{a}\right), \tag{A.6}$$

where $M_{b,i}$ denotes the total mass of the binary before the SN explosion.

We assume that the mass of the envelope, ΔM, is instantaneously ejected by the primary star during its explosion, and its mass becomes $M_{1,f} = M_{1,i} - \Delta M$; thus the total mass of the binary after the SN is $M_{b,f} = M_{b,i} - \Delta M$. During the explosion, the distance between the stars does not vary, but the primary star experiences a velocity kick whose modulus v_k is randomly drawn from a Maxwellian with one-dimensional variance equal to 265 km s^{-1} (Hobbs et al., 2005); if the remnant is a BH (i.e. $M_{1,f} > 3M_\odot$), the kick velocity is then normalized to the mass of the remnant, assuming linear momentum conservation. The kick velocity vector can be expressed as

$$\mathbf{v_k} = v_k(\hat{\mathbf{i}}\cos\omega\cos\phi + \hat{\mathbf{j}}\sin\omega\cos\phi + \hat{\mathbf{k}}\sin\phi); \tag{A.7}$$

the direction of the kick is assumed to be isotropic in space, thus ϕ is distributed between $-\pi/2$ and $\pi/2$ as $P(\phi) \propto \cos\phi$, while ω is uniformly distributed between 0 and 2π. After the SN explosion took place, the new velocity between the stars is:

$$\begin{aligned}\mathbf{v}_f &= \mathbf{v} + \mathbf{v}_k \\ &= (v_k\cos\omega\cos\phi - v_0\sin\beta)\,\hat{\mathbf{i}} + \\ &\quad (v_k\sin\omega\cos\phi - v_0\cos\beta)\,\hat{\mathbf{j}} + v_k\sin\phi\hat{\mathbf{k}}\,,\end{aligned}$$

and its modulus is, according to equation (A.6),

$$v_f^2 = GM_{b,f}\left(\frac{2}{r} - \frac{1}{a_f}\right) \tag{A.8}$$

$$= v_k^2 + v_0^2 - 2v_0v_k\left(\cos\omega\cos\phi\sin\beta + \sin\omega\cos\phi\cos\beta\right). \tag{A.9}$$

Note that we use the subscript f to denote the new binary orbital parameters after the SN kick. The previous equation can be solved to obtain the new semimajor axis a_f of the binary system. The system specific angular momentum after the SN is equal to

$$\mathbf{h}_f = \mathbf{r} \times \mathbf{v}_f, \tag{A.10}$$

and its squared modulus is

$$|\mathbf{r} \times \mathbf{v}_f|^2 = GM_{b,f}a_f\left(1 - e_f^2\right), \tag{A.11}$$

where

$$|\mathbf{r} \times \mathbf{v}_f|^2 = r^2\left[v_k^2\sin^2\phi + (v_k\cos\omega\cos\phi - v_{\rm orb}\sin\beta)^2\right]; \tag{A.12}$$

the previous equation can be solved to compute the new value for the eccentricity e_f. The new angular momentum vector is shifted with respect to the initial one by an angle η such that

$$\cos\eta = \frac{v_0\sin\beta - v_k\cos\omega\cos\phi}{\left[v_k^2\sin^2\phi + (v_k\cos\omega\cos\phi - v_0\sin\beta)^2\right]^{1/2}}. \tag{A.13}$$

Since an amount of mass ΔM is ejected from the primary star, the centre of mass of the system now exhibit a velocity shift equal to

$$\mathbf{v}_s = \frac{M_{1,f}}{M_{b,f}}\mathbf{v}_k - \frac{\Delta M M_2}{M_{b,f} M_{b,i}}\mathbf{v} \tag{A.14}$$

with respect to the initial reference frame.

Bibliography

S. Aarseth. *Gravitational N-Body Simulations: Tools and Algorithms*. Cambridge Monographs on Mathematical Physics. Cambridge University Press, 2003. ISBN 9781139441070. URL `https://books.google.it/books?id=WYQmYyy3f98C`.

B. P. Abbott, R. Abbott, T. D. Abbott, M. R. Abernathy, F. Acernese, K. Ackley, C. Adams, T. Adams, P. Addesso, R. X. Adhikari, and et al. Observation of Gravitational Waves from a Binary Black Hole Merger. *Physical Review Letters*, 116(6):061102, Feb. 2016. doi: 10.1103/PhysRevLett.116.061102.

D. Aharon and H. B. Perets. Formation and Evolution of Nuclear Star Clusters with In Situ Star Formation: Nuclear Cores and Age Segregation. ApJ, 799:185, Feb. 2015. doi: 10.1088/0004-637X/799/2/185.

D. Aharon and H. B. Perets. The Impact of Mass Segregation and Star Formation on the Rates of Gravitational-wave Sources from Extreme Mass Ratio Inspirals. ApJ, 830:L1, Oct. 2016. doi: 10.3847/2041-8205/830/1/L1.

T. Alexander. The Distribution of Stars near the Supermassive Black Hole in the Galactic Center. ApJ, 527:835–850, Dec. 1999. doi: 10.1086/308129.

T. Alexander. EMRIs and the relativistic loss-cone: The curious case of the fortunate coincidence. In *Journal of Physics Conference Series*, volume 840 of *Journal of Physics Conference Series*, page 012019, May 2017. doi: 10.1088/1742-6596/840/1/012019.

T. Alexander and C. Hopman. Strong Mass Segregation Around a Massive Black Hole. ApJ, 697:1861–1869, June 2009. doi: 10.1088/0004-637X/697/2/1861.

C. Alig, M. Schartmann, A. Burkert, and K. Dolag. Numerical Simulations of the Possible Origin of the Two Sub-parsec Scale and Counterrotating Stellar Disks around SgrA*. ApJ, 771:119, July 2013. doi: 10.1088/0004-637X/771/2/119.

P. Amaro-Seoane. Relativistic dynamics and extreme mass ratio inspirals. *Living Reviews in Relativity*, 21:4, May 2018. doi: 10.1007/s41114-018-0013-8.

P. Amaro-Seoane and X. Chen. The Fragmenting Past of the Disk at the Galactic Center: The Culprit for the Missing Red Giants. ApJ, 781:L18, Jan. 2014. doi: 10.1088/2041-8205/781/1/L18.

P. Amaro-Seoane and M. Preto. The impact of realistic models of mass segregation on the event rate of extreme-mass ratio inspirals and cusp re-growth. *Classical and Quantum Gravity*, 28(9):094017, May 2011. doi: 10.1088/0264-9381/28/9/094017.

P. Amaro-Seoane, J. R. Gair, M. Freitag, M. C. Miller, I. Mandel, C. J. Cutler, and S. Babak. TOPICAL REVIEW: Intermediate and extreme mass-ratio inspirals–astrophysics, science applications and detection using LISA. *Classical and Quantum Gravity*, 24:R113–R169, Sept. 2007. doi: 10.1088/0264-9381/24/17/R01.

P. Amaro-Seoane, C. F. Sopuerta, and M. D. Freitag. The role of the supermassive black hole spin in the estimation of the EMRI event rate. MNRAS, 429:3155–3165, Mar. 2013. doi: 10.1093/mnras/sts572.

P. Amaro-Seoane, H. Audley, S. Babak, J. Baker, E. Barausse, P. Bender, E. Berti, P. Binetruy, M. Born, D. Bortoluzzi, J. Camp, C. Caprini, V. Cardoso, M. Colpi, J. Conklin, N. Cornish, C. Cutler, K. Danzmann, R. Dolesi, L. Ferraioli, V. Ferroni, E. Fitzsimons, J. Gair, L. Gesa Bote, D. Giardini, F. Gibert, C. Grimani, H. Halloin, G. Heinzel, T. Hertog, M. Hewitson, K. Holley-Bockelmann, D. Hollington, M. Hueller, H. Inchauspe, P. Jetzer, N. Karnesis, C. Killow, A. Klein, B. Klipstein, N. Korsakova, S. L. Larson, J. Livas, I. Lloro, N. Man, D. Mance, J. Martino, I. Mateos, K. McKenzie, S. T. McWilliams, C. Miller, G. Mueller, G. Nardini, G. Nelemans, M. Nofrarias, A. Petiteau, P. Pivato, E. Plagnol, E. Porter, J. Reiche, D. Robertson, N. Robertson, E. Rossi, G. Russano, B. Schutz, A. Sesana, D. Shoemaker, J. Slutsky, C. F. Sopuerta, T. Sumner, N. Tamanini, I. Thorpe, M. Troebs, M. Vallisneri, A. Vecchio, D. Vetrugno, S. Vitale, G. Wanner, H. Ward, P. Wass, W. Weber, J. Ziemer, and P. Zweifel. Laser Interferometer Space Antenna. *ArXiv e-prints*, Feb. 2017.

F. Antonini and D. Merritt. Relativity and the Evolution of the Galactic Center S-star orbits. ApJ, 763:L10, Jan. 2013. doi: 10.1088/2041-8205/763/1/L10.

F. Antonini, R. Capuzzo-Dolcetta, and D. Merritt. A counterpart to the radial-orbit instability in triaxial stellar systems. MNRAS, 399:671–682, Oct. 2009. doi: 10.1111/j.1365-2966.2009.15342.x.

F. Antonini, J. Faber, A. Gualandris, and D. Merritt. Tidal Breakup of Binary Stars at the Galactic Center and Its Consequences. ApJ, 713:90–104, Apr. 2010. doi: 10.1088/0004-637X/713/1/90.

F. Antonini, J. C. Lombardi, Jr., and D. Merritt. Tidal Breakup of Binary Stars at the Galactic Center. II. Hydrodynamic Simulations. ApJ, 731:128, Apr. 2011. doi: 10.1088/0004-637X/731/2/128.

F. Antonini, R. Capuzzo-Dolcetta, A. Mastrobuono-Battisti, and D. Merritt. Dissipationless Formation and Evolution of the Milky Way Nuclear Star Cluster. ApJ, 750:111, May 2012. doi: 10.1088/0004-637X/750/2/111.

F. Antonini, E. Barausse, and J. Silk. The Imprint of Massive Black Hole Mergers on the Correlation between Nuclear Star Clusters and Their Host Galaxies. ApJ, 806:L8, June 2015a. doi: 10.1088/2041-8205/806/1/L8.

F. Antonini, E. Barausse, and J. Silk. The Coevolution of Nuclear Star Clusters, Massive Black Holes, and Their Host Galaxies. ApJ, 812:72, Oct. 2015b. doi: 10.1088/0004-637X/812/1/72.

V. A. Antonov. On the Instability of Stationary Spherical Models with Purely Radial Motion. In P. T. de Zeeuw, editor, *Structure and Dynamics of Elliptical Galaxies*, volume 127 of *IAU Symposium*, page 549, 1987.

M. Arca-Sedda and R. Capuzzo-Dolcetta. Dynamical Friction in Cuspy Galaxies. ApJ, 785:51, Apr. 2014. doi: 10.1088/0004-637X/785/1/51.

M. Arca-Sedda, R. Capuzzo-Dolcetta, F. Antonini, and A. Seth. Henize 2–10: The Ongoing Formation of a Nuclear Star Cluster around a Massive Black Hole. ApJ, 806:220, June 2015. doi: 10.1088/0004-637X/806/2/220.

M. Arca-Sedda, R. Capuzzo-Dolcetta, and M. Spera. The dearth of nuclear star clusters in bright galaxies. MNRAS, 456:2457–2466, Mar. 2016. doi: 10.1093/mnras/stv2835.

M. Arca-Sedda, P. Berczik, R. Capuzzo-Dolcetta, G. Fragione, M. Sobolenko, and R. Spurzem. Supermassive black holes coalescence mediated by massive perturbers: gravitational waves emission and the Milky Way - Andromeda fate. *ArXiv e-prints*, Dec. 2017.

Z. Arzoumanian, D. F. Chernoff, and J. M. Cordes. The Velocity Distribution of Isolated Radio Pulsars. ApJ, 568:289–301, Mar. 2002. doi: 10.1086/338805.

S. Babak, J. Gair, A. Sesana, E. Barausse, C. F. Sopuerta, C. P. L. Berry, E. Berti, P. Amaro-Seoane, A. Petiteau, and A. Klein. Science with the space-based interferometer LISA. V. Extreme mass-ratio inspirals. Phys. Rev. D, 95(10):103012, May 2017. doi: 10.1103/PhysRevD.95.103012.

J. N. Bahcall and R. A. Wolf. Star distribution around a massive black hole in a globular cluster. ApJ, 209:214–232, Oct. 1976. doi: 10.1086/154711.

J. N. Bahcall and R. A. Wolf. The star distribution around a massive black hole in a globular cluster. II Unequal star masses. ApJ, 216:883–907, Sept. 1977. doi: 10.1086/155534.

V. C. Bailey and M. B. Davies. Red giant collisions in the Galactic Centre. MNRAS, 308:257–270, Sept. 1999. doi: 10.1046/j.1365-8711.1999.02740.x.

M. Balcells, A. W. Graham, and R. F. Peletier. Galactic Bulges from Hubble Space Telescope NICMOS Observations: Global Scaling Relations. ApJ, 665:1104–1114, Aug. 2007. doi: 10.1086/519753.

V. F. Baldassare, A. E. Reines, E. Gallo, and J. E. Greene. A $\sim$50,000 $M_{\odot}$ Solar Mass Black Hole in the Nucleus of RGG 118. ApJ, 809:L14, Aug. 2015. doi: 10.1088/2041-8205/809/1/L14.

B. Balick and R. L. Brown. Intense sub-arcsecond structure in the galactic center. ApJ, 194:265–270, Dec. 1974. doi: 10.1086/153242.

A. Ballone, M. Schartmann, A. Burkert, S. Gillessen, R. Genzel, T. K. Fritz, F. Eisenhauer, O. Pfuhl, and T. Ott. Hydrodynamical Simulations of a Compact Source Scenario for the Galactic Center Cloud G2. ApJ, 776:13, Oct. 2013. doi: 10.1088/0004-637X/776/1/13.

B. Bar-Or and T. Alexander. Steady-state Relativistic Stellar Dynamics Around a Massive Black hole. ApJ, 820:129, Apr. 2016. doi: 10.3847/0004-637X/820/2/129.

E. Barausse, V. Cardoso, and P. Pani. Can environmental effects spoil precision gravitational-wave astrophysics? Phys. Rev. D, 89(10):104059, May 2014. doi: 10.1103/PhysRevD.89.104059.

E. I. Barnes, P. A. Lanzel, and L. L. R. Williams. The Radial Orbit Instability in Collisionless N-Body Simulations. ApJ, 704:372–384, Oct. 2009. doi: 10.1088/0004-637X/704/1/372.

J. E. Barnes. Merger Time Scales. In T. von Hippel, C. Simpson, and N. Manset, editors, *Astrophysical Ages and Times Scales*, volume 245 of *Astronomical Society of the Pacific Conference Series*, page 382, 2001.

H. Bartko, F. Martins, T. K. Fritz, R. Genzel, Y. Levin, H. B. Perets, T. Paumard, S. Nayakshin, O. Gerhard, T. Alexander, K. Dodds-Eden, F. Eisenhauer, S. Gillessen, L. Mascetti, T. Ott, G. Perrin, O. Pfuhl, M. J. Reid, D. Rouan, A. Sternberg, and S. Trippe. Evidence for Warped Disks of Young Stars in the Galactic Center. ApJ, 697:1741–1763, June 2009. doi: 10.1088/0004-637X/697/2/1741.

H. Baumgardt, P. Amaro-Seoane, and R. Schödel. The distribution of stars around the Milky Way's black hole III: Comparison with simulations. *ArXiv e-prints*, Jan. 2017.

M. C. Begelman, R. D. Blandford, and M. J. Rees. Massive black hole binaries in active galactic nuclei. Nature, 287:307–309, Sept. 1980. doi: 10.1038/287307a0.

P. Beniamini and T. Piran. Formation of double neutron star systems as implied by observations. MNRAS, 456:4089–4099, Mar. 2016. doi: 10.1093/mnras/stv2903.

P. Berczik, D. Merritt, R. Spurzem, and H.-P. Bischof. Efficient Merger of Binary Supermassive Black Holes in Nonaxisymmetric Galaxies. ApJ, 642:L21–L24, May 2006. doi: 10.1086/504426.

C. P. L. Berry and J. R. Gair. Observing the Galaxy's massive black hole with gravitational wave bursts. MNRAS, 429:589–612, Feb. 2013a. doi: 10.1093/mnras/sts360.

C. P. L. Berry and J. R. Gair. Extreme-mass-ratio-bursts from extragalactic sources. MNRAS, 433:3572–3583, Aug. 2013b. doi: 10.1093/mnras/stt990.

J. Binney and S. Tremaine. *Galactic dynamics*. 1987.

T. Böker, S. Laine, R. P. van der Marel, M. Sarzi, H.-W. Rix, L. C. Ho, and J. C. Shields. A Hubble Space Telescope Census of Nuclear Star Clusters in Late-Type Spiral Galaxies. I. Observations and Image Analysis. AJ, 123:1389–1410, Mar. 2002. doi: 10.1086/339025.

P. Bonfini, T. Bitsakis, A. Zezas, P.-A. Duc, E. Iodice, O. González-Martín, G. Bruzual, and A. J. González Sanoja. Connecting traces of galaxy evolution: the missing core mass-morphological fine structure relation. MNRAS, 473: L94–L100, Jan. 2018. doi: 10.1093/mnrasl/slx169.

I. A. Bonnell and W. K. M. Rice. Star Formation Around Supermassive Black Holes. *Science*, 321:1060, Aug. 2008. doi: 10.1126/science.1160653.

T. A. Boroson and T. R. Lauer. A candidate sub-parsec supermassive binary black hole system. Nature, 458:53–55, Mar. 2009. doi: 10.1038/nature07779.

E. Bortolas, A. Gualandris, M. Dotti, M. Spera, and M. Mapelli. Brownian motion of massive black hole binaries and the final parsec problem. MNRAS, 461:1023–1031, Sept. 2016. doi: 10.1093/mnras/stw1372.

E. Bortolas, M. Mapelli, and M. Spera. Supernova kicks and dynamics of compact remnants in the Galactic Centre. MNRAS, 469:1510–1520, Aug. 2017. doi: 10.1093/mnras/stx930.

E. Bortolas, A. Gualandris, M. Dotti, and J. I. Read. The influence of massive black hole binaries on the morphology of merger remnants. MNRAS, 477:2310–2325, June 2018a. doi: 10.1093/mnras/sty775.

E. Bortolas, M. Mapelli, and M. Spera. Star cluster disruption by a massive black hole binary. MNRAS, 474:1054–1064, Feb. 2018b. doi: 10.1093/mnras/stx2795.

P. Brem, P. Amaro-Seoane, and C. F. Sopuerta. Blocking low-eccentricity EMRIs: a statistical direct-summation N-body study of the Schwarzschild barrier. MNRAS, 437:1259–1267, Jan. 2014. doi: 10.1093/mnras/stt1948.

A. Bressan, P. Marigo, L. Girardi, B. Salasnich, C. Dal Cero, S. Rubele, and A. Nanni. PARSEC: stellar tracks and isochrones with the PAdova and TRieste Stellar Evolution Code. MNRAS, 427:127–145, Nov. 2012. doi: 10.1111/j.1365-2966.2012.21948.x.

R. L. Brown. Precessing jets in Sagittarius A - Gas dynamics in the central parsec of the galaxy. ApJ, 262:110–119, Nov. 1982. doi: 10.1086/160401.

W. R. Brown, M. J. Geller, S. J. Kenyon, and M. J. Kurtz. Discovery of an Unbound Hypervelocity Star in the Milky Way Halo. ApJ, 622:L33–L36, Mar. 2005. doi: 10.1086/429378.

W. R. Brown, M. J. Geller, S. J. Kenyon, and M. J. Kurtz. Hypervelocity Stars. I. The Spectroscopic Survey. ApJ, 647:303–311, Aug. 2006. doi: 10.1086/505165.

W. R. Brown, J. Anderson, O. Y. Gnedin, H. E. Bond, M. J. Geller, and S. J. Kenyon. Proper Motions and Trajectories for 16 Extreme Runaway and Hypervelocity Stars. ApJ, 804:49, May 2015. doi: 10.1088/0004-637X/804/1/49.

W. R. Brown, M. G. Lattanzi, S. J. Kenyon, and M. J. Geller. Gaia and the Galactic Center Origin of Hypervelocity Stars. *ArXiv e-prints*, May 2018.

R. M. Buchholz, R. Schödel, and A. Eckart. Composition of the galactic center star cluster. Population analysis from adaptive optics narrow band spectral energy distributions. A&A, 499:483–501, May 2009. doi: 10.1051/0004-6361/200811497.

A. Burkert, M. Schartmann, C. Alig, S. Gillessen, R. Genzel, T. K. Fritz, and F. Eisenhauer. Physics of the Galactic Center Cloud G2, on Its Way toward the Supermassive Black Hole. ApJ, 750:58, May 2012. doi: 10.1088/0004-637X/750/1/58.

R. Capuzzo-Dolcetta. The Evolution of the Globular Cluster System in a Triaxial Galaxy: Can a Galactic Nucleus Form by Globular Cluster Capture? ApJ, 415:616, Oct. 1993. doi: 10.1086/173189.

R. Capuzzo-Dolcetta and P. Miocchi. Self-consistent simulations of nuclear cluster formation through globular cluster orbital decay and merging. MNRAS, 388:L69–L73, July 2008. doi: 10.1111/j.1745-3933.2008.00501.x.

R. Capuzzo-Dolcetta, M. Spera, and D. Punzo. A fully parallel, high precision, N-body code running on hybrid computing platforms. *Journal of Computational Physics*, 236:580–593, Mar. 2013. doi: 10.1016/j.jcp.2012.11.013.

C. M. Carollo, M. Stiavelli, P. T. de Zeeuw, and J. Mack. Spiral Galaxies with WFPC2.I.Nuclear Morphology, Bulges, Star Clusters, and Surface Brightness Profiles. AJ, 114:2366, Dec. 1997. doi: 10.1086/118654.

D. J. Carson, A. J. Barth, A. C. Seth, M. den Brok, M. Cappellari, J. E. Greene, L. C. Ho, and N. Neumayer. The Structure of Nuclear Star Clusters in Nearby Late-type Spiral Galaxies from Hubble Space Telescope Wide Field Camera 3 Imaging. AJ, 149:170, May 2015. doi: 10.1088/0004-6256/149/5/170.

M. Celoria, R. Oliveri, and A. Sesana. Lecture notes on black hole binary astrophysics. *ArXiv e-prints*, July 2018.

S. Chandrasekhar. *Principles of stellar dynamics*. 1942.

S. Chandrasekhar. Dynamical Friction. I. General Considerations: the Coefficient of Dynamical Friction. ApJ, 97:255, Mar. 1943. doi: 10.1086/144517.

P. Chatterjee, L. Hernquist, and A. Loeb. Effects of Wandering on the Coalescence of Black Hole Binaries in Galactic Centers. ApJ, 592:32–41, July 2003. doi: 10.1086/375552.

X. Chen and P. Amaro-Seoane. A Rapidly Evolving Region in the Galactic Center: Why S-stars Thermalize and More Massive Stars are Missing. ApJ, 786:L14, May 2014. doi: 10.1088/2041-8205/786/2/L14.

X. Chen and W.-B. Han. A New Type of Extreme-mass-ratio Inspirals Produced by Tidal Capture of Binary Black Holes. *ArXiv e-prints*, Jan. 2018.

Y. Chen, A. Bressan, L. Girardi, P. Marigo, X. Kong, and A. Lanza. PARSEC evolutionary tracks of massive stars up to 350 $M_\odot$ at metallicities $0.0001 \leq Z \leq 0.04$. MNRAS, 452:1068–1080, Sept. 2015. doi: 10.1093/mnras/stv1281.

Y. Clénet, D. Rouan, E. Gendron, F. Lacombe, A.-M. Lagrange, D. Mouillet, Y. Magnard, G. Rousset, T. Fusco, J. Montri, R. Genzel, R. Schödel, T. Ott, A. Eckart, O. Marco, and L. Tacconi-Garman. The infrared L'-band view of the Galactic Center with NAOS-CONICA at VLT. A&A, 417:L15–L19, Apr. 2004a. doi: 10.1051/0004-6361:20040031.

Y. Clénet, D. Rouan, D. Gratadour, F. Lacombe, E. Gendron, R. Genzel, T. Ott, R. Schödel, and P. Léna. Detection of the Sgr A* activity at 3.8 and 4.8 μm with NACO. A&A, 424:L21–L25, Sept. 2004b. doi: 10.1051/0004-6361:200400045.

M. Colpi. Massive Binary Black Holes in Galactic Nuclei and Their Path to Coalescence. Space Sci. Rev., 183:189–221, Sept. 2014. doi: 10.1007/s11214-014-0067-1.

M. Colpi and A. Sesana. *Gravitational Wave Sources in the Era of Multi-Band Gravitational Wave Astronomy*, pages 43–140. World Scientific Publishing Co, 2017. doi: 10.1142/9789813141766_0002.

M. Colpi, L. Mayer, and F. Governato. Dynamical Friction and the Evolution of Satellites in Virialized Halos: The Theory of Linear Response. ApJ, 525:720–733, Nov. 1999. doi: 10.1086/307952.

M. Colpi, M. Mapelli, and A. Possenti. Probing the Presence of a Single or Binary Black Hole in the Globular Cluster NGC 6752 with Pulsar Dynamics. ApJ, 599: 1260–1271, Dec. 2003. doi: 10.1086/379543.

P. Côté, J. P. Blakeslee, L. Ferrarese, A. Jordán, S. Mei, D. Merritt, M. Milosavljević, E. W. Peng, J. L. Tonry, and M. J. West. The ACS Virgo Cluster Survey. I. Introduction to the Survey. ApJS, 153:223–242, July 2004. doi: 10.1086/421490.

P. Côté, S. Piatek, L. Ferrarese, A. Jordán, D. Merritt, E. W. Peng, M. Haşegan, J. P. Blakeslee, S. Mei, M. J. West, M. Milosavljević, and J. L. Tonry. The ACS Virgo Cluster Survey. VIII. The Nuclei of Early-Type Galaxies. ApJS, 165: 57–94, July 2006. doi: 10.1086/504042.

T. J. Cox, S. N. Dutta, T. Di Matteo, L. Hernquist, P. F. Hopkins, B. Robertson, and V. Springel. The Kinematic Structure of Merger Remnants. ApJ, 650: 791–811, Oct. 2006. doi: 10.1086/507474.

M. B. Davies and A. King. The Stars of the Galactic Center. ApJ, 624:L25–L27, May 2005. doi: 10.1086/430308.

R. Davies, J. Schubert, M. Hartl, J. Alves, Y. Clénet, F. Lang-Bardl, H. Nicklas, J.-U. Pott, R. Ragazzoni, E. Tolstoy, T. Agocs, H. Anwand-Heerwart, S. Barboza, P. Baudoz, R. Bender, P. Bizenberger, A. Boccaletti, W. Boland, P. Bonifacio, F. Briegel, T. Buey, F. Chapron, M. Cohen, O. Czoske, S. Dreizler, R. Falomo, P. Feautrier, N. Förster Schreiber, E. Gendron, R. Genzel, M. Glück, D. Gratadour, R. Greimel, F. Grupp, M. Häuser, M. Haug, J. Hennawi, H. J. Hess, V. Hörmann, R. Hofferbert, U. Hopp, Z. Hubert, D. Ives, W. Kausch, F. Kerber, H. Kravcar, K. Kuijken, F. Lang-Bardl, M. Leitzinger, K. Leschinski, D. Massari, S. Mei, F. Merlin, L. Mohr, A. Monna, F. Müller, R. Navarro, M. Plattner, N. Przybilla, R. Ramlau, S. Ramsay, T. Ratzka, P. Rhode, J. Richter, H.-W. Rix, G. Rodeghiero, R.-R. Rohloff, G. Rousset, R. Ruddenklau, V. Schaffenroth,

J. Schlichter, A. Sevin, R. Stuik, E. Sturm, J. Thomas, N. Tromp, M. Turatto, G. Verdoes-Kleijn, F. Vidal, R. Wagner, M. Wegner, W. Zeilinger, B. Ziegler, and G. Zins. MICADO: first light imager for the E-ELT. In *Ground-based and Airborne Instrumentation for Astronomy VI*, volume 9908 of Proc. SPIE, page 99081Z, Aug. 2016. doi: 10.1117/12.2233047.

T. de Zeeuw and M. Franx. Structure and dynamics of elliptical galaxies. ARA&A, 29:239–274, 1991. doi: 10.1146/annurev.aa.29.090191.001323.

V. P. Debattista, B. Moore, T. Quinn, S. Kazantzidis, R. Maas, L. Mayer, J. Read, and J. Stadel. The Causes of Halo Shape Changes Induced by Cooling Baryons: Disks versus Substructures. ApJ, 681:1076-1088, July 2008. doi: 10.1086/587977.

W. Dehnen. A Family of Potential-Density Pairs for Spherical Galaxies and Bulges. MNRAS, 265:250, Nov. 1993. doi: 10.1093/mnras/265.1.250.

W. Dehnen. Phase-space mixing and the merging of cusps. MNRAS, 360:892–900, July 2005. doi: 10.1111/j.1365-2966.2005.09099.x.

W. Dehnen and J. I. Read. N-body simulations of gravitational dynamics. *European Physical Journal Plus*, 126:55, May 2011. doi: 10.1140/epjp/i2011-11055-3.

J. Dexter and R. M. O'Leary. The Peculiar Pulsar Population of the Central Parsec. ApJ, 783:L7, Mar. 2014. doi: 10.1088/2041-8205/783/1/L7.

P. Di Matteo, C. J. Jog, M. D. Lehnert, F. Combes, and B. Semelin. Generation of rotationally dominated galaxies by mergers of pressure-supported progenitors. A&A, 501:L9–L13, July 2009. doi: 10.1051/0004-6361/200912354.

T. Do, J. R. Lu, A. M. Ghez, M. R. Morris, S. Yelda, G. D. Martinez, S. A. Wright, and K. Matthews. Stellar Populations in the Central 0.5 pc of the Galaxy. I. A New Method for Constructing Luminosity Functions and Surface-density Profiles. ApJ, 764:154, Feb. 2013. doi: 10.1088/0004-637X/764/2/154.

E. N. Dorband, M. Hemsendorf, and D. Merritt. Systolic and hyper-systolic algorithms for the gravitational N-body problem, with an application to Brownian motion. *Journal of Computational Physics*, 185:484–511, Mar. 2003. doi: 10.1016/S0021-9991(02)00067-0.

F. Dosopoulou and F. Antonini. Dynamical Friction and the Evolution of Supermassive Black Hole Binaries: The Final Hundred-parsec Problem. ApJ, 840:31, May 2017. doi: 10.3847/1538-4357/aa6b58.

M. Dotti, A. Sesana, and R. Decarli. Massive Black Hole Binaries: Dynamical Evolution and Observational Signatures. *Advances in Astronomy*, 2012:940568, 2012. doi: 10.1155/2012/940568.

J. Dubinski. The Origin of the Brightest Cluster Galaxies. ApJ, 502:141–149, July 1998. doi: 10.1086/305901.

B. T. Dullo and A. W. Graham. Core Shapes and Orientations of Core-Sérsic Galaxies. ApJ, 798:55, Jan. 2015. doi: 10.1088/0004-637X/798/1/55.

T. Ebisuzaki, J. Makino, and S. K. Okumura. Merging of two galaxies with central black holes. Nature, 354:212–214, Nov. 1991. doi: 10.1038/354212a0.

A. Einstein. On a Stationary System with Spherical Symmetry Consisting of Many Gravitating Masses. *Annals of Mathematics*, 40:922, Oct. 1939.

A. Einstein and R. Lawson. *Relativity: The Special and the General Theory*. Relativity: The Special and the General Theory. Crown Trade Paperbacks, 1961. ISBN 9780517884416. URL `https://books.google.it/books?id=mEsIakMMIGIC`.

A. Escala, R. B. Larson, P. S. Coppi, and D. Mardones. The Role of Gas in the Merging of Massive Black Holes in Galactic Nuclei. I. Black Hole Merging in a Spherical Gas Cloud. ApJ, 607:765–777, June 2004. doi: 10.1086/386278.

O. Fakhouri, C.-P. Ma, and M. Boylan-Kolchin. The merger rates and mass assembly histories of dark matter haloes in the two Millennium simulations. MNRAS, 406:2267–2278, Aug. 2010. doi: 10.1111/j.1365-2966.2010.16859.x.

X. Fan, M. A. Strauss, D. P. Schneider, R. H. Becker, R. L. White, Z. Haiman, M. Gregg, L. Pentericci, E. K. Grebel, V. K. Narayanan, Y.-S. Loh, G. T. Richards, J. E. Gunn, R. H. Lupton, G. R. Knapp, Ž. Ivezić, W. N. Brandt, M. Collinge, L. Hao, D. Harbeck, F. Prada, J. Schaye, I. Strateva, N. Zakamska, S. Anderson, J. Brinkmann, N. A. Bahcall, D. Q. Lamb, S. Okamura, A. Szalay, and D. G. York. A Survey of z>5.7 Quasars in the Sloan Digital Sky Survey. II. Discovery of Three Additional Quasars at z>6. AJ, 125:1649–1659, Apr. 2003. doi: 10.1086/368246.

A. Feldmeier-Krause, N. Neumayer, R. Schödel, A. Seth, M. Hilker, P. T. de Zeeuw, H. Kuntschner, C. J. Walcher, N. Lützgendorf, and M. Kissler-Patig. KMOS view of the Galactic centre. I. Young stars are centrally concentrated. A&A, 584:A2, Dec. 2015. doi: 10.1051/0004-6361/201526336.

L. Ferrarese and H. Ford. Supermassive Black Holes in Galactic Nuclei: Past, Present and Future Research. Space Sci. Rev., 116:523–624, Feb. 2005. doi: 10.1007/s11214-005-3947-6.

L. Ferrarese and D. Merritt. A Fundamental Relation between Supermassive Black Holes and Their Host Galaxies. ApJ, 539:L9–L12, Aug. 2000. doi: 10.1086/312838.

L. Ferrarese, F. C. van den Bosch, H. C. Ford, W. Jaffe, and R. W. O'Connell. Hubble Space Telescope photometry of the central regions of Virgo cluster elliptical galaxies. 3: Brightness profiles. AJ, 108:1598–1609, Nov. 1994. doi: 10.1086/117180.

L. Ferrarese, P. Côté, E. Dalla Bontà, E. W. Peng, D. Merritt, A. Jordán, J. P. Blakeslee, M. Haşegan, S. Mei, S. Piatek, J. L. Tonry, and M. J. West. A Fundamental Relation between Compact Stellar Nuclei, Supermassive Black Holes, and Their Host Galaxies. ApJ, 644:L21–L24, June 2006. doi: 10.1086/505388.

A. V. Filippenko and L. C. Ho. A Low-Mass Central Black Hole in the Bulgeless Seyfert 1 Galaxy NGC 4395. ApJ, 588:L13–L16, May 2003. doi: 10.1086/375361.

C. Foster, J. van de Sande, F. D'Eugenio, L. Cortese, R. M. McDermid, J. Bland-Hawthorn, S. Brough, J. Bryant, S. M. Croom, M. Goodwin, I. S. Konstantopoulos, J. Lawrence, Á. R. López-Sánchez, A. M. Medling, M. S. Owers, S. N. Richards, N. Scott, D. S. Taranu, C. Tonini, and T. Zafar. The SAMI Galaxy Survey: the intrinsic shape of kinematically selected galaxies. MNRAS, 472: 966–978, Nov. 2017. doi: 10.1093/mnras/stx1869.

T. Fragos, B. Willems, V. Kalogera, N. Ivanova, G. Rockefeller, C. L. Fryer, and P. A. Young. Understanding Compact Object Formation and Natal Kicks. II. The Case of XTE J1118 + 480. ApJ, 697:1057–1070, June 2009. doi: 10.1088/0004-637X/697/2/1057.

M. Frigo and M. Balcells. Dynamical masses and non-homology of massive elliptical galaxies grown by dry mergers. *ArXiv e-prints*, Nov. 2016.

C. Fryer, A. Burrows, and W. Benz. Population Syntheses for Neutron Star Systems with Intrinsic Kicks. ApJ, 496:333–351, Mar. 1998. doi: 10.1086/305348.

C. L. Fryer, K. Belczynski, G. Wiktorowicz, M. Dominik, V. Kalogera, and D. E. Holz. Compact Remnant Mass Function: Dependence on the Explosion Mechanism and Metallicity. ApJ, 749:91, Apr. 2012. doi: 10.1088/0004-637X/749/1/91.

M. Fujii, M. Iwasawa, Y. Funato, and J. Makino. Evolution of Star Clusters near the Galactic Center: Fully Self-Consistent N-Body Simulations. ApJ, 686:1082-1093, Oct. 2008. doi: 10.1086/591483.

J. R. Gair, M. Vallisneri, S. L. Larson, and J. G. Baker. Testing General Relativity with Low-Frequency, Space-Based Gravitational-Wave Detectors. *Living Reviews in Relativity*, 16:7, Sept. 2013. doi: 10.12942/lrr-2013-7.

E. Gallego-Cano, R. Schödel, H. Dong, F. Nogueras-Lara, A. T. Gallego-Calvente, P. Amaro-Seoane, and H. Baumgardt. The distribution of old stars around the Milky Way's central black hole I: Star counts. *ArXiv e-prints*, Jan. 2017.

J.-L. Gan, X. Kang, J.-L. Hou, and R.-X. Chang. Modeling the dynamical friction timescale of a sinking satellite. *Research in Astronomy and Astrophysics*, 10: 1242–1254, Dec. 2010. doi: 10.1088/1674-4527/10/12/005.

A. K. Gautam, T. Do, A. M. Ghez, J. R. Lu, M. R. Morris, S. Sakai, G. Witzel, B. N. Sitarski, and S. Chappell. Constraining the Variability and Binary Fraction of Galactic Center Young Stars. In R. M. Crocker, S. N. Longmore, and G. V. Bicknell, editors, *The Multi-Messenger Astrophysics of the Galactic Centre*, volume 322 of *IAU Symposium*, pages 237–238, Jan. 2017. doi: 10.1017/S1743921316011996.

K. Gebhardt, R. Bender, G. Bower, A. Dressler, S. M. Faber, A. V. Filippenko, R. Green, C. Grillmair, L. C. Ho, J. Kormendy, T. R. Lauer, J. Magorrian, J. Pinkney, D. Richstone, and S. Tremaine. A Relationship between Nuclear Black Hole Mass and Galaxy Velocity Dispersion. ApJ, 539:L13–L16, Aug. 2000. doi: 10.1086/312840.

R. Genzel, N. Thatte, A. Krabbe, H. Kroker, and L. E. Tacconi-Garman. The Dark Mass Concentration in the Central Parsec of the Milky Way. ApJ, 472: 153, Nov. 1996. doi: 10.1086/178051.

R. Genzel, F. Eisenhauer, and S. Gillessen. The Galactic Center massive black hole and nuclear star cluster. *Reviews of Modern Physics*, 82:3121–3195, Oct. 2010. doi: 10.1103/RevModPhys.82.3121.

O. Gerhard. The Galactic Center HE I Stars: Remains of a Dissolved Young Cluster? ApJ, 546:L39–L42, Jan. 2001. doi: 10.1086/318054.

O. E. Gerhard and J. Binney. Triaxial galaxies containing massive black holes or central density cusps. MNRAS, 216:467–502, Sept. 1985. doi: 10.1093/mnras/216.2.467.

A. M. Ghez, G. Duchêne, K. Matthews, S. D. Hornstein, A. Tanner, J. Larkin, M. Morris, E. E. Becklin, S. Salim, T. Kremenek, D. Thompson, B. T. Soifer, G. Neugebauer, and I. McLean. The First Measurement of Spectral Lines in a Short-Period Star Bound to the Galaxy's Central Black Hole: A Paradox of Youth. ApJ, 586:L127–L131, Apr. 2003. doi: 10.1086/374804.

A. M. Ghez, S. D. Hornstein, J. R. Lu, A. Bouchez, D. Le Mignant, M. A. van Dam, P. Wizinowich, K. Matthews, M. Morris, E. E. Becklin, R. D. Campbell, J. C. Y. Chin, S. K. Hartman, E. M. Johansson, R. E. Lafon, P. J. Stomski, and D. M. Summers. The First Laser Guide Star Adaptive Optics Observations of the Galactic Center: Sgr A*'s Infrared Color and the Extended Red Emission in its Vicinity. ApJ, 635:1087–1094, Dec. 2005. doi: 10.1086/497576.

A. M. Ghez, S. Salim, N. N. Weinberg, J. R. Lu, T. Do, J. K. Dunn, K. Matthews, M. R. Morris, S. Yelda, E. E. Becklin, T. Kremenek, M. Milosavljevic, and J. Naiman. Measuring Distance and Properties of the Milky Way's Central Supermassive Black Hole with Stellar Orbits. ApJ, 689:1044–1062, Dec. 2008. doi: 10.1086/592738.

N. Giacobbo and M. Mapelli. The impact of electron-capture supernovae on merging double neutron stars. *ArXiv e-prints*, May 2018.

S. Gillessen, F. Eisenhauer, S. Trippe, T. Alexander, R. Genzel, F. Martins, and T. Ott. Monitoring Stellar Orbits Around the Massive Black Hole in the Galactic Center. ApJ, 692:1075–1109, Feb. 2009. doi: 10.1088/0004-637X/692/2/1075.

S. Gillessen, R. Genzel, T. K. Fritz, E. Quataert, C. Alig, A. Burkert, J. Cuadra, F. Eisenhauer, O. Pfuhl, K. Dodds-Eden, C. F. Gammie, and T. Ott. A gas cloud on its way towards the supermassive black hole at the Galactic Centre. Nature, 481:51–54, Jan. 2012. doi: 10.1038/nature10652.

S. Gillessen, R. Genzel, T. K. Fritz, F. Eisenhauer, O. Pfuhl, T. Ott, M. Schartmann, A. Ballone, and A. Burkert. Pericenter Passage of the Gas Cloud G2 in the Galactic Center. ApJ, 774:44, Sept. 2013. doi: 10.1088/0004-637X/774/1/44.

S. Gillessen, P. M. Plewa, F. Eisenhauer, R. Sari, I. Waisberg, M. Habibi, O. Pfuhl, E. George, J. Dexter, S. von Fellenberg, T. Ott, and R. Genzel. An Update on

Monitoring Stellar Orbits in the Galactic Center. ApJ, 837:30, Mar. 2017. doi: 10.3847/1538-4357/aa5c41.

T. Goerdt, B. Moore, J. I. Read, and J. Stadel. Core Creation in Galaxies and Halos Via Sinking Massive Objects. ApJ, 725:1707–1716, Dec. 2010. doi: 10.1088/0004-637X/725/2/1707.

F. G. Goicovic, A. Sesana, J. Cuadra, and F. Stasyszyn. Infalling clouds on to supermassive black hole binaries - II. Binary evolution and the final parsec problem. MNRAS, 472:514–531, Nov. 2017. doi: 10.1093/mnras/stx1996.

A. C. González-García and T. S. van Albada. Encounters between spherical galaxies - II. Systems with a dark halo. MNRAS, 361:1043–1054, Aug. 2005. doi: 10.1111/j.1365-2966.2005.09243.x.

A. W. Graham. Core Depletion from Coalescing Supermassive Black Holes. ApJ, 613:L33–L36, Sept. 2004. doi: 10.1086/424928.

A. W. Graham and R. Guzmán. HST Photometry of Dwarf Elliptical Galaxies in Coma, and an Explanation for the Alleged Structural Dichotomy between Dwarf and Bright Elliptical Galaxies. AJ, 125:2936–2950, June 2003. doi: 10.1086/374992.

A. W. Graham and L. R. Spitler. Quantifying the coexistence of massive black holes and dense nuclear star clusters. MNRAS, 397:2148–2162, Aug. 2009. doi: 10.1111/j.1365-2966.2009.15118.x.

A. W. Graham, P. Erwin, I. Trujillo, and A. Asensio Ramos. A New Empirical Model for the Structural Analysis of Early-Type Galaxies, and A Critical Review of the Nuker Model. AJ, 125:2951–2963, June 2003. doi: 10.1086/375320.

Gravity Collaboration, R. Abuter, A. Amorim, N. Anugu, M. Bauböck, M. Benisty, J. P. Berger, N. Blind, H. Bonnet, W. Brandner, A. Buron, C. Collin, F. Chapron, Y. Clénet, V. Coudé Du Foresto, P. T. de Zeeuw, C. Deen, F. Delplancke-Ströbele, R. Dembet, J. Dexter, G. Duvert, A. Eckart, F. Eisenhauer, G. Finger, N. M. Förster Schreiber, P. Fédou, P. Garcia, R. Garcia Lopez, F. Gao, E. Gendron, R. Genzel, S. Gillessen, P. Gordo, M. Habibi, X. Haubois, M. Haug, F. Haußmann, T. Henning, S. Hippler, M. Horrobin, Z. Hubert, N. Hubin, A. Jimenez Rosales, L. Jochum, K. Jocou, A. Kaufer, S. Kellner, S. Kendrew, P. Kervella, Y. Kok, M. Kulas, S. Lacour, V. Lapeyrère, B. Lazareff, J.-B. Le Bouquin, P. Léna, M. Lippa, R. Lenzen, A. Mérand, E. Müler, U. Neumann, T. Ott, L. Palanca, T. Paumard, L. Pasquini, K. Perraut, G. Perrin, O. Pfuhl, P. M. Plewa, S. Rabien, A. Ramírez, J. Ramos, C. Rau, G. Rodríguez-Coira, R.-R. Rohloff, G. Rousset, J. Sanchez-Bermudez, S. Scheithauer, M. Schöller, N. Schuler, J. Spyromilio, O. Straub, C. Straubmeier, E. Sturm, L. J. Tacconi, K. R. W. Tristram, F. Vincent, S. von Fellenberg, I. Wank, I. Waisberg, F. Widmann, E. Wieprecht, M. Wiest, E. Wiezorrek, J. Woillez, S. Yazici, D. Ziegler, and G. Zins. Detection of the gravitational redshift in the orbit of the star S2 near the Galactic centre massive black hole. A&A, 615:L15, July 2018. doi: 10.1051/0004-6361/201833718.

A. Gualandris and D. Merritt. Ejection of Supermassive Black Holes from Galaxy Cores. ApJ, 678:780-797, May 2008. doi: 10.1086/586877.

A. Gualandris and D. Merritt. Perturbations of Intermediate-mass Black Holes on Stellar Orbits in the Galactic Center. ApJ, 705:361–371, Nov. 2009. doi: 10.1088/0004-637X/705/1/361.

A. Gualandris and D. Merritt. Long-term Evolution of Massive Black Hole Binaries. IV. Mergers of Galaxies with Collisionally Relaxed Nuclei. ApJ, 744:74, Jan. 2012. doi: 10.1088/0004-637X/744/1/74.

A. Gualandris, M. Colpi, S. Portegies Zwart, and A. Possenti. Has the Black Hole in XTE J1118+480 Experienced an Asymmetric Natal Kick? ApJ, 618:845–851, Jan. 2005. doi: 10.1086/426126.

A. Gualandris, M. Dotti, and A. Sesana. Massive black hole binary plane reorientation in rotating stellar systems. MNRAS, 420:L38–L42, Feb. 2012a. doi: 10.1111/j.1745-3933.2011.01188.x.

A. Gualandris, M. Mapelli, and H. B. Perets. Eccentric disc instability in stellar discs formed from inspiralling gas clouds in the Galactic Centre. MNRAS, 427: 1793–1799, Dec. 2012b. doi: 10.1111/j.1365-2966.2012.22133.x.

A. Gualandris, J. I. Read, W. Dehnen, and E. Bortolas. Collisionless loss-cone refilling: there is no final parsec problem. MNRAS, 464:2301–2310, Jan. 2017. doi: 10.1093/mnras/stw2528.

M. Gullieuszik, L. Greggio, R. Falomo, L. Schreiber, and M. Uslenghi. Probing the nuclear star cluster of galaxies with extremely large telescopes. A&A, 568:A89, Aug. 2014. doi: 10.1051/0004-6361/201424279.

M. A. Gürkan and F. A. Rasio. The Disruption of Stellar Clusters Containing Massive Black Holes near the Galactic Center. ApJ, 628:236–245, July 2005. doi: 10.1086/430694.

M. Habibi, S. Gillessen, F. Martins, F. Eisenhauer, P. M. Plewa, O. Pfuhl, E. George, J. Dexter, I. Waisberg, T. Ott, S. von Fellenberg, M. Bauböck, A. Jimenez-Rosales, and R. Genzel. Twelve Years of Spectroscopic Monitoring in the Galactic Center: The Closest Look at S-stars near the Black Hole. ApJ, 847:120, Oct. 2017. doi: 10.3847/1538-4357/aa876f.

M. G. Haehnelt, P. Natarajan, and M. J. Rees. High-redshift galaxies, their active nuclei and central black holes. MNRAS, 300:817–827, Nov. 1998. doi: 10.1046/j.1365-8711.1998.01951.x.

C. J. Hailey, K. Mori, F. E. Bauer, M. E. Berkowitz, J. Hong, and B. J. Hord. A density cusp of quiescent X-ray binaries in the central parsec of the Galaxy. Nature, 556:70–73, Apr. 2018. doi: 10.1038/nature25029.

A. S. Hamers and H. B. Perets. Relaxation near Supermassive Black Holes Driven by Nuclear Spiral Arms: Anisotropic Hypervelocity Stars, S-stars, and Tidal Disruption Events. ApJ, 846:123, Sept. 2017. doi: 10.3847/1538-4357/aa7f29.

D. C. Heggie. Binary evolution in stellar dynamics. MNRAS, 173:729–787, Dec. 1975.

J. G. Hills. The effect of low-velocity, low-mass intruders (collisionless gas) on the dynamical evolution of a binary system. AJ, 88:1269–1283, Aug. 1983. doi: 10.1086/113418.

J. G. Hills. Hyper-velocity and tidal stars from binaries disrupted by a massive Galactic black hole. Nature, 331:687–689, Feb. 1988. doi: 10.1038/331687a0.

J. G. Hills. Computer simulations of encounters between massive black holes and binaries. AJ, 102:704–715, Aug. 1991. doi: 10.1086/115905.

D. Hils and P. L. Bender. Gradual approach to coalescence for compact stars orbiting massive black holes. ApJ, 445:L7–L10, May 1995. doi: 10.1086/187876.

M. Hilz, T. Naab, J. P. Ostriker, J. Thomas, A. Burkert, and R. Jesseit. Relaxation and stripping - The evolution of sizes, dispersions and dark matter fractions in major and minor mergers of elliptical galaxies. MNRAS, 425:3119–3136, Oct. 2012. doi: 10.1111/j.1365-2966.2012.21541.x.

M. Hilz, T. Naab, and J. P. Ostriker. How do minor mergers promote inside-out growth of ellipticals, transforming the size, density profile and dark matter fraction? MNRAS, 429:2924–2933, Mar. 2013. doi: 10.1093/mnras/sts501.

A. Hobbs and S. Nayakshin. Simulations of the formation of stellar discs in the Galactic Centre via cloud-cloud collisions. MNRAS, 394:191–206, Mar. 2009. doi: 10.1111/j.1365-2966.2008.14359.x.

G. Hobbs and S. Dai. A review of pulsar timing array gravitational wave research. *ArXiv e-prints*, July 2017.

G. Hobbs, D. R. Lorimer, A. G. Lyne, and M. Kramer. A statistical study of 233 pulsar proper motions. MNRAS, 360:974–992, July 2005. doi: 10.1111/j.1365-2966.2005.09087.x.

K. Holley-Bockelmann, J. C. Mihos, S. Sigurdsson, L. Hernquist, and C. Norman. The Evolution of Cuspy Triaxial Galaxies Harboring Central Black Holes. ApJ, 567:817–827, Mar. 2002. doi: 10.1086/338683.

E. Holmberg. On the Clustering Tendencies among the Nebulae. II. a Study of Encounters Between Laboratory Models of Stellar Systems by a New Integration Procedure. ApJ, 94:385, Nov. 1941. doi: 10.1086/144344.

J. S. Hong, M. van den Berg, J. E. Grindlay, and S. Laycock. Radial Distribution of X-Ray Point Sources Near the Galactic Center. ApJ, 706:223–237, Nov. 2009. doi: 10.1088/0004-637X/706/1/223.

C. Hopman and T. Alexander. The Orbital Statistics of Stellar Inspiral and Relaxation near a Massive Black Hole: Characterizing Gravitational Wave Sources. ApJ, 629:362–372, Aug. 2005. doi: 10.1086/431475.

C. Hopman and T. Alexander. The Effect of Mass Segregation on Gravitational Wave Sources near Massive Black Holes. ApJ, 645:L133–L136, July 2006. doi: 10.1086/506273.

J. R. Hurley, C. A. Tout, and O. R. Pols. Evolution of binary stars and the effect of tides on binary populations. MNRAS, 329:897–928, Feb. 2002. doi: 10.1046/j.1365-8711.2002.05038.x.

G. Iorio and V. Belokurov. The shape of the Galactic halo with *Gaia* DR2 RR Lyrae. Anatomy of an ancient major merger. *ArXiv e-prints*, Aug. 2018.

H.-T. Janka. Natal kicks of stellar mass black holes by asymmetric mass ejection in fallback supernovae. MNRAS, 434:1355–1361, Sept. 2013. doi: 10.1093/mnras/stt1106.

J. H. Jeans. The origin of binary systems. MNRAS, 79:408, Apr. 1919. doi: 10.1093/mnras/79.6.408.

N. Kacharov, N. Neumayer, A. C. Seth, M. Cappellari, R. McDermid, C. J. Walcher, and T. Böker. Stellar populations and star formation histories of the nuclear star clusters in six nearby galaxies. MNRAS, July 2018. doi: 10.1093/mnras/sty1985.

H. E. Kandrup, I. V. Pogorelov, and I. V. Sideris. Chaotic mixing in noisy Hamiltonian systems. MNRAS, 311:719–732, Feb. 2000. doi: 10.1046/j.1365-8711.2000.03097.x.

H. E. Kandrup, I. V. Sideris, B. Terzić, and C. L. Bohn. Supermassive Black Hole Binaries as Galactic Blenders. ApJ, 597:111–130, Nov. 2003. doi: 10.1086/378287.

Y. Kato, M. Miyoshi, R. Takahashi, H. Negoro, and R. Matsumoto. Measuring spin of a supermassive black hole at the Galactic centre - implications for a unique spin. MNRAS, 403:L74–L78, Mar. 2010. doi: 10.1111/j.1745-3933.2010.00818.x.

N. Katz. Dissipationless collapse in an expanding universe. ApJ, 368:325–336, Feb. 1991. doi: 10.1086/169696.

W. M. Keck Observatory. More Mystery Objects Detected Near Milky Way's Supermassive Black Hole. June 2018. URL `http://www.keckobservatory.org/g-objects/`.

J. A. Kennea, D. N. Burrows, C. Kouveliotou, D. M. Palmer, E. Göğüş, Y. Kaneko, P. A. Evans, N. Degenaar, M. T. Reynolds, J. M. Miller, R. Wijnands, K. Mori, and N. Gehrels. Swift Discovery of a New Soft Gamma Repeater, SGR J1745-29, near Sagittarius A*. ApJ, 770:L24, June 2013. doi: 10.1088/2041-8205/770/2/L24.

F. M. Khan, A. Just, and D. Merritt. Efficient Merger of Binary Supermassive Black Holes in Merging Galaxies. ApJ, 732:89, May 2011. doi: 10.1088/0004-637X/732/2/89.

F. M. Khan, M. Preto, P. Berczik, I. Berentzen, A. Just, and R. Spurzem. Mergers of Unequal-mass Galaxies: Supermassive Black Hole Binary Evolution and Structure of Merger Remnants. ApJ, 749:147, Apr. 2012. doi: 10.1088/0004-637X/749/2/147.

F. M. Khan, K. Holley-Bockelmann, P. Berczik, and A. Just. Supermassive Black Hole Binary Evolution in Axisymmetric Galaxies: The Final Parsec Problem is Not a Problem. ApJ, 773:100, Aug. 2013. doi: 10.1088/0004-637X/773/2/100.

F. M. Khan, D. Fiacconi, L. Mayer, P. Berczik, and A. Just. Swift coalescence of supermassive black holes in cosmological mergers of massive galaxies. *ArXiv e-prints*, Mar. 2016.

F. M. Khan, P. R. Capelo, L. Mayer, and P. Berczik. Dynamical Evolution and Merger Time-scales of LISA Massive Black Hole Binaries in Disk Galaxy Mergers. *ArXiv e-prints*, July 2018.

T. F. Kieffer and T. Bogdanović. Can Star-Disk Collisions Explain the Missing Red Giants Problem in the Galactic Center? ApJ, 823:155, June 2016. doi: 10.3847/0004-637X/823/2/155.

S. S. Kim and M. Morris. Dynamical Friction on Star Clusters near the Galactic Center. ApJ, 597:312–322, Nov. 2003. doi: 10.1086/378347.

S. S. Kim, D. F. Figer, and M. Morris. Dynamical Friction on Galactic Center Star Clusters with an Intermediate-Mass Black Hole. ApJ, 607:L123–L126, June 2004. doi: 10.1086/422032.

A. King. Black Holes, Galaxy Formation, and the M_{BH}-σ Relation. ApJ, 596: L27–L29, Oct. 2003. doi: 10.1086/379143.

I. R. King. The structure of star clusters. III. Some simple dynamical models. AJ, 71:64, Feb. 1966. doi: 10.1086/109857.

H. A. Kobulnicky and C. L. Fryer. A New Look at the Binary Characteristics of Massive Stars. ApJ, 670:747–765, Nov. 2007. doi: 10.1086/522073.

J. Kormendy. Brightness profiles of the cores of bulges and elliptical galaxies. ApJ, 292:L9–L13, May 1985. doi: 10.1086/184463.

J. Kormendy and L. C. Ho. Coevolution (Or Not) of Supermassive Black Holes and Host Galaxies. ARA&A, 51:511–653, Aug. 2013. doi: 10.1146/annurev-astro-082708-101811.

J. Kormendy and D. Richstone. Inward Bound—The Search For Supermassive Black Holes In Galactic Nuclei. ARA&A, 33:581, 1995. doi: 10.1146/annurev.aa.33.090195.003053.

J. Kormendy, D. B. Fisher, M. E. Cornell, and R. Bender. VizieR Online Data Catalog: Surface photometry of Virgo ellipticals (Kormendy+, 2009). *VizieR Online Data Catalog*, 218, Nov. 2009.

Y. Kozai. Secular perturbations of asteroids with high inclination and eccentricity. AJ, 67:591, Nov. 1962. doi: 10.1086/108790.

P. Kroupa. On the variation of the initial mass function. MNRAS, 322:231–246, Apr. 2001. doi: 10.1046/j.1365-8711.2001.04022.x.

G. Lake and C. Norman. Stellar and gaseous dynamics of triaxial galaxies. ApJ, 270:51–70, July 1983. doi: 10.1086/161097.

T. R. Lauer, E. A. Ajhar, Y.-I. Byun, A. Dressler, S. M. Faber, C. Grillmair, J. Kormendy, D. Richstone, and S. Tremaine. The Centers of Early-Type Galaxies with HST.I.An Observational Survey. AJ, 110:2622, Dec. 1995. doi: 10.1086/117719.

A. Le Tiec and J. Novak. *Theory of Gravitational Waves*, pages 1–41. World Scientific Publishing Co, 2017. doi: 10.1142/9789813141766_0001.

H. M. Lee. Dynamical effects of successive mergers on the evolution of spherical stellar systems. ApJ, 319:801–818, Aug. 1987. doi: 10.1086/165498.

Y. Levin. Formation of massive stars and black holes in self-gravitating AGN discs, and gravitational waves in LISA band. *ArXiv Astrophysics e-prints*, July 2003.

M. L. Lidov. The evolution of orbits of artificial satellites of planets under the action of gravitational perturbations of external bodies. Planet. Space Sci., 9: 719–759, Oct. 1962. doi: 10.1016/0032-0633(62)90129-0.

D. Lin, J. Strader, E. R. Carrasco, D. Page, A. J. Romanowsky, J. Homan, J. A. Irwin, R. A. Remillard, O. Godet, N. A. Webb, H. Baumgardt, R. Wijnands, D. Barret, P.-A. Duc, J. P. Brodie, and S. D. J. Gwyn. A luminous X-ray outburst from an intermediate-mass black hole in an off-centre star cluster. *Nature Astronomy*, June 2018. doi: 10.1038/s41550-018-0493-1.

H. H. Loose, E. Kruegel, and A. Tutukov. Bursts of star formation in the galactic centre. A&A, 105:342–350, Jan. 1982.

C. X. Lu and S. Naoz. SNe Kicks in Hierarchical Triple Systems. *ArXiv e-prints*, May 2018.

J. R. Lu, T. Do, A. M. Ghez, M. R. Morris, S. Yelda, and K. Matthews. Stellar Populations in the Central 0.5 pc of the Galaxy. II. The Initial Mass Function. ApJ, 764:155, Feb. 2013. doi: 10.1088/0004-637X/764/2/155.

D. Lynden-Bell. Statistical mechanics of violent relaxation in stellar systems. MNRAS, 136:101, 1967. doi: 10.1093/mnras/136.1.101.

D. Lynden-Bell. Galactic Nuclei as Collapsed Old Quasars. Nature, 223:690–694, Aug. 1969. doi: 10.1038/223690a0.

J. D. MacMillan, L. M. Widrow, and R. N. Henriksen. On Universal Halos and the Radial Orbit Instability. ApJ, 653:43–52, Dec. 2006. doi: 10.1086/508602.

J.-P. Macquart and N. Kanekar. On Detecting Millisecond Pulsars at the Galactic Center. ApJ, 805:172, June 2015. doi: 10.1088/0004-637X/805/2/172.

P. Madau and M. Dickinson. Cosmic Star-Formation History. ARA&A, 52:415–486, Aug. 2014. doi: 10.1146/annurev-astro-081811-125615.

Y. Maeda, F. K. Baganoff, E. D. Feigelson, M. Morris, M. W. Bautz, W. N. Brandt, D. N. Burrows, J. P. Doty, G. P. Garmire, S. H. Pravdo, G. R. Ricker, and L. K. Townsley. A Chandra Study of Sagittarius A East: A Supernova Remnant Regulating the Activity of Our Galactic Center? ApJ, 570:671–687, May 2002. doi: 10.1086/339773.

J. Magorrian, S. Tremaine, D. Richstone, R. Bender, G. Bower, A. Dressler, S. M. Faber, K. Gebhardt, R. Green, C. Grillmair, J. Kormendy, and T. Lauer. The Demography of Massive Dark Objects in Galaxy Centers. AJ, 115:2285–2305, June 1998. doi: 10.1086/300353.

J. Makino and Y. Funato. Evolution of Massive Black Hole Binaries. ApJ, 602: 93–102, Feb. 2004. doi: 10.1086/380917.

I. Mandel. Estimates of black hole natal kick velocities from observations of low-mass X-ray binaries. MNRAS, 456:578–581, Feb. 2016. doi: 10.1093/mnras/stv2733.

M. Mapelli. 12th Edoardo Amaldi Conference on Gravitational Waves (AMALDI 12). In *Journal of Physics Conference Series*, volume 957 of *Journal of Physics Conference Series*, page 011001, Feb. 2018. doi: 10.1088/1742-6596/957/1/011001.

M. Mapelli and N. Giacobbo. The cosmic merger rate of neutron stars and black holes. MNRAS, 479:4391–4398, Oct. 2018. doi: 10.1093/mnras/sty1613.

M. Mapelli and A. Gualandris. Star Formation and Dynamics in the Galactic Centre. In F. Haardt, V. Gorini, U. Moschella, A. Treves, and M. Colpi, editors, *Lecture Notes in Physics, Berlin Springer Verlag*, volume 905 of *Lecture Notes in Physics, Berlin Springer Verlag*, page 205, 2016. doi: 10.1007/978-3-319-19416-5_6.

M. Mapelli, M. Colpi, A. Possenti, and S. Sigurdsson. The fingerprint of binary intermediate-mass black holes in globular clusters: suprathermal stars and angular momentum alignment. MNRAS, 364:1315–1326, Dec. 2005. doi: 10.1111/j.1365-2966.2005.09653.x.

M. Mapelli, T. Hayfield, L. Mayer, and J. Wadsley. In Situ Formation of SgrA* Stars Via Disk Fragmentation: Parent Cloud Properties and Thermodynamics. ApJ, 749:168, Apr. 2012. doi: 10.1088/0004-637X/749/2/168.

M. Mapelli, A. Gualandris, and T. Hayfield. Perturbations induced by a molecular cloud on the young stellar disc in the Galactic Centre. MNRAS, 436:3809–3819, Dec. 2013a. doi: 10.1093/mnras/stt1858.

M. Mapelli, L. Zampieri, E. Ripamonti, and A. Bressan. Dynamics of stellar black holes in young star clusters with different metallicities - I. Implications for X-ray binaries. MNRAS, 429:2298–2314, Mar. 2013b. doi: 10.1093/mnras/sts500.

A. Marconi and L. K. Hunt. The Relation between Black Hole Mass, Bulge Mass, and Near-Infrared Luminosity. ApJ, 589:L21–L24, May 2003. doi: 10.1086/375804.

A. Marconi, G. Risaliti, R. Gilli, L. K. Hunt, R. Maiolino, and M. Salvati. Local supermassive black holes, relics of active galactic nuclei and the X-ray background. MNRAS, 351:169–185, June 2004. doi: 10.1111/j.1365-2966.2004.07765.x.

H. Matsui and A. Habe. Effects of Minor Mergers on the Coalescence of a Supermassive Black Hole Binary. PASJ, 61:421–428, June 2009. doi: 10.1093/pasj/61.3.421.

S. L. W. McMillan and S. F. Portegies Zwart. The Fate of Star Clusters near the Galactic Center. I. Analytic Considerations. ApJ, 596:314–322, Oct. 2003. doi: 10.1086/377577.

F. Melia. *The black hole at the center of our galaxy.* 2003.

D. Merritt. Relaxation and tidal stripping in rich clusters of galaxies. II. Evolution of the luminosity distribution. ApJ, 276:26–37, Jan. 1984. doi: 10.1086/161590.

D. Merritt. Brownian Motion of a Massive Binary. ApJ, 556:245–264, July 2001. doi: 10.1086/321550.

D. Merritt. A Note on Gravitational Brownian Motion. ApJ, 628:673–677, Aug. 2005. doi: 10.1086/429398.

D. Merritt. The Distribution of Stars and Stellar Remnants at the Galactic Center. ApJ, 718:739–761, Aug. 2010. doi: 10.1088/0004-637X/718/2/739.

D. Merritt. *Dynamics and Evolution of Galactic Nuclei.* July 2013a.

D. Merritt. Loss-cone dynamics. *Classical and Quantum Gravity*, 30(24):244005, Dec. 2013b. doi: 10.1088/0264-9381/30/24/244005.

D. Merritt and L. Ferrarese. Black hole demographics from the M_L-σ relation. MNRAS, 320:L30–L34, Jan. 2001. doi: 10.1046/j.1365-8711.2001.04165.x.

D. Merritt and T. Fridman. Triaxial Galaxies with Cusps. ApJ, 460:136, Mar. 1996. doi: 10.1086/176957.

D. Merritt and G. D. Quinlan. Dynamical Evolution of Elliptical Galaxies with Central Singularities. ApJ, 498:625–639, May 1998. doi: 10.1086/305579.

D. Merritt and M. Valluri. Chaos and Mixing in Triaxial Stellar Systems. ApJ, 471:82, Nov. 1996. doi: 10.1086/177955.

D. Merritt and E. Vasiliev. Orbits Around Black Holes in Triaxial Nuclei. ApJ, 726:61, Jan. 2011. doi: 10.1088/0004-637X/726/2/61.

D. Merritt, P. Berczik, and F. Laun. Brownian Motion of Black Holes in Dense Nuclei. AJ, 133:553–563, Feb. 2007a. doi: 10.1086/510294.

D. Merritt, S. Mikkola, and A. Szell. Long-Term Evolution of Massive Black Hole Binaries. III. Binary Evolution in Collisional Nuclei. ApJ, 671:53–72, Dec. 2007b. doi: 10.1086/522691.

D. Merritt, J. D. Schnittman, and S. Komossa. Hypercompact Stellar Systems Around Recoiling Supermassive Black Holes. ApJ, 699:1690–1710, July 2009. doi: 10.1088/0004-637X/699/2/1690.

D. Merritt, T. Alexander, S. Mikkola, and C. M. Will. Stellar dynamics of extreme-mass-ratio inspirals. Phys. Rev. D, 84(4):044024, Aug. 2011. doi: 10.1103/PhysRevD.84.044024.

D. N. Mikhaloff and H. B. Perets. Short- and long-term evolution of a stellar disc around a massive black hole: the role of the cusp, stellar evolution and binaries. MNRAS, 465:281–292, Feb. 2017. doi: 10.1093/mnras/stw2813.

S. Mikkola and K. Tanikawa. Explicit Symplectic Algorithms For Time-Transformed Hamiltonians. *Celestial Mechanics and Dynamical Astronomy*, 74: 287–295, Aug. 1999a. doi: 10.1023/A:1008368322547.

S. Mikkola and K. Tanikawa. Algorithmic regularization of the few-body problem. MNRAS, 310:745–749, Dec. 1999b. doi: 10.1046/j.1365-8711.1999.02982.x.

M. C. Miller, M. Freitag, D. P. Hamilton, and V. M. Lauburg. Binary Encounters with Supermassive Black Holes: Zero-Eccentricity LISA Events. ApJ, 631:L117–L120, Oct. 2005. doi: 10.1086/497335.

M. Milosavljević. On the Origin of Nuclear Star Clusters in Late-Type Spiral Galaxies. ApJ, 605:L13–L16, Apr. 2004. doi: 10.1086/420696.

M. Milosavljević and D. Merritt. Formation of Galactic Nuclei. ApJ, 563:34–62, Dec. 2001. doi: 10.1086/323830.

M. Milosavljević and D. Merritt. Long-Term Evolution of Massive Black Hole Binaries. ApJ, 596:860–878, Oct. 2003a. doi: 10.1086/378086.

M. Milosavljević and D. Merritt. The Final Parsec Problem. In J. M. Centrella, editor, *The Astrophysics of Gravitational Wave Sources*, volume 686 of *American Institute of Physics Conference Series*, pages 201–210, Oct. 2003b. doi: 10.1063/1.1629432.

M. Milosavljević, D. Merritt, A. Rest, and F. C. van den Bosch. Galaxy cores as relics of black hole mergers. MNRAS, 331:L51–L55, Apr. 2002. doi: 10.1046/j.1365-8711.2002.05436.x.

F. Mirabel. The formation of stellar black holes. New A Rev., 78:1–15, Aug. 2017. doi: 10.1016/j.newar.2017.04.002.

C. W. Misner, K. S. Thorne, and J. A. Wheeler. *Gravitation*. 1973.

M. Miyoshi, J. Moran, J. Herrnstein, L. Greenhill, N. Nakai, P. Diamond, and M. Inoue. Evidence for a black hole from high rotation velocities in a sub-parsec region of NGC4258. Nature, 373:127–129, Jan. 1995. doi: 10.1038/373127a0.

C. J. Moore, R. H. Cole, and C. P. L. Berry. Gravitational-wave sensitivity curves. *Classical and Quantum Gravity*, 32(1):015014, Jan. 2015. doi: 10.1088/0264-9381/32/1/015014.

K. Mori, E. V. Gotthelf, S. Zhang, H. An, F. K. Baganoff, N. M. Barrière, A. M. Beloborodov, S. E. Boggs, F. E. Christensen, W. W. Craig, F. Dufour, B. W. Grefenstette, C. J. Hailey, F. A. Harrison, J. Hong, V. M. Kaspi, J. A. Kennea, K. K. Madsen, C. B. Markwardt, M. Nynka, D. Stern, J. A. Tomsick, and W. W. Zhang. NuSTAR Discovery of a 3.76 s Transient Magnetar Near Sagittarius A*. ApJ, 770:L23, June 2013. doi: 10.1088/2041-8205/770/2/L23.

M. Morris. Massive star formation near the Galactic center and the fate of the stellar remnants. ApJ, 408:496–506, May 1993. doi: 10.1086/172607.

W. A. Mulder. Dynamical friction on extended objects. A&A, 117:9–16, Jan. 1983.

M. P. Muno, J. R. Lu, F. K. Baganoff, W. N. Brandt, G. P. Garmire, A. M. Ghez, S. D. Hornstein, and M. R. Morris. A Remarkable Low-Mass X-Ray Binary within 0.1 Parsecs of the Galactic Center. ApJ, 633:228–239, Nov. 2005. doi: 10.1086/444586.

T. Naab. Modelling the formation of today's massive ellipticals. In D. Thomas, A. Pasquali, and I. Ferreras, editors, *The Intriguing Life of Massive Galaxies*, volume 295 of *IAU Symposium*, pages 340–349, July 2013. doi: 10.1017/S1743921313005334.

T. Naab and J. P. Ostriker. Theoretical Challenges in Galaxy Formation. *ArXiv e-prints*, Dec. 2016.

T. Naab, P. H. Johansson, and J. P. Ostriker. Minor Mergers and the Size Evolution of Elliptical Galaxies. ApJ, 699:L178–L182, July 2009. doi: 10.1088/0004-637X/699/2/L178.

S. Naoz, A. M. Ghez, A. Hees, T. Do, G. Witzel, and J. R. Lu. Confusing Binaries: The Role of Stellar Binaries in Biasing Disk Properties in the Galactic Center. ApJ, 853:L24, Feb. 2018. doi: 10.3847/2041-8213/aaa6bf.

S. Nayakshin and R. Sunyaev. The 'missing' young stellar objects in the central parsec of the Galaxy: evidence for star formation in a massive accretion disc and a top-heavy initial mass function. MNRAS, 364:L23–L27, Nov. 2005. doi: 10.1111/j.1745-3933.2005.00097.x.

S. Nayakshin, J. Cuadra, and V. Springel. Simulations of star formation in a gaseous disc around Sgr A* - a failed active galactic nucleus. MNRAS, 379:21–33, July 2007. doi: 10.1111/j.1365-2966.2007.11938.x.

K. Nitadori and J. Makino. Sixth- and eighth-order Hermite integrator for N-body simulations. New A, 13:498–507, Oct. 2008. doi: 10.1016/j.newast.2008.01.010.

C. Norman and J. Silk. The dynamics and fueling of active nuclei. ApJ, 266:502–515, Mar. 1983. doi: 10.1086/160798.

G. Novak, J. L. Dotson, C. D. Dowell, R. H. Hildebrand, T. Renbarger, and D. A. Schleuning. Submillimeter Polarimetric Observations of the Galactic Center. ApJ, 529:241–250, Jan. 2000. doi: 10.1086/308231.

E. Öpik. . *Pulications de L'Observatoire Astronomique de l'Université de Tartu*, 25:6, July 1924.

L. Oser, T. Naab, J. P. Ostriker, and P. H. Johansson. The Cosmological Size and Velocity Dispersion Evolution of Massive Early-type Galaxies. ApJ, 744:63, Jan. 2012. doi: 10.1088/0004-637X/744/1/63.

R. O'Shaughnessy, D. Gerosa, and D. Wysocki. Inferences about Supernova Physics from Gravitational-Wave Measurements: GW151226 Spin Misalignment as an Indicator of Strong Black-Hole Natal Kicks. *Physical Review Letters*, 119(1): 011101, July 2017. doi: 10.1103/PhysRevLett.119.011101.

J. P. Ostriker. Elliptical Galaxies are not Made by Merging Spiral Galaxies. *Comments on Astrophysics*, 8:177, 1980.

T. Panamarev, B. Shukirgaliyev, Y. Meiron, P. Berczik, A. Just, R. Spurzem, C. Omarov, and E. Vilkoviskij. Star-disc interaction in galactic nuclei: formation of a central stellar disc. MNRAS, 476:4224–4233, May 2018. doi: 10.1093/mnras/sty459.

T. Paumard, R. Genzel, F. Martins, S. Nayakshin, A. M. Beloborodov, Y. Levin, S. Trippe, F. Eisenhauer, T. Ott, S. Gillessen, R. Abuter, J. Cuadra, T. Alexander, and A. Sternberg. The Two Young Star Disks in the Central Parsec of the Galaxy: Properties, Dynamics, and Formation. ApJ, 643:1011–1035, June 2006. doi: 10.1086/503273.

P. J. E. Peebles. Star Distribution Near a Collapsed Object. ApJ, 178:371–376, Dec. 1972a. doi: 10.1086/151797.

P. J. E. Peebles. Gravitational collapse and related phenomena from an empirical point of view, or, black holes are where you find them. *General Relativity and Gravitation*, 3:63–82, June 1972b. doi: 10.1007/BF00755923.

S. Peirani, R. M. Crockett, S. Geen, S. Khochfar, S. Kaviraj, and J. Silk. Composite star formation histories of early-type galaxies from minor mergers: prospects for WFC3. MNRAS, 405:2327–2338, July 2010. doi: 10.1111/j.1365-2966.2010.16666.x.

C. Y. Peng. How Mergers May Affect the Mass Scaling Relation between Gravitationally Bound Systems. ApJ, 671:1098–1107, Dec. 2007. doi: 10.1086/522774.

H. B. Perets and T. Alexander. Massive Perturbers and the Efficient Merger of Binary Massive Black Holes. ApJ, 677:146-159, Apr. 2008. doi: 10.1086/527525.

H. B. Perets and A. Gualandris. Dynamical Constraints on the Origin of the Young B-stars in the Galactic Center. ApJ, 719:220–228, Aug. 2010. doi: 10.1088/0004-637X/719/1/220.

H. B. Perets, G. Kupi, and T. Alexander. Getting a Kick out of the Stellar Disk(s) in the Galactic Center. In E. Vesperini, M. Giersz, and A. Sills, editors, *Dynamical Evolution of Dense Stellar Systems*, volume 246 of *IAU Symposium*, pages 275–276, May 2008. doi: 10.1017/S1743921308015780.

H. B. Perets, A. Gualandris, G. Kupi, D. Merritt, and T. Alexander. Dynamical Evolution of the Young Stars in the Galactic Center: N-body Simulations of the S-Stars. ApJ, 702:884–889, Sept. 2009. doi: 10.1088/0004-637X/702/2/884.

P. C. Peters. Gravitational Radiation and the Motion of Two Point Masses. *Physical Review*, 136:1224–1232, Nov. 1964. doi: 10.1103/PhysRev.136.B1224.

B. M. Peterson. Measuring the Masses of Supermassive Black Holes. Space Sci. Rev., 183:253–275, Sept. 2014. doi: 10.1007/s11214-013-9987-4.

J. A. Petts and A. Gualandris. Infalling Young Clusters in the Galactic Centre: implications for IMBHs and young stellar populations. *ArXiv e-prints*, Jan. 2017.

E. Pfahl and A. Loeb. Probing the Spacetime around Sagittarius A* with Radio Pulsars. ApJ, 615:253–258, Nov. 2004. doi: 10.1086/423975.

E. Pfahl, S. Rappaport, P. Podsiadlowski, and H. Spruit. A New Class of High-Mass X-Ray Binaries: Implications for Core Collapse and Neutron Star Recoil. ApJ, 574:364–376, July 2002. doi: 10.1086/340794.

O. Pfuhl, T. K. Fritz, M. Zilka, H. Maness, F. Eisenhauer, R. Genzel, S. Gillessen, T. Ott, K. Dodds-Eden, and A. Sternberg. The Star Formation History of the Milky Way's Nuclear Star Cluster. ApJ, 741:108, Nov. 2011. doi: 10.1088/0004-637X/741/2/108.

O. Pfuhl, T. Alexander, S. Gillessen, F. Martins, R. Genzel, F. Eisenhauer, T. K. Fritz, and T. Ott. Massive Binaries in the Vicinity of Sgr A*. ApJ, 782:101, Feb. 2014. doi: 10.1088/0004-637X/782/2/101.

O. Pfuhl, S. Gillessen, F. Eisenhauer, R. Genzel, P. M. Plewa, T. Ott, A. Ballone, M. Schartmann, A. Burkert, T. K. Fritz, R. Sari, E. Steinberg, and A.-M. Madigan. The Galactic Center Cloud G2 and its Gas Streamer. ApJ, 798:111, Jan. 2015. doi: 10.1088/0004-637X/798/2/111.

A. C. Phillips, G. D. Illingworth, J. W. MacKenty, and M. Franx. Nuclei of Nearby Disk Galaxies.I.A Hubble Space Telescope Imaging Survey. AJ, 111:1566, Apr. 1996. doi: 10.1086/117896.

T. Piffl, C. Scannapieco, J. Binney, M. Steinmetz, R.-D. Scholz, M. E. K. Williams, R. S. de Jong, G. Kordopatis, G. Matijevič, O. Bienaymé, J. Bland-Hawthorn, C. Boeche, K. Freeman, B. Gibson, G. Gilmore, E. K. Grebel, A. Helmi, U. Munari, J. F. Navarro, Q. Parker, W. A. Reid, G. Seabroke, F. Watson, R. F. G. Wyse, and T. Zwitter. The RAVE survey: the Galactic escape speed and the mass of the Milky Way. A&A, 562:A91, Feb. 2014. doi: 10.1051/0004-6361/201322531.

H. C. Plummer. On the problem of distribution in globular star clusters. MNRAS, 71:460–470, Mar. 1911.

A. Pontzen, J. I. Read, R. Teyssier, F. Governato, A. Gualandris, N. Roth, and J. Devriendt. Milking the spherical cow - on aspherical dynamics in spherical coordinates. MNRAS, 451:1366–1379, Aug. 2015. doi: 10.1093/mnras/stv1032.

M. Y. Poon and D. Merritt. Orbital Structure of Triaxial Black Hole Nuclei. ApJ, 549:192–204, Mar. 2001. doi: 10.1086/319060.

M. Y. Poon and D. Merritt. Triaxial Black Hole Nuclei. ApJ, 568:L89–L92, Apr. 2002. doi: 10.1086/340395.

M. Y. Poon and D. Merritt. A Self-Consistent Study of Triaxial Black Hole Nuclei. ApJ, 606:774–787, May 2004. doi: 10.1086/383190.

S. F. Portegies Zwart, S. L. W. McMillan, and O. Gerhard. The Origin of IRS 16: Dynamically Driven In-Spiral of a Dense Star Cluster to the Galactic Center? ApJ, 593:352–357, Aug. 2003. doi: 10.1086/376439.

S. F. Portegies Zwart, S. L. W. McMillan, and M. Gieles. Young Massive Star Clusters. ARA&A, 48:431–493, Sept. 2010. doi: 10.1146/annurev-astro-081309-130834.

M. Preto and P. Amaro-Seoane. On Strong Mass Segregation Around a Massive Black Hole: Implications for Lower-Frequency Gravitational-Wave Astrophysics. ApJ, 708:L42–L46, Jan. 2010. doi: 10.1088/2041-8205/708/1/L42.

M. Preto, I. Berentzen, P. Berczik, and R. Spurzem. Fast Coalescence of Massive Black Hole Binaries from Mergers of Galactic Nuclei: Implications for Low-frequency Gravitational-wave Astrophysics. ApJ, 732:L26, May 2011. doi: 10.1088/2041-8205/732/2/L26.

S. Prodan, F. Antonini, and H. B. Perets. Secular Evolution of Binaries near Massive Black Holes: Formation of Compact Binaries, Merger/Collision Products and G2-like Objects. ApJ, 799:118, Feb. 2015. doi: 10.1088/0004-637X/799/2/118.

G. D. Quinlan. The dynamical evolution of massive black hole binaries I. Hardening in a fixed stellar background. New A, 1:35–56, July 1996. doi: 10.1016/S1384-1076(96)00003-6.

G. D. Quinlan and L. Hernquist. The dynamical evolution of massive black hole binaries – II. Self-consistent N-body integrations. New A, 2:533–554, Dec. 1997. doi: 10.1016/S1384-1076(97)00039-0.

K. Rajwade, D. Lorimer, and L. Anderson. Detecting pulsars in the Galactic centre. *ArXiv e-prints*, Nov. 2016.

K. P. Rauch. Dynamical evolution of star clusters around a rotating black hole with an accretion disc. MNRAS, 275:628–640, Aug. 1995. doi: 10.1093/mnras/275.3.628.

K. P. Rauch and S. Tremaine. Resonant relaxation in stellar systems. New A, 1:149–170, Oct. 1996. doi: 10.1016/S1384-1076(96)00012-7.

N. Rea, P. Esposito, J. A. Pons, R. Turolla, D. F. Torres, G. L. Israel, A. Possenti, M. Burgay, D. Viganò, A. Papitto, R. Perna, L. Stella, G. Ponti, F. K. Baganoff, D. Haggard, A. Camero-Arranz, S. Zane, A. Minter, S. Mereghetti, A. Tiengo, R. Schödel, M. Feroci, R. Mignani, and D. Götz. A Strongly Magnetized Pulsar within the Grasp of the Milky Way's Supermassive Black Hole. ApJ, 775:L34, Oct. 2013. doi: 10.1088/2041-8205/775/2/L34.

M. J. Rees. Black Hole Models for Active Galactic Nuclei. ARA&A, 22:471–506, 1984. doi: 10.1146/annurev.aa.22.090184.002351.

A. E. Reines and M. Volonteri. Relations between Central Black Hole Mass and Total Galaxy Stellar Mass in the Local Universe. ApJ, 813:82, Nov. 2015. doi: 10.1088/0004-637X/813/2/82.

S. Repetto, M. B. Davies, and S. Sigurdsson. Investigating stellar-mass black hole kicks. MNRAS, 425:2799–2809, Oct. 2012. doi: 10.1111/j.1365-2966.2012.21549.x.

S. Repetto, A. P. Igoshev, and G. Nelemans. The Galactic distribution of X-ray binaries and its implications for compact object formation and natal kicks. MNRAS, 467:298–310, May 2017. doi: 10.1093/mnras/stx027.

A. Rimoldi, E. M. Rossi, T. Piran, and S. Portegies Zwart. The fate of supernova remnants near quiescent supermassive black holes. MNRAS, 447:3096–3114, Mar. 2015. doi: 10.1093/mnras/stu2630.

C. Rodriguez, G. B. Taylor, R. T. Zavala, A. B. Peck, L. K. Pollack, and R. W. Romani. A Compact Supermassive Binary Black Hole System. ApJ, 646:49–60, July 2006. doi: 10.1086/504825.

J. Rossa, R. P. van der Marel, T. Böker, J. Gerssen, L. C. Ho, H.-W. Rix, J. C. Shields, and C.-J. Walcher. Hubble Space Telescope STIS Spectra of Nuclear Star Clusters in Spiral Galaxies: Dependence of Age and Mass on Hubble Type. AJ, 132:1074–1099, Sept. 2006. doi: 10.1086/505968.

L. J. Rubbo, K. Holley-Bockelmann, and L. S. Finn. Event Rate for Extreme Mass Ratio Burst Signals in the Laser Interferometer Space Antenna Band. ApJ, 649:L25–L28, Sept. 2006. doi: 10.1086/508326.

P. Saha. Unstable modes of a spherical stellar system. MNRAS, 248:494–502, Feb. 1991. doi: 10.1093/mnras/248.3.494.

H. Sana and C. J. Evans. The multiplicity of massive stars. In C. Neiner, G. Wade, G. Meynet, and G. Peters, editors, *Active OB Stars: Structure, Evolution, Mass Loss, and Critical Limits*, volume 272 of *IAU Symposium*, pages 474–485, July 2011. doi: 10.1017/S1743921311011124.

H. Sana, G. James, and E. Gosset. The massive star binary fraction in young open clusters - III. IC 2944 and the Cen OB2 association. MNRAS, 416:817–831, Sept. 2011. doi: 10.1111/j.1365-2966.2011.18698.x.

D. B. Sanders, B. T. Soifer, J. H. Elias, B. F. Madore, K. Matthews, G. Neugebauer, and N. Z. Scoville. Ultraluminous infrared galaxies and the origin of quasars. ApJ, 325:74–91, Feb. 1988. doi: 10.1086/165983.

R. H. Sanders. The circumnuclear material in the Galactic Centre - A clue to the accretion process. MNRAS, 294:35, Feb. 1998. doi: 10.1046/j.1365-8711.1998.01127.x.

W. C. Saslaw, M. J. Valtonen, and S. J. Aarseth. The Gravitational Slingshot and the Structure of Extragalactic Radio Sources. ApJ, 190:253–270, June 1974. doi: 10.1086/152870.

M. Schartmann, A. Burkert, C. Alig, S. Gillessen, R. Genzel, F. Eisenhauer, and T. K. Fritz. Simulations of the Origin and Fate of the Galactic Center Cloud G2. ApJ, 755:155, Aug. 2012. doi: 10.1088/0004-637X/755/2/155.

M. Schmidt. 3C 273 : A Star-Like Object with Large Red-Shift. Nature, 197:1040, Mar. 1963. doi: 10.1038/1971040a0.

M. Schmidt and R. F. Green. Quasar evolution derived from the Palomar bright quasar survey and other complete quasar surveys. ApJ, 269:352–374, June 1983. doi: 10.1086/161048.

R. Schödel, T. Ott, R. Genzel, R. Hofmann, M. Lehnert, A. Eckart, N. Mouawad, T. Alexander, M. J. Reid, R. Lenzen, M. Hartung, F. Lacombe, D. Rouan, E. Gendron, G. Rousset, A.-M. Lagrange, W. Brandner, N. Ageorges, C. Lidman, A. F. M. Moorwood, J. Spyromilio, N. Hubin, and K. M. Menten. A star in a 15.2-year orbit around the supermassive black hole at the centre of the Milky Way. Nature, 419:694–696, Oct. 2002. doi: 10.1038/nature01121.

R. Schödel, A. Feldmeier, D. Kunneriath, S. Stolovy, N. Neumayer, P. Amaro-Seoane, and S. Nishiyama. Surface brightness profile of the Milky Way's nuclear star cluster. A&A, 566:A47, June 2014a. doi: 10.1051/0004-6361/201423481.

R. Schödel, A. Feldmeier, N. Neumayer, L. Meyer, and S. Yelda. The nuclear cluster of the Milky Way: our primary testbed for the interaction of a dense star cluster with a massive black hole. *Classical and Quantum Gravity*, 31(24): 244007, Dec. 2014b. doi: 10.1088/0264-9381/31/24/244007.

R. Schödel, E. Gallego-Cano, H. Dong, F. Nogueras-Lara, A. T. Gallego-Calvente, P. Amaro-Seoane, and H. Baumgardt. The distribution of stars around the Milky Way's central black hole II: Diffuse light from sub-giants and dwarfs. *ArXiv e-prints*, Jan. 2017a.

R. Schödel, E. Gallego-Cano, F. Nogueras Lara, H. Dong, and T. Gallego Calvente. The stellar cusp around the Milky Way's central black hole. In S. Arribas, A. Alonso-Herrero, F. Figueras, C. Hernández-Monteagudo, A. Sánchez-Lavega, and S. Pérez-Hoyos, editors, *Highlights on Spanish Astrophysics IX*, pages 308–315, Mar. 2017b.

N. Scott and A. W. Graham. Updated Mass Scaling Relations for Nuclear Star Clusters and a Comparison to Supermassive Black Holes. ApJ, 763:76, Feb. 2013. doi: 10.1088/0004-637X/763/2/76.

N. Scott, A. W. Graham, and J. Schombert. The Supermassive Black Hole Mass-Spheroid Stellar Mass Relation for Sérsic and Core-Sérsic Galaxies. ApJ, 768: 76, May 2013. doi: 10.1088/0004-637X/768/1/76.

J. L. Sersic. *Atlas de Galaxias Australes*. 1968.

A. Sesana. Self Consistent Model for the Evolution of Eccentric Massive Black Hole Binaries in Stellar Environments: Implications for Gravitational Wave Observations. ApJ, 719:851–864, Aug. 2010. doi: 10.1088/0004-637X/719/1/851.

A. Sesana and F. M. Khan. Scattering experiments meet N-body I: a practical recipe for the evolution of massive black hole binaries in stellar environments. *ArXiv e-prints*, May 2015.

A. Sesana, F. Haardt, and P. Madau. Interaction of Massive Black Hole Binaries with Their Stellar Environment. I. Ejection of Hypervelocity Stars. ApJ, 651: 392–400, Nov. 2006. doi: 10.1086/507596.

A. Sesana, M. Volonteri, and F. Haardt. The imprint of massive black hole formation models on the LISA data stream. MNRAS, 377:1711–1716, June 2007. doi: 10.1111/j.1365-2966.2007.11734.x.

A. Seth, M. Agüeros, D. Lee, and A. Basu-Zych. The Coincidence of Nuclear Star Clusters and Active Galactic Nuclei. ApJ, 678:116–130, May 2008. doi: 10.1086/528955.

P. Severgnini, C. Cicone, R. Della Ceca, V. Braito, A. Caccianiga, L. Ballo, S. Campana, A. Moretti, V. La Parola, C. Vignali, A. Zaino, G. A. Matzeu, and M. Landoni. Swift data hint at a binary supermassive black hole candidate at sub-parsec separation. MNRAS, 479:3804–3813, Sept. 2018. doi: 10.1093/mnras/sty1699.

S. Sigurdsson and E. S. Phinney. Binary–Single Star Interactions in Globular Clusters. ApJ, 415:631, Oct. 1993. doi: 10.1086/173190.

S. Sigurdsson and M. J. Rees. Capture of stellar mass compact objects by massive black holes in galactic cusps. MNRAS, 284:318–326, Jan. 1997. doi: 10.1093/mnras/284.2.318.

J. Silk and M. J. Rees. Quasars and galaxy formation. A&A, 331:L1–L4, Mar. 1998.

M. C. Smith, G. R. Ruchti, A. Helmi, R. F. G. Wyse, J. P. Fulbright, K. C. Freeman, J. F. Navarro, G. M. Seabroke, M. Steinmetz, M. Williams, O. Bienaymé, J. Binney, J. Bland-Hawthorn, W. Dehnen, B. K. Gibson, G. Gilmore, E. K. Grebel, U. Munari, Q. A. Parker, R.-D. Scholz, A. Siebert, F. G. Watson, and T. Zwitter. The RAVE survey: constraining the local Galactic escape speed. MNRAS, 379:755–772, Aug. 2007. doi: 10.1111/j.1365-2966.2007.11964.x.

A. Soltan. Masses of quasars. MNRAS, 200:115–122, July 1982. doi: 10.1093/mnras/200.1.115.

M. Spera, M. Mapelli, and A. Bressan. The mass spectrum of compact remnants from the PARSEC stellar evolution tracks. MNRAS, 451:4086–4103, Aug. 2015. doi: 10.1093/mnras/stv1161.

L. Spitzer. Book Review: Dynamical evolution of globular clusters. / Princeton U Press, 1987. *Physics Today*, 41:70, 1988. doi: 10.1063/1.2811501.

G. R. Stewart and S. Ida. Velocity Evolution of Planetesimals: Unified Analytical Formulas and Comparisons with N-Body Simulations. Icarus, 143:28–44, Jan. 2000. doi: 10.1006/icar.1999.6242.

A. Stolte, B. Hußmann, M. R. Morris, A. M. Ghez, W. Brandner, J. R. Lu, W. I. Clarkson, M. Habibi, and K. Matthews. The Orbital Motion of the Quintuplet Cluster–A Common Origin for the Arches and Quintuplet Clusters? ApJ, 789: 115, July 2014. doi: 10.1088/0004-637X/789/2/115.

O. Straub, O. Godet, N. Webb, M. Servillat, and D. Barret. Investigating the mass of the intermediate mass black hole candidate HLX-1 with the slimbh model. A&A, 569:A116, Sept. 2014. doi: 10.1051/0004-6361/201423874.

D. Syer, C. J. Clarke, and M. J. Rees. Star-disc interactions near a massive black hole. MNRAS, 250:505–512, June 1991. doi: 10.1093/mnras/250.3.505.

T. Tamfal, P. R. Capelo, S. Kazantzidis, L. Mayer, D. Potter, J. Stadel, and L. M. Widrow. Formation of LISA Black Hole Binaries in Merging Dwarf Galaxies: The Imprint of Dark Matter. ApJ, 864:L19, Sept. 2018. doi: 10.3847/2041-8213/aada4b.

K. Tanaka. ALMA Images of the Host Cloud of the Intermediate-mass Black Hole Candidate CO-0.40-0.22*: No Evidence for Cloud-Black Hole Interaction, but Evidence for a Cloud-Cloud Collision. ApJ, 859:86, June 2018. doi: 10.3847/1538-4357/aabd77.

J. Thomas, R. P. Saglia, R. Bender, P. Erwin, and M. Fabricius. The Dynamical Fingerprint of Core Scouring in Massive Elliptical Galaxies. ApJ, 782:39, Feb. 2014. doi: 10.1088/0004-637X/782/1/39.

K. S. Thorne. *Black holes and time warps: Einstein's outrageous legacy*. 1994.

K. S. Thorne and V. B. Braginskii. Gravitational-wave bursts from the nuclei of distant galaxies and quasars - Proposal for detection using Doppler tracking of interplanetary spacecraft. ApJ, 204:L1–L6, Feb. 1976. doi: 10.1086/182042.

A. Toomre and J. Toomre. Galactic Bridges and Tails. ApJ, 178:623–666, Dec. 1972. doi: 10.1086/151823.

A. Trani, M. Mapelli, M. Spera, and A. Bressan. Dynamics of tidally captured planets in the Galactic Center. *ArXiv e-prints*, Aug. 2016.

A. A. Trani, M. S. Fujii, and M. Spera. The Keplerian three-body encounter I. Insights on the origin of the S-stars and the G-objects in the Galactic center. *ArXiv e-prints*, Sept. 2018.

S. Tremaine and M. D. Weinberg. Dynamical friction in spherical systems. MNRAS, 209:729–757, Aug. 1984. doi: 10.1093/mnras/209.4.729.

S. D. Tremaine, J. P. Ostriker, and L. Spitzer, Jr. The formation of the nuclei of galaxies. I - M31. ApJ, 196:407–411, Mar. 1975. doi: 10.1086/153422.

I. Trujillo, P. Erwin, A. Asensio Ramos, and A. W. Graham. Evidence for a New Elliptical-Galaxy Paradigm: Sérsic and Core Galaxies. AJ, 127:1917–1942, Apr. 2004. doi: 10.1086/382712.

M. Tsuboi, A. Miyazaki, and S. K. Okumura. A Galactic Center 50-km s^{-1} Molecular Cloud with an Expanding Shell. PASJ, 61:29–37, Feb. 2009. doi: 10.1093/pasj/61.1.29.

M. Tsuboi, A. Miyazaki, and K. Uehara. Cloud-cloud collision in the Galactic center 50 km s^{-1} molecular cloud. PASJ, 67:109, Dec. 2015. doi: 10.1093/pasj/psv076.

M. Tsuboi, Y. Kitamura, K. Uehara, T. Tsutsumi, R. Miyawaki, M. Miyoshi, and A. Miyazaki. ALMA view of the circumnuclear disk of the Galactic Center: tidally disrupted molecular clouds falling to the Galactic Center. PASJ, July 2018. doi: 10.1093/pasj/psy080.

L. Šubr and J. Haas. Dynamical evolution of the young stellar disc in the Galactic centre. *Journal of Physics Conference Series*, 372(1):012018, July 2012. doi: 10.1088/1742-6596/372/1/012018.

L. Šubr and J. Haas. Two-body Relaxation Driven Evolution of the Young Stellar Disk in the Galactic Center. ApJ, 786:121, May 2014. doi: 10.1088/0004-637X/786/2/121.

L. Šubr and J. Haas. The Properties of Hypervelocity Stars and S-stars Originating from an Eccentric Disk around a Supermassive Black Hole. ApJ, 828:1, Sept. 2016. doi: 10.3847/0004-637X/828/1/1.

M. J. Valtonen. Are supermassive black holes confined to galactic nuclei? *Comments on Astrophysics*, 18:191–206, 1996.

M. J. Valtonen, H. J. Lehto, K. Nilsson, J. Heidt, L. O. Takalo, A. Sillanpää, C. Villforth, M. Kidger, G. Poyner, T. Pursimo, S. Zola, J.-H. Wu, X. Zhou, K. Sadakane, M. Drozdz, D. Koziel, D. Marchev, W. Ogloza, C. Porowski, M. Siwak, G. Stachowski, M. Winiarski, V.-P. Hentunen, M. Nissinen, A. Liakos, and S. Dogru. A massive binary black-hole system in OJ287 and a test of general relativity. Nature, 452:851–853, Apr. 2008. doi: 10.1038/nature06896.

E. Vasiliev. A new Monte Carlo method for dynamical evolution of non-spherical stellar systems. MNRAS, 446:3150–3161, Jan. 2015. doi: 10.1093/mnras/stu2360.

E. Vasiliev. A New Fokker-Planck Approach for the Relaxation-driven Evolution of Galactic Nuclei. ApJ, 848:10, Oct. 2017. doi: 10.3847/1538-4357/aa8cc8.

E. Vasiliev, F. Antonini, and D. Merritt. The Final-parsec Problem in Nonspherical Galaxies Revisited. ApJ, 785:163, Apr. 2014. doi: 10.1088/0004-637X/785/2/163.

E. Vasiliev, F. Antonini, and D. Merritt. The Final-parsec Problem in the Collisionless Limit. ApJ, 810:49, Sept. 2015. doi: 10.1088/0004-637X/810/1/49.

F. Verbunt, A. Igoshev, and E. Cator. The observed velocity distribution of young pulsars. A&A, 608:A57, Dec. 2017. doi: 10.1051/0004-6361/201731518.

M. Volonteri, P. Madau, and F. Haardt. The Formation of Galaxy Stellar Cores by the Hierarchical Merging of Supermassive Black Holes. ApJ, 593:661–666, Aug. 2003. doi: 10.1086/376722.

L. Wang, P. Berczik, R. Spurzem, and M. B. N. Kouwenhoven. The Link between Ejected Stars, Hardening and Eccentricity Growth of Super Massive Black Holes in Galactic Nuclei. ApJ, 780:164, Jan. 2014. doi: 10.1088/0004-637X/780/2/164.

M. Wardle and F. Yusef-Zadeh. On the Formation of Compact Stellar Disks around Sagittarius A*. ApJ, 683:L37, Aug. 2008. doi: 10.1086/591471.

B. L. Webster and P. Murdin. Cygnus X-1-a Spectroscopic Binary with a Heavy Companion ? Nature, 235:37–38, Jan. 1972. doi: 10.1038/235037a0.

S. D. M. White. Simulations of merging galaxies. MNRAS, 184:185–203, July 1978. doi: 10.1093/mnras/184.2.185.

S. D. M. White. Further simulations of merging galaxies. MNRAS, 189:831–852, Dec. 1979. doi: 10.1093/mnras/189.4.831.

B. Willems, M. Henninger, T. Levin, N. Ivanova, V. Kalogera, K. McGhee, F. X. Timmes, and C. L. Fryer. Understanding Compact Object Formation and Natal Kicks. I. Calculation Methods and the Case of GRO J1655-40. ApJ, 625:324–346, May 2005. doi: 10.1086/429557.

G. Witzel, A. M. Ghez, M. R. Morris, B. N. Sitarski, A. Boehle, S. Naoz, R. Campbell, E. E. Becklin, G. Canalizo, S. Chappell, T. Do, J. R. Lu, K. Matthews, L. Meyer, A. Stockton, P. Wizinowich, and S. Yelda. Detection of Galactic Center Source G2 at 3.8 μm during Periapse Passage. ApJ, 796:L8, Nov. 2014. doi: 10.1088/2041-8205/796/1/L8.

X.-B. Wu, F. Wang, X. Fan, W. Yi, W. Zuo, F. Bian, L. Jiang, I. D. McGreer, R. Wang, J. Yang, Q. Yang, D. Thompson, and Y. Beletsky. An ultraluminous quasar with a twelve-billion-solar-mass black hole at redshift 6.30. Nature, 518: 512–515, Feb. 2015. doi: 10.1038/nature14241.

D. Wysocki, D. Gerosa, R. O'Shaughnessy, K. Belczynski, W. Gladysz, E. Berti, M. Kesden, and D. E. Holz. Explaining LIGO's observations via isolated binary evolution with natal kicks. Phys. Rev. D, 97(4):043014, Feb. 2018. doi: 10.1103/PhysRevD.97.043014.

S. Yelda, A. M. Ghez, J. R. Lu, T. Do, L. Meyer, M. R. Morris, and K. Matthews. Properties of the Remnant Clockwise Disk of Young Stars in the Galactic Center. ApJ, 783:131, Mar. 2014. doi: 10.1088/0004-637X/783/2/131.

Q. Yu. Evolution of massive binary black holes. MNRAS, 331:935–958, Apr. 2002. doi: 10.1046/j.1365-8711.2002.05242.x.

K. Zubovas, G. A. Wynn, and A. Gualandris. Supernovae in the Central Parsec: A Mechanism for Producing Spatially Anisotropic Hypervelocity Stars. ApJ, 771: 118, July 2013. doi: 10.1088/0004-637X/771/2/118.

Acknowledgements
Ringraziamenti

This thesis is the final outcome of three long years full of hard work. First of all, I would like to thank my PhD supervisor, Michela, and my co-supervisor, Alessia, for introducing me to scientific research and for being so passionate about their job.

I thank Hagai Perets and Elena Rossi for carefully reading this manuscript and for providing relevant feedback. I also thank the numerous scientists I had the pleasure to meet and/or to collaborate with, especially people in Padova, Guildford and people I met at conferences and schools.

I thank the ones who cared about me and sustained me in these years, despite not having a clue about what the content of these pages is. In particular, I thank my whole family, and my old and new friends, especially those I rarely meet, for being always there for me. I thank Luca for making each day so much better. Finally, I would like to thank my beloved dad, to whom this thesis is dedicated. Your have been climbing the highest mountains of life, in spite of your non-moving legs. Thanks for teaching me the wonder for the beauty of this Universe. Most of what I am, I owe to you.

Questa tesi è il risultato di tre anni di duro lavoro. Vorrei innanzitutto ringraziare la mia supervisor, Michela, e la mia co-supervisor, Alessia, per avermi aiutato a capire cosa significa fare ricerca, e per la passione profonda e contagiosa che anima il loro lavoro.

Vorrei ringraziare Hagai Perets e Elena Rossi, che con pazienza hanno letto questo manoscritto e mi hanno aiutato a migliorarlo. Ringrazio tutte le persone con cui ho avuto il piacere di collaborare e/o avere discussioni scientifiche costruttive a Padova, a Guildford e ai tanti meeting a cui ho avuto la possibilità di partecipare.

Ringrazio tutti quelli che non hanno idea di cosa sia scritto in queste pagine, ma mi sono stati vicini e mi hanno sostenuto in questo faticoso percorso. In particolare vorrei ringraziare tutta la mia famiglia, soprattutto la mia mamma e la mia nonna. Ringrazio tutti i miei amici di vecchia e nuova data, in particolare quelli che vedo raramente ma ci sono sempre. Ringrazio di cuore Luca, senza il quale probabilmente avrei gettato la spugna da un pezzo, per aver reso ogni giornata infinitamente migliore. Infine ringrazio il mio papà, a cui questa tesi è dedicata, e a cui voglio un bene viscerale. Le tue gambe immobili non ti hanno impedito di scalare le montagne più alte della vita. Grazie per avermi insegnato lo stupore per le cose belle, la tenacia, la forza d'animo. Tantissimo di quello che sono, lo devo a te.